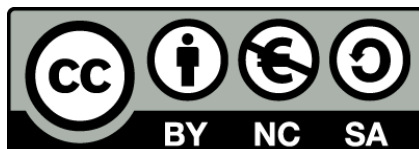UNIVERSITAT DE
BARCELONA

Quantum Confinement of Gaseous Molecules in Nanostructures: Effects on the Dynamics and Internal Structure

Manel Mondelo-Martell
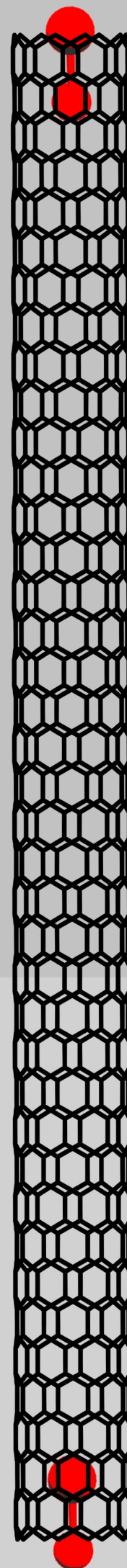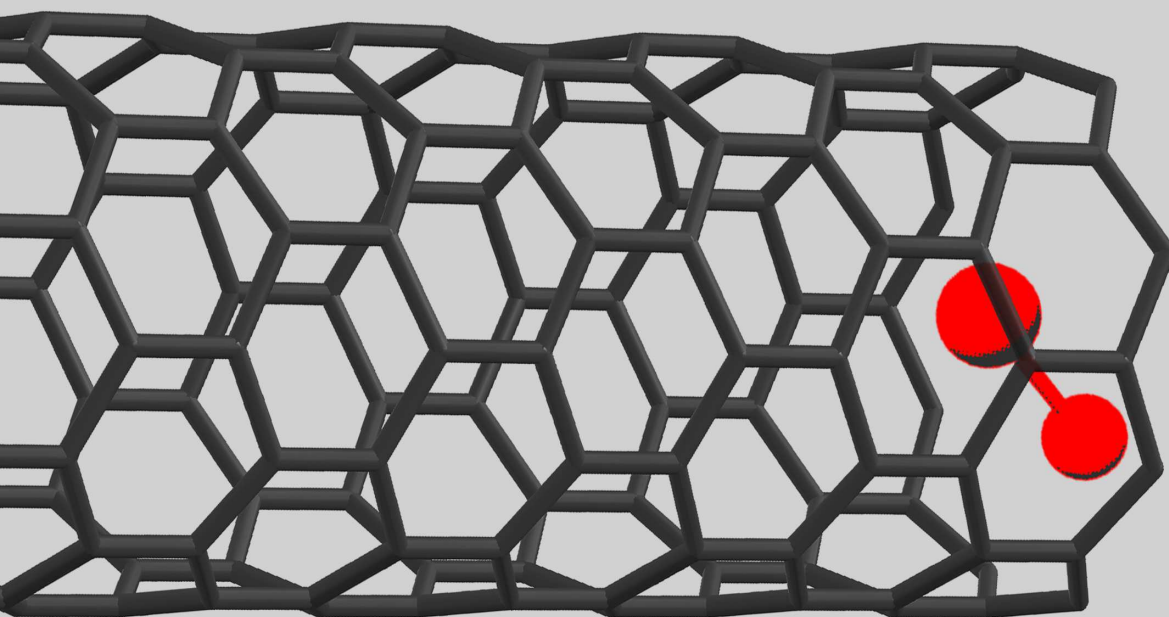
Quantum Confinement of Gaseous Molecules in Nanostructures:

Effects on the Dynamics and Internal Structure

Manel Mondelo Martell

UNIVERSITAT DE BARCELONA

UNIVERSITAT DE BARCELONA

Quantum Confinement of Gaseous Molecules in Nanostructures: Effects on the Dynamics and Internal Structure

*A thesis submitted in fulfillment of the requirements
for the degree of Doctor of Philosophy*

in the

Department of Materials Science and Physical Chemistry

by

Manel MONDELO–MARTELL

Supervisor:
Dr. Fermín HUARTE–LARRAÑAGA
Department of Materials Science and Physical Chemistry
Institute of Theoretical and Computational Chemistry
Universitat de Barcelona
Tutor:
Dr. Juan Carlos PANIAGUA VALLE
Department of Materials Science and Physical Chemistry
Institute of Theoretical and Computational Chemistry
Universitat de Barcelona

May 8, 2018

Declaration of Authorship

I, Manel MONDELO–MARTELL, declare that this thesis titled, "Quantum Confinement of Gaseous Molecules in Nanostructures: Effects on the Dynamics and Internal Structure" and the work presented in it are my own. I confirm that:

- This work was done wholly or mainly while in candidature for a research degree at this University.

- Where any part of this thesis has previously been submitted for a degree or any other qualification at this University or any other institution, this has been clearly stated.

- Where I have consulted the published work of others, this is always clearly attributed.

- Where I have quoted from the work of others, the source is always given. With the exception of such quotations, this thesis is entirely my own work.

- I have acknowledged all main sources of help.

- Where the thesis is based on work done by myself jointly with others, I have made clear exactly what was done by others and what I have contributed myself.

Signed:

_____

Date:

_____

"I can appreciate the beauty of a flower. At the same time, I see much more about the flower than he sees. I could imagine the cells in there, the complicated actions inside, which also have a beauty. I mean it's not just beauty at this dimension, at one centimeter; there's also beauty at smaller dimensions, the inner structure, also the processes. The fact that the colors in the flower evolved in order to attract insects to pollinate it is interesting; it means that insects can see the color. It adds a question: does this aesthetic sense also exist in the lower forms? Why is it aesthetic? All kinds of interesting questions which the science knowledge only adds to the excitement, the mystery and the awe of a flower. It only adds. I don't understand how it subtracts. "

Richard Feynman

UNIVERSITAT DE BARCELONA

Abstract

Faculty of Chemistry
Department of Materials Science and Physical Chemistry

Doctor of Philosophy

Quantum Confinement of Gaseous Molecules in Nanostructures: Effects on the Dynamics and Internal Structure

by Manel MONDELO–MARTELL

Quantum confinement effects, understood as the changes on the structure and dynamics of a molecule when it goes from a free environment to a cavity with some characteristic length of the order of the nanometer, represent both a challenge and an opportunity. A challenge, because there is still work to be done in order to be able to understand and model them properly. An opportunity, because they offer the means to tune molecular properties such as adsorption, diffusion, or even reactivity.

The present Doctoral Thesis is focused on the theoretical and computational study of the system consisting on a single H_2 (or D_2) molecule trapped in the hollow cavity of a narrow Single–walled Carbon Nanotube. Since Dillon and coworkers suggested in 1997 the existence of quantum confinement effects as an explanation for the unexpectedly high H_2 uptake in carbon nanotubes, this particular system has received much attention from theoretical and experimental points of view. Here we intend to gain more insight on it by developing new analysis tools for high dimensional eigenstates, and by improving the model with respect to previous works. The former has been achieved through the use of overlap and partial overlap functions, which has provided with an intuitive way to understand the coupling between the different degrees of freedom by comparison of the actual eigenstates of the system with a separable model. Regarding the improvement of the model, we have worked on it from two perspectives: first, we have included new molecular degrees of freedom to the system, namely the motion of the center of mass of the molecule along the axis of the nanotube. This has allowed us to obtain diffusion rates for H_2 and D_2 inside the nanotube in a full quantum mechanics framework, which to the best of our knowledge had not been achieved before. The study of the diffusion dynamics has also allowed us to define an adiabatic representation of the Hamiltonian, taking advantage of the quasi separability of the diffusion coordinate and the remaining degrees of freedom, to increase the efficiency of the propagations with high accuracy. As a second means to improve the model, we have developed a system–bath coupling Hamiltonian in order to see how the phonons of the nanostructure affect the dynamics of the confined molecule. We have seen that both sets of degrees of freedom (molecular and phonons) are strongly coupled due to the linear momentum exchange between them. Time–dependent Perturbation Theory calculations have determined that the characteristic time for the momentum exchange is shorter than that for diffusion, which suggests that the friction with the nanotube may have a relevant effect on the transport properties of the confined molecule.

UNIVERSITAT DE BARCELONA

Resum en Català

Facultat de Química
Departament de Ciència de Materials i Química Física

Doctorat

Confinament Quàntic de Molècules Gasoses en Nanoestructures: Efectes sobre la Dinàmica i l'Estructura Interna

per Manel MONDELO–MARTELL

Els efectes de confinament quàntic, entesos com els canvis en l'estructura i la dinàmica d'una molècula quan va des d'un entorn lliure a una cavitat amb alguna longitud característica de l'ordre del nanòmetre, representen un repte i una oportunitat. Un repte, perquè encara hi ha feina per poder comprendre-les i modelar-les correctament. Una oportunitat, perquè ofereixen els mitjans per ajustar les propietats moleculars, com adsorció, difusió o fins i tot reactivitat.

La present tesi doctoral es centra en l'estudi teòric i computacional del sistema consistent en una sola molècula de H_2 (o bé de D_2) atrapada a la cavitat interna d'un nanotub de carboni estrets d'una sola paret. Desde que Dillon i coautors van suggerir al 1997 l'existència d'efectes de confinament quàntic com a explicació de la inesperadament alta adsorció de H_2 en nanotubs de carboni, aquest tema ha rebut molta atenció des de punts de vista teòrics i experimentals. La intencíd'aquesta Tesi és obtenir més informació sobre aquest fenòmen mitjançant el desenvolupament de noves eines d'anàlisi per a estats propis d'alta dimensionalitat, i la millora del model respecte a treballs anteriors. El primer s'ha aconseguit mitjançant l'ús de funcions de solapament i solapaments parcial, que han proporcionat una manera intuïtiva d'entendre l'acoblament entre els diferents graus de llibertat per comparació amb estats propis reals d'un model separable del sistema. Pel que fa a la millora del model, hem treballat des de dues perspectives: en primer lloc, hem inclòs nous graus de llibertat moleculars al sistema, concretament el moviment del centre de massa de la molècula al llarg de l'eix del nanotub. Això ens ha permès obtenir coeficients de difusió per al H_2 i el D_2 dins del nanotub utilitzant un formalisme totalment mecànic–quàntic, cosa que no s'havia fet prèviament. L'estudi de la dinàmica de difusió també ens ha permès definir una representació adiabàtica de l'Hamiltonià del sistema, aprofitant la quasi separabilitat entre la coordenada de difusió i la resta de graus de llibertat, per tal d'augmentar l'eficàcia de les propagacions amb gran precisió. Com a segon mitjà per millorar el model, hem desenvolupat un Hamiltonià d'acoblament sistema–bany per tal de veure com els fonons de la nanoestructura afecten la dinàmica de la molècula confinada. Hem vist que ambdós conjunts de graus de llibertat (moleculars i fonons) estan fortament acoblats a causa de l'intercanvi de moment lineal entre ells. Càlculs de Teoria de Perturbacions Dependents del Temps han determinat que el temps característic de l'intercanvi de moment és més curt que el de la difusió, cosa que suggereix que la fricció amb el nanotub pot tenir un efecte rellevant sobre les propietats del transport de la molècula confinada.

Agraïments

De vegades no te n'adones de com ha passat el temps fins que no has d'escriure uns agraïments, i comences a recapitular, i te n'adones de la quantitat de gent que has tingut al teu costat. Amb aquesta Tesi acabo un cicle vital de gairebé 5 anys. En aquest temps he crescut, vull pensar, com a científic i com a persona; de vegades de forma més gradual, de vegades a batzegades i cops. Però si ho he aconseguit ha estat gràcies a la gent que ha passat per la meva vida en aquest temps, ja fos temporalment o per quedar–s'hi, ja haguessin format part d'ella des d'abans, o arribessin de nou.

Abans que res vull agraïr al meu Director, en Fermín, qui m'ha guiat des dels meus primers dies com a becari de col·laboració fins avui mateix. Han estat molts anys barallant–nos amb nanotubs i funcions d'ona, discutint sobre MCTDH i papers, compartint impressions i, durant una temporada fins i tot barri! Gràcies per pel seu suport, per demostrar sempre la teva confiança en mi, i ensenyar–me amb això a valorar la meva pròpia feina. Al Jaime Suárez, *former* post–doc que va inicial la branca de recerca que ha donat lloc a aquesta tesi, i que tant em va ajudar després del Màster. També a la resta de membres del Grup de Dinàmica de Reaccions Químiques: a l'Antonio, tota una referència per a mi a nivell científic i personal; al Josep Maria, a través de qui vaig introduïr–me al Grup; a la Margarita, per contagiar–me sempre la seva energia; i al Jaime, que malauradament no podrà veure finalitzar aquesta Tesi. Com trobem a faltar els teus tès, i sobretot les trobades que motivaven!

I would like to acknowledge the supervisor of my research stays in Unversität Bielefeld, Prof Uwe Manthe, who has become my second mentor. Through our discussions I have learnt of quantum dynamics, computer science, Germany, politics and history. Thank you for your patience, for pushing my limits and for welcoming me in your group any time I have visited you. To all the members I have met in the *Theoretische Chemie* group: Wolfgang, Thorstein, Till, Ralph, Niels, Florian, Roman, Tim, Daniella, David, Thomas; thank you for offering me your friendship. Roman and Tim, I particularly *blame* you for discovering *boulder* to me, one of the few sports I have genuinely enjoyed –even though it has caused me to brake my arm!–.

Als meus companys del despatx 443A: el Daniel, el Gerard i l'Héctor, que han viscut les frustracions i éxits d'aquesta Tesi de ben aprop, i a la Estefi, que tot i no compartir espai ha estat sempre amb nosaltres, us he de donar gràcies per la vostra ajuda, a nivell tècnic i sobretot moral. No sabeu el plaer que és treballar envoltat de gent com vosaltres, d'amics. També a tots els que han passat pel despatx durant aquests anys: el Víctor i el Javi, que ja hi eren quan vaig arribar; el Toni i el Carles, que ens van abandonar en acabar els respectius Màsters; l'Adrià, el Pablo, el Biel i el Joan, que han començat el seu camí en la recerca entre aquestes quatre parets; el Juan i l'Ángel, que han compartit la seva experiència com a Post–Docs amb nosaltres; i a tots els que m'he deixat. A la resta de membres del Departament i l'Institut de Química Teòrica i Computacional, que m'han vist crèixer en aquests anys, i particularment al nostre *veí* Albert Solè, qui m'ha salvat de més d'una catàstrofe informàtica (i d'algún *mental breakdown*), i l'Iberio Moreira, qui m'ha ajudat a endinsar–me en el món de la física de l'estat sòlid. També als companys de promoció amb qui he aconseguit mantenir el contacte, tot i que en molts casos menys del que m'hagués agradat: Alba i Pablo, Mariona, Alejandro, Javi, Raquel, Ari, i a tota la gent que m'heu presentat. Als que he arribat a conèixer només recentment, dins i fora del Departament, dir–vos: tan de bo hagués estat abans! I finalment, a la gent amb qui vaig començar aquest camí, els últims alumnes del *Màster Català* en Química Teòrica

i Computacional, tot i que els nostres camins es vagin separant espero que aquest nexe no s'arribi a difuminar mai del tot (sempre ens quedarà la Xarxa!).

Però per suposat, hi ha molta gent fòra de la Facultat a qui dec moltíssim, i sense qui probablement no hagués estat capcaç de tancar aquesta etapa mantenint la meva salut mental. Raúl, Xavi, Hector i Carlota: no sé si mai sereu conscients del pilar que representeu per a mi. A la resta dels meus imprescindibles; Mercè, David, Judit, Marta, Ivana, Lluis, Àlex, Irene: sabeu que de vegades em refereixo a vosaltres com a *família*, i ho faig perquè ho sento així: ja fa 10 anys que us vaig conèixer, i malgrat tot el que hagi passat en aquest temps, heu estat una constant en la meva vida i sé que ho seguireu sent. A l'Eva, la persona que més de prop ha viscut aquest cicle que hem tancat i amb qui més he compartit, no puc dir–li res que no sàpiga ja. A l'Anna, l'Antònia i el Josep Lluís; a la Montse, la Carme i la Irene, només puc donar-vos les gràcies per haver-me deixat ser part de la vostra família. A la Maria i l'Alicia, amb qui m'he retrobat aquest últim any i mig: heu aparegut just quan més ho he necessitat, i això ho guardaré sempre. I encara més gent que, sabent-ho o no, per molt o poc temps, m'ha acompanyat i influït en diversos trams: companys de música, d'alemany, d'escalada i tir.

Però si hi ha algú a qui he d'agraïr haver arribat a aquest punt és a la meva família. Al meu pare, de qui algun dia arribaré a aprendre, espero, com a mínim *la mitad de lo que ya has olvidado*; perquè amb la mama m'heu trasmés els vostres valors i experiències de la forma més natural que puc imaginar. Al meu germà Pau, a qui estimo tant que de vegades no sé si ho demostro prou. És impressionant haver–te vist crèixer en tants sentits, i només espero que la nostra complicitat també creixi encara més. A la resta de família: tot i que els mals moments hagin acabat passant factura, gràcies per tots els bons moments viscuts i per viure.

Aquesta última part dels agraïments és la més difícil, i la que no hagués volgut escriure mai. La dedico, així com tota la Tesi en el seu conjunt, a la meva mare i la meva àvia, que ens han deixat abans de poder veure'm tancar aquest cicle. Mama, si sóc qui sóc i he arribat on he arribat, si he après a lluitar pel que és important per a mi, ha estat gràcies a tu i al Papa. La teva absència em pesarà sempre, però sempre et tindré com a referència. Yaya, has hecho tanto por mi y todos nosotros que nunca te lo hubieramos sabido devolver. Us estimo, i us trobo (us trobaré sempre) a faltar.

Contents

List of Abbreviations

AFM	Atomic Force Microscope
a.u.	arbitrary units
BO	Born–Oppenheimer
CDVR	Correlation Discrete Variable Representation
cePES	Confined Eigenstates Potential Energy Surface
CMS	Carbon Molecular Sieve
c.o.m.	Center of Mass
CRP	Cumulative Reaction Probability
DVR	Discrete Variable Representation
DOF	Degree of Freedom
EOM	Equation of Motion
FBR	Finite Basis Representation
FM	Fourier Method
FFT	Fast Fourier Transform
HEG	Harris-Engerhorn-Gwinn
KEO	Kinetic Energy Operator
KIE	Kinetic Isotope Effect
LJ	Lennard–Jones
MCTDH	Multiconfigurational Time–dependent Hartree
ML-MCTDH	Multi–layer Multiconfigurational Time–dependent Hartree
MOF	Metal–Organic Framework
PBC	Periodic Boundary Conditions
PES	Potential Energy Surface
SA-MCTDH	State–Averaged Multiconfigurational Time–dependent Hartree
SEM	Scanning Electron Microscope
STM	Scanning Tunneling Microscope
SPF	Single Particle Function
SWCNT	Single–Walled Carbon Nanotube
TDDVR	Time–Dependent Discrete Variable Representation
TDH	Time–dependent Hartree
TDPT	Time–Dependent Perturbation Theory
TDQD	Time Dependent Quantum Dynamics
TDSE	Time–Dependent Schrödinger Equation
TIQD	Time Independent Quantum Dynamics
TISE	Time–Independent Schrödinger Equation
VBR	Variational Basis Representation
ZPE	Zero–Point Energy

A la meva mare

Chapter 1

Introduction: Nanoscience and Quantum Confinement Effects

Nanoscience and Nanotechnology are interdisciplinary fields which deal with the study and manipulation of systems with at least one characteristic dimension between 1 and 100 nm. Many of the main ideas and concepts which would latter define these disciplines were laid out by Feynman in his lecture *There's Plenty of Room at the Bottom* in the meeting of the American Physical Society held in Caltech in 1962[1]. There, he envisioned how we would be capable of the observation and manipulation of matter with ever increasing precision, and how this would lead to an extreme miniaturization of electronic and mechanical components, and even to individually control of the atoms and molecules themselves. In spite of the revolutionary ideas of Feynman's seminar, its impact in the scientific community was rather low due to the technical limitations of the Scanning Electron Microscopes (SEM), which were the most potent instruments at the time: according to Feynman, their resolution was 100 times too low to be able to actually see or manipulate atoms, and that value was already in the theoretical limit for a SEM's resolution. The lack of better instrumentation caused the ideas of the talk to be seen as little more than interesting science fiction exercise. The technical limitations, however, were overcome in 1982 with the invention of the Scanning Tunneling Microscope (STM)[2], an instrument based on measuring the current which appeared between a metallic surface and an extremely sharp tip. With this brand new instrument the actual observation and manipulation of matter at atomic scale became a real possibility: the atomic resolution was first observed in 1983 for the Au(110) surface[3], metallic structures were manipulated in 1987[4], and individual molecules manipulated in 1988[5]. Finally, in 1990 individual Xe atoms were arranged onto a nickel surface to conform a pattern reading *IBM*[6]: control of matter at atomic level had been achieved. The importance of this invention granted the main contributors to its development the Nobel Prize in physics in 1986[7]. That very same year the Atomic Force Microscope (AFM) was developed by Binnig[8, 9], one of the developers of the STM, broadening the possibilities of visualization and manipulation at the most fundamental level.

However, the advent of nanotechnology came not only from technical development, but also from new discoveries. A new breakthrough in the field was the discovery of buckminsterfullerene in 1985[10], during the simulation in the laboratory of chemical reactions in the atmospheres of red giant stars. This structure was the first nanostructured material to be found in nature. The subsequent discovery of carbon nanotubes by Iijima[11] in 1991, together with the large amount of technical possibilities that these materials offered, boosted the newly created field of Nanoscience and Nanotechnology. Moreover, new phenomena at the nanoscale were discovered which did not appear in larger systems: as the dimensions of the systems got close to

the de Broglie wavelength of the atoms and electrons, the properties of the bulk material changed appreciably due to the strong interactions present. As new research was conducted on nanostructured materials, the potential applications increased and broadened from nanoelectronics to medicine, and nowadays nanotechnology is a topic of general interest onto which a large amount of resources are invested.

1.1   Quantum confinement effects and Nanotechnology

Energy storage: a driving force for research

One characteristic which clearly distinguishes a nanostructured material from a regular bulk system is the high surface-area ratio of the former. It is well known that microporous materials can present a high uptake of gaseous substances by physisorption of the molecules in the different cavities of the material, thus storing large quantities of low-density compounds in a reduced space[12]. Research made on micro and nanoporous materials (such as amorphous silica) in the late 1980s already hinted at interesting new behavior of the adsorbed molecules[13]. Therefore, the natural step was to try to use nanostructured materials as storage devices for particularly light gases, such as hydrogen or methane. The first attempts to use carbon nanotubes to capture pure hydrogen were made in the late 90s and resulted in promising uptake values: the first Temperature programed Desorption experiments made in 1997 predicted storage densities ranging from 5 to 10% in weight[14]. These values seemed to indicate again a change of the behavior of the H_2 molecules when they were trapped in the nanomaterial, since the density of molecules was reported to be 2.5 to 5 times larger than the theoretical predictions. The theoretical works around that time also predicted a change in the inner structure of CO and H_2 when adsorbed in solid C_{60}[15, 16], and a change of the dynamics of H_2 and D_2 in carbon nanotubes and zeolites[17], thus supporting the interpretation. Further experiments at room temperature, however, reported a slightly lower storage capacity of 4.2%[18]. The interest for the storage of gases in nanostructured materials increased due to the enormous popularity of hydrogen as an alternative to fossil fuels in modern societies[19, 20], and the difficulties to store it for transport and mobile applications. At the time, either conventional tanks at very high pressures –which required thick walls, and therefore high weight of the container— or liquid storage —involving very low temperatures, and thus more energy consumption— where used, which drastically decreased the overall efficiency of H_2 as a fuel. According to the US Department of Energy, the storage capacity of hydrogen for a new device to be accepted should have been of 6% in weight by 2010 and 9% by 2015. With such a high quality standard, the research for more efficient storage devices based on nanostructured materials was a driving force leading to great advances in the beginning of the 21st century, both at experimental and theoretical levels, with hydrogen and different nanostructured carbon materials as protagonists. These investigations confirmed the special behavior of the molecules adsorbed in nanostructured materials.

A new behavior in nanospace

The interaction between bulk solid materials and molecules lies at the origin of critically important phenomenon such as gas adsorption or liquid wetting, and have been studied since the early days of physical chemistry. These same interactions,

usually consisting on attractive Van der Waals forces and other electrostatic influences, also appear when a molecule approaches a nanostructured material. However, in contrast to the well-known phenomena occurring in bulk systems, the properties of the adsorbate change notably in this latter case: molecules might be packed more tightly than expected in nanoporous materials, or usually wetting liquids might become repelled by a nanostructured surface. The underlying reason for all these unexpected behaviors is the presence of some characteristic dimension of the material of the order of the nanometer, being it one (thin–layers), two (nanotubes) or three (nanopores). The interactions between substrate and adsorbate then appear in a range comparable to the de Broglie wavelength of molecules, and therefore the very same quantum structure of the system is affected. This results in the unexpected properties of nanoconfined species. In a molecular context, the changes in the electronic structure, conformations and dynamics of molecules resulting of their adsorption in cavities with a characteristic length of the order of the nanometer are collectively known as *quantum confinement effects*[1]. These phenomena have arose a great interest in the scientific community, both for their fundamental implications and for the possibility to take advantage of them to design better storage and gas separation devices, and even to tune the reactivity of certain chemical systems, and its theoretical study is the main topic of this Thesis.

The origins of the research on quantum confinement are the experimental evidences of special behavior of adsorbates trapped in nanostructured amorphous silica (see Ref. [13] and references therein). Those works led Beenakker et al. to the theoretical study of gas flow through nanoscopic channels[21] and of the adsorption of structureless particles in tight confining potentials[22]. Earlier studies[23] had already proposed that separation of H_2 and D_2 in bulk alumina could be possible due to their different diffusion coefficient. Beenakker et al. were able to explain this phenomenon by studying the Zero Point Energy (ZPE) remaining in the confining degrees of freedom when a particle entered in a nanoscopic pore: if the cavity had a diameter small enough, the energy levels associated with the motion of the center of mass, which form a continuum in the case of a free particle, would quantize. This quantization would lead to a ZPE, which would be inversely proportional to the mass of the particle. The authors coined the term *quantum molecular sieve* to describe materials capable to separate species based on these purely quantum effects. The theory was latter revisited by Wang et al.[17], introducing explicit molecules such as H_2 and T_2, and more realistic potential to model the nanopore.

Experimental and Theoretical advances

The end of the 90s and the beginning of the 21st century witnessed an expansion of the quantum confinement field, with numerous contributions appearing at both experimental and theoretical levels. Experimentally, neutron diffraction experiments provided with accurate information about the structure of confined molecules, showing that H_2 in solid C_{60} was adsorbed preferentially in octahedral sites in the interstitial space with no preferred orientation[16]. Moreover, ortho–para conversion of the diatoms was observed. In the case of single–walled carbon nanotubes, initial findings did not find any critical confinement effect in the eigenvalue spectrum of hydrogen[24], while a quasi–one dimensional phase appeared for Xenon[25]. At the

---

[1]In more physics or condensed matter contexts, this name accounts for the change on electronic and optical properties of a material with some dimension of the order of 10 nm or less.

same time, semiclassical electronic structure calculations were used to study the co–adsorption of lithium and hydrogen in zig–zag nanotubes[26], suggesting that a funcionalization of the nanostructure could improve its adsorption properties. On another research line, model Hamiltonians where used to compute the nuclear eigenstates of hydrogen in fullerenes[27, 28] or narrow carbon nanotubes[26, 29], thus helping to explain the experimental findings in terms of rotational–translational coupling and to propose these materials as potential separation devices for hydrogen isotopologues. In the following years some other works appeared which studied, at both experimental and computational level, other adsorbates, such as CO_2[30] or CH_4[31, 32], and adsorbents, such as Metal–organic Frameworks[33]. Still, the simplicity of H_2, its relevance as a potential fuel and the problem of its storage, and the interest in its isotopic separation, kept the hydrogen molecule and its isotopologues as the most prominent subjects of study. A major impact work was released by Lu et al., who computed nuclear eigenstates of rigid H_2, D_2 and T_2 embedded in carbon nanotubes with different diameters, and predicted a huge selective adsorption of the heavier isotopes in narrow SWCNTs, with D_2 being adsorbed up to 10^6 times more favorably than H_2 for nanotubes with less than 3.5 Å of radius[34]. The analysis of the eigenstates of the system allowed them to propose *Extreme Two–dimensional Confinement*, as appearing when the nanotube's radius was almost equal to the characteristic length of the C–H interaction, as the reason for this high selectivities. This work was complemented by Garberoglio et al., who carefully assessed several C–H interaction models to justify the different results obtained[35]. A similar contribution including the molecule's vibration on the system, acting as a precursor to our work, appeared in 2012[36]. At roughly the same time as the description of the extreme 2D confinement and the huge selectivities predicted, Kumar and Bhatia revisited the topic of *kinetic* quantum sieving, *i.e.* the possibility to use the different diffusion velocity of hydrogen isotopologues, rather than its selective adsorption, to induce separation in Carbon Molecular Sieves (CMS). They performed different computational techniques, namely Monte Carlo and Feynman–Hibbs molecular dynamics[37–39], and found an *inverse isotope kinetic effect* at low temperatures which made D_2 diffusion faster than that of H_2 in those materials, due to the same ZPE effects inducing selective adsorption. Later, Hankel et al. used Transition State Theory to get to similar conclusions[40] which were backed up by experimental findings[41, 42]. Recently, we have also contributed in this area by presenting quantum dynamics studies on the diffusion in carbon nanotubes[43, 44] and showing that in this system the tunnel effect, neglected in previous works, is so important at the temperature range studied that the zero–point effects are overcomed, and H_2 diffuses faster than D_2 at all temperatures. Lately this effect has been also predicted for He isotopes crossing nanoporous graphene membranes[45].

In the last decade the general availability of powerful computers and computation clusters has permitted research on more complex systems with different tools, such as molecular dynamics[46] or purely ab initio electronic structure calculations[47–49]. Due to the practical limitations of pure Carbon Nanotubes as storage devices for hydrogen[50] attention has been shifted to functionalized carbon materials[49, 51–53], MOFs[54–62], and also on different substrates as methane[63–66], CO_2[33, 51, 67–69] or water[39, 70–74]. The contribution of Bazic and coworkers[58, 75–80], combining inelastic neutron scattering experiments and theoretical modeling and computation of nuclear eigenfunctions for a number of different systems has been particularly multidisciplinar and comprehensive, and therefore deserves special mention.

1.2 Overview and main objectives

It is clear from the historical development of nanoscience, specifically regarding molecular confinement effects, that experiments and theory complement each other: either experimental evidences need to be theoretically investigated in order to understand and model them, or theoretical predictions must be confirmed, thus providing with new ideas and challenges for experiments.

This Thesis is focused on the modeling, theoretical and computational investigation of the hydrogen molecule confined in narrow SWCNTs using quantum dynamics tools. The Objectives pursued during the development of this work have been the following:

- Constructing a model to describe a molecule confined in the hollow cavity of a SWCNT. This will be done in two steps: first considering only the DOFs of the adsorbate, and secondly adding the vibration of the nanostructure and its coupling to the molecular DOFs.

- Understanding the coupling between different degrees of freedom of the adsorbate, from two different perspectives: first, the coupling between the confined degrees of freedom; second, the correlation between these confined DOFs and the motion along the nanotube axis.

- Obtaining diffusion rates for the hydrogen and deuterium molecules in a fully quantum formalism. This will allow us to better understand the diffusion mechanism, as well as to investigate the Kinetic Isotope Effect in this system.

- Investigating the time scales of the different motions of the adsorbate when confined in carbon nanotubes, with the prospect of developing alternative representations based on the adiabatic theorem.

- Improving the model of the system by including the vibrations of the nanostructure and their coupling to the adsorbate's motion.

Contribution of the Thesis

Our final goal has been to improve the simulation model and to study different processes in the nanoscale. The research performed during this Thesis has advanced always towards an increase of the complexity and understanding of the system. In our first contribution, we developed a tool to visualize the effects of quantum confinement in the molecular structure of a diatom fixed in a particular point along the nanotube. This was done by partially overlapping its wave function with some reference system, as explained in Chapter 5 and **Publication 1**. The results clearly confirmed previous observations about the importance of rotranslational coupling in the system. Then, by adding the motion of the c.o.m. of the molecule along the axis of the nanotube and using the tools previously made we assessed the coupling between the diffusing motion of the molecule and the remaining degrees of freedom. Our simulations showed that these two sets of coordinates were nearly decoupled (**Publication 3**). This lead to the elaboration of a time–scale separation scheme, based on considering the motion of the fast, high–frequency motion in the confined degrees of freedom as averages, generating a potential for the motion along the nanostructure. This part of the Thesis has been reported in form of two publications (**Publication 3** and **Publication 4**), and is reviewed in Chapter 7. With the 6 degrees of freedom taken into account, we were able to find diffusion rates for

H_2, and to investigate the kinetic quantum sieving effect predicted by Beenakker et al.[22] and confirmed by Kumar and Bhatia[37]. During the first full–dimensional calculations, deuterium was found to diffuse faster than hydrogen at low temperatures. This was consistent with computational and experimental studies on diffusion along Carbon Molecular Sieves. However, a posterior study using the time–scale separation scheme allowed us to extend the propagation times, yielding numerically converged results, and unveiled the importance of the tunnel effect in the diffusion of both isotopologues, being this effect so important at low temperatures that H_2 diffused faster than D_2 in all the temperature range studied. The first results were published in **Publication 2**, and together with the final results in **Publication 4** and some unpublished data conform Chapter 6. The final contribution of this Thesis is related to going beyond one of the most widely spread approximations used when dealing with confined systems: the frozen structure approximation, which considers all the atoms forming the substrate as fixed in their equilibrium positions, without any kind of vibration. This procedure vastly simplifies the study of the system, since one only considers the degrees of freedom of the adsorbate itself. However, due to the importance of phonon dispersion in most dynamical events appearing in the solid state, it is expected that its inclusion has a major effect on processes such as diffusion. This is the reason why we have developed a system–bath coupling model, considering an arbitrary number of phonons of the nanostructure as acting as a *bath* of harmonic oscillators coupled with our system, which is the adsorbate molecule. By using time–dependent perturbation theory, we computed the transition rates between 6D states of the system and also their life times as a function of the bath's temperature. These results are found in Chapter 8, and are to be published soon.

Chapter 2

Quantum Dynamics

Ranging from the exchange of energy when a molecule interacts with an electromagnetic field to the conformational changes of a protein, through the rearranging of atoms during a chemical reaction, change is the essence of chemistry. It is precisely the microscopic evolution of the different components of a chemical system (the *dynamics* of the electrons and nuclei) that explains observations such as the kinetics or spectroscopic phenomena in the macroscopic world. The study of these processes require of specialized tools due to their scale and complexity. For instance, classical mechanics laws are not able to describe electrons, present in any chemical process, due to their size, and for this reason a quantum mechanical framework is needed for them, as well as for light atoms such as hydrogen. The complexity of the resulting equations require several assumptions and approximations in order to be solvable, and the implementation of the final problem in a computer program is also an important issue. And finally, one has to bridge the microscopic results with something meaningful at a macroscopic level, which requires the use of statistical mechanics.

The present Chapter is dedicated to the description of such tools, and is organized in three different sections. The first section will serve as a reference for the basic concepts of quantum mechanics, specially focusing in the branch dealing with the motion of the particles in the system, known as quantum dynamics. Here we will discuss generally relevant topics such as the Born-Oppenheimer approximation, which allows to deal with otherwise impossible to study systems. The second section is devoted to the representation of the wave function and operators in a finite–dimension Hilbert space, which is required for the numerical resolution of quantum systems. The third section is specifically devoted to Time-dependent Quantum dynamics, and will present this approach to Quantum Dynamics by using wave packets, defining the evolution operator and the approximate methods for propagating a function in time.

2.1   Formalism of Quantum Dynamics

In classical mechanics, the concept of dynamics is intrinsically linked with that of *trajectory* and *action*: at each time it is possible to perfectly reproduce the position of a particle as a function of time, as well as its energy, by knowing the instantaneous forces acting on it in a single time instant and applying Newton's second law. This view is blurred in a microscopic system: instead of a trajectory for each particle, the whole system is described by a *wave function*, $\Psi(x, t)$ which contains the probability density amplitude at each point in space for each value of time. For a function to be able to describe a particular physical system, and therefore to be a wave function, it

must be complex, square–integrable and double differentiable. The set of all functions obeying these criteria form an infinite–dimensional vector space known as the *Hilbert Space*, $\mathcal{H}$[81].

For time–independent Hamiltonians, which define conservative systems, a particularly important basis of the Hilbert space arises from the set of solutions to the Time–independent Schrödinger Equation (TISE):

$$\hat{H}\Psi_j = E_j\Psi_j, \tag{2.1}$$

where the operator $\hat{H}$ is the *Hamiltonian* of the system, which reads:

$$\hat{H} = -\frac{\hbar^2}{2m}\nabla^2 + V(\vec{x}), \tag{2.2}$$

with ∇^2 the Laplacian of the system. Classically, this operator corresponds to the total energy of the system, and therefore in a quantum mechanical context its eigenvalues, E_j, correspond to the available energy levels of the system. Similarly, the eigenfunctions of this equation, Ψ_j, correspond to *stationary states* of the system under study, *i.e.*, states with a well-defined energy which, unless perturbed, will not change in time[1]. They are extremely relevant in physics and chemistry, since their energies are related to spectroscopic transitions.

For such conservative systems it is possible to build the whole formalism of quantum dynamics from this time–independent view of the system: one needs to set the correct boundary conditions to Eq (2.1) and obtain the *scattering functions* for each energy, $\Psi_f(E)$. This was the first approach developed in the early stages of the field, due to the suitability for the problems of interest at the time, which were basically related with understanding line spectra of different bound systems[82]. However, the everyday familiarity of human minds with classical mechanics and its trajectory-based approaches might make it difficult to obtain an intuitive understanding of a dynamical process in a time–independent framework. If we include time in the formalism, the dynamics of the system is then related with the time evolution of the wave function, which is given by the Time–dependent Schrödinger Equation (TDSE)[2]:

$$i\hbar\frac{\partial\Psi(x,t)}{\partial t} = \hat{H}\Psi(x,t). \tag{2.3}$$

Note that, as in the Hamilton formulation of classical mechanics, the total energy operator (the Hamiltonian) rules the motion of the system. There is some controversy[83] to whether this equation can be simply postulated or must be rigorously derived from the TISE of a system interacting with a classical environment, as originally made by Schrödinger.

It can be shown[82, 84] that a function $\Phi_f(x,t)$ propagated in time following Eq. (2.3) is related with the solutions of the TISE by a Fourier Transform:

$$\Psi(x, E_f) = \int_{-\infty}^{\infty} dt e^{iE_f t/\hbar} \Phi_f(t). \tag{2.4}$$

---

[1]Except for a complex phase factor. We will talk again about this topic later on, when the *propagation* of a wave function is discussed.

[2]This is the so-called Schrödinger Picture. Another equivalent view on the time evolution of a quantum system, is given by the Heisenberg and Interaction Pictures, into which the time evolution is applied to a operator rather than a wave function. Only the first formalism will be used in this work.

This expression allows us to establish a fundamental equivalence between the time–dependent and the time–independent formalisms: a function propagated for infinite time holds the information of all the eigenstates of a dynamical event, while a given eigenstate of the system for a given energy contains information about all times of the process. This connection, which shows that both the time–dependent and time–independent formalism lead to the same results[84], will be further analyzed and used in Chapters 3 and 5. However, the intrinsic nature of the mathematical problem they present, as well as the interpretation of the results, differs significantly. The time–independent formalism is an eigenvalue, or boundary conditions problem. Therefore, it is solved by setting specific constraints to the wave functions, and finding all the eigenvalues and eigenvectors of the time–independent Schrödinger equation, *i.e.*, all its possible states and energies. On the other hand, the time–dependent formalism is an initial value problem: one needs to specify a well–defined function at $t = 0$, and the system is solved by propagating it up to infinity. This kind of problem is, mathematically, much simpler than an eigenvalue problem, and furthermore is more suited for our cause–consequence perspective of dynamical processes. For these reasons, and in spite of the fact that they ultimately lead to the same final result, both formalisms are not equivalent in terms of numerical efficiency and interpretation. In some cases, such as when studying spectroscopic transitions, a time–independent formalism is preferred: since just some specific eigenstates are involved, it is easier to solve the TISE for the desired energies right off. However, if many energies are involved in a certain process, a time–dependent formalism might be preferred, since it is not necessary to propagate up to infinity: only until the wave function leaves the interaction region. Similarly, there are certain problems which are simply best understood in one of the frameworks, so the interchange between the time and energy domains is a useful tool to work with. The choice is ultimately a matter of the specific situation at hand. See Ref. [84] for an interesting discussion on the equivalence of both formalisms and their applications.

2.1.1 The Born-Oppenheimer Approximation and the Potential Energy Surface

The full dimensional Schrödinger Equation, whether in its time–dependent or time–independent form, only has an analytical solution for systems with up to two particles. For larger systems, which in a molecular simulation context implies anything beyond the hydrogen atom, it is only possible to find approximate numerical solutions based on variational principles, perturbation theory or simplified Hamiltonians. The number of atoms and nuclei present in most systems of chemical interest prevent one to obtain even an approximate wave function of the system in a reasonable computational time. In order to turn a molecular system into a manageable problem, Born and Oppenheimer[85] proposed a factorization of the wave function, separating the motion of the heavy nuclei from that of the fast and light electrons, proving through perturbation theory that the approximation was valid in most circumstances.

A molecular Hamiltonian composed of N nuclei with coordinates $\vec{R}$ and n electrons with coordinates $\vec{r}$ can be in general written as:

$$\hat{H} = \hat{T}_{el}(\vec{r}) + \hat{T}_{nuc}(\vec{R}) + \hat{U}(\vec{r}, \vec{R}), \tag{2.5}$$

where $\hat{T}_{el}(\vec{r})$ and $\hat{T}_{nuc}(\vec{R})$ stand for the electronic and nuclear kinetic energy operators, respectively, and $\hat{U}(\vec{r}, \vec{R})$ represents all the electron–electron, nucleus–electron

and nucleus–nucleus potential energy terms. This last term couples the motion of electrons and nuclei together. The first step for the factorization of the Hamiltonian is to set the kinetic energy of the nuclei to zero, thus effectively freezing them at a given configuration, $\vec{R}_0$. Then, we can define an *electronic* Hamiltonian, $\hat{H}_{el}(\vec{r}; \vec{R}_0)$, with eigenvalues $\left\{ V_j \right\}$ and eigenfunctions $\{\Phi_j(\vec{r}; \vec{R})\}$, which will depend *parametrically* on the nuclear coordinates, $\vec{R}_0$:

$$\hat{H}_{el}\Phi_i(\vec{r}; \vec{R}_0) = V_i\Phi_i(\vec{r}; \vec{R}_0). \tag{2.6}$$

As these electronic eigenfunctions form a complete basis set (and can be taken as orthogonal), we use them to represent the full–dimensional wave function:

$$\Psi(\vec{r}, \vec{R}, t) = \sum_j \chi_j(\vec{R})\Phi_j(\vec{r}; \vec{R}), \tag{2.7}$$

This equation, known as the Born Representation of the wave function, is formally exact. It can be shown that by substitution of Eq (2.7) in the TDSE, Eq (2.3), after some rearranging one obtains the equations of motion for the expansion coefficients, $\chi_j(\vec{R})$:

$$i\hbar\frac{\partial \chi_j(\vec{R})}{\partial t} = \left[\hat{T}_{nuc}(\vec{R}) + V_j(\vec{R}) \right] \chi_j(\vec{R}) - \sum_i \Lambda_{ji}\chi_i(\vec{R}), \tag{2.8}$$

where the second term of the right–hand side of Eq.(2.8) contains the so–called non-adiabatic coupling matrix elements:

$$\hat{\Lambda}_{ji} = \hat{T}_{nuc}\delta_{ij} - \left\langle \Phi_i|\hat{T}_{nuc}|\Phi_j \right\rangle, \tag{2.9}$$

that couple the different electronic eigenstates. The non-adiabatic coupling matrices, $\boldsymbol{\Lambda}$, are operators on the space spanned by $\chi_j(\vec{R})$, which consist of a matrix representation of the nuclear KEO onto the electronic basis set, $\{\Phi_j(\vec{r}; \vec{R})\}$ (hereafter referred to as the scalar part) and a direct application of this KEO to the unbound functions (the operator part). If the effect of $\hat{T}_{nuc}$ onto the $\{\Phi_j(\vec{r}; \vec{R})\}$ set is small and the basis changes smoothly with $\vec{R}$, then the adiabatic theorem holds and the non-adiabatic coupling operator becomes small enough to be safely neglected (See for instance Ref. [86] for details). Then Eq (2.8) can be simplified to:

$$i\hbar\frac{\partial \chi_j(\vec{R})}{\partial t} = \left[\hat{T}_{nuc} + V_j(\vec{R}) \right] \chi_j(\vec{R}), \tag{2.10}$$

which is known as the *adiabatic approximation* to the nuclear TDSE. The interpretation of Eq (2.10) can be given in terms of a set of electronic states, Φ_j, each one providing with a potential energy surface (PES), $V_j(R)$, onto which a quasi-particle with coordinates equal to the nuclear coordinates, $\vec{R}$, evolves. Through this approximation, the dynamics of a molecular system can be divided in two essential steps: first, the PES of the system is obtained by solving the electronic Schrödinger equation for different electronic configurations; then this PES is used to find the solution for the nuclear Hamiltonian.

It is precisely this separation of the problem into electronic and nuclear degrees of freedom that allows the treatment of chemically relevant systems. However, the structure of the Hamiltonians involved in each step is different enough so that the

methods to solve the respective equations vary vastly, up to the point that each problem has given rise to different areas in physical chemistry. Generally, the branch dealing with the electronic Schrödinger equation is known as *Electronic Structure* or *Quantum Chemistry*, while the one facing the nuclear problem goes by the name of *Quantum Dynamics* or *Molecular Dynamics*, depending on whether classical or quantum laws are applied to the particular problem.

A way to illustrate the differences between the electronic and the nuclear problem is to observe the size of systems that can be treated at each level using state–of–the–art methods. Nowadays it is straightforward to effectively obtain electronic energies and states for systems with hundreds of electrons. On the contrary, nowadays it is not possible to solve the nuclear Schrödinger equation for that many atoms: except for particular model systems coupled to bath modes, even the most advanced methods are limited to the study of some tenths of atoms. The main reason why the nuclear problem is so much complicated to tackle is the different behavior of the Potential Energy Operator in Eqs (2.5) and (2.8) (or (2.10)). In case of the electronic problem, this operator is a sum of rather structureless, electrostatic terms. Due to this, the solutions to the problem are smooth functions, so that the size of the basis set needed to represent them accurately is generally small. In contrast, the potential energy surfaces ruling the nuclear motion are much more complex and introduce a different amount of correlation between the degrees of freedom, thus resulting in larger basis sets needed and more complicated equations to be solved. Moreover, while usually only the first few electronic excited states (if any) are relevant in most chemical contexts, many vibrational and rotational excitations occur at the nuclear level, and thus a large number of states are involved in molecular processes. Due to all this, numerical methods which proved effective for solving the electronic Schrödinger equation are not valid for its nuclear counterpart.

The Born–Oppenheimer approximation, albeit powerful and accurate, rests on the assumption that the coupling between electronic and nuclear motion is negligible: electrons "move" so fast that they can instantly adapt to any nuclear configuration. However, in cases where different electronic states become degenerate this is no longer true: the coupling terms then become strong, and any small change in the nuclear configuration results in a huge modification of the electronic structure. This is a relevant issue of molecular dynamics which must be kept in mind when working with any problem. The treatment of these *non–adiabatic* systems is still possible through ab initio direct dynamics approaches[87], and was reviewed by Worth and Cederbaum[86].

2.2 Representation of the nuclear wave function: discretization of the space.

Although the theory of quantum mechanics is developed in an infinite dimensional Hilbert Space of complex functions, $\mathcal{H}$, the numerical resolution of the differential equations that describe the dynamics of molecular systems requires a discretization of the simulation space. This is achieved by the truncation of the *complete basis set*, $\{\phi_i\}$, to a finite dimension N. Fortunately, this finite–dimensional space can be defined as a subspace of $\mathcal{H}$, thus retaining its mathematical structure and thus the formal definitions of quantum mechanics. One can therefore represent the continuous

functions, $\Psi(x)$, as a linear combination of the N basis elements, $\{\phi_i\}_N$:

$$\Psi(x) \approx \sum_{i=1}^{N} a_i \phi_i(x). \tag{2.11}$$

If a basis of delocalized, orthonormal functions is used in the previous Equation, then one refers to the *spectral method*[3]. The truncation can be interpreted as the effect of an operator, $\hat{P}_N$, which projects the functions from the infinite–dimensional Hilbert space to the subspace spanned by the basis, so that we have:

$$\hat{P}_N \Psi = \hat{P}_N \sum_{i=1}^{\infty} a_i \phi_i = \sum_{i=1}^{N} a_i \phi_i = \Psi_N. \tag{2.12}$$

With this truncated representation come three main sources of deviation from the infinite–dimensional solution to a molecular system. First, and most obvious, the wave functions defined in the N–dimensional subspace of $\mathcal{H}$ are only approximation to the actual functions Ψ. By the variational theorem of time–independent quantum mechanics[81], we know that the larger the dimension N of the basis set, the better the approximation to Ψ, and that the more the basis functions ϕ_i resemble the actual solutions of the TISE, the fewer we will need to generate an accurate representation, Ψ_N. The second error source comes from the approximate evaluation of operators in the subspace, which is again directly related to the basis set chosen. As a last source of error, we have the resolution to the TDSE itself, which is again only exact in an infinite dimensional Hilbert space. We will deal with this problem in the next Section, where the approximation to the *evolution operator* and the *Dirac–Frenkel–McLachlan* Variational principle will be presented.

In the first approaches to the quantum resolution of the nuclear Hamiltonian, which were based on a time–independent formalism, the wave functions were represented using the spectral method, Eq (2.11), which had been successfully used for the representation of the electronic wave function: the basis set was constructed from a set of stationary functions, and the Hamiltonian matrix was diagonalized in this basis (See Ref. [88] and references therein). In the context of quantum dynamics, after Light et al.[89], this is also known as the *Variational Basis Representation* (VBR). However, the representation of the nuclear Hamiltonian in a spectral basis suffers from both an efficiency and an accuracy problem which does not appear as starkly in electronic structure calculations. Even though the kinetic energy operator, $\hat{T}$, can be efficiently and accurately computed using derivative relations between orthogonal functions[82], the complex shape of the potential energy operator compared to that of the electronic Hamiltonian makes the evaluation of $\hat{V}$ in a spectral basis both numerically demanding and inaccurate. It would be beneficial, both efficiency and accuracy–wise, to find an alternate representation of the wave function which minimized the problems with $\hat{V}$ evaluation. In this section we will review the main tools to obtain the representation of the wave function and the Hamiltonian in an N–dimensional space, so that the evaluation of the different matrix elements needed to perform a quantum dynamics calculation becomes efficient and accurate.

---

[3]This method is widely used in Quantum Chemistry, where the basis functions are generally chosen to be Gaussian or Slater–type orbitals centered at the different atoms of the system (technique known as Linear Combination of Atomic Orbitals).
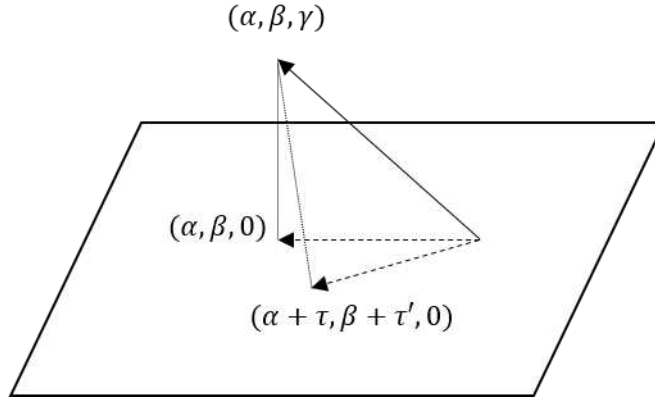
FIGURE 2.1: Scheme showing an orthogonal and a non-orthogonal projection in 3D. In the first case, the projection affects only the *z* coordinate, while the latter affects other coordinates too.

2.2.1 Grid representation of the wave function

A grid representation is based on writing a wave function as a set of complex amplitudes in discrete points in space, $\{x_g\}$, so one may write $\Psi(x) \mapsto \bar{\Psi}(x_g)$. The main advantage of such an approach, as we will see, is that the representation of the potential energy matrix becomes diagonal, and it can thus be more efficient than spectral methods. Once the grid is defined, the amplitudes of the function in the grid points x_g are then related with a spectral basis of functions ϕ_i by the expansion coefficients. These are found by *collocation*:

$$\Psi(x_g) \approx \bar{\Psi}_N(x_g) = \sum_{i=1}^{N} c_i \phi_i(x_g), \tag{2.13}$$

which allows one to define a transformation matrix between the grid–represented function and the spectral basis (the *collocation matrix*):

$$\bar{\boldsymbol{\Psi}} = \boldsymbol{\phi} c, \tag{2.14}$$

with $\bar{\Psi}_g = \bar{\psi}(x_g)$ and matrix elements $\phi_{ig} = \phi_i(x_g)$. This is formally equivalent to projecting the wave function onto the N–point grid:

$$\bar{\Psi}_N(x_g) = \hat{P}_N \Psi(x_g) = \sum_{i=1}^{N} c_i \phi_i(x_g). \tag{2.15}$$

This representation, using a truncated functional basis only on the gridpoints $\{x_N\}$, is sometimes named *Finite Basis Representation* (FBR). Note that the expansion coefficients differ in Eq (2.12) and Eq (2.13), which means that, even though both the spectral projector and the grid projector map to the same N–dimensional space, the actual state resulting from the projection will differ, as illustrated in Figure 2.1. The accuracy of the collocation will critically depend on a choice of the grid points and on this mapping between the collocation scheme and the spectral basis. One of the main problems of grid collocations methods is that, since we do not impose any orthogonality condition, it is possible to have quasi–linear dependencies in the spectral basis related to the grid points, which would lead to singularities in the $\boldsymbol{\phi}$ matrix and therefore numerical inaccuracies.

The work by McCullough and Wyatt[90] was the first to use a grid representation of the wavefunction, rather than a VBR, to solve the collinear H_2+H reaction in a time–dependent formalism using a finite difference representation of the evolution operator (see Section 2.3.2). However, their method was not able to compete with time–independent formalisms based on spectral representations in terms of accuracy and numerical stability[91]. The development of accurate grid representations allowing accurate, numerically stable, and efficient evaluation of functions and operators came only later, with the development of *pseudospectral* representations.

The idea behind these methods is to obtain a representation with the benefits of a collocation scheme (*i.e.*, a better evaluation of the local potential energy operator) but retaining the structure of a variational spectral basis set (namely, orthonormality and completeness relations). It can be shown that these properties can be obtained if the spectral basis set is built from functions obeying the discrete orthogonality relation:

$$\sum_{g=1}^{N} \phi_m(x_g)\phi_n(x_g)\Delta_g = \delta_{n,m}, \tag{2.16}$$

with Δ_g the *weight* of the gth point. Similarly, by defining $\Phi_i(x_g) = \phi_i(x_g)\sqrt{\Delta_g}$:

$$\sum_{g=1}^{N} \Phi_m(x_g)\Phi_n(x_g) = \delta_{n,m}. \tag{2.17}$$

In this case, the collocation matrix in Eq (2.14) becomes unitary, and therefore no numerical problems related with overcompleteness of the basis appear. Moreover, this unitarity forces another relation, since it implies:

$$\mathbf{\Phi}^\dagger\mathbf{\Phi} = \mathbf{\Phi}\mathbf{\Phi}^\dagger = \mathbf{1}, \tag{2.18}$$

and therefore:

$$\sum_{n=1}^{N} \Phi_n(x_i)\Phi_n(x_j) = \delta_{i,j}. \tag{2.19}$$

This last equation is an orthogonality relation for the grid points, and allows the definition of the pseudospectral functions, χ, by using it to unitarily transform the spectral basis, ϕ:

$$\sum_{n=1}^{N} \phi_n(x)\Phi_n^*(x_j) \equiv \chi_j(x). \tag{2.20}$$

Since the spectral and pseudospectral basis are connected by a unitary transformation, the mapping to the N–dimensional subspace of $\mathcal{H}$ spanned by the $\{\phi\}$ and $\{\chi\}$ functions is maintained, and therefore one obtains a collocation scheme equivalent to a variational basis representation.

The pseudospectral functions behave as δ–functions in the discrete grid points, since following Eq (2.19) we have:

$$\sum_{n=1}^{N} \phi_n(x_i)\sqrt{\Delta_i}\Phi_n^*(x_j) = \delta_{i,j} = \sqrt{\Delta_i}\chi_j(x_i). \tag{2.21}$$

Furthermore, as expected from their relation to an spectral basis, it can be shown that they present the analogous completeness and orthogonality relations.

It can also be shown that a pseudospectral basis behaves as a Gaussian quadrature scheme with the grid points $\left\{x_g\right\}$ being the quadrature nodes, and weights

w_j:

$$\int w(x) f(x)\, \mathrm{d}x = \sum_{j=1}^{N} w_j f(x_j), \tag{2.22}$$

thus allowing the exact evaluation of polynomial integrals of $2N - 1$ dimensions (see Apendix B in Ref. [92] and [82]). It can be shown that the quadrature points and weights can then be found by diagonalization of the position operator $\hat{x}$:

$$\boldsymbol{I} = \boldsymbol{\Phi}^{\dagger} \boldsymbol{I} \boldsymbol{\Phi} \tag{2.23}$$

$$\boldsymbol{X} = \boldsymbol{\Phi}^{\dagger} \boldsymbol{X}^{col} \boldsymbol{\Phi}, \tag{2.24}$$

with the diagonal elements of $\boldsymbol{X}^{col}$ being the collocation points, or by general quadrature theory. The VBR of the Hamiltonian operator in a spectral basis $\{\phi\}$ is given by:

$$\boldsymbol{H} = \boldsymbol{T} + \boldsymbol{V} \tag{2.25}$$

$$T_{ij}^{VBR} = \int_{-\infty}^{\infty} \phi_i^* \hat{T} \phi_j \, \mathrm{d}x \tag{2.26}$$

$$V_{ij}^{VBR} = \int_{-\infty}^{\infty} \phi_i^* \hat{V} \phi_j \, \mathrm{d}x. \tag{2.27}$$

The objective of pseudospectral representations is to ease the computation of the Hamiltonian matrix. This is specially relevant in case of the potential energy operator, because for low–dimensional problems the kinetic energy operator has an analytic expression in most representations.

The most relevant pseudospectral approaches generally used nowadays in quantum dynamics are the *Fourier Method* (FM or FFT, from Fast Fourier Transform) by Kosloff and Kosloff[88, 91] and the *Discrete Variable Representation* (DVR) by Light et al.[89]. Now we will briefly review these representations, focusing on 1D real functions for the sake of clarity. See Refs [89], [91] and Appendix B in Ref. [92] for a rigorous description of these methods. Chapter 11 in Ref. [82] contains a comprehensive review on general pseudospectral methods.

2.2.2 The DVR method

The DVR method is based on using a set of classical orthogonal polynomials, $p_n(x)$ as spectral basis. The first step is to select an adequate basis set of dimension N, whose elements should ideally resemble as much as possible the solutions of the system under study. Then, taking advantage of the quadrature equivalence in Eq. (2.22), one can compute the position operator matrix, $\boldsymbol{X}$. This will make it possible to obtain the transformation matrix $\boldsymbol{\Phi}$ and the grid points $\{x_\alpha\}$ by diagonalization. Once these quadrature points are found, the potential energy operator can be approximated as:

$$V_{ij}^{VBR} \approx \sum_{\alpha}^{N} w_\alpha p_n(x_\alpha) = V_{ij}^{FBR}. \tag{2.28}$$

The evaluation of Eq. (2.28) is still computationally demanding. However, if the potential energy operator can be written as an analytic function, then one can write:

$$\boldsymbol{V}^{FBR} = V(\boldsymbol{X}^{DVR}), \tag{2.29}$$

which means that in the DVR the potential energy matrix becomes diagonal, with elements $V_{ij}^{DVR} = V(X_i^{DVR})\delta_{ij}$. This expression holds because an analytic function can be locally decomposed as a power series, and for a Hermitian matrix (such as X) we can write any power of it as:

$$\boldsymbol{\Phi} \boldsymbol{X}^n \boldsymbol{\Phi}^\dagger = \left(\boldsymbol{\Phi} \boldsymbol{X} \boldsymbol{\Phi}^\dagger\right)^n = \left(\boldsymbol{X}^{DVR}\right)^n. \tag{2.30}$$

This decomposition is exact only in the limit of an infinite basis set. It can be shown that the approximation introduced by an incomplete basis is exactly equivalent to the quadrature approximation in Eq. (2.28)

Although the potential energy matrix becomes easy to compute in the DVR, the kinetic energy operator has no direct analytic expression in this representation. Instead of computing it numerically, it is often beneficial (accuracy and efficiency–wise) to compute the matrix in the FBR, and then transform the resulting matrix to the DVR:

$$\boldsymbol{T}^{DVR} = \boldsymbol{\Phi}^\dagger \boldsymbol{T}^{VBR} \boldsymbol{\Phi}. \tag{2.31}$$

To sum up, the algorithm for the computation of the Hamiltonian matrix through a DVR scheme is as follows:

1. Compute the position operator matrix in the spectral basis of orthogonal polynomials, and diagonalize it to obtain the DVR functions and grid points.

2. Obtain the potential energy matrix in the DVR by evaluation of the potential energy function at the grid points.

3. Calculate the kinetic energy matrix in the spectral basis, using analytical relations for the operators, and transform to the DVR basis with the unitary transform obtained in 1.

4. Obtain the Hamiltonian as a sum of the kinetic and potential energy matrices.

The DVR method was preceded by the Harris–Engerhorn–Gwinn (HEG) method[93], who represented the operators in the spectral basis instead of using the localized functions. Even though the DVR does not present relevant advantages over the HEG method for 1D problems, it allows for an straightforward generalization of the formalism to non–classical polynomial spectral basis (the so–called *improper* DVR method) and to multidimensional grids[89, 94].

2.2.3 The Fast Fourier Transform scheme

The *Fourier Method* or *Fast Fourier Transform* (FFT) representation scheme was the first successful pseudospectral method developed for quantum dynamics. It is based on the use of exponential functions as a spectral basis set, with a general form:

$$e^{i2\pi k x/L} \quad , \quad k = -(N/2 - 1), \dots, N/2, \tag{2.32}$$

with $L = N \cdot \Delta x$ being the length of the interval represented in the coordinate. These functions present orthonormality and completeness relations similar to those of a proper DVR, and therefore act also as a collocation scheme. It can be shown that the grid resulting from a FFT representation is made of equidistant points, and therefore the weight function is constant.

The FFT representation also provides with a direct relation between the coordinate and momentum representations of the simulation space, linked by the expressions:

$$\Delta k = \frac{2\pi}{L} \tag{2.33}$$

$$|k_{max}| = \frac{\pi}{\Delta x} \tag{2.34}$$

which permits a very efficient evaluation of the kinetic energy operator by transforming the wave function onto the momentum domain, where the momentum operator becomes multiplicative instead of differential.

2.3 Time–dependent Quantum Dynamics

As it was pointed out above, both the time–dependent and time–independent formalisms of quantum mechanics give an equivalent result in the limit of an infinite propagation time and a complete basis set, respectively. The suitability of one over the other will depend mainly on the problem at hand, and on the relevant information to be extracted from the calculations. For instance, time–dependent methods give more emphasis to the cause–effect relation in a chemical process, since we can actually see how the system evolves with time. However, it might be more difficult to converge for low–energy processes such as resonances, and in those cases a time–independent formalism can give more accurate information.

The general scheme for a time–dependent quantum dynamics calculations is as follows: first, an *initial non–stationary state*, whose properties will depend on the specific problem at hand, is constructed and represented in a pseudospectral basis set. This state will then be *propagated* in time. The convergence of the calculation is generally achieved once the propagated wave function abandons any interaction region of the PES. Finally, the full story of the propagation is *analyzed* in order to obtain the required information, for instance process rates or spectroscopic transitions. This formalism of quantum dynamics has a number of features which makes it very attractive for the study of physical processes, namely its direct call on the concepts of *trajectory* and *time evolution* —which might result in a simpler interpretation based on intuitive analogies with classical mechanics—, its nature as an initial value problem —which eases the implementation of new algorithms—, and the possibility to treat several energies, including discrete and continuum spectra using the same formalism. However, it only started to become popular in the 80s and 90s due to several breakthroughs which increased its performance and accuracy, namely the development of better representation schemes for the wave function and of accurate and efficient propagation schemes. From that point, time–dependent methods started to rival time–independent ones for certain applications. See Refs [91, 95] for an overview on the history of these breakthroughs.

This Section is devoted to the main aspects of the time–dependent formalism which distinguishes it from its time–independent counterpart: the non-stationary states, wave packets, propagation of wave functions, and the time–dependent Dirac–Frenkel–McLachlan variational principle.

2.3.1 Stationary vs Non-stationaty states. Wave packets

The relevance of the individual solutions of the TISE, the stationary states, was clear from the very beginning of quantum mechanics due to their direct relation with

spectral transitions of atoms and molecules. With suitable boundary conditions, the eigenstates of a given Hamiltonian can also give information about dynamical processes, which forms the basis of the Time–independent approach to quantum molecular dynamics. It can be shown that any stationary state is also a solution of the TDSE. A particularly important feature of the Hamiltonian's eigenfunctions appears if we introduce them in the TDSE: if $\psi(x,t)$ is a solution of the TISE, we can integrate Eq (2.3) to obtain:

$$\psi(x,t') = e^{-\frac{i}{\hbar}\hat{H}}\psi(x,t) = e^{-\frac{i}{\hbar}E}\psi(x,t), \tag{2.35}$$

which, since E is constant, means that a stationary state evolving under the effect of a time–independent Hamiltonian will remain constant in time, except for a complex phase factor. Therefore, a stationary state is not a suitable function for a time-dependent formalism, since it will not give any information upon propagation: it will just remain the same function as that at $t = 0$. How can we then connect the time–independent formalism, whose solutions are stationary states, with the time–dependent view, which requires an evolution of the wave function? The answer lies in the fact that, even though stationary states are particular solutions of the TDSE, any linear combination of those functions will also be a solution of the TDSE. These *superposition* states do change in time, and are thus called *non–stationary states*. A general solution to the TDSE is thus given by a linear combination of all eigenstates of a system:

$$\Psi(x,t) = \sum_{n=1}^{\infty} c_n\psi_n(x)e^{-\frac{i}{\hbar}E_n t} \tag{2.36}$$

By analogy to an infinite sum of plane waves with well defined energy, this general superposition state is called a *wave packet*. It is possible in fact to use the eigenstates of the free particle, which have a continuous eigenvalue spectrum, to build a wave packet centered at certain values of position and momentum:

$$\Psi(x,t) = \int_{-\infty}^{\infty} c(k)e^{-iE_k t/\hbar}e^{ik(x-x_0)}\,\mathrm{d}k, \tag{2.37}$$

where the coefficients $c(k)$ correspond to the Fourier Transform of the wave packet itself at $t = 0$:

$$c(k) = \frac{1}{2\pi}\int_{-\infty}^{\infty} \Psi(x,0)e^{-i(k-k_0)x}\,\mathrm{d}x. \tag{2.38}$$

In the previous equations, k is the *wavenumber* of the function, a measure of the number of oscillations of the wave per unit distance which is directly related with the linear momentum of the particle, $p = \hbar k$.

The coefficients in Eq. (2.37) can be chosen to be any arbitrary function as long as it obeys Parseval's theorem:

$$\int_{-\infty}^{\infty} |c(k)|^2\,\mathrm{d}k = \int_{-\infty}^{\infty} |\Psi(x,t)|^2\,\mathrm{d}x. \tag{2.39}$$

Eq. (2.39) is a general expression for magnitudes related by a Fourier Transform, and it ensures that the functions can be unitarily transformed between the position and momentum representations. Then, it is straightforward to find that the coefficient function must obey:

$$\int_{-\infty}^{\infty} \left|\sqrt{2\pi}c(k)\right|^2\,\mathrm{d}k = 1, \tag{2.40}$$

in order for the wave function to be normalized at all times. Defining $c(k,t) = c(k)e^{-iE_k t/\hbar}$, one can invert Eq. (2.37), thus obtaining the *momentum representation* of the wave packet:

$$c(k,t) = \frac{1}{2\pi} \int_{-\infty}^{\infty} \Psi(x,t)e^{-i(k-k_0)x} \, dx. \tag{2.41}$$

Wave packets present a series of properties arising from their nature as superposition states. Among the most important of them appear the phase space localization, the group velocity, and the dispersion of the wave packet. The phase space localization is a direct consequence of Heisenberg's Uncertainty principle, which for the conjugate variables position (x) and momentum (p) reads:

$$\Delta x \Delta p \geq \frac{\hbar}{2}. \tag{2.42}$$

From this equation we can see that the less uncertainty we have in momentum, the more we will have in position and vice versa, which is consistent with the delocalization in space of stationary states (which have a well–defined energy and momentum). Moreover, this means that we can choose to define a wave packet localized in space by adding different stationary states in Eq. (2.36) (or (2.37)) and thus increasing the uncertainty in momentum. A particularly interesting case appears when the coefficients of the linear combination, $c(k)$ follow a Gaussian distribution:

$$c(k) = \left(\frac{a^2}{2\pi^3} \right)^{1/4} e^{-a^2(k-k_0)}, \tag{2.43}$$

with a being a parameter related with the width of the distribution. It can be shown[81, 82] that for these *Gaussian wave packets* the equality in Eq (2.42) holds, and thus they are the minimum uncertainty wave packets which can be built. Moreover, for potentials up to quadratic, a Gaussian wave packet will remain as a Gaussian upon propagation, and according to Ehrenfest's Theorem, its maximum will follow the same trajectory as a classical particle. The group and phase velocities of the functions are also well described. All these features make Gaussian wave packets the most commonly used functions to represent a given particle in quantum dynamics.

Propagation of a wave packet: group and phase velocities, dispersion

Dispersion and group velocity are two concepts originated in wave mechanics. They are defined from the so–called *dispersion relation*, *i.e.* how the angular frequency ω of a wave depends on the different values of momentum k it contains. For a quantum free particle, this relation is:

$$\omega(k) = \frac{\hbar k^2}{2m}. \tag{2.44}$$

The group and phase velocity are then defined respectively as:

$$v_g = \frac{\partial \omega}{\partial k} \tag{2.45}$$

$$v_p = \frac{\omega}{k}. \tag{2.46}$$

It can be shown that, for a quantum particle represented by a wave packet, the group velocity is defined through the time evolution of the center of the wave packet, corresponding to the expectation value of x[81, 82]. It can be shown that the velocity of

the center of the wave packet corresponds to the group velocity, v_g:

$$v_g = \frac{d\omega}{dk} = \frac{d\langle x \rangle}{dt} = \frac{\langle p \rangle}{m}. \tag{2.47}$$

This is an important result, for it shows a correspondence between classical and quantum mechanics: the center of a wave packet representing a free quantum particle, moves at the same velocity as a classical particle. Moreover, as in the classical case, the momentum of the system is a constant of the motion and does not change in time.

In spite of the correspondence just mentioned, the wave packet still presents purely quantum phenomena. Since a wave packet is formed from an *a priori* infinite sum of plain waves with different k values, and according to Eq. (2.46) each plain wave has its own phase velocity, it is expected that the *profile* of the wave packet changes with time: the components with lower k will move more slowly, while components with high k values will move faster. It is the distribution of phase velocities which gives rise to the phenomenon known as the *dispersion* of the wave packet, which is the change in its width as a function of time.

Being an initial value problem, the efficiency of a time–dependent solution to a problem will depend critically on the shape and properties of the function that will be propagated at $t = 0$. Sometimes it will be required that the initial state is similar to a previously calculated wave function. This is the case in photochemistry applications, where the excited state is defined as a lower–energy stationary state times the dipole moment operator. Since the Hamiltonian of the system changes, the new function will not be an stationary state of the excited state, and therefore will evolve in time. However, in most other cases the problem requires the description of free or quasi–free particles, which start being confined to a certain region of space. Gaussian wave packets might be a suitable choice in these cases. An appropriate examination of the problem prior to the simulation is critical for the success of any time–dependent study.

2.3.2   Time evolution of a wave function: propagation operators, variational principles and equations of motion.

The Time–dependent Schrödinger equation, Eq (2.3), is a first order differential equation with respect to time and a second order differential equation with respect to each spacial coordinate. In the previous section we assumed that we knew a complete basis set consisting on the stationary states of the Hamiltonian. Therefore we could straightforwardly represent any function in this basis set, substitute the Hamiltonian operator in Eq (2.35) by the corresponding eigenenergies and obtain the time–evolved wave function from the different amplitudes and scalar products of the linear combination. However, this *spectral propagation* cannot be used in practical problems, since it would imply the diagonalization of the Hamiltonian in order to obtain its complete eigenstate spectrum, which is extremely expensive and takes us again to the time–independent framework. Moreover, it would be impossible to do so in the case of time–dependent Hamiltonians. The propagation of a wave packet under the action of a general Hamiltonian is formally derived after the definition of the *time evolution operator*, $\hat{U}(t', t)$.

The time evolution operator maps the wave function at a time t to itself at a time t':

$$\Psi(x, t') = \hat{U}(t', t)\Psi(x, t). \tag{2.48}$$

For this operator to have a physical meaning, it must fulfill two conditions: norm conservation, and composition property[96]. The first feature reflects the fact that the overall probability of finding a particle in space cannot change with time, *i.e.*:

$$\langle \Psi(x,t) | \Psi(x,t) \rangle = \langle \Psi(x,t') | \Psi(x,t') \rangle = \langle \Psi(x,t) | \hat{U}^\dagger(t',t)\hat{U}(t',t) | \Psi(x,t) \rangle \quad (2.49)$$

and is fulfilled whenever $U(t',t)$ is an unitary operator. The second property is related with the need that the evolution of a system from a time t_1 to a time $t_3 > t_1$ must be the same as the evolution from t_1 to an intermediate time t_2, and a second evolution from t_2 to t_3. Mathematically:

$$\Psi(x,t_3) = \hat{U}(t_3,t_1)\Psi(x,t_1) = \hat{U}(t_3,t_2)\hat{U}(t_2,t_1)\psi(x,t_1). \quad (2.50)$$

It can be shown that an operator thus defined is directly related to the TDSE[96].

Until now we have not given the time–evolution operator any explicit form. For time–independent Hamiltonians, it is straightforward to see that it corresponds to the exponential operator found in Eq (2.35):

$$\hat{U}(t',t) = e^{\frac{i}{\hbar}\hat{H}(t'-t)}. \quad (2.51)$$

Since $\hat{U}(t',t)$ has the form of an exponential function of the Hamiltonian, it is not trivial to apply this operator on a wave function. If we discard the possibility to diagonalize $\hat{H}$ there are two distinct approaches to the solution of the TDSE: the *global* and the *local* propagator schemes. These approaches are thoroughly discussed in several books and reviews (see, for instance, Refs [82], [96] and [95]) and, since they are not directly used in this thesis, will now be only briefly described.

Global propagators are based on the idea of approximating the evolution operator as a polynomial expansion of the exponential function. Thus, for a general set of N interpolating polynomials P_n, we have:

$$\hat{U}(t',t) = e^{-\frac{i}{\hbar}\hat{H}(t'-t)} \approx \sum_{n=1}^{N} a_n P_n \left(-\frac{i}{\hbar}\hat{H}(t'-t) \right). \quad (2.52)$$

The problem is then turned into choosing a set of interpolating polynomials which minimizes the global representation error, or the error for a given function. However, they can only be used if the Hamiltonian is time–independent within that time step. The most prominent examples of global propagators are the Chevysev[97] and the Short Iterative Lanczos[98] schemes.

Short–time propagators, on the other hand, divide the time evolution operator into N segments, so that the Hamiltonian operator does not vary in each time interval:

$$\hat{U}(t',t) = \prod_{n=0}^{N-1} \hat{U}\left[(n+1)\Delta t, n\Delta t \right] = \prod_{n=0}^{N-1} e^{-\frac{i}{\hbar}H\hat{}\Delta t}. \quad (2.53)$$

The approaches based on this representation are the only ones that can be used for time–dependent Hamiltonians. However, the time step Δt must always be smaller than the convergence time step, $\Delta t_c = \frac{\hbar}{E_{max}}$ (where E_{max} is the maximum energy in the representation grid), otherwise the algorithm becomes extremely unstable or even meaningless. Among the different short–time propagators, it is worthwhile to mention the Second Order Differences scheme[99], the Split–operator method[100], and the integral equation approaches[101]. Global propagators are generally more efficient than Short–time propagators, because they are numerically stable for larger

time steps, and also more accurate.

2.3.3   The Dirac-Frenkel-McLachlan Variational Principle

The time–dependent Schrödinger equation, as written in Eq (2.3), cannot be formally solved for more than two particles due to the infinite dimension of the Hilbert space, just like we cannot find exact eigenvalues and eigenfunctions of the time–independent Schrödinger equation for such systems. Instead, since we must work within a N–dimensional subspace of $\mathcal{H}$, which we call $\mathcal{M}$, we will only have approximations to the actual wave function Ψ. Moreover, in this space it is not possible to obtain the exact time evolution of a wave function, since it might have components outside the subspace. All we can do then is to find the equations of motion (EOM) which yield the *optimal* time evolution, *i.e.*, that which minimizes the difference between the approximate wave function, $u(t)$, and the actual wave function, $\Psi(t)$, when propagated from t to $t' = t + \Delta t$. In order to solve this problem, a variational principle needs to be fulfilled. In quantum dynamics this is the Dirac-Frenkel-McLachlan Variational Principle. Since the derivation of the main computational tool used during the development of these Thesis, the Multiconfigurational Time–dependent Hartree approach, is based on this variational principle, here we will briefly discuss its formula and interpretation, based on Ref. [102].

Suppose an approximation to the exact state of the system ($\Psi(t)$) in the N–dimensional subspace $\mathcal{M}$, which we will call $u(t)$. This approximation will be a linear combination of N basis functions with coefficients λ_n, and will correspond to a state vector in $\mathcal{M}$. Suppose also that, for $t = 0$, the real state of the system lies within the subspace $\mathcal{M}$, *i.e.* $\Psi(0) = u(0)$. Our goal is to find a function such that $t \mapsto u(t)$, where the difference between $\Psi(t)$ and $u(t)$ is minimal. This is equivalent to say that we want to find the variation in the N λ_n coefficients that yields a final state the most similar possible to $\Psi(t)$. From the TDSE, we know that the exact time evolution of the function will be given by:

$$\frac{\mathrm{d}\Psi}{\mathrm{d}t} = \frac{1}{i\hbar}\hat{H}\Psi, \tag{2.54}$$

which due to the initial boundary conditions can be set as:

$$\frac{\mathrm{d}\Psi}{\mathrm{d}t} = \frac{1}{i\hbar}\hat{H}u. \tag{2.55}$$

Furthermore, we know that the approximate time evolution, $\frac{\mathrm{d}u}{\mathrm{d}t}$, will lie in the tangent space of $\mathcal{M}$, $\mathcal{T}_u\mathcal{M}$. This space is formed by all partial derivatives of u with respect to the coefficients λ_n which define its position on $\mathcal{M}$, and therefore contains all the allowed variations of u. This concept is illustrated in Figure 2.2, from which is easy to see that the minimum difference between $u(t)$ and $\Psi(t)$ will be obtained when this difference vector is orthogonal to the tangent space. Mathematically, this can be put as:

$$\left\langle \mathrm{d}u \,\middle|\, \frac{\mathrm{d}u}{\mathrm{d}t} - \frac{1}{i\hbar}\hat{H}u \right\rangle = 0, \tag{2.56}$$

i.e., the optimal time evolution of the approximate state, $u(t)$, corresponds to the orthogonal projection of $\Psi(t)$ onto the tangent space $\mathcal{T}_u\mathcal{M}$. This is the so–called Dirac–Frenkel–McLachlan Time–dependent Variational Principle. It can be shown that this principle conserves both the norm and the energy for a time–independent
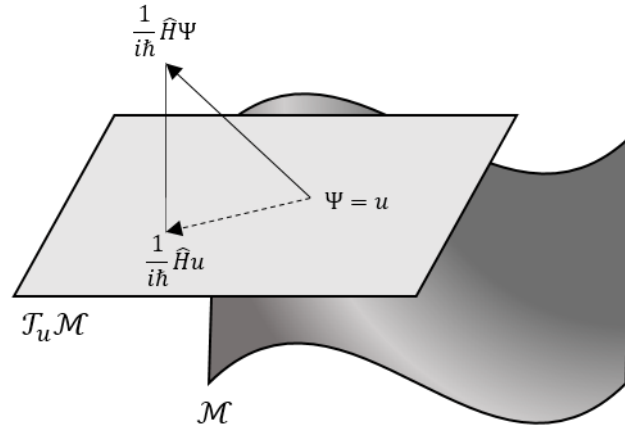
FIGURE 2.2: Representation of a reduced subspace $\mathcal{M}$ as a surface embedded in a 3D space. The tangent space $\mathcal{T}_u\mathcal{M}$ is shown as a surface tangent to the origin point u. The variational principle ensures the best variation in the reduced space to be the orthogonal projection of the *true* variation in the full (3D) space.

Hamiltonian (see Appendix A in Ref [92]). Note also that this principle is *local* in time, since it assumes that we know precisely the wave function at $t = 0$. This is in general true, since we can choose our initial wave function, but more importantly after the application of the variational principle we do not have a perfect reference anymore, and therefore any subsequent application of the variational principle will be, in this sense, flawed. This means that the results from a global integration of the equations of motion from a time t_1 to t_3 will not be the same as the result of iteratively propagating the function from time t_1 to an intermediate time t_2, and then to the final time t_3, since the reference function at t_2 will not be exact. This is in general not a relevant issue, but must be kept in mind.

Other variational principles exist in the literature, namely the McLachlan:

$$\delta \left\| \theta - \hat{H}\Psi \right\| = 0, \tag{2.57}$$

with $\theta = i\dot{\Psi}$, and Lagrange variational principle:

$$\delta \int_{t_1}^{t_2} \left\langle \Psi \left| \frac{\mathrm{d}\Psi}{\mathrm{d}t} - \frac{1}{i\hbar}\hat{H}\Psi \right. \right\rangle \mathrm{d}t = 0. \tag{2.58}$$

However, for complex parameters λ_n and complex differential functions u it has been shown that all three variational principles are completely equivalent (see Ref. [92] and references therein).

In order to derive the equations of motion of a system in a reduced Hilbert space one must fix the functional form of the *Ansatz*, and then introduce it into the variational principle. Thus the differential equations ruling the evolution of the different functions and coefficients forming it are obtained. An example of this would be the so-called *Standard Propagation* method, which is based on the simplest *Ansatz*: a sum of products of low–dimensional, time–independent functions, χ_k. Each one of the functions represent a single degree of freedom q_k of the system, and are usually chosen as a DVR or FFT set. This method is discussed thoroughly in Ref. [82].

For a system with f degrees of freedom, the *Ansatz* reads:

$$\Psi(q_1,\ldots,q_f) = \sum_{j_1=1}^{N_1} \cdots \sum_{j_f=1}^{N_f} c_{j_1,\ldots,j_f}(t) \prod_{k=1}^{f} \chi_{j_k}(q_k), \tag{2.59}$$

where N_k is the number of basis functions used to represent the kth DOF, and where the jth basis function of the kth DOF is labeled by j_k. The evolution of the wave function will be tied to the evolution of time–dependent coefficients of the linear combination, $c_{j_1,\ldots,j_k}$, so we must find the equations of motion for this set. We start by defining the possible elements of the tangential space, or allowed variations, $\delta\Psi$, as the partial derivative of Ψ with respect to the coefficients:

$$\delta\Psi = \sum_{c_{l_1,\ldots,l_k}} \frac{\partial\Psi}{\partial c_{l_1,\ldots,l_k}} \delta c_{l_1,\ldots,l_f} = \sum_{l_1,\ldots,l_f} \prod_{k=1}^{f} \chi_{l_k}^{(k)}(q_k) \delta c_{l_1,\ldots,l_f}. \tag{2.60}$$

Each one of the terms in the sum represent a component of the tangential space. By the Dirac–Frenkel–McLachlan Variational Principle, the difference between optimal variation of the *Ansatz*, written as:

$$\frac{\mathrm{d}\Psi}{\mathrm{d}t} = \dot{\Psi} = \sum_{j_1,\ldots,j_f} \dot{c}_{j_1,\ldots,j_f} \prod_{k=1}^{f} \chi_{l_k}^{(k)}(q_k), \tag{2.61}$$

and the actual evolution of the state, given formally by the TDSE, must be orthogonal to each variation component in Eq. (2.60), *i. e.* to each term of the sum in that equation. Substituting Eq. (2.61) and a given $l_1,\ldots,l_f$ term of Eq. (2.60) in the Dirac–Frenkel–McLachlan Variational Principle, Eq. (2.56), one gets:

$$\left\langle \prod_{k=1}^{f} \chi_{l_k}^{(k)}(q_k) \right| \sum_{j_1,\ldots,j_f} \dot{c}_{j_1,\ldots,j_f} \prod_{k=1}^{f} \chi_{l_k}^{(k)}(q_k) - \frac{1}{i\hbar}\hat{H} \left| \Psi \right\rangle = 0$$

which after introducing the *Ansatz* for Ψ, Eq (2.59) and rearranging becomes:

$$i\hbar \left\langle \prod_{k=1}^{f} \chi_{l_k}^{(k)}(q_k) \right| \sum_{j_1,\ldots,j_f} \dot{c}_{j_1,\ldots,j_f} \prod_{k=1}^{f} \chi_{l_k}^{(k)}(q_k) \right\rangle =$$
$$\left\langle \prod_{k=1}^{f} \chi_{l_k}^{(k)}(q_k) \right| \hat{H} \left| \sum_{j_1=1}^{N_1} \cdots \sum_{j_f=1}^{N_f} c_{j_1,\ldots,j_f}(t) \prod_{k=1}^{f} \chi_{j_k}(q_k) \right\rangle. \tag{2.62}$$

Finally, by defining the compound indexes $J = j_1,\ldots,j_f$ and $L = l_1,\ldots,l_f$ and the configurations $\chi_J = \prod_{k=1}^{f} \chi_{j_k}^{(k)}(q_k)$, one can write the previous equation as:

$$i\hbar\dot{c}_L = \sum_{J} \left\langle \chi_L | \hat{H} | \chi_J \right\rangle c_J, \tag{2.63}$$

and integrate it with different methods available in order to obtain the evolution of the coefficients c_L as a function of time.

Eq (2.63), although accurate and easy to implement, has a major problem due to the exponential increase of the basis size with the number of degrees of freedom of the system: for a f–dimensional problem, considering we use an average number of N basis functions (or grid points, in a pseudospectral representation), the total

number of coefficients needed to describe the function will be N^f. To put this in perspective, a 5D wave packet expanded in a grid of 50 points *per* DOF will require $3.125 \cdot 10^8$ grid points, and storing it will require 5 GB of memory. This makes problems with more than 6 DOFs too expensive to be practical to solve, even with modern computers, thus limiting its application to at most 4–atomic systems. In the next Chapter the MCTDH approach is presented as an approximate, yet very rigorous and efficient method for propagating wave functions.

Chapter 3

The Multiconfigurational Time–dependent Hartree (MCTDH) approach

In the previous Chapter we reviewed some of the most relevant aspects of Quantum Dynamics as a whole. The actual propagation of wave packets in a finite–dimensional Hilbert space is not a simple problem: either the exact propagator is too complex, or the the Dirac–Frenkel–McLachlan Variational Principle yields too many equations of motion to render a practically solvable problem. This later problem arises from the exponential increase of the number of coefficients with the number of degrees of freedom, a phenomenon which is known as the *exponential wall* and lies at the core of the limitation of the size of systems treatable by quantum dynamics. In this Chapter we will present the Multiconfigurational Time–dependent Hartree approach, developed in the early 90s by Meyer et al., an approach to the solution of the TDSE based on an particular choice of the *Ansatz*. This method and its variants are arguably the best algorithms currently available for efficiently and accurately propagating wave packets, and have been the main simulation tool used in the research undergone during this Thesis.

In the first part of this Chapter a precursor of the MCTDH approach, the Time–dependent Hartree (TDH) method by McLachlan and Ba[104], will be briefly presented. It was the first method to use time–dependent basis functions, and the starting point of more sophisticated algorithms. The description of the MTCDH method itself will follow in Section 3.2, containing an overview of the most relevant achievements and mathematical aspects and including short introductions to the most popular post–MCTDH approaches: the *Multilayer MCTDH* scheme (ML–MCTDH) and the *State averaged* MCTDH approach (SA–MCTDH). Finally, the algorithms for two relevant applications of the method, namely the calculation of correlation functions and eigenstates, will be presented. For simplicity, atomic units are used throughout this Chapter.

3.1 The Time–Dependent Hartree approach

The so–called Standard Propagation Method, presented in previous Chapter, is a straightforward application of the Dirac–Frenkel–McLachlan Variational Principle to an expansion in a time–independent basis set. Its main problem, as already discussed, lies in the fact that a large number of basis functions per DOF are needed in order to correctly describe a chemical system, which together with the exponential scaling law for the number of coefficients and coupled linear equations makes problems with more than 4 DOFs impractical to solve.

One way to overcome the size problem is to use a time–dependent basis set. The functions of such a set would be able to evolve and adapt to the wave function, thus providing an optimal basis at each time step. This property thus implies that a small number of elements will be needed to describe each DOF of the system. This is the idea behind the Time–dependent Hartee (TDH) approach, developed by McLachlan in 1964[104]. This method uses the simplest *Ansatz* for a system with f degrees of freedom, which reads:

$$\Psi(q_1, ..., q_f, t) = a(t) \prod_{k=1}^{f} \varphi^{(k)}(q_k, t), \tag{3.1}$$

i.e. just a single Hartree product of f time–dependent 1D functions, called the *Single Particle Functions* (SPFs), $\varphi^{(k)}(q_k)$.

Eq. (3.1) is fundamentally ill–defined, since any norm or phase variation in any SPF can be compensated by an inverse change in any other SPF:

$$\varphi_1 \varphi_2 = (\varphi_1 \lambda) \left(\frac{\varphi_2}{\lambda} \right). \tag{3.2}$$

In order to correct this inconsistent definition of the wave function, one multiplies each SPF by an arbitrary complex factor α, and gathers all these terms in a redundant time–dependent quantity, $a(t)$. It can be seen that, with the addition of this term, non–redundant equations of motion are obtained by defining the constraint:

$$i \left\langle \varphi^{(k)} | \dot{\varphi}^{(k)} \right\rangle = g^{(k)}(t), \tag{3.3}$$

with $g^{(k)}(t)$ being any real number. The final value of the constraint will be chosen in order to get the better equations of motion for the system.

In order to derive the equations of motion for the TDH approach, one starts by defining the allowed variations, $\delta\Psi$, which are the elements of the tangential space:

$$\delta\Psi(q_1, \ldots, q_f, t) = \delta a(t) \prod_{k=1}^{f} \varphi^{(k)}(q_k) + \sum_{k=1}^{f} a(t) \delta\varphi^{(k)}(q_k) \prod_{\substack{v=1 \\ v \neq k}}^{f} \varphi^{(v)}(q_v)$$

$$= \delta a(t)\Phi + \sum_{k=1}^{f} a(t)\delta\varphi^{(k)}(q_k)\Phi^{(k)}, \tag{3.4}$$

where we have defined the *configuration*:

$$\Phi = \prod_{k=1}^{f} \varphi^{(k)}(q_k, t), \tag{3.5}$$

and the *single–hole function*:

$$\Phi^{(k)} = \prod_{\substack{j=1 \\ j \neq k}}^{f} \varphi_j^{(k)}, \tag{3.6}$$

so that:

$$\Phi = \Phi^{(k)} \varphi^{(k)}. \tag{3.7}$$

The time derivative of the Ansatz becomes:

$$\dot{\Psi} = \dot{a(t)}\Phi + a(t) \sum_{k=1}^{f} \dot{\varphi}^{(k)}(q_k)\Phi^{(k)}. \tag{3.8}$$

Introducing Eqs (3.4) and (3.8) into the Dirac–Frenkel–McLachlan Variational Principle, Eq (2.56), and taking into account that each variation is independent of the rest, after some manipulations the equation of motion for the coefficient $a(t)$ becomes:

$$i\dot{a} = a\left(E - \sum_{k=1}^{f} g^{(k)}\right), \tag{3.9}$$

where the expectation value of the energy is defined as $\left\langle \Phi|\hat{H}|\Phi \right\rangle = E$, and a separate EOM for the time evolution of each SPF:

$$i\dot{\varphi}^{(k)} = \left(\mathcal{H}^{(k)} - E + g^{(k)}\right)\varphi^{(k)}, \tag{3.10}$$

where $\mathcal{H}^{(k)}$ denotes the *mean–field operator*:

$$\left\langle \Phi^{(k)}|\hat{H}|\Phi^{(k)} \right\rangle. \tag{3.11}$$

Note that the TDH scheme has turned the resolution of a single f–dimensional differential equation to the solution of f one–dimensional differential equations. The choice of constraints will not affect to the actual solution of the problem, but might be important for the sake of efficiency and numerical stability, and even for interpretation purposes. See Ref. [92] for details on the choice of constraints.

3.1.1 Validity of the TDH approximation

The simple form of the TDH *Ansatz* is at the same level of theory as the successful and ubiquitous Self–consistent Field methods used in Electronic Structure Theory. However, the results yielded by the TDH approach are in general much more inaccurate than the electronic counterparts. This can be understood in terms of the correlation between the different degrees of freedom in the electronic and the nuclear cases.

It can be shown[92, 105] that the TDH approximation becomes exact in case of a separable Hamiltonian. The error in the approximation is therefore directly related with the coupling between the different degrees of freedom. In case of electronic Hamiltonians, the coupling appears in the electron–electron repulsion term, and this electronic correlation cannot be correctly described with a direct product *Ansatz*. The resulting error, even though relevant, is small when compared with the rest of the terms. Conversely, in a nuclear Hamiltonian the structure of the PES generates strong couplings between the different degrees of freedom, and the *correlation energy*, *i. e.* the difference between the actual energy of the system and the one obtained with the TDH approach, is comparatively much larger.

3.2   The Multiconfigurational Time–dependent Hartree approach

The last part of the discussion on the TDH method showed that its main source of error lies in its inability to describe correlation between different degrees of freedom. As in the case of electronic structure wave functions, an straightforward way to include the correlation between the different DOFs in the system is to increase the flexibility of the wave function by adding more *configurations* to it. Some attempts based on this idea were made in the late 80s, but proved unsuccessful due to the difficulty to solve the resulting equations of motion. It was not until 1990 that Meyer, Manthe and Cederbaum proposed a new method based on what could be called a weighted configurations *Ansatz*: the Multiconfigurational Time–dependent Hartree (MCTDH) approach. This method has proved to succeed in many areas of physics and chemistry due to both its efficiency, which allows the simulation of systems with tens of degrees of freedom, and its accuracy. The first relevant application of the MCTDH algorithm treated the photodissociation of NOCl[106], and represented a breakthrough in the molecular dynamics community. Later, the method was used to accurately compute the photo–absorption spectrum of pyrazine using a realistic 24–D vibronic coupling Hamiltonian[107]. Many more spectra have been computed in the last years, including photo–ionization and photo–detachment, showing outstanding results (see Ref [108] and references therein). Studies of system–bath models with more than 100 DOFs are possible[109–111]. Reactivity studies combining flux–correlation functions methods and the MCTDH propagation scheme have also been extremely successful, breaking the barrier of 4–atoms systems in 2000 with the full–dimensional calculation of the reaction rate for the $CH_4 + H \longrightarrow CH_3 + H_2$ and the $CH_4 + O \longrightarrow CH_3 + OH$ systems[112] . Nowadays, state–resolved reactivity information can also be obtained using the MCTDH method[113–117]. The computation of nuclear eigenstates has also been achieved within the MCTDH framework, through different imaginary time propagation and diagonalization techniques which have been used to compute the vibrational spectrum of the protonated water dimer[118, 119] and tunneling splitting of malonaldehyde[120, 121].

In the last years some extensions of the MCTDH method have been developed to deal with indistinguishable particles (the MCTDHB and MCTDHF for bosons and fermions, respectively, reviewed in Ref.[105] and references therein). Moreover, the numerical efficiency of algorithm was increased through the the latter development of the Multilayer MCTDH (ML–MCTDH) [122, 123], which has allowed to treat even larger problems, performing calculations on model systems with up to 1000 correlated degrees of freedom. Finally, the State-Average MCTDH variation (SA–MCTDH) has further increased the capabilities of the method by allowing the simultaneous propagation of several wave packets without a significant increase of the computational effort, which eases the calculation of eigenstates of different operators, including the Hamiltonian and the Thermal Flux Operator[124]. Combined with the ML–MCTDH approach, it has allowed the exact calculation of tunneling splitting for ground and excited vibrational states of the malonaldehyde molecule with 21 DOFs[125].

In this section we will review the MCTDH equations of motion and discuss some of the particularities of the method, such as the Hamiltonian representation and the particular integration scheme used, known as the *Constant Mean–field* integrator[126, 127]. The ML–MCTDH and SA–MCTDH variations will also be briefly outlined. For a complete derivation of the methods and most relevant applications, see previous comprehensive reviews given in Refs [92, 108, 128].

3.2.1   The MCTDH *Ansatz*

The MCTDH approach relies in what is called a *double–layer* representation of the wave packet: the wave function is given as a linear combination of Hartree products of orthonormal, time–dependent low–dimensional (generally 1D) functions. The functional form of the wave function then reads:

$$\Psi(q_1,\ldots,q_f,t) = \sum_{j_1=1}^{n_1} \cdots \sum_{j_f=1}^{n_f} A_{j_1 \ldots j_f}(t) \prod_{k=1}^{f} \varphi_{j_k}^{(k)}(q_k,t). \tag{3.12}$$

As in the case of the TDH, these are called Single–particle Functions (SPFs), and their time–dependency permits to significantly decrease the number of basis functions needed to represent Ψ when compared to the standard propagation method, Eq. (2.59). In the MCTDH approach, a second layer is needed in order to properly represent the SPFs. This *primitive* basis set, $\left\{ \chi_l^{(k)} \right\}$, onto which the SPFs are expanded, is time–independent, and is generally constructed from pseudospectral methods such as DVR or FFT:

$$\varphi_j^{(k)}(q_k,t) = \sum_{l=1}^{N_k} a_{l_j}^{(k)}(t) \chi_l^{(k)}(q_k). \tag{3.13}$$

The primitive basis must span all the simulation space (as in the case of the standard propagation method), but still the number of coefficients needed to define the wave function is much lower than in the single–layer representation. It is clear now from the previous Chapter that the number of coefficients needed to describe a wave function in a time–independent basis is N^f, with N the number of basis elements and f the number of DOFs. However, consider that we use the MCTDH *Ansatz* and introduce a layer of n time–dependent SPF to represent each DOF. Then, we will have n^f Hartree products (*i.e.* n^f A coefficients), plus N primitive basis elements *per* DOF and SPF. The final number of coefficients then is $n^f + f \cdot n \cdot N$ for the MCTDH representation[1]. Even though there is still an exponential scaling, the basis of this scaling law is n rather than N, and therefore much larger problems can be treated. Following the example in the previous Chapter, a 5D system using 50 grid points *per* DOF, in a MCTDH representation with 5 SPFs describing each coordinate would be described by 4375 coefficients, which can be stored in just 68 kB (compared with the 5 GB needed in the Standard method).

As mentioned during the discussion of the TDH approach, for a separable system just a single Hartree product would suffice to exactly represent the motion of a wave packet (in the finite–dimension Hilbert space). Keeping this in mind, one can establish a correspondence between the double–layer representation and the separability of the system in correlated and uncorrelated parts: the $a_{l_j}^{(k)}(t)$ coefficients in Eq. (3.13) evolve according to the separable contributions of $\hat{H}$, so that the SPFs are an optimal basis set at each time step. In a similar fashion, the $A_{j_1,\ldots,j_f}(t)$ vector of Eq. (3.12) contains the information about the correlation between different DOFs of the system, and is ruled by the non–separable terms of the Hamiltonian.

---

[1]It should be noted that this expression considers that the SPFs are 1–dimensional. The use of multidimensional SPFs, termed *mode combination*, will be discussed when presenting the ML–MCTDH

3.2.2 The MCTDH Equations of Motion

Similarly to the case of the TDH method discussed previously, the description of the SPFs in the *Ansatz* of the MCTDH approach is not unique: one can perform an unitary transformation of the basis in a given DOF, and this rotation would be compensated by an inverse transform on the expansion coefficients, $A_{j_1,\ldots,j_f}$. In order to remove this inconsistency in the definition, a constraint or gauge condition must be added to the equations. Just as the scalar product $i\langle\varphi|\dot{\varphi}\rangle$ was fixed in the TDH approach case, here the constraint chosen will be:

$$i\left\langle\varphi_l^{(k)}|\dot{\varphi}_j^{(k)}\right\rangle = \left\langle\varphi_l^{(k)}|\hat{g}^{(k)}|\varphi_j^{(k)}\right\rangle, \tag{3.14}$$

with $\hat{g}^{(k)}$ an arbitrary hermitian operator. It can be shown that the hermiticity of the constraint operator maintains the orthonormality of the SPFs basis set. Once the constraint has been established, one needs to compute the elements of the tangent space in order to use the Dirac–Frenkel–McLachlan variational principle, Eq. (2.56). Before this, however, it is convenient to rewrite the MCTDH *Ansatz*, Eq. (3.12), as:

$$\begin{aligned}\Psi(q_1,\ldots,q_f,t) &= \sum_{j_1=1}^{n_1}\cdots\sum_{j_f=1}^{n_f} A_{j_1\ldots j_f}(t)\prod_{k=1}^{f}\varphi_{j_k}^{(k)}(q_k,t)\\ &= \sum_J A_J\Phi_J,\end{aligned} \tag{3.15}$$

where we have defined the *composite index*, $J = j_1,\ldots,j_f$, and the *configurations*, $\Phi_J = \prod_{k=1}^{f}\varphi_{j_k}^{(k)}(q_k,t)$. With these new nomenclature, the variation with respect to the A_J vector becomes simply the Jth configuration:

$$\frac{\partial\Psi}{\partial A_J} = \Phi_J\cdot\delta A_J. \tag{3.16}$$

On the other hand, the variation with respect to a given SPF $\varphi_l^{(k)}$ will be given by the expression:

$$\begin{aligned}\frac{\partial\Psi}{\partial\varphi_j^{(k)}} &= \delta\varphi_j^{(k)}\sum_{j_1}^{n_1}\cdots\sum_{j_{k-1}}\sum_{j_{k+1}}\cdots\sum_{j_f} A_{j_1,\ldots,j_{k-1},l,j_{k+1},\ldots j_f}\prod_{\substack{v=1\\v\neq k}}^{f}\varphi_{j_v}^{(v)}\\ &= \delta\varphi_j^{(k)}\sum_{J^k} A_{J_l^k}\Phi_{J^k}\\ &= \delta\varphi_j^{(k)}\Psi_l^{(k)},\end{aligned} \tag{3.17}$$

where one introduces the composite indexes $J^k = j_1,\ldots,j_{k-1},j_{k+1},\ldots,j_f$ and $J_l^k = j_1,\ldots,j_{k-1},l,j_{k+1},\ldots,j_f$, and the *single–hole function*, $\Psi_{j_k}^{(k)}$. This last quantity, obtained from removing the j_kth SPF of the kth DOF, $\varphi_{j_k}^{(k)}$, from the total wave function, allows for the elegant definition of the *mean field operators* as:

$$\langle A\rangle_{jm}^{(k)} = \left\langle\Psi_j^{(k)}|\hat{A}|\Psi_m^{(k)}\right\rangle. \tag{3.18}$$

Note that, in contrast to the TDH approach, now the mean field for each DOF is a $n_k\times n_k$ matrix, where n_k is the number of SPFs used to describe the kth coordinate.

Another important quantity defined from the single–hole functions is the *density matrix*, $\boldsymbol{\rho}^{(k)}$, whose elements read:

$$\rho_{jm}^{(k)} = \left\langle \Psi_j^{(k)} | \Psi_m^{(k)} \right\rangle. \tag{3.19}$$

With these new definitions, and knowing that the time derivative of the wave packet will be:

$$\dot{\Psi} = \sum_J \dot{A}_J \Phi_J + \sum_{k=1}^f \sum_{j=1}^{n_k} \dot{\varphi}_j^{(k)} \Psi_j^{(k)}, \tag{3.20}$$

we are ready to apply the Dirac–Frenkel–McLachlan Variational Principle. The equation of motion for the coefficient vector is then:

$$i\dot{A}_J = \sum_L A_L \left\langle \Phi_J | \hat{H} | \Phi_L \right\rangle - \sum_{k=1}^f \sum_{l=1}^{n_k} g_{jkl}^{(k)}, \tag{3.21}$$

and for the SPFs we have:

$$i\dot{\varphi}_m^{(k)} = \hat{g}^{(k)} \varphi_m^{(k)} + \sum_{j,l}^{n_k} \left(\rho^{(k)} \right)_{mj}^{-1} \left(1 - \hat{P}^{(k)} \right) \langle H \rangle_{jl} \varphi_l^{(k)}, \tag{3.22}$$

where a projector onto the SPFs basis, $\hat{P}^{(k)} = \sum_{j=1}^{n_k} \left| \varphi_j^{(k)} \right\rangle \left\langle \varphi_j^{(k)} \right|$, is defined. Equations (3.21) and (3.22) are the standard equations of motion of the MCTDH approach. Again, an f–order differential equation is turned into a set of $f + 1$ first order, coupled differential equations. However, prior to have them in working form, there are two issues to be dealt with: the choice of the constraint operator, and the regularization of the density matrix.

Since the constraint operator is chosen to be hermitian, the space spanned by the wave function will be the same regardless of the choice: g^k merely distributes the amount of time evolution described by the A coefficients and in the SPFs. The two most usual choices for the constraint operator are:

- $g^{(k)} = 0$: With this choice, the evolution of the SPFs is minimized, and the EOM become:

$$i\dot{A}_J = \sum_L \left\langle \Phi_J | \hat{H} | \Phi_L \right\rangle, \tag{3.23}$$

$$i\dot{\varphi}^{(k)} = \left(1 - \hat{P} \right) \left(\rho^{(k)} \right)^{-1} \langle H \rangle^{(k)} \varphi^{(k)} \tag{3.24}$$

- $g^{(k)} = \hat{h}^{(k)}$, with $\hat{h}^{(k)}$ the separable part of the Hamiltonian in the kth DOF. This choice includes the uncorrelated motion of the SPFs as rotations.

$$i\dot{A}_J = \sum_L \left\langle \Phi_J | \hat{H}_R | \Phi_L \right\rangle, \tag{3.25}$$

$$i\dot{\varphi}^{(k)} = \left[h^{(k)} \mathbf{1}_{n_x} + \left(1 - \hat{P} \right) \left(\rho^{(k)} \right)^{-1} \langle H_R \rangle^{(k)} \right] \varphi^{(k)}, \tag{3.26}$$

with $\hat{H}_R$ being the non–separable part of $\hat{H}$.

As in the case of the TDH approach, the constraints do not affect to the final result of the propagation, but the overall efficiency might be affected. For instance, the *Constant Mean–field* integrator generally used in most MCTDH calculations benefits

from setting the constraint operator to 0. Other integrators work better with the second choice of constraints.

The presence of the inverse of ρ^k in the EOM of the MCTDH approach is a critically important point. The eigenvalues and eigenvectors of the density matrix, known as the *natural populations* and *natural SPFs* respectively, form a unique representation of the wave function of a given system which is not affected by the constraint operators $\hat{g}^{(k)}$ or the initial set of SPFs chosen. Moreover, the natural populations give the contribution of each natural SPF to the particular state of the system. Since the SPFs and the natural SPFs span the same variational space, the natural populations can be used as a convergence criterion: if the last natural SPF has a population near to 0, we are correctly sampling the variational space and therefore the calculation is converging satisfactorily. However, this introduces some kind of paradox: the population of a natural SPF is required to be nearly 0 for good convergence, but this implies that there are quasi–linear dependencies in the SPF basis set, which would lead to a singular and non–invertible single density matrix. This problem has been generally overcome by regularizing the density matrix:

$$\tilde{\rho}^{(k)} = \rho^{(k)} + \epsilon e^{-\rho^{(k)}/\epsilon}, \tag{3.27}$$

with ϵ ranging between 10^{-6} and 10^{-12}. Recently, however, Manthe showed that with a convenient choice of unoccupied SPFs it could be possible to obtain an invertible single density matrix even with an overcomplete basis set[129].

3.2.3 Hamiltonian representation: Kinetic and Potential Energy Operators

The numerical efficiency of the MCTDH method depends most critically on the evaluation of the several matrices appearing in the equations of motion for the *A*–coefficients, Eqs (3.23) and (3.25), and the Single–Particle Functions, Eqs (3.24) and (3.26), namely the mean–field operators and the Hamiltonian action onto the different configurations. For general non–separable Hamiltonians, the evaluation of the different matrix elements in these objects would require the explicit calculation of multidimensional integrals in the primitive basis set, which is specially problematic for the potential energy matrix elements:

$$\left\langle \varphi_{i_1}^1 \cdots \varphi_{i_f}^f | \hat{V} | \varphi_{j_1}^1 \cdots \varphi_{j_f}^f \right\rangle =$$
$$= \sum_{k_1,\dots,k_f} a_{k_1\dots k_{d_1},i_1}^{(1)*} \cdots a_{k_{f-d_p+1}\dots k_f,i_f}^{(f)*} a_{k_1\dots k_{d_1},j_1}^{(1)} \cdots a_{k_{f-d_p+1}\dots k_f,j_f}^{(f)} V(q_{k_1}^{(1)},\dots,q_{k_f}^{(f)}) \tag{3.28}$$

which would take the same effort as the standard propagation method. These multidimensional integrals can be avoided if the Hamiltonian is written as a sum of products of operators, each of them acting on a single DOF:

$$\hat{H} = \sum_{r=1}^{n_s} \prod_{k=1}^{f} \hat{h}_r^{(k)}. \tag{3.29}$$

With Eq. (3.29), the evaluation of the matrix elements becomes a product of one–dimensional integrals:

$$\left\langle \varphi_{j_1}^{(1)} \cdots \varphi_{j_f}^{(f)} | \hat{H} | \varphi_{j_1}^{(1)} \cdots \varphi_{j_1}^{(1)} \right\rangle = \sum_{r=1}^{n_s} c_r \left\langle \varphi_{k_1}^{(1)} | \hat{h}^{(1)} | \varphi_{k_1}^{(1)} \right\rangle \cdots \left\langle \varphi_{k_f}^{(f)} | \hat{h}^{(f)} | \varphi_{k_f}^{(f)} \right\rangle, \tag{3.30}$$

each of which can be efficiently evaluated in the primitive grid of pseudospectral functions. Being clear that a Hamiltonian factorized as a sum of products of 1D operators presents numerical advantages, the question stands to whether general Hamiltonians can be written in such a form.

The product form representation of a kinetic energy operator is always achievable since the introduction of the polyspherical approach developed by Gatti and coworkers, reviewed in Ref. [130]. The potential energy operator, on the other hand, is not generally available as a sum of products, since it is usually obtained from the fitting of *ab initio* electronic structure calculations to general functions which are not in the desired form. There are currently two approaches to solving this issue: using the *potfit* algorithm to convert a general PES into product form, or employing the *Correlation Discrete Variable Representation* (*CDVR*) to compute potential energy matrix elements directly on the grid of SPFs without resorting to the primitive grid.

The *potfit* algorithm was initially developed by Jäckle and Meyer[131]. It aims at fitting any PES into a product form equivalent to that of the MCTDH wave function. In order to do so, one computes the *potential density matrices*, $\rho_{nm}^{(k)}$:

$$
\begin{aligned}
\rho_{nm}^{(k)} &= \sum_{i_1}^{N_1} \cdots \sum_{i_{k-1}}^{N_{k-1}} \sum_{i_{k+1}}^{N_{k+1}} \cdots \sum_{i_f}^{N_f} V_{i_1 \ldots i_{k-1} n i_{k+1} \ldots i_f} V_{i_1 \ldots i_{k-1} m i_{k+1} \ldots i_f} = \\
&= \sum_{I^k} V_{I_n^k}^{(k)} V_{I_m^k}^{(k)},
\end{aligned}
\tag{3.31}
$$

with I^k defined as the composite index containing the indexes of the primitive basis set elements in all but the kth DOF. The diagonalization of these matrices yields a set of N_k eigenvectors, known as *natural potentials*, $v_{i_1 j_1}$ and their respective weights for each DOF. The potential energy function then can be written as a linear combination of direct products of the natural potentials:

$$
V_I = V_{i_1, \ldots, i_f} = \sum_{j_1}^{N_1} \cdots \sum_{j_f}^{N_f} C_{j_1 \ldots j_f} v_{i_1 j_1}^{(1)} \cdots v_{i_f j_f}^{(f)} = \sum_J C_J \prod_{k=1}^{f} v_{IJ}^{(f)}(q_{i_k}^{(k)}).
\tag{3.32}
$$

If all N_k natural potentials are used for the representation of the potential, no approximation is made and Eq. (3.32) is exact. However, its computation still requires the same number of operations as the direct computation in the grid. In order to obtain a computational advantage, the number of natural potentials used to represent each DOF is truncated, so that the potential representation becomes approximate but its evaluation much more efficient. The original *potfit* algorithm is limited to roughly 6 or 7 DOFs, since it needs to store the whole potential energy function evaluated at each grid point in order to retrieve the natural potentials. More recently a new algorithm that uses a *coarse grid* approach to obtain the natural potentials in a more efficient way, the *Multigrid* potfit, has been developed by Peláez and Meyer[132]. This new algorithm expands the applicability of the representation to 12 DOFs, since the number of PES evaluations scales linearly with the number of grid points.

The approach used in the CDVR method is entirely different: instead of fitting the potential energy to an approximate sum of products form, the grid representation schemes explained in Section 2.2 are used to construct a time–dependent grid onto which the potential energy operator is evaluated. In order to do so, the SPFs (time–dependent) are used as a spectral basis, and by diagonalization of the coordinate operator matrix at each time step one obtains the pseudo spectral localized

functions $\xi(q_k)$ and grid points g_k, analogously to Eq (2.24):

$$X_k = \xi_k Q_k^{col} xi_k ,\tag{3.33}$$

where $X_{ij;k} = \left\langle \varphi_i^{(k)} | \hat{x}_k | \varphi_j^{(k)} \right\rangle$, and the diagonal elements of Q_k^{col} are the time–dependent grid points $\{g_k\}$.

In the original formulation of the CDVR, the Time–dependent DVR (TDDVR) presented in annex of Ref [106], the potential energy matrix was directly evaluated as a function of the diagonal grid–points matrix, so that one obtained:

$$\left\langle \xi_{j_1} \cdots \xi_{j_f} | \hat{V}(q_1, \ldots, q_f) | \xi_{l_1} \cdots \xi_{l_f} \right\rangle \approx V(g_{j_1}, \ldots, g_{j_f}) \delta_{j_1 l_1} \cdots \delta_{j_f l_f},\tag{3.34}$$

and for the mean–field:

$$
\left\langle \xi_{j_1} \cdots \xi_{j_{k-1}} \xi_{j_{k+1}} \cdots \xi_{j_k} | \hat{V}(q_1, \ldots, q_f) | \xi_{l_1} \cdots \xi_{l_{k-1}} \xi_{l_{k+1}} \cdots \xi_{l_f} \right\rangle
$$
$$
\approx V(g_{j_1}, \ldots, g_{j_k 1}^{(k-1)}, q_k, g_{j_k+1}^{(k+1)}, \ldots, g_{j_f}^{(f)}) \delta_{j_1 l_1} \cdots \delta_{j_{k-1} l_{k-1}} \delta_{j_{k+1} l_{k+1}} \cdots \delta_{j_f l_f}\tag{3.35}
$$

The similarity with the usual DVR scheme would seem to indicate that the TDDVR could give accurate results for the evaluation of the potential in the SPF basis. This is however not the case, since this approach has a critical problem deriving from the nature of the basis set used to define the time–dependent grid. This is clearly seen by choosing a separable Hamiltonian, which can be perfectly described by a single Hartree product, *i.e.* with just a single SPF in each DOF. If we compare the exact evaluation of $\hat{V}$ in this case:

$$
\left\langle \varphi^{(1)} \cdots \varphi^{(k)} | V | \varphi^{(1)} \cdots \varphi^{(k)} \right\rangle =
$$
$$
\left\langle \varphi^{(1)} | V_1 | \varphi^{(1)} \right\rangle + \cdots + \left\langle \varphi^{(f)} | V_f | \varphi^{(f)} \right\rangle\tag{3.36}
$$

with the TDDVR representation:

$$
\left\langle \varphi^{(1)} \cdots \varphi^{(k)} | V | \varphi^{(1)} \cdots \varphi^{(k)} \right\rangle \approx V_1 \left(\left\langle \varphi^{(1)} | q_1 | \varphi^{(1)} \right\rangle \right) + \cdots + V_f \left(\left\langle \varphi^{(f)} | q_f | \varphi^{(f)} \right\rangle \right),\tag{3.37}
$$

it is clearly seen that the approximation is inaccurate. The underlying reason for this is that the size of the SPFs basis depends only on the amount of correlation in the different coordinates. Therefore, the basis obtained through a TDDVR scheme is too small to be able to take into account all the information of the separable portions of the potential: it only catches the correlation between the DOFs. In order to be able to correctly describe a separable potential, the quadrature scheme in Eq. (3.34) is modified to obtain the CDVR:

$$
\left\langle \xi_{j_1} \cdots \xi_{j_1} | \hat{V}(q_1, \ldots, q_f) | \xi_{l_1} \cdots \xi_{l_1} \right\rangle \approx V(g_{j_1}, \ldots, g_{j_f}) \delta_{j_1 l_1} \cdots \delta_{j_f l_f} +
$$
$$
+ \sum_{k=1}^{f} \left\langle \xi_{j_k}^{(k)} | \Delta V(g_{j_1}, \ldots, g_{j_k 1}^{(k-1)}, q_k, g_{j_k+1}^{(k+1)}, \ldots, g_{j_f}^{(f)} | \xi_{l_k}^{(k)} \right\rangle\tag{3.38}
$$
$$
\times \delta_{j_1 l_1} \cdots \delta_{j_{k-1} l_{k-1}} \delta_{j_{k+1} l_{k+1}} \cdots \delta_{j_f l_f},
$$
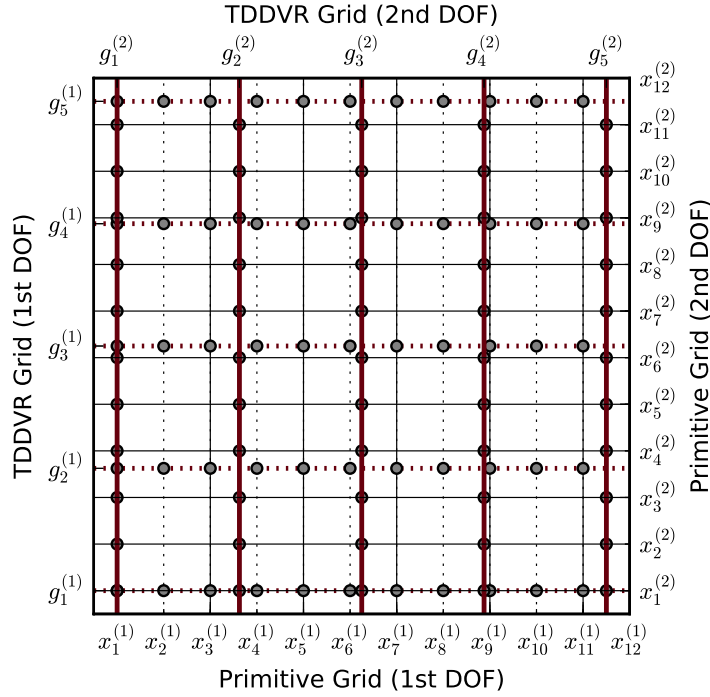
FIGURE 3.1: Scheme of the CDVR approach for two degrees of free-dom (solid and dashed lines, respectively): coarse grid represents the SPFs collocation points, fine grid represents the primitive basis. Po-tential evaluations are made at the grey points.

with the correction term defined as:

$$
\begin{aligned}
\left\langle \xi_{j_k}^{(k)} | \Delta V(g_{j_1}, \dots, g_{j_k1}^{(k-1)}, q_k, g_{j_k+1}^{(k+1)}, \dots, g_{j_f}^{(f)} | \xi_{l_k}^{(k)} \right\rangle &= \\
= \left\langle \xi_{j_k}^{(k)} | V(g_{j_1}, \dots, g_{j_k1}^{(k-1)}, q_k, g_{j_k+1}^{(k+1)}, \dots, g_{j_f}^{(f)}) | \xi_{l_k}^{(k)} \right\rangle &- \\
- V\left(g_{j_1}^1, \dots, g_{j_f}^{(f)} \right) \delta_{j_k l_k}.
\end{aligned}
\tag{3.39}
$$

This modified expression can be visualized by considering that the SPF basis gen-erates a coarse, time–dependent grid, and the primitive basis a fine, fix one. The evaluation of the potential energy operator is then made at the points of the coarse grid, but corrected with evaluations in the intersections between the fine and the coarse grid. This is represented in Figure 3.1 for a 2D problem with different num-ber of primitive and SPFs basis sets in each one. It is important to note that the CDVR scheme does not increase the numerical effort with respect to the simpler TD-DVR, since the correction terms have to be computed in either case to evaluate the mean–field potentials. However, it has two important issues that must be taken into account. First, the evaluation of the mean–field potential matrices within the CDVR scheme is usually the bottleneck of the calculation, taking up to 90% of the total com-putation time[106]. Secondly, it is not possible to improve the quadrature scheme by arbitrarily adding SPFs to the basis set. This is so because an overcomplete SPFs basis, with some functions very poorly populated, will generate grid points in ir-relevant areas of the simulation space, thus worsening the quadrature rather than improving it. However, the trade–off between its problems and the capability of using any PES in the MCTDH scheme is generally favorable.

3.3   Beyond the MCTDH method

The success and popularity of the original MCTDH method propitiated the further development of the algorithm in order to overcome some of its limitations and make it suitable for different kind of systems. Probably the most important contribution in this regard is the *Multi–layer* (ML) MCTDH approach developed by Wang and Thoss[122], due to its success in breaking the exponential scaling up to a certain point, thus allowing the study of systems with dozens or more degrees of freedom. A second variant, which has been extensively used in this work, is the *State–averaged* (SA) MCTDH method by Manthe[124], which greatly simplifies the computation of eigenvalues of the Hamiltonian and the flux operators, and therefore is more suited for the study of dynamics of complex systems.

3.3.1   The Multi–layer MCTDH approach

As it was already discussed, the main advantage of the MCTDH approach over the standard wave packet method is that the double–layer representation decreases the number of coefficients by a factor of roughly $\left(\frac{n}{N}\right)^f$. However, the method still scales exponentially as $n^f + Nnf$. For problems with a large number of degrees of freedom, the first term clearly dominates the effort, so a first step for increasing the numerical efficiency is to try to reduce f by using multidimensional coordinates (Q) instead of the one–dimensional coordinates (q). These new coordinates are termed *logical coordinates* or *particles*, so that we have for instance $Q_1 = (q_1, q_2)$. This is known as *mode–combination*.

In order to represent the multidimensional SPFs, one could use a multidimensional primitive grid, so that the number of DOFs is reduced, but at the cost of requiring the evaluation of multidimensional integrals to obtain the potential matrix elements. The cost of this operation will scale exponentially with the number of modes combined in a SPF, so that in the case of combining up to 4 or 5 coordinates in a single DOF the effort for evaluating the matrix elements for that SPF becomes comparable with the number of coefficients in the upper layer. This rends this approach unusable for high–dimensional problems.

Nevertheless, there is an alternative to the direct representation of multidimensional SPFs in a multidimensional primitive grid: to represent them in a basis of time–dependent, one–dimensional functions, just as the total wave function is represented in the regular MCTDH *Ansatz*. This is the idea of the *Multi layer*–MCTDH approach: to recursively represent high dimensional SPFs in basis sets of lower–dimensional SPFs, so that one has an additional representation layer. Suppose that the kth DOF of an MCTDH wave function is represented by a set of n_k d_k–dimensional SPFs, $\varphi^{(1,k)}$. The total wave function will then read:

$$\Psi(Q_1, \ldots, Q_p, t) = \sum_{j_1=1}^{n_1} \cdots \sum_{j_p=1}^{n_p} A^1_{j_1 \ldots j_p}(t) \prod_{k=1}^{p} \varphi^{1;k}_{j_k}(Q_k, t), \tag{3.40}$$

and the mth multidimensional SPF in the kth DOF becomes, in the ML–MCTDH approach:

$$\varphi^{1;k}_m(Q_k, t) = \sum_{j_1=1}^{\tilde{n}_{\alpha_k+1}} \cdots \sum_{j_{d_k}=1}^{n_{\alpha_k+d_k}} A^{2,k}_{m;j_1 \ldots j_{d_k}}(t) \prod_{\lambda=1}^{d_k} \varphi^{2;k,\lambda}_{j_\lambda}(q_{\alpha_k+\lambda}, t). \tag{3.41}$$
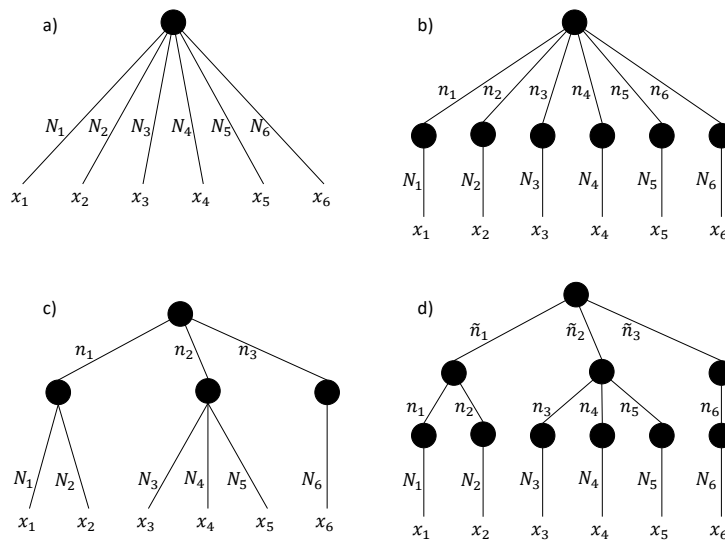
FIGURE 3.2: Schematic representation of different wave function structures: the standard representation (a), the MCTDH wave function (b), the mode–combination form (c) and the ML–MCTDH scheme (d).

This second–layer SPFs, $\varphi_{j_\lambda}^{2;k,\lambda}$, can then be represented in a third SPF layer, $\varphi_{j_\lambda}^{3;k,\lambda}$, or, if their dimensionality is low enough, in the final primitive grid $\chi_{j_\lambda}^{3;k,\lambda}$. The different structures of the representation of a wave function discussed up to now are represented schematically in Figure 3.2: the standard wave packet representation (panel *a*), the MCTDH method (panel *b*), the mode combination scheme (panel *a*), and the ML–MCTDH approach (panel *d*). In the schemes shown in this Figure, a f 1D primitive basis of N_k elements are connected to p sets of $n_{k'}$ SPFs (black dots). It is then easy to visualize the addition of layers from the standard wave function representation to the ML–MCTDH approach. Mathematically, this procedure corresponds to a tensor contraction scheme of the wave function. The ML–MCTDH approach thus provides with the means to overcome the exponential scaling of the wave function with the dimensionality of the problem by recursively applying the MCTDH representation to several levels of SPFs. See Ref. [129] and references therein for a discussion on the scaling laws for the ML–MCTDH approach.

3.3.2 The State Averaged MCTDH approach

The different flavors of the MCTDH algorithm generally focus on the efficient propagation of a single wave function, optimizing the SPF basis set at each time step. The *State Averaged* MCTDH scheme, conversely, aims at the simultaneous propagation of a set of m wave packets sharing the same SPF basis set. The SA–MCTDH approach has two main features which may make it beneficial in a number of applications: first, the fact that the SPF basis set is common between all simultaneously propagated functions makes the operations between them straightforward. We will deal with this later in this Chapter. The second important characteristic is the possible efficiency increase of the algorithm itself. This feature can be rationalized by observing the EOMs of the SA–MCTDH approach. In order to derive the equations of motion for this representation, a virtual index m is added to the coefficient vector

A, so that we have:

$$\Psi^m(Q_1,\ldots,Q_f,t) = \sum_{j_1=1}^{n_1} \cdots \sum_{j_p=1}^{n_p} A_{j_1\ldots j_p,m}(t) \prod_{k=1}^{p} \varphi_{j_k}^{(k)}(Q_k,t), \qquad (3.42)$$

where m ranges from 1 to the number of wave packets, n_{packet}. The resulting EOM are identical to those of the regular MCTDH approach, with only two differences: first, instead of one differential equation for the time evolution of the coefficient, now we have one for each wave function (*i.e. m* independent equations):

$$i\dot{A}_J^m = \sum_L A_L^m \left\langle \Phi_J|\hat{H}|\Phi_L \right\rangle - \sum_{k=1}^{f} \sum_{l=1}^{n_k} g_{j_k l}^{(k)}, \qquad (3.43)$$

with $A_J^m = A_{j_1\ldots j_p,m}$. Secondly, the EOM for the common SPF basis set replaces the individual mean–field operators and density matrices for its sum over all m wave functions:

$$i\dot{\varphi}_j^{(k)} = \hat{g}^{(k)} \varphi_j^{(k)} + \sum_{i,l}^{n_k} \sum_{m}^{n_{packet}} \left(\rho^{(k)}\right)_{ji}^{-1} \left(1 - \hat{P}^{(k)}\right) \sum_{m}^{n_{packet}} \langle H \rangle_{il} \, \varphi_l^{(k)}. \qquad (3.44)$$

It is readily seen from Eq. (3.44) that the cost of propagating the SPF basis set in the SA–MCTDH approach is roughly independent of the number of wave functions are simultaneously propagated, while Eq. (3.43) shows that the propagation time of the A coefficients will scale linearly with the number of functions n_{packet}. Therefore, the efficiency SA–MCTDH approach will depend on the particular case under study. If the propagation of the SPFs basis is the time–determining step of the computation, as it is the case when multidimensional SPFs are used in a mode–combination approach, the SA–MCTDH scheme presents a huge advantage compared with the individual propagation of m functions. Conversely, in the more common case where the coefficient propagation is the time consuming step, the SA–MCTDH approach will consume approximately the same amount of resources as the individual propagation of the m wave packets. However, there is a last factor to take into account when working with this approach: since a *common* SPF basis set is used to represent a *set* of different functions, the SPF are no longer optimized for a single state of the system, but rather are the optimal basis for the *average* of all wave packets propagated. This might mean that a larger number of SPF could be needed to represent correctly all the states than it would if only one function were propagated. As a final remark, it is important to highlight that, if a CDVR scheme is used for the evaluation of the potential energy operator, this operation will be the bottleneck of the computation. Since the CDVR is the same independently of m, the problem will benefit of the SA–MCTDH scheme regardless of other considerations.

3.4   Working with the MCTDH approach

3.4.1   Eigenvalue calculation: Iterative Lanczos Scheme and the SA–MCTDH approach

The Lanczos scheme is one of the most popular methods to obtain a limited number of eigenstates and eigenvalues of hermitian operators. It is based on the construction of a Krylov subspace of the operator $\hat{O}$ by choosing an arbitrary initial function Ψ_0

and then applying the recursion relation:

$$\Psi_m = N \left(\hat{O}\Psi_{m-1} - \sum_{i=0}^{m-1} \Psi_i \left\langle \Psi_i | \hat{O} | \Psi_{m-1} \right\rangle \right), \tag{3.45}$$

with N a normalization constant. Once a set of M functions has been obtained, one diagonalizes $\hat{O}$ in this basis to obtain the M first eigenstates and eigenvalues of the operator. The dimension of the subspace M can be increased, if needed, until convergence is achieved.

The scheme to generate the Krylov subspace presented in Eq. (3.45) is unfortunately not suitable for the MCTDH algorithm. The reason for this is that the SPFs basis will generally change after the operation of $\hat{O}$, and therefore the addition of two functions Ψ_1 and Ψ_2 function will lie in the direct sum space of all configurations of the two functions. The increase of the basis size renders the Lanczos iterative scheme unfeasible. A modified Lanczos scheme suitable for the MCTDH algorithm was developed by Manthe and Matzkies[133]. It is based on the use of projection operators onto a given configuration space, so that the addition operation does not increase the SPF basis size:

$$\Psi_m = N \left(\hat{O}\Psi_{m-1} - \sum_{i=0}^{m-1} \hat{P}\Psi_i \alpha_i \right), \tag{3.46}$$

with α the solution of the set of linear equations:

$$\left\langle \hat{P}\Psi_j | \hat{O} | \Psi_{m-1} \right\rangle = \sum_{i=0}^{m-1} \left\langle \hat{P}\Psi_j | \hat{P}\Psi_i \right\rangle \alpha_i \; j = 0, \dots, m-1. \tag{3.47}$$

In this scheme the maximum order M of the Lanczos diagonalization scheme is given by the number of configurations appearing in the initial wave function.

A second alternative to obtain the eigenstates and eigenvalues of hermitian operators is based on the use of the SA–MCTDH approach to perform a block Lanczos diagonalization approach[124]. The idea of such a method is to start not from a single guess function, but from a set of n_{packet} functions $\left\{ \Psi_m^{(0)}, \; m = 1, \dots, n_{packet} \right\}$, all of them represented in the same SPF basis set. The operator $\hat{O}$ is then represented in this set and diagonalized to obtain approximated eigenstates and eigenvalues:

$$\left\langle \Psi_m^{(i)} | \hat{O} | \Psi_{m'}^{(i)} \right\rangle = \sum_{j=1}^{n_{packet}} U_{mj}^{(i)} a_j^{(i)} U_{jm'}^{(i)}. \tag{3.48}$$

The original basis $\left\{ \Psi_m^{(i)}, \; m = 1, \dots, n_{packet} \right\}$ is transformed to the approximate eigenstate basis, $\left\{ \Phi_m^{(i)}, \; m = 1, \dots, n_{packet} \right\}$, by the unitary transform matrix $\boldsymbol{U}$. The resulting states are rearranged in order of increasing absolute eigenvalue, and orthogonalized with a Gramm-Schmidt scheme to obtain a new basis $\{ \Psi_m^{(i+1)}, \; m = 1, \dots, n_{packet} \}$:

$$\Psi_m^{(i+1)} = N_m \left(\Phi_m^{(i)} - \sum_{j=1}^{m-1} \Psi_j^{(i+1)} \left\langle \Psi_j^{(i+1)} | \Phi_m^{(i)} \right\rangle \right). \tag{3.49}$$

The procedure is repeated increasing the iteration counter i until convergence of

the M eigenstates of the operator. Since all functions in the basis span the same configuration space at each time step (because they are expanded in the same SPFs basis), addition poses no problem in the orthonormalization step.

3.4.2   The Boltzmann Operator and Stationary States Calculations

When working with the MCTDH algorithm, it is not possible to use the Hamiltonian operator, $\hat{H}$, directly within a Lanczos scheme to obtain energy eigenstates. This is so because the application of $\hat{H}$ to a wave function does not conserve the sum of products form, thus preventing the recursive application of the operator to the wave function in Eq. (3.45). Nevertheless, it can be shown that the eigenvalue spectrum of the Boltzmann operator, defined as $e^{-\beta \hat{H}}$ with $\beta = \frac{1}{k_B T}$, corresponds to that of the Hamiltonian operator $\hat{H}$. To see this, we can just define a given wave function $\Psi(x, t)$ which we express as a linear combination of stationary states $\phi(x)$:

$$\Psi(x, t) = \sum_{i=1}^{N} c_i \phi_i(x), \tag{3.50}$$

and see the action of the Boltzmann operator onto it:

$$e^{-\beta \hat{H}} \Psi(x, t) = e^{-\beta \hat{H}} \sum_{i=1}^{N} c_i \phi_i(x) = \sum_{i=1}^{N} e^{-\beta \hat{H}} c_i \phi_i(x) = \sum_{i=1}^{N} e^{-\beta E_i} c_i \phi_i(x). \tag{3.51}$$

There are two conclusions to be extracted from Eq. (3.51): first, it is readily seen that the effect of the Boltzmann operator is to damp the high energy contributions to the total wave function $\Psi(x)$: the higher the energy of the basis function, the smaller the exponential multiplying factor. In the limit of a single stationary state, Eq. (3.51) becomes an eigenvalue equation, and therefore both $\hat{H}$ and $e^{-\beta \hat{H}}$ share the same eigenfunctions. A second feature of this operator can be seen by comparing the last term in Eq. (3.51) with the propagation of a wave packet, Eq. (2.35). Both equations have the same elements, and become equal when we make the relation $\beta = it$. Thus, the application of the Boltzmann operator can be interpreted as a propagation of a wave function in imaginary time, which has the effect of dampening the high–energy contributions to Ψ. This operator can thus be used within the MCTDH framework for the calculation of nuclear eigenstates following the Lanczos scheme above, since a propagation (either in real or imaginary time) does conserve the MCTDH form, and thus can be applied recursively.

  A final remark on the use of the Boltzmann operator to find eigenstates of the Hamiltonian is noteworthy. The spectrum of this operator does not depend on the particular value of T, so in principle any temperature value will yield the same eigenstates. However, the convergence efficiency of the calculation does depend on T: since the effect of the imaginary time propagation is to damp high–energy contributions to the wave function, longer propagations (meaning lower T values) will remove more of these contributions. This will favor the convergence of low–energy eigenstates, since the orthogonalization process will introduce less contamination on them. On the other hand, these long propagations will make convergence of high–energy eigenstates difficult, because their contribution will be minimal and the orthogonalization process will introduce too much noise.

3.4.3 Power spectra from the autocorrelation function

As it was discussed in Section 2.1, it is in principle possible to obtain all the information of a system by computing all the stationary states of the Hamiltonian, or by propagating a wave packet for a formally infinite time. This means that there must be a way to convert the information from the time to the energy domain, and vice versa. One of the simplest and more powerful relations in this regard is the correspondence between the eigenvalue spectrum (or *power spectrum*) of a system, $\sigma(\omega)$, and the *autocorrelation function*, $S(t)$ of a wave packet. Using the definition of a wave packet in a bonding potential as a sum of stationary states, Eq. (2.36), the spectrum is defined as:

$$\sigma(\omega) = \sum_n |c_n|^2 \delta(\omega - \omega_n), \tag{3.52}$$

with $\omega_n = E_n/\hbar$ and c_n the amplitudes of the different energy components of the wave packet (see Eq.(2.36)). It can be shown that this quantity can be also computed as the Fourier Transform of the *autocorrelation function* of the wave packet, $S(t) = \langle \Psi(0)|\Psi(t) \rangle$[84]:

$$\begin{aligned} \sigma(\omega) &= \frac{1}{2\pi} \int_{-\infty}^{\infty} \langle \Psi(0)|\Psi(t) \rangle e^{i\omega t} \, \mathrm{d}t \\ &= \frac{1}{2\pi} \sum_m |c_n|^2 \delta(\omega - \omega_n). \end{aligned} \tag{3.53}$$

If the initial function is chosen to be real, the autocorrelation function has the property:

$$S(2t) = \langle \Psi(0)|\Psi(t) \rangle, \tag{3.54}$$

meaning that the propagation of a function for a total time t_f allows us to calculate the autocorrelation function up to $2t_f$.

It is interesting to remark some features of this relation in order to work effectively with it. As in any pair of conjugate variables, the representation of the time and energy domains are related by the general expressions:

$$E_{max} = \frac{2\pi}{\Delta t} \tag{3.55}$$

$$\Delta E = \frac{2\pi}{t_f}, \tag{3.56}$$

where t_f is the total time of the propagation of the wave packet, and ΔE and Δt are the energy and time resolution, respectively. This means that the total propagation time will set the final resolution of the power spectrum, while the sampling interval of the wave packet's motion will fix the energy window onto which the spectrum will be calculated. However, there is more to be extracted from these relations, since one can apply them to individual features of the functions transformed. Consider for instance a Gaussian wave packet trapped in a harmonic potential evolving according to the TDSE. Its oscillation around the potential energy minimum results in the periodic autocorrelation function shown in the left–hand side of Figure 3.3, and the corresponding power spectrum obtained from Fourier transforming $S(t)$, also depicted in the right–hand side. Inspecting the autocorrelation function we can see that there are three different time scales involved in this process. From shorter to longer, we have the width of the peaks, the separation between consecutive features, and the separation between consecutive recursions with the same amplitude. Each
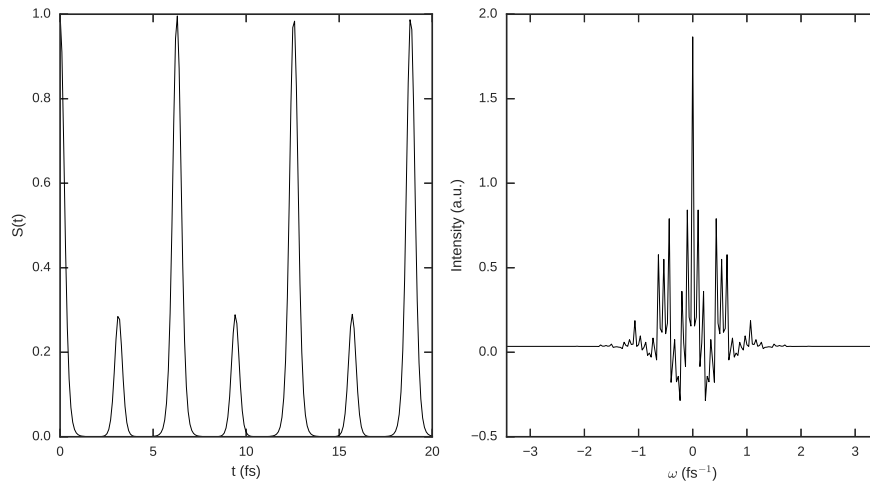
FIGURE 3.3: Autocorrelation function of a Gaussian wave packet propagated under a harmonic potential (left) and the power spectrum resulting from its Fourier transform (right)

one of these characteristic times will have an equivalent characteristic frequency profile in the power spectrum: the width of the recurrences will determine the separation between the spectrum lines, the separation between peaks will fix the envelope function in the frequency domain (note that there are two envelope functions, one for each peak separation in the time domain). There is still more insight on the relation between the power spectrum and the autocorrelation function to be gained from Figure 3.3 and Eq. (3.52). Note for instance that the spectrum is localized in a certain region of the frequency domain, even though we know there are infinite eigenvalues for a harmonic oscillator. This is a direct consequence of the choice of the initial wave packet: the amplitudes in the power spectrum have no physical meaning, they just represent the amplitudes of the wave packet for a certain energy. This is a relevant issue, since it means that in principle only those states which contribute to the initial wave packet will appear in the frequency domain after Fourier Transforming. Thus, the initial function propagated will be of crucial importance to obtain enough information from the power spectrum. Another striking characteristic of the power spectrum shown is the existence of negative amplitudes. These come from of the truncation of the autocorrelation function at an arbitrary value of time: the Fourier transform is defined for infinite times, and therefore using this operation for only a short time window introduces aliasing errors. For decaying functions, this aliasing error does not appear if the propagation time is long enough for the autocorrelation function to go to zero, but bound states will always have this problem. Two ways to overcome it are to propagate for long enough times, so that the error is minimized, or to introduce a *damping function* which smoothly switches the autocorrelation function to 0. Figure 3.4 shows the same system as in Figure 3.3, but with the addition of the damping function:

$$g(t) = \cos\left(\frac{\pi t}{2t_f}\right) \Theta\left(\frac{|t|}{t_f}\right), \tag{3.57}$$

with $\Theta\left(\frac{|t|}{t_f}\right)$ a Heaviside function switching to 0 for values of t longer than t_f. Now the width of the peaks will be related with the frequency of the damping function.

The relation between the autocorrelation function and the power spectrum shown
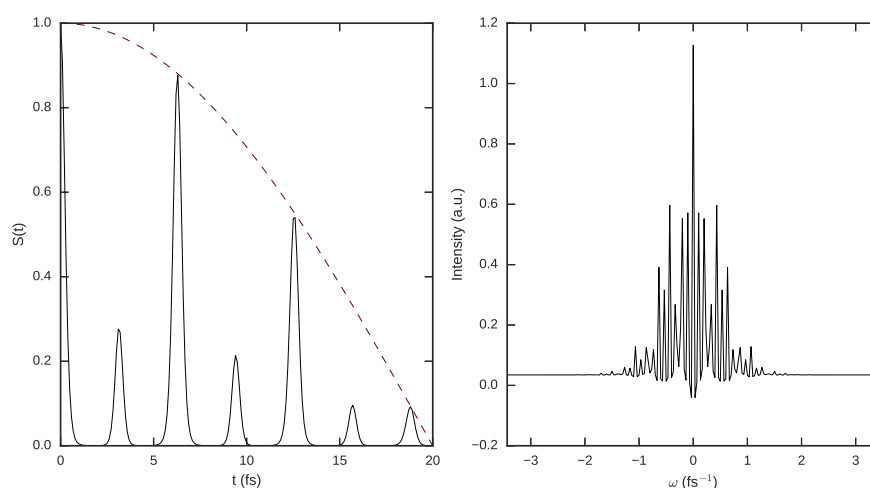
FIGURE 3.4: Same as Figure 3.3, but adding a cosine damping function (Eq. (3.57)) (dashed line)

by Eq. (3.52) is powerful but not always of practical use. This is so specially because the information will depend on the relative weight of the different contributions to the initial wave packet, which are in principle arbitrary. However, there are several modifications of the autocorrelation function that yield results which are more directly related with practical observables. The most important of them in the context of chemical dynamics is the flux–flux autocorrelation function, $C_{ff}(t, t', T)$, which was shown by Miller et al. to be related with the Cumulative Reaction Probability, $N(E)$[134]. We will introduce this formalism later in Chapter 6.

Chapter 4

Model of the H$_2$@SWCNT system

The subject of study of this whole Thesis has been the system consisting of a single H$_2$ or D$_2$ molecule adsorbed in the hollow cavity of a narrow Single–walled Carbon Nanotube. Hereafter we will refer to the system as H$_2$@SWCNT.

The modeling of the system, *i.e.* the definition of the specific geometries and interactions by setting a particular coordinate set and Hamiltonian, is the first step in any simulation, and will be discussed in this Chapter. Since we have two distinct components in our problem, namely the adsorbate (H$_2$ or D$_2$) and the substrate (the nanotube), we have 3 different parts to model: first, the nanostructure must be defined and its geometry optimized, second the Hamiltonian of the confined molecule has to be chosen, and last the interaction between both subsystems must be established.

4.1   Optimization of the nanostructure

The geometry of the substrate is expected to have a critical importance in the outcome of the simulations, since it defines the actual confining cage. Moreover, an optimized structure is required in order to improve the interaction model by the inclusion of phonon scattering, as it will be discussed later in this Chapter and in Chapter 8, where we will present our approach to the molecule–phonon coupling.

The structure of Carbon nanotubes has been largely studied and modeled in terms of a rolled graphene sheet[135, 136]. With this idea in mind, the usual nomenclature to describe a Carbon Nanotube is a pair of *chiral indices*, (m, n), which corresponds to the rolling vector converting the 2D material into a cylinder. Due to the resulting cylindric shape, a nanotube has a particular property: it is commensurate in two dimensions of space, namely x and y, but arbitrarily long in the 3rd dimension (z), so that one can consider it to be infinite in order to simplify the structural model. As any crystalline material, nanotubes are characterized for being *periodic*, and therefore having a *translational symmetry*. This means that if one would move the structure a certain distance along its axis, the resulting atomic disposition would be indistinguishable from the initial one. Such property allows us to define a *crystal lattice*, a set of points of the space related by this translational symmetry. For a general 3D crystal, the lattice is defined as the set of points $\vec{R}$ related by:

$$\vec{R} = n_1\vec{a_1} + n_2\vec{a_2} + n_3\vec{a_3}, \tag{4.1}$$

with $(\vec{a}_1, \vec{a}_2, \vec{a}_3)$ a set of linearly independent vectors connecting equivalent points of the crystal, and (n_1, n_2, n_3) a set of integer numbers. In order to recover an infinite crystal, one defines a *unit cell*, which is the minimum arrangement of atoms in the minimum volume needed to be able to reconstruct a whole infinite structure by using its translational symmetry, and copies this arrangement at all the points of the

crystal lattice defined by Eq. (4.1). In our case, since we have periodicity only along the z axis, the crystal lattice is defined by a single translation vector $\vec{a}$ with module L, and then the infinite structure is recovered by copying the unit cell at intervals L following the direction of $\vec{a}$.

According to the chiral indices, SWCNTs are classified in three distinct types presenting different geometries and properties: *zig–zag* $-(m, 0)-$, *Armchair* $-(m, m)-$, and *chiral* $-(m, n)$, with $m \neq n-$. Zig–zag and armchair nanotubes present a relatively simple and short unit cell consisting on a ring of carbon hexagons sharing a side or a vertex, respectively. The unit cell of a chiral nanotube has an helical symmetry, and can potentially be very long. Some properties, such as the conductivity of the material, are directly linked with the symmetry of the nanotube, and therefore to the chiral indices. Ref. [135] contains a brief introduction on the relation of the symmetry of SWCNT and their electronic structure, as well as a comprehensive review on their vibrational properties. During this Thesis we will work with an insulating (8,0) carbon nanotube, which has been reported to be the narrower one presenting an attractive potential for the hydrogen molecule[46]. We will also briefly work with a narrower (5,0) nanotube during the study of the rovibrational–translational coupling.

The geometry optimization process, as it is common in molecular electronic structure theory, is based on finding an arrangement of atoms corresponding to a minimum of the PES of the system. Due to the translational symmetry of a nanotube, there are two approaches to optimize the geometry of such a system: the *cluster* model, and the *periodic* model. The cluster model is based on representing just a portion of the material by concatenating a certain number of unit cells, and then saturating any partially coordinated atoms at the edges of the representation with hydrogens. Once this *supermolecule* or *cluster* has been built, we can optimize its structure using semiclassical or wavefunction methods, or Density Functional Theory (DFT). In order to obtain converged results, the number of unit cells included in the model has to be large enough so that edge effects can be neglected. These calculations are usually very computationally time–consuming, due to the sheer number of atoms present. Moreover, in some cases it might not be possible to sufficiently reduce edge effects for the calculation of certain properties, thus leading to inaccuracies. On the other hand, the periodic model aims at the resolution of the TISE for the electrons of a perfectly periodic crystal consisting of infinitely many atoms. Of course, it is not possible to explicitly include infinite particles in out problem, and one has to use a workaround to be able to obtain information of an *a priori* infinite system only with a limited number of unit cells. Fortunately, the same translational symmetry which generates an infinite number of atoms in the system also provides with a scheme to solve the Schrödinger equation. First, one defines a *reciprocal lattice*, which is a mathematical construct related with the crystal (or *direct*) lattice by the expression:

$$a_i \cdot b_j = 2\pi \delta_{ij}, \tag{4.2}$$

where b_j is the jth vector defining this reciprocal lattice. Secondly, it can be shown that, for a lattice with cell parameters $(\vec{a}_1, \vec{a}_2, \vec{a}_3)$ which defines a potential with the same periodicity, the eigenfunctions of the Hamiltonian of the system obey Bloch's Theorem:

$$\Psi(\vec{r} + \vec{R}; \vec{k}) = e^{i\vec{k} \cdot \vec{R}} \Psi(\vec{r}; \vec{k}). \tag{4.3}$$

This theorem establishes a relation between the wave function at a given point in the original unit cell with a translationally–equivalent point in any other unit cell

through a *wave vector*, k. This wave vector is in turn related with the *crystal momentum* of the lattice, $\vec{K} = \hbar\vec{k}$. This is a relevant quantity since it arises from a conservation law derived from the translational symmetry of the crystal, and is therefore conserved in different scattering processes. We will discuss this quantity again in Chapter 8.

The eigenfunctions in the right–hand side of Eq. (4.3), named *Bloch functions*, are still not normalizable, since the exponential factor spans the whole space. This is consistent with the infinite number of units cells present in a bulk solid, but again delivers a set of equations that we cannot work with. To maintain the periodicity of the system and at the same time keep the number of unit cells finite, one defines a certain number of unit cells, $N = N_1 N_2 N_3$, and introduces the Born–von Karman periodic boundary conditions (PBC):

$$\Psi(\vec{r} + N_i a_i; \vec{k}) = \Psi(\vec{r}; \vec{k}) \; ; \; \Psi(0) = \Psi(N) \; . \tag{4.4}$$

This model, containing a finite number of cells, results in a *sampling* of the wave vector $\vec{k}$, which due to the inclusion of the PBCs in Eq. (4.4) can be shown to be directly related with the *reciprocal lattice* of the solid:

$$\vec{k} = \sum_{i=1}^{3} \frac{2\pi}{\vec{R}_i} \frac{n_i}{N_i} = \sum_{i=1}^{3} \vec{b}_i \frac{n_i}{N_i} \; , \tag{4.5}$$

with $\frac{2\pi}{\vec{R}_i} = \vec{b}_i$ the cell parameters of the reciprocal lattice and n_i any integer number between 0 and N_i. In the limit of $N \to \infty$, Bloch functions span the whole space and k becomes a quasi–continuous variable. However, with a sufficient sampling of k points it is possible to describe the whole system by interpolating between the discrete values. Thus, by introducing the PBCs and using Bloch's theorem one approximates the solution of a differential equation in the direct space, involving an infinite number of particles in an infinite basis, to the solution of N equations in the reciprocal space, each one involving a finite number of particles, corresponding the number of electrons in a unit cell, N_{el}.

The periodic approach exploits the symmetry of the system better than the cluster one, and therefore can be more efficient. Moreover, it is able to reproduce features originated from the periodicity of the crystal lattice more accurately. However, it also has important drawbacks: defects are not straightforward to treat, and wave function methods beyond Hartree–Fock become exceptionally expensive on this framework, so one can generally is limited to DFT calculations to take electronic correlation into account. Details on electronic structure calculations for periodic systems are beyond the scope of this Thesis, the interested reader is referred to excellent books on general solid state physics[137, 138] and reviews on the specific topic of electronic structure calculations[139, 140].

Unless otherwise noted, the studies carried out during this Thesis have been done after optimizing the (8,0) SWCNT using the B3LYP functional implemented in the Crystal09 code[141, 142], with a 6-311G basis set. The resulting unit cell, consisting on 32 atoms and depicted in Figure 4.1, had a diameter d of 12.1 a_0 and a length L of 8.0 a_0.

4.1.1 Nanotube's vibration

For the most of the works conforming this Thesis, excluding the studies presented in Chapter 8, we have relied on the so–called *frozen structure* approximation. This
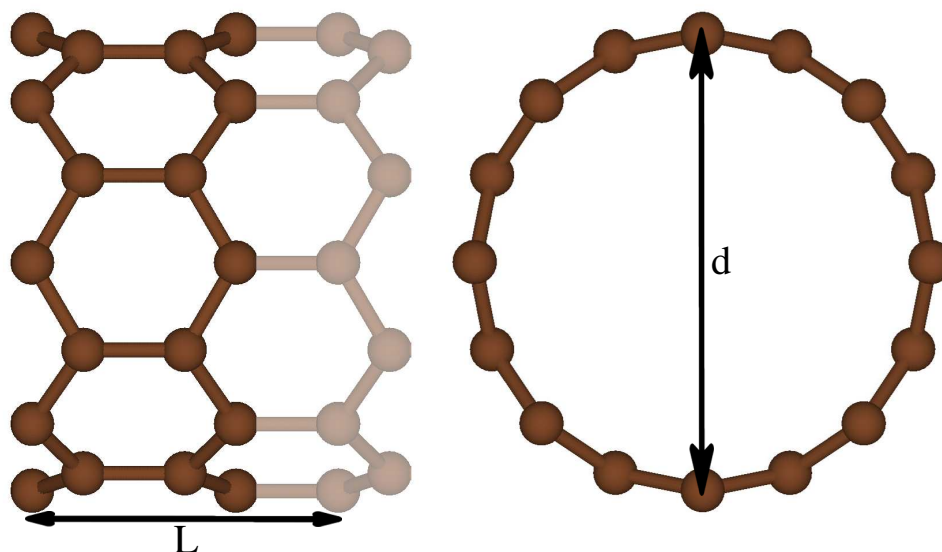
FIGURE 4.1: Representation of the unit cell of the (8,0) SWCNT after optimization. Shaded atoms correspond to a different unit cell.

means that the carbon atoms are explicitly taken into account, but they are fixed in their equilibrium positions. This means that they only contribute to the system's physics by providing the confining potential for the adsorbate, but otherwise there is no energy exchange between the molecule and the nanostructure. This approximation is considered a valid first–order approximation for the system under study and is used, to the best of our knowledge, in all works dealing with quantum confinement effects. This is so due to the difficulty to obtain an accurate and computationally affordable coupling model between the degrees of freedom of the adsorbate and the substrate. One major contribution of this Thesis is to include the vibration of the nanotube in the simulation model, together with the adsorbate–substrate coupling. Chapter 8 will discuss our approach to this issue through a *system–bath* Hamiltonian model.

4.2 The adsorbate's Hamiltonian

The coordinate system chosen to describe the H₂ molecule confined inside a SWCNT is depicted schematically in Figure 4.2. For an isolated diatomic molecule one usually needs three coordinates accounting for the internuclear distance and the molecular orientation to define the system, due to the translational invariance in the molecular frame. In our case, the presence of the nanotube fixes the reference frame and brakes the isotropy of space, so that we need to take into account all $3N = 6$ degrees of freedom (DOFs) to describe a diatomic molecule. Three of them are chosen to be the Cartesian coordinates of the center of mass (c.o.m) of the diatom, x, y and z, with z coinciding with the nanotube's axis. Two more coordinates, θ and ϕ, will represent the orientation of the molecule, being θ the polar angle formed between the nanotube's and the diatom's axes, and ϕ the azimuthal angle in the xy plane. Finally, the sixth coordinate will be the internuclear distance, ρ, accounting for the vibration
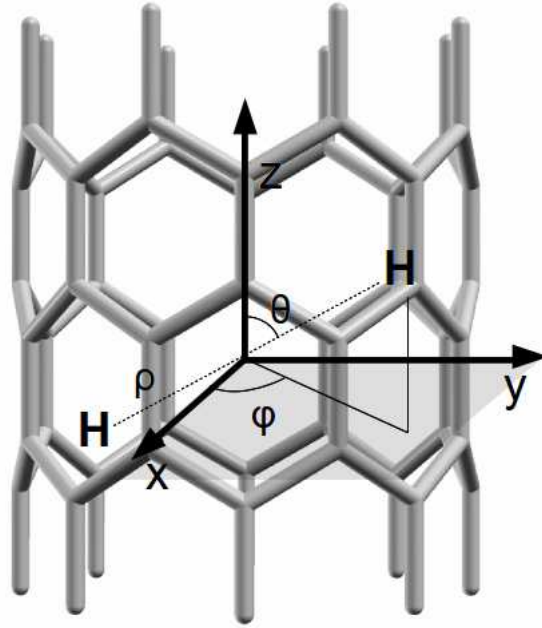
FIGURE 4.2: Scheme of the coordinate system used to describe the H_2 molecule in the hollow cavity of a SWCNT (extracted from Ref [44]).

of the molecule. Thus, the Hamiltonian for the confined molecule will be:

$$\hat{H}_{H_2} = -\frac{\hbar^2}{2\mu_{H_2}}\left(\frac{\partial^2}{\partial\rho^2} + \frac{2}{\rho}\frac{\partial}{\partial\rho} + \frac{1}{\rho^2}\frac{\partial^2}{\partial\theta^2} + \frac{1}{\rho^2}\frac{1}{\sin^2\theta}\frac{\partial^2}{\partial\phi^2}\right) -$$
$$-\frac{\hbar^2}{2m_{H_2}}\left(\frac{\partial^2}{\partial x^2} + \frac{\partial^2}{\partial y^2} + \frac{\partial^2}{\partial z^2}\right) + \hat{V}(\rho,\theta,\phi,x,y), \quad (4.6)$$

with m_{H_2} and μ_{H2} the total and reduced masses of the molecule, respectively. It shall be noted that the kinetic energy operator coincides with that of a free diatomic molecule, and that all couplings between the different DOFs are considered without approximation in this expression. Most works in the bibliography dealing with this and similar molecules have used reduced dimensionality approaches, neglecting either the vibration of the diatom (ρ), its motion along the nanotube's axis (z), or both. The first studies carried out during this Thesis, dealing with the coupling between the different molecular DOFs and their effect on the energy spectrum and the shape of the eigenfunctions, presented in Chapter 5, were also made at a fix z point. Vibration, however, was always taken into account. On the other hand, the potential energy surface is a sum of intramolecular and intermolecular terms. The intramolecular potential is represented through the well-known Morse function which defines the dissociation curve of H_2[143]:

$$V(\rho) = D_e(1 - e^{-a(\rho-R_e)})^2, \quad (4.7)$$

with $D_e = 0.1746$ Hartree, $a = 1.0271$ bohr, and $R_e = 1.4$ bohr.

TABLE 4.1: Lennard–Jones parameters used to define H—C interactions in the present work

	ε (cm^{-1})	σ (Å)
AH PES	21.16	2.82
FB PES	19.26	3.08

4.3   Adsorbate–substrate interaction

The interaction between the confined molecule and the nanostructure is the ultimate reason of the very existence of quantum confinement effects: it defines the confining potential and couples all degrees of freedom together, thus giving rise to the special behavior of the trapped molecules. In most works dealing with quantum confinement effects, this interaction has been modeled as a sum of pair-wise Lennard–Jones (LJ) interactions:

$$\hat{V}_{C-H}(\rho, \theta, \phi, x, y, z) = \sum_{i=1}^{2} \sum_{j=1}^{N_C} V_{i,j}^{LJ}(d_{H_i-C_j}), \tag{4.8}$$

$$V(d_{H_i-C_j})^{LJ} = 4\varepsilon \left[\left(\frac{\sigma}{d_{H_i-C_j}} \right)^{12} - \left(\frac{\sigma}{d_{H_i-C_j}} \right)^{6} \right] \tag{4.9}$$

There is a number of possible choices for the parameters σ and ε appearing in Eq. (4.9) that can be found in the literature. The different sets are derived from systems containing H–C interactions that resemble those of a hydrogen molecule in a nanotube, and have been reported to yield different results regarding the preferential adsorption (or selectivity) of D$_2$ over H$_2$ in narrow SWCNTs[34, 35]. Garberoglio et al.[35] carefully studied these discrepancies, showing than variations of 10% in the values of σ resulted in differences of up to two orders of magnitude in the preferential adsorption results. Conversely, the changes in ε were much less relevant, needing to multiply this factor by two in order to observe variations of a single order of magnitude in the selectivity. However, to the best of our knowledge there is still not a clear answer to the question of which LJ interaction model defines better the H$_2$@SWCNT system. In this Thesis two sets of parameters have been used, which are shown in Table 4.1. The first set was previously used in our group by Huarte-Larrañaga and Albertí to study the adsorption of H$_2$ in different carbon nanotubes using classical molecular dynamics[46]. We will refer to this set as the AH PES. These parameters were also used to investigate changes of the eigenstates of confined hydrogen in (8,0) and (10,0) nanotubes[36]. Throughout the studies conforming this Thesis, the AH PES has been used throughout the study of the rovibrational–translational coupling in a z–fixed H$_2$ molecule embedded in a SWCNT, presented in Chapter 5, as well as in part of the works on diffusion of the diatomic molecule along the nanostructure, discussed in Chapters 6 and 7. The second set of parameters was proposed by Frankland and Brenner[144] based on the interactions in the cyclohexane molecule. This PES, hereafter referred to as the FB PES, has been used in relevant works in the nanoconfinement field[34, 35, 40] yielding high selectivities, and seems to be widely accepted in the community. In this Thesis, the FB PES has been used to calculate diffusion coefficients of H$_2$ and D$_2$ in an (8,0) carbon nanotube, both with a full dimensional model and within an adiabatic approximation, and during the study of the phonon–hydrogen coupling shown in Chapter 8.
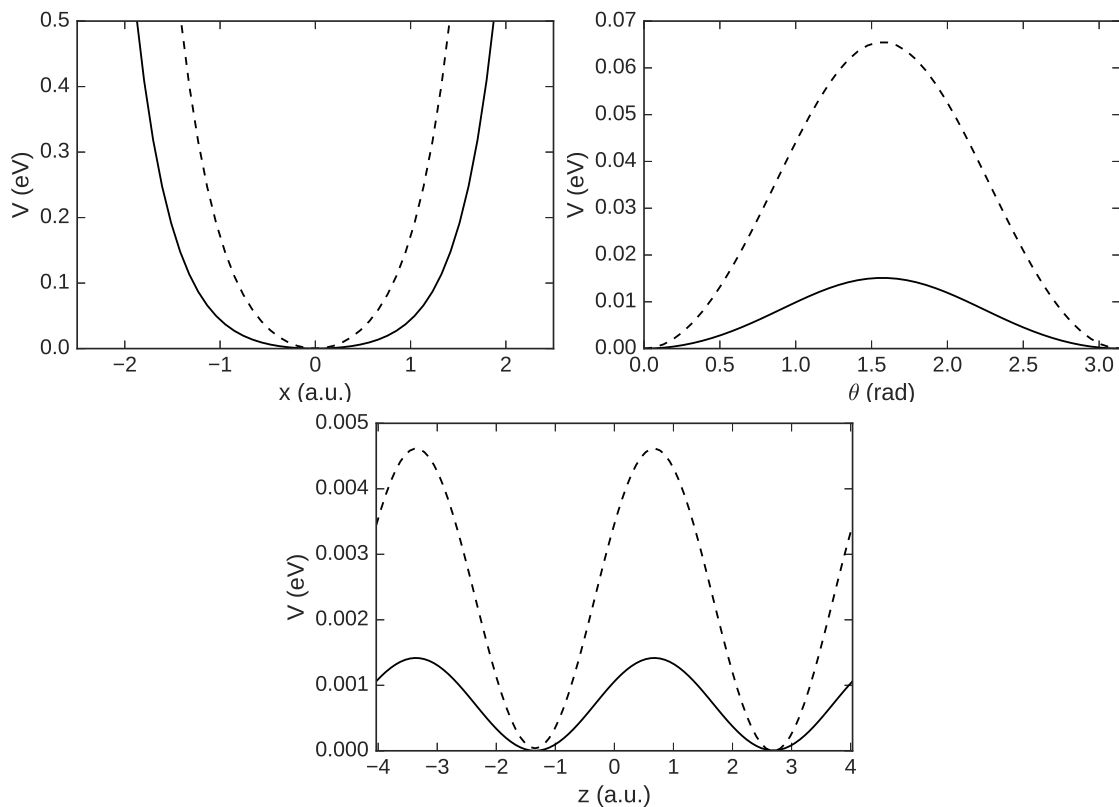
FIGURE 4.3: Relaxed projection of the AH (solid) and FB (dashed) potential energy surfaces along the x (top–left), θ (top–right) and z (bottom) DOFs.

The differences between the two PES are highlighted in **Publication 2**. In spite of this, and for reference within this Thesis, we reproduce the in Figure 4.3 1D cuts of both PESs along significant dimensions, such as the orientation of the molecule (θ, upper right panel), its position along the axis of the nanotube (z, lower panel), and the distance of the c.o.m. from this center of the nanotube. It is readily seen that the FB PES produces a tighter potential, and therefore confinement effects are expected to be more important for this set of parameters. This is specially noticeable in the barriers for rotation and diffusion, which are approximately three times larger in the case of the FB PES compared with the AH PES. However, as it is discussed in **Publication 2**, these changes result mainly in quantitative differences, without a change in qualitative behavior.

Taking a step back, we could consider the whole substrate–plus–adsorbate pair as a whole system. Then, the total Hamiltonian would be a sum of the adsorbate Hamiltonian, Eq. (4.6), and a set of operators describing the collective motion of the carbon atoms in the nanotube. However, both sets of motions are not separable: the vibrations affect the motion of the adsorbate, and in turn the presence of the confined molecule distorts the vibration of the nanostructure. Therefore, we need to account for the coupling between the DOFs of the substrate and the adsorbate in some way. As already pointed out in Section 4.1, this correlation can be included as a set of terms deriving from a system–bath coupling model. This will be presented and discussed in Chapter 8.

Chapter 5

Confinement effects in H$_2$: energetic and structural changes

5.1 Distortions of molecules in nanoconfined environments

When a molecule or atom is adsorbed in a nanocavity, the adsorbate–substrate interactions appear within a range comparable to that of the de Broglie wavelength of the confined species. For this reason the structure of the particle is affected much more harshly than in case of adsorption on regular surfaces: new quantizations may appear due to the finite dimensions of the cavity, leading to relevant couplings between otherwise independent degrees of freedom, other motions may become hindered or favored, and the whole eigenvalue spectrum of the system can be altered at both nuclear and electronic levels. All these aspects are part of what we call quantum confinement effects. The understanding of these structural changes plays a critical role in the explanation of other phenomena such as quantum molecular sieving or reactivity changes of confined species, and many studies have been devoted to this topic in several systems, as it was reviewed in the Introduction of this Thesis. This Chapter is devoted to the qualitative and quantitative discussion of the effects of confinement on the rovibrational levels of the H$_2$ molecule, when it is embedded in the hollow cavity of narrow carbon nanotubes.

During this first study of the H$_2$@SWCNT system we wanted to focus our attention on the structural changes undergone by the adsorbate in the confined degrees of freedom. In order to do so, and for better comparison with the isolated molecule, all the simulations were made considering that the center of mass of the diatom was fixed at a given point along the axis of the nanotube, *i.e.* we neglected the motion along this particular coordinate. This assumption is generally believed to be reasonable: due to the low corrugation of the PES in this DOF, the overall structure of the wave function in the remaining coordinates is expected to be, to a large extent, independent of the particular position along the nanotube. This model has been extensively used in relevant works in the field (see for instance Refs [28], [34] or [36]) and has provided with a large amount of insight on nanoconfined systems. In our model we have used the Hamiltonian described in Chapter 4, Eq. (4.6), only removing the kinetic energy operator of the z dimension, so that all the remaining coordinates, as well as the couplings between them, are taken into account without approximation. Regarding the PES, this work was carried out exclusively using the AH PES.

The study of the quantum confinement effects on the structure of H$_2$ was tackled from two different points of view. First, the overall effect of confinement on the eigenvalue spectrum of H$_2$ was analyzed by computing the power spectrum of the H$_2$@(8,0) system through Fourier transforming its autocorrelation function, as explained in detail in Section 3.4. Secondly, we focused on the inspection of the

changes undergone by individual vibrational–rotational states when changing from a free into a confined environment. I order to do so, we computed the eigenstates of the first 50 nuclear eigenstates of hydrogen adsorbed in a (8,0) and a (5,0) carbon nanotube, and analyzed them through comparison with the states of a separable 5D model. This second part is discussed in greater detail in **Publication 1**.

5.2 Result Discussion

5.2.1 Overall assessment of quantum confinement: effect on the power spectrum

The power spectrum of a system offers a general view of its eigenvalues, with each band being related to the energy of a particular eigenstate. In contrast with diagonalization methods, which explicitly find a certain number of eigenstates and eigenvalues, the power spectrum gives results for a large energy window after just one propagation. It is this feature that makes it a particularly convenient tool to examine the consequences of quantum confinement effects: by direct comparison of the band structure of a confined molecule with the eigenenergies of the free species, we can obtain relevant information about new quantization or couplings between the eigenstates, just by the emergence at certain areas of the confined system spectrum of new bands which are not present in the one for the free molecule.

In order to obtain the power spectrum for the H_2@SWCNT system we propagated a single wave packet for a total propagation time $t_{final} = 1000$ fs, and we computed the autocorrelation function of the propagated function. Then, in order to prevent spurious bands due to aliasing, we added a cosine damping function (Eq. (3.57)) and computed the power spectrum through a Fourier Transform. The resulting spectrum, shown in Figure 5.1, spanned an energy window from 0 to 16000 cm^{-1} with a resolution of 5 cm^{-1}. In the figure, for the sake of clarity, only the window from 2000 to 6000 cm^{-1} is shown. Moreover, the eigenergies of the free hydrogen molecule, shifted in order to match the ZPE of the power spectrum of the confined system, are also depicted as vertical dotted lines.

The most relevant feature that can be extracted from Figure 5.1 is the abundance of eigenstates appearing in the confined system, compared to those existing for the free molecule. This already hints at the great effects that confinement causes in a molecular system. This densification of the spectrum can be studied by direct observation of the projection of some eigenstates along relevant dimensions. This simple analysis allows us to explain the differences in the spectrum of the free and confined systems through three different, albeit related, factors. First, and probably foremost, the adsorption inside the nanotube introduces the molecule in a tight potential in the x and y coordinates. This leads to the quantization of these DOFs, thus resulting in the appearance of multiple bands corresponding to the new eigenstates of the system. A second source of new bands is the breaking of the isotropy of the space, which is a consequence of the cylindrical shape of the nanotube and the confining potential that generates. This reduction of the symmetry causes the breaking of the degeneracy of the rotational levels: states with same total angular momentum quantum number l, but different absolute value of its z–projection $|m_z|$, will no longer be degenerate. As a final factor, we have the coupling between the rotational and translational degrees of freedom, which is much more important in the confined system due to the tight potential, and gives some more fine structure to the eigenvalue spectrum. All these factors affect not only the number of eigenstates in a given energy range, but also the overall ZPE of the system: the confined molecule presents a ZPE
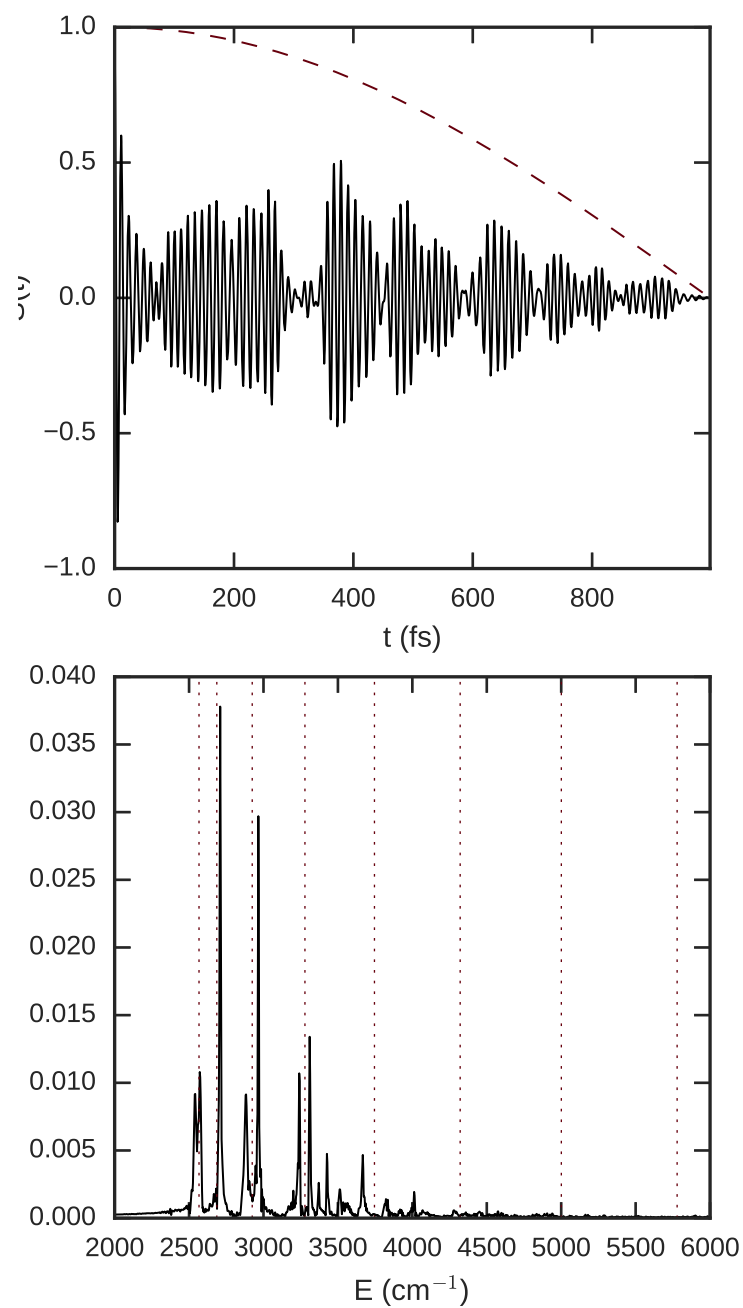
FIGURE 5.1: Top panel: Autocorrelation function (solid line) and damping function (dotted line) for the H_2@SWCNT system. Bottom panel: Power spectrum (solid line), and energy values corresponding to the eigenstates of the free H_2 molecule (dotted vertical lines)

of 2540 cm^{-1}, which is 421 cm^{-1} above that of free H_2. Part of this difference appears due to the quantization on the translational degrees of freedom, x and y. However this factor does not account for all the increase in the ZPE, as discussed in Ref. [36]. The remaining ZPE is explained precisely by the existence of a coupling between the rotational and translational motions.

As it was already discussed in Section 3.4, a significant property of the power spectrum obtained through Fourier Transform of the autocorrelation function is that the intensities of the different bands depend only on the initial state propagated: since the autocorrelation function contains the overlap of the function propagated at a certain time t with the initial wave packet, the more a given eigenstate contributes to the initial wave packet, the more intense will be the corresponding band in the power spectrum. This can be a disadvantage, since it is possible that some bands end up having intensities too low to be detected. However, we can also take profit of this property to investigate different energy regions of the spectrum by propagating initial states that resemble some excited levels of the system. This is clearly seen in Figure 5.2, where we display 3 different power spectra for the H_2@SWCNT system. All them were computed after the same propagation time and using the same convolution function, but the initial state was different in each case. The red spectrum (which coincides with that of Figure 5.1) was obtained using an initial state with a high probability density around the equilibrium value of the internuclear distance ($\rho = 1.4\ a_0$) and the center of the nanotube, $x = y \approx 0$, but the probability density in the polar angle was centered at $\theta = \pi/2$, corresponding to a molecule perpendicular to the nanotube's axis. The resulting spectrum has intense bands corresponding to rotationally excited eigenstates, but focused only in the region in which there are no vibrational excitations. On the other hand, the green spectrum used a similar initial state, but with the initial probability density in ρ set to values closer to 2 a_0, resulting in a spectrum with similar relative intensities in the region without vibrational excitations. However, we can now see clusters of bands at higher energies. Each one of these clusters can be related with a vibrational excitation, so we see bands up to $v = 2$. Finally, the blue spectrum is obtained when, in addition to the previous change, the maximum probability density of the initial state in the xy plane is shifted away from the nanotubes axis to $x = -y = 0.5$. This yields a very low–intensity spectrum with a large amount of numerical noise, and multiple spurious bands not corresponding to any eigenstate of the system. This is better seen in Figure 5.3, where we display a close–up to the region between 2400 cm^{-1} and 3500 cm^{-1} for all three spectra just discussed together with the eigenenergies of the individual H_2@(8,0) molecular states, which will be discussed in the next Section. Note the different relative intensities of the bands. Consistently with the previous discussion, we see how the bands correspond to different eigenstates of the system, and we can identify some more trends. For instance, the rotationally excited wave packet (red spectrum) has large intensities for a limited number of eigenstates, which are expected to be rotational excitations, but at the same time a large amount of other states do not appear clearly. Conversely, using a vibrationally excited initial wave packet (green spectrum) decreases the intensity of some bands, providing with a larger number of significant peaks corresponding clearly to molecular states. Finally, if translational excitation is also included in the initial wave packet (blue spectrum), the intensities of the bands are too low to be able to distinguish actual bands from spurious peaks appearing due to aliasing and numerical noise. Note however that none of the spectra are able to resolve all individual bands, due to the very low energy separation between the eigenstates at energies higher than 2800 cm^{-1}.
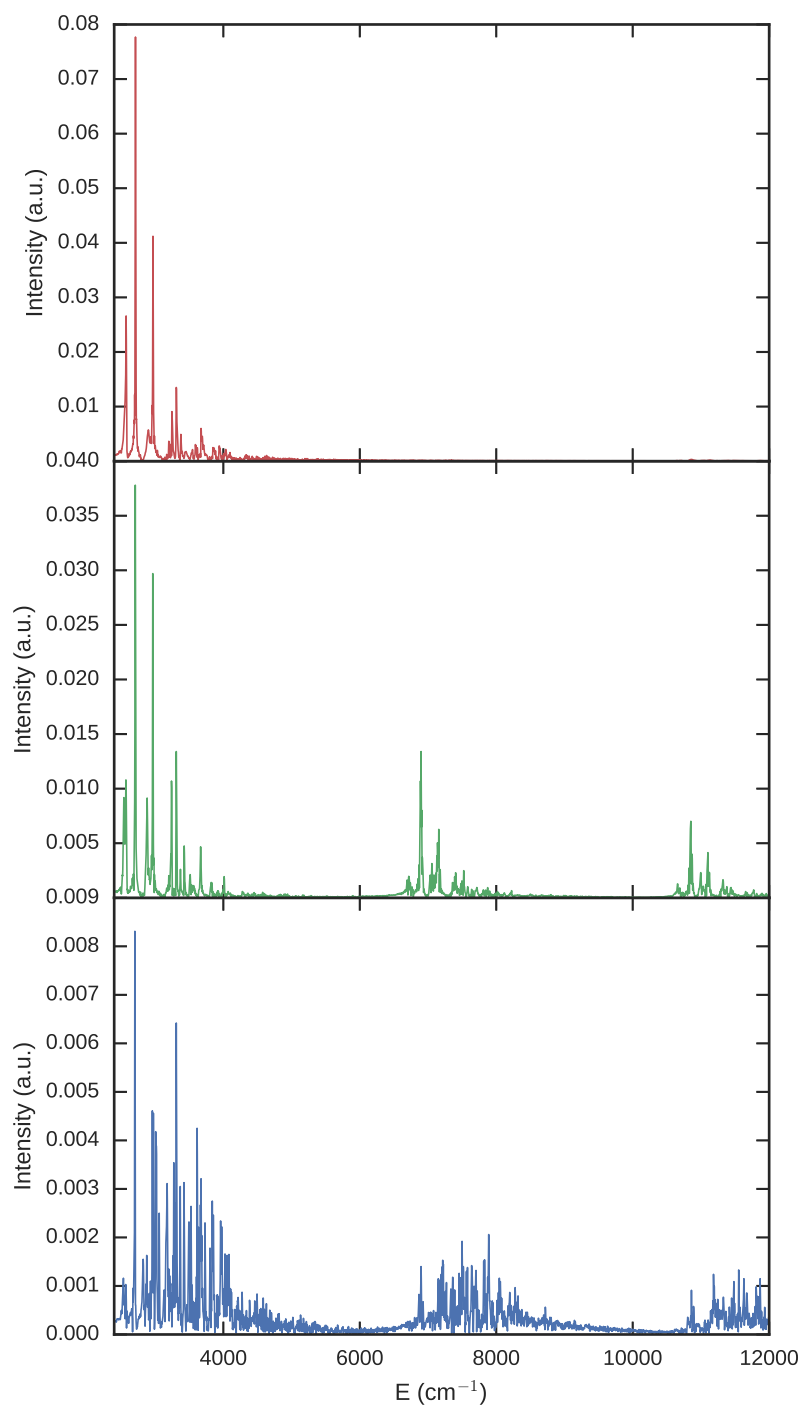
FIGURE 5.2: Power spectra for the H_2@(8,0) system, obtained from an initially rotationally excited (red), rotation and vibrationally excited (green) and rotation, vibration and translationally exited (blue) wave packet.
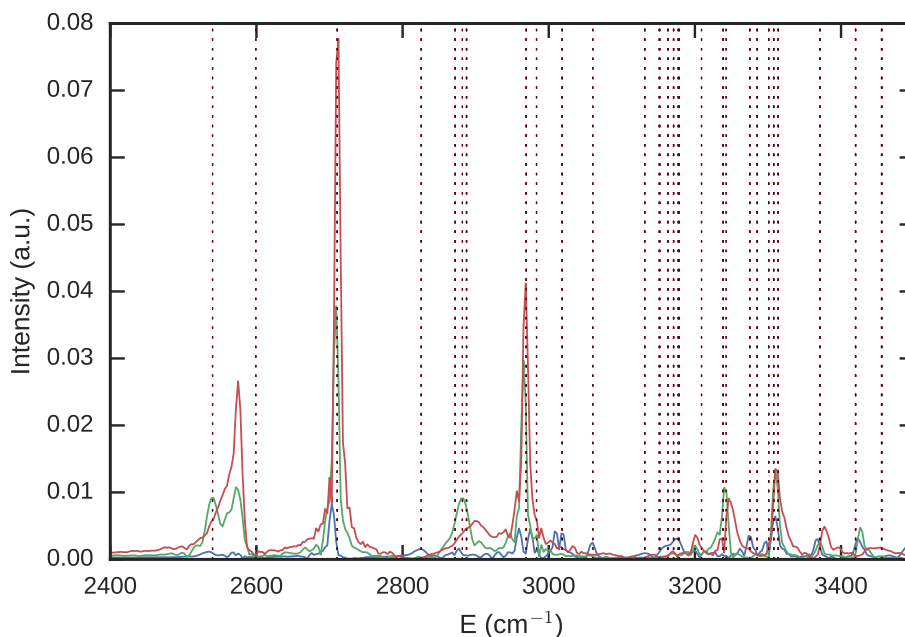
FIGURE 5.3: Close up to the low–energy region of three power spectra of the H_2@(8,0) system, obtained from an initially rotationally excited (red), rotation and vibrationally excited (green) and rotation, vibration and translationally exited (blue) wave packet. The energies corresponding to H_2@(8,0) eigenstates appear as dotted vertical lines.

5.2.2   Understanding the confinement of nuclear eigenstates

This Section summarizes the contents of *Publication 1*, reproduced in Section 5.3.

The discussion on the power spectrum just presented evidences the enormous effect that adsorption onto a nanocavity has on the physics of the H_2 molecule. However, rather than just confirming the existence of such changes we want to be able to justify and understand their origin and implications. Although this can be made to a certain extent by taking advantage of the propagation of different wave packets, as seen in Section 5.2.1, in order to get the most information of the system we need to compute the actual eigenstates of the confined molecule. Once they are found, we can analyze them in order to understand the structural changes in H_2 when it goes from a free to a confined environment, as well as the coupling introduced by the nanotube's potential. However, a direct examination of the wave functions is not possible: they are 5D objects, and therefore cannot be fully represented in our space. For this reason we must resort to some other tools in order to extract information from our eigenstates.

In our work we have employed three schemes for obtaining a picture of such high–dimensional functions. The first one is to project the function onto particular coordinates of the representation, so that we reduce its dimensionality until we are able to graphically visualize the eigenstate in some DOFs. We can repeat the projection along different coordinates to obtain a more or less general picture of the wave function. As reported in **Publication 1**, we used this simple procedure in our system to confirm the hypothesis that the rotation of the H_2 molecule is hindered inside the nanotube, and that this symmetry breaking is reflected in the non–degeneracy

of states with the same total angular momentum. We also found that the quantization in the *xy* plane was similar to that of an anharmonic oscillator, although the projections of some excited states had unusual shapes. This prevented us to assign quantum numbers to all DOFs of the system. A second common tool for the eigenstate analysis is to compute the scalar product of a given eigenstate with a set of reference functions, such as the ones obtained from analytically solving the eigenvalue equation for simple Hamiltonians or from the numerical solution of a similar, better understood problem. In our case, we used as a reference an *ad–hoc* 5D function consisting on the direct product of a Morse wave function ($M_k(\rho)$) to represent vibration, an spherical harmonic ($Y_l^m(\theta, \phi)$) for the rotation, and anharmonic oscillator eigenstates ($\Xi_{n_x,n_y}(x, y)$) for the motion of the c.o.m. of the molecule. The first two sets of functions are described analytically, while for the third set we numerically computed the eigenstates of an structureless particle in the actual confining potential. Thus, we obtained a reference function in an hypothetic separable system which we understand, and can evaluate the confinement effects by computing the overlap between these references and the actual eigenstates of the adsorbate. This procedure confirmed that there was an important amount of mixing between the degrees of freedom when compared with our separable model, as reported in Table ST1 of **Publication 1**. This mixing, which comes as a result of the strong coupling between the DOFs, indicates that the separable model is not suitable to label the eigenstates of the confined system accurately.

Both of the approaches just discussed provided with a general interpretation of the confinement effects of the H_2 molecule in the hollow cavity of a SWCNT. However, we found that these approaches, although powerful and well-known, might hide some information which might be useful to really understand the coupling between the degrees of freedom: a scalar product quantifies the coupling, but we lose all visual information after the operation; a projection helps us to visualize a particular degree of freedom, but by averaging all the other ones we again lose the possibility to see the coupling. In order to overcome this difficulty, we developed an approach based on establishing a relationship between the 5D eigenfunctions of the confined system and those of familiar low dimensional problems by computing *partial overlaps* in selected degrees of freedom. Depending on the reference function used for the overlap, we talk of *translational* partial overlap functions, when we use anharmonic oscillator functions as reference:

$$\sigma_{n_x,n_y}(\rho, \theta, \phi) = \left\langle \Psi(\rho, \theta, \phi, x, y) | \Xi_{n_x,n_y}(x, y) \right\rangle, \tag{5.1}$$

and *rotational* partial overlap functions, when the overlap is made with spherical harmonics:

$$\sigma_{l,m}(\rho, x, y) = \left\langle \Psi(\rho, \theta, \phi, x, y) | Y_l^m(\theta, \phi) \right\rangle. \tag{5.2}$$

These objects offer a unique view of the coupling between two sets of DOFs: we can visualize how the overlap between the whole wave function and a selected test case in a given DOF changes as a function of other DOFs, thus obtaining a picture of the global shape of the wave function at different points of the space. Several examples of this can be seen in **Publication 1** for the H_2@(8,0) system, where for the sake of clarity just 1D cuts of these functions are shown, keeping the other two coordinates at the probability maximum. In addition to the hydrogen molecule inside a (8,0) nanotube, the same procedure was applied in case of the H_2@(5,0) system, an hypothetical system which served as an example of how the methodology allowed to understand even extremely distorted wave functions. The observation of these

$$0.026\,Y_0^0 + 0.006\,Y_2^0 \qquad\qquad 0.020\,Y_0^0 + 0.01\,Y_2^0$$
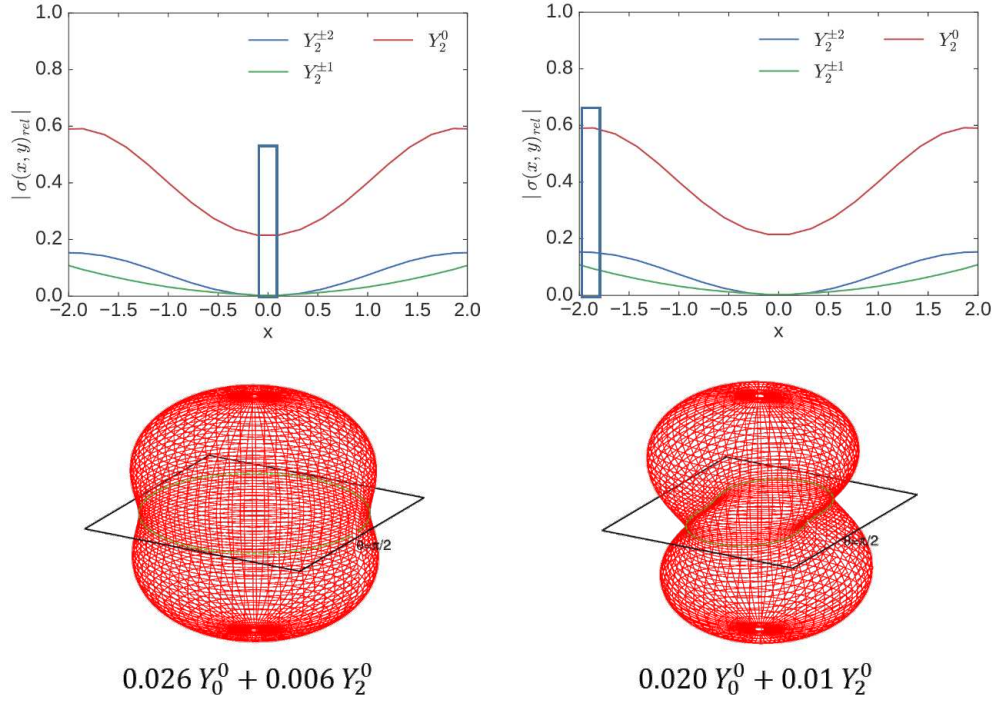
FIGURE 5.4: Absolute value of the Relative Partial overlap functions, $\sigma_{l,m}^{rel}(x,y)$, of the ground state of the H_2@(8,0) system with different spherical harmonics (top), and the shape of the rotational wave function (bottom) at different points along x: the center of the cavity (left), and near the nanotube wall (right).

functions gives us an intuitive idea of the coupling between the DOFs, since we can see how the contribution of a certain separable model function depends on the other coordinates of the system.

In some particular cases, if the overlap with a single given reference function is much larger than with the others, but still we have a relevant contribution of other states, it can be useful to inspect the *relative partial overlap* function. For the rotational partial overlap function, this is defined as:

$$\sigma_{l,m}^{rel}(\rho,x,y) = \frac{\sigma_{l,m}(\rho,x,y)}{\sigma_{l^{main},m^{main}}(\rho,x,y)} \tag{5.3}$$

Therefore, it gives us the relative contribution of a given reference function with respect to the most relevant one, and that helps us to visualize the changes of the wave function. As an illustrative case, the most relevant relative rotational partial overlap function of the ground state of the H_2@(8,0) system is shown in Figure 5.4, together with the graphical representation of the wave function in the rotational degrees of freedom in two different situations. These representations correspond to two different positions of the c.o.m. of the diatom: on the left–hand side the translational DOFs are fixed at the center of the cavity, while on the right–hand side the molecule is located near the wall of the nanotube. It is clearly seen that the shape of this *rotational* wave function changes from one position to the other, being cylindrically symmetrical at $x = 0\,a_0$ and becoming distorted at $x \approx 2\,a_0$. The relative partial overlap functions help us to rationalize such change in terms of the contribution of the different reference functions: as the c.o.m. is displaced towards the nanotube walls we

see an increase of the contribution of the Y_2^0 function, and of the asymmetric functions $Y_2^{\pm 1}$ and $Y_2^{\pm 2}$. Since we can represent these model functions to see their shape, it becomes easier to visualize how the wave function will behave near the nanotube wall. A potential drawback of the relative partial overlap functions appears in areas with a low probability density, and particularly on nodal points or surfaces: on these areas, the function will artificially grow to infinity, and therefore one must be careful with their interpretation. Nevertheless, all things taken into account we find they are a useful tool that provides with an intuitive vision of the system, and thus can help in getting more insight on it.

5.3 Publication 1: *5D quantum dynamics of the H_2@SWNT system: Quantitative study of the rotational–translational coupling*

5D quantum dynamics of the H₂@SWNT system: Quantitative study of the rotational-translational coupling

M. Mondelo-Martell and F. Huarte-Larrañaga[a)]
Departament de Química Física & Institut de Química Teòrica i Computacional (IQTCUB),
Universitat de Barcelona, C/ Martí i Franqués 1, 08028 Barcelona, Spain

The dynamics of the dihydrogen molecule when confined in carbon nanotubes with different chiralities and diameters are studied by using a 5 dimensional model considering the most relevant degrees of freedom of the system. The nuclear eigenstates are calculated for an (8,0) and a (5,0) carbon nanotubes by the State-Average Multiconfigurational Time-dependent Hartree, and then studied using qualitative tools (mapping of the total wave functions onto given subspaces) and more rigorous analysis (different kinds of overlaps with reference functions). The qualitative analysis is seen to fail due to a strong coupling between the internal and translational degrees of freedom. Using more accurate tools allows us to gain a deeper insight into the behaviour of confined species. © 2015 AIP Publishing LLC. [http://dx.doi.org/10.1063/1.4913293]

I. INTRODUCTION

The study of the confinement of gaseous species inside nanostructured materials (*quantum confinement*) has become a matter of study in the last years, both theoretically and experimentally.[1–3] This interest arises due to the unique phenomena that take place when a molecule is embedded in cavities within the nanometric scale, which may be seen as quasi-zero or quasi-one-dimensional spaces. Among these effects, we find distortions of the electronic structure and geometry of the species,[4] as well as changes in their dynamic behavior due to a strong translation-rotation coupling.[5–8] These effects lead to potential applications in chemistry and physics: they allow a tight control of certain reactions,[9] or the separation of isotopes of gaseous species at the molecular level, known as *quantum sieving*.[3,10] In particular, the hydrogen molecule (H₂) has been a popular target for these studies due to the interest of nanostructures as hydrogen storage devices for technological applications. Back in 1999, FitzGerald *et al.*[11] studied the neutron scattering spectra of the hydrogen molecule confined in the octahedral and tetrahedral interstitial sites of a C₆₀ lattice both theoretically and experimentally, in one of the first works on the dynamics of a confined molecule considering both rotation and translation. Later on, attention was shifted to other carbon allotropes, such as carbon nanotubes (CNTs). For this kind of system, Yildirim *et al.* made an extensive formal study of the energetic levels of hydrogen using a cylindrical-symmetry potential energy surface model.[6,12] Later on, Gray and coworkers improved the potential model and were able to give deeper insight into the system with a four dimensional Hamiltonian which did not take into account the vibrational degree of freedom (DoF).[5] The first five-dimensional study of hydrogen confined in carbon nanotubes, considering hydrogen's vibration, was later carried out by some of us.[13] This research field has been greatly benefited lately by

the valuable contributions of Bačić and coworkers, who have made rigorous calculations of the hydrogen molecule in metal-organic frameworks (MOFs),[7] of hydrogen endofullerenes,[2] and of the HD molecule confined in a clathrate hydrate structure.[1]

In the absence of a confining potential, the internal (rotation and vibration) and translational degrees of freedom of a given molecule would be perfectly separable. This means that the total wave function could be described as the direct product of a free particle and an internal motion function, with quantum numbers l, m (rotation), and v (vibration),

$$\Phi^v(\vec{x}, \theta, \phi) = e^{ik\vec{x}} \psi_l^{vm}(\rho, \theta, \phi). \tag{1}$$

When confinement appears, the potential does not only affect the translational degree of freedom, which is now quantized as it corresponds to a bound system, but also couples the internal degrees of freedom and the translation of the molecule. Due to this coupling term, the wave functions describing the final system will not be a direct product of the functions for the individual degrees of freedom, but rather a mixture of them

$$\Phi^v(\vec{x}, \theta, \phi) = \sum_{n_x=0}^{\infty} \sum_{n_y=0}^{\infty} \sum_{l=0}^{\infty} \sum_{m=-l}^{l} c_{n_x, n_y, l, m} H_{n_x n_y}(\vec{x})$$
$$\times Y_l^m(\theta, \phi), \tag{2}$$

and therefore the internal and translational quantum numbers cannot be considered good quantum numbers.

It is commonly accepted that very light molecules, such as H₂ and D₂, represent an exception to the previous statement. This is so because these species present an exceptionally large moment of inertia that causes the separation between energy levels in the unconfined problem to be very large. Therefore, the mixing of states with different l values due to the coupling with the translational degree of freedom in a confined case is small enough to consider l as a good quantum number. This is the idea followed by Yildirim *et al.* for their formal analysis of the confinement of molecular hydrogen in different

nanostructures.[6] However, Gray *et al.* gave the first hints on the fact that this assumption does not hold for the tightest confining potentials, such as the one generated by a (8,0) Single-Walled Carbon Nanotube (SWCNT).[5]

In the present work, we want to go one step further from the previous studies of nanoconfined species by performing a rigorous quantitative study of the quantum eigenstates of a hydrogen molecule inside single-walled carbon nanotubes of different chiralities: (8,0), which accounts for the narrowest nanotube in which physisorption of hydrogen is energetically favourable, and (5,0), which will serve as example of an extremely tight confining potential. The full dimensional eigenstates of the nanoconfined molecule will be interpreted in terms of the eigenfunctions of a separable H_2@SWCNT model.

This paper is organized as follows: first, the model used to describe the physical system and the potential energy surface is discussed. In Sec. III, the approach used to compute the eigenstates of the system is explained. Also, details are given of the multiconfigurational time-dependent Hartree method (MCTDH), which is used to carry out the quantum dynamics calculations. Section IV is devoted to the analysis of the eigenstates themselves and is divided into Subsections IV A and IV B. In Sec. IV A, we focus in the qualitative description, based on the graphical inspection of two dimensional projections of the total wave function in different subspaces (namely, the translational subspace, which takes into account the x and y coordinates, and the rotational subspace in which we find θ and ϕ). Subsection IV B presents a quantitative approach that allows a rigorous description of the wave function based on its overlap with a set of known basis functions. Section V summarizes our results.

II. DESCRIPTION OF THE SYSTEM

Our model consists of a single hydrogen molecule embedded in the hollow cavity of a SWCNT with either (8,0) or (5,0) chirality, hereafter referred to as H_2@(8,0) and H_2@(5,0), respectively. Both nanotubes are represented by concatenating 20 unit cells in order to mimic an infinitely long nanotube, thus making edge effects disregardable. The geometry of the corresponding unit cells has been obtained from a CRYSTAL09[14,15] optimization using the B3LYP functional and a 6-21G basis set. These optimizations yield a nanotube diameter of 7.0 bohrs for the (5,0) CNT and 12.1 bohrs for the (8,0), with an internuclear C-C distance of ~4.5 bohrs.

Regarding the confined molecule, five degrees of freedom (DoFs) are considered, as it can be seen in Figure 1: translation of the center of mass of the molecule in the xy plane, full rotation (θ, ϕ), and vibration (ρ). Note that we do not account for the translation along the nanotube's axis (z). This is justified in terms of the length of the nanotube. Moreover, in case of the (8,0) nanotube, the corrugation of the potential along this direction is small enough not to expect changes of the overall results due to the fixing of the coordinate in a given arbitrary point of the z dimension. This corrugation is much more important in case of the (5,0) nanotube, and the study is carried out fixing the z coordinate of the c.o.m. at exactly the
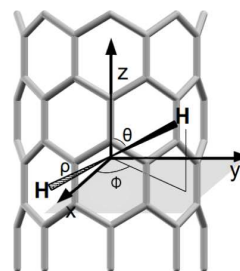
FIG. 1. Scheme of the degrees of freedom considered for the H_2 molecule in the present work.

minimum of the Potential Energy Surface (PES) corresponding to center of the unit cell of the system.

The full Hamiltonian for this system, H_{5D}, is therefore given by

$$\hat{H}_{5D} = -\frac{\hbar^2}{2\mu_{H_2}} \left(\frac{\partial^2}{\partial \rho^2} + \frac{2}{\rho}\frac{\partial}{\partial \rho} + \frac{1}{\rho^2}\frac{\partial^2}{\partial \theta^2} + \frac{1}{\rho^2}\frac{1}{\sin^2\theta}\frac{\partial^2}{\partial \phi^2} \right)$$
$$- \frac{\hbar^2}{2m_{H_2}} \left(\frac{\partial^2}{\partial x^2} + \frac{\partial^2}{\partial y^2} \right) + \hat{V}(\rho, \theta, \phi, x, y). \quad (3)$$

To model the five dimensional potential energy operator, we used the same 5D potential energy function used by Suárez and Huarte-Larrañaga.[13] This is a semiempirical potential which accounts for two separable terms: the H–H interaction, V_{H-H} and the van der Waals interactions between the hydrogen atoms and *each* of the carbon atoms in the nanotube, V_{C-H}. The covalent interaction is modelled by a Morse potential,[16] using the parameters $D_e = 0.1746$ hartree, a = 1.0271 bohr^{-1}, and $R_e = 1.4$ bohrs. The weak dispersion forces are approximated using the Novaco and Wroblewski potential[17] previously used by Gray:[5] a pair-interaction Lennard-Jones potential with parameters $\epsilon = 2.82$ Å and $\sigma = 0.0605$ kcal/mol,

$$\hat{V}_{5D} = V_{H-H}(\rho) + V_{C-H}(\rho, \theta, \phi, x, y), \quad (4)$$

$$\hat{V}_{C-H}(\rho, \theta, \phi, x, y) = \sum_{i=1}^{2}\sum_{j=1}^{Nc} V_{i,j}^{LJ}(d_{H_i-C_j}). \quad (5)$$

It is worthwhile mentioning at this point that there has been some controversy concerning the values of the Lennard-Jones parameters to be used in this kind of systems. However, given that the aim of our work is providing a systematic scheme to characterize the eigenstates of the confined molecule rather than predicting accurate energy splittings, we restrain ourselves to the Lennard-Jones values we have used in the recent past.

Relevant qualitative information about H_2@(8,0) and H_2@(5,0) systems can be extracted just from the shape of their respective PES's. Comparing some features of the potential with experimental results tells us about the suitability of the overall function, and it helps to understand the results of the simulations in the different degrees of freedom. Therefore, a brief discussion of the potential energy surface is given next.

Figure 2 shows a cut of the relaxed PES along the ρ coordinate for the free hydrogen molecule and both the H_2@(8,0) and H_2@(5,0). This representation allows us to find the equilibrium internuclear distance of the molecule in different conditions, as
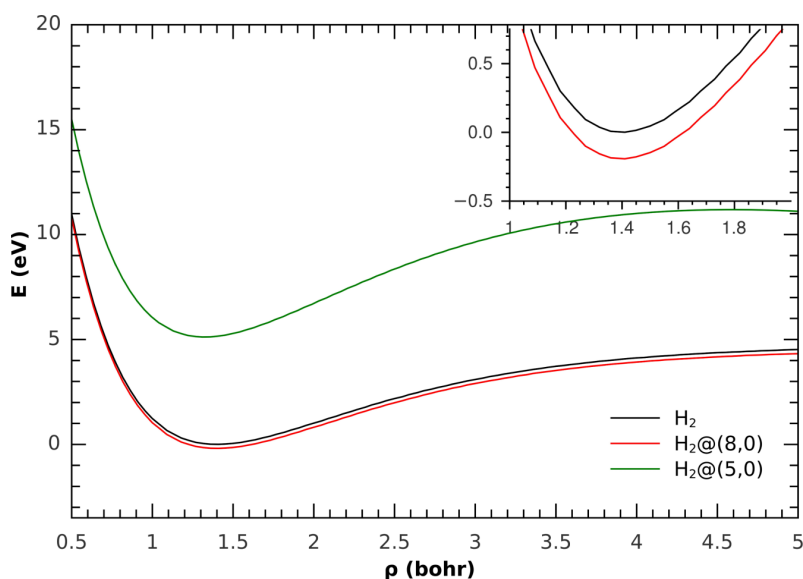
FIG. 2. Potential cut along the ρ coordinate for three different systems: a free hydrogen molecule, a hydrogen molecule embedded in a (8,0) carbon nanotube, and the same molecule in a (5,0) nanotube. Inset: detail of the energy difference between the free molecule and the H_2@(8,0) system. Energy values are referred to the energy of the free H_2 molecule at equilibrium distance.

well as a first approximation to the adsorption energy. Concerning the equilibrium distance, it is seen that there is not a significant change with respect to the free molecule (1.41 bohrs) when the molecule is confined in a (8,0) nanotube. Instead, this distance is slightly decreased to 1.3 bohrs when the nanotube has a (5,0) chirality. This is related to the small diameter and size of the unit cell of this last nanotube: the hydrogen molecule feels a strong repulsion from the C atoms in the cage and tends to shorten the bond to minimize this repulsion. This is related to the second feature that can be extracted from this particular potential cut: the system's minimum energy is slightly lower for the molecule trapped in a (8,0) nanotube than that of the free H_2, which indicates that the absorption is energetically favourable. On the other hand, this minimum is much higher for the (5,0) nanotube, which means that now adsorption is not energetically favourable. This is consistent with some molecular dynamics calculations which show that these nanotubes are way too narrow for hydrogen to be physisorbed in their endohedral sites.[18] The H_2@(5,0) system is therefore not a realistic one, but nevertheless will be useful to illustrate extreme confinement situations. Concerning the translational degrees of freedom, the 2D relaxed energy plots show that both nanotubes create an anharmonic potential with an absolute minimum in the center of the structure. As it can be seen in Figure 3, the potential created by the (5,0) structure is much tighter than the one of the (8,0) CNT due to the smaller diameter. Hence, the wave functions of the former system are expected to be much more distorted than the ones obtained for the latter.

Finally, the cut of the PES along the rotational (θ, ϕ) coordinates gives us another feature of the system: the hindrance that the potential imposes to the rotation of the H_2 molecule (see Figures SF1 and SF2 in the supplementary material[19] for the plots of these projections). For the wider (8,0) nanotube, this rotation occurs through a quite low barrier (20 meV), and the profile in the ϕ dimension is constant even for the perpendicular orientation of the diatom $(\theta = 2/\pi)$. This may lead to thinking that the rotational functions will be very similar to

the ones of a free rotator. Instead, the rotational barrier for the H_2 molecule in the (5,0) carbon nanotube is exceptionally higher (3.41 eV). This energy is too high for the molecule to overcome, and therefore rotation along the θ dimension would not be possible inside this nanotube. Due to the symmetry of the system and this high barrier, we end up with a symmetric double-well potential, and the functions are expected to be only loosely related to spherical harmonics.

III. CALCULATION OF THE NUCLEAR EIGENSTATES

The eigenstates of the studied system were calculated following the State Average Multiconfigurational Time-dependent Hartree (SA-MCTDH) scheme developed by Manthe.[20] It is based on the iterative application of the operator to be diagonalised onto a set of wave functions. In the case of energy eigenstates, one can apply the Boltzmann operator, $e^{-\beta \hat{H}}$ instead of the Hamiltonian operator, which is equivalent to the propagation of the set of wavepackets in imaginary time, β.

A. State-average multiconfigurational time-dependent Hartree approach

The MCTDH approach is an efficient algorithm to propagate high-dimensional wavepackets.[21] In this method, an f-dimensional system is described by p logical coordinates Q_k, such that $p \leq f$. Then, an ansatz is constructed as linear combination of Hartree products, each one of these being a direct product of time-dependent functions corresponding to the different logical coordinates, the so called Single Particle Functions (SPFs). Hence, the expression for the ansatz is

$$\Psi(Q_1, \ldots, Q_p, t) = \sum_{j_1=1}^{n_1} \cdots \sum_{j_P=1}^{n_P} A_{j_1 \cdots j_P}(t) \prod_{k=1}^{p} \varphi_{j_k}^{(k)}(Q_k, t),$$
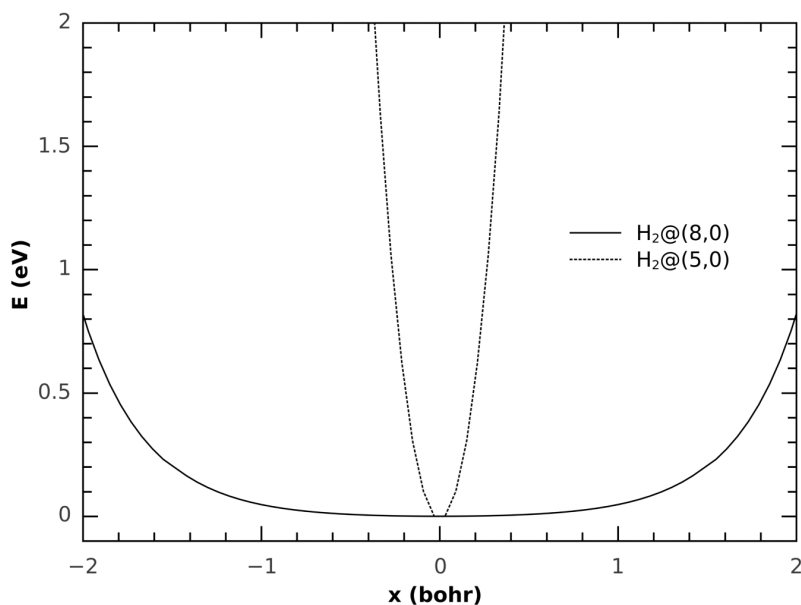
$$(6)$$

FIG. 3. Cut of the relaxed 5D potential energy surface along the x coordinate for both the (8,0) and the (5,0) nanotubes. The energy origin has been shifted to 0 in both cases.

where the SPFs are denoted by $\varphi_{j_k}^{(k)}(Q_k,t)$ and k runs over all coordinates of the system. $A_{j_1\cdots j_p}(t)$ represent the coefficients of the different Hartree products of the linear combination, and a sum runs for each coordinate in the system depending on the number of SPFs used to describe each coordinate k, j_k.

The SPFs are in turn represented in a *primitive* time-independent basis set, which is in general based on a Discrete Variable Representation (DVR) or FFT grid

$$\varphi_j^{(k)}(Q_k) = \sum_{l=1}^{N_k} a_{l_j}^{(k)} \chi_l^{(k)}(Q_k). \tag{7}$$

Applying the Dirac-Frenkel variational principle to this ansatz, two sets of coupled equations of motion are derived: one set for the $A_{j_1\cdots j_p}(t)$ coefficients and another one for the SPFs. The *double layer* representation is the reason why the MCTDH scheme has a such great efficiency compared to the *standard wavepacket* approach, in which the total wave function is represented completely in a time-independent basis: since the SPFs are time-dependent, they adapt to the total wave function at each time step, and therefore, a relatively small number of them are needed for a good description of the system. This decreases the numerical effort required to integrate the equations of motion for the ansatz, while retaining much of the accuracy. For further detail, the reader is referred to the monograph edited by Meyer *et al.*[22]

As mentioned before, the SA-MCTDH approach has been used in the present work to obtain the eigenenergies and eigenstates of the system under study, through diagonalization of the Boltzmann operator on a basis formed by a set of orthonormal wavepackets propagated in imaginary time. This set of wavepackets is represented in a common basis of SPFs, which allows an easy orthogonalization of the set after each propagation. However, it also carries implicitly an important drawback: since the best basis set to represent the average wave function will not be necessarily the optimal set for each individual state, one may need more basis functions to converge the results than if an individual wavepacket was propagated

for each state. Nevertheless, as it is shown elsewhere,[20] it is a powerful approach to calculate nuclear eigenstates.

One last remark must be made about the MCTDH scheme: its maximum efficiency is reached when the whole Hamiltonian is expressed in a product-like form, since then the integration of the equations of motion is much more straightforward. This can be easily achieved for the kinetic energy operator,[23] but not for the potential energy operator in its general form. The *Correlation Discrete Variable Representation* (CDVR) scheme developed by Manthe[24] allows using a general potential energy surface in a MCTDH calculation while largely retaining the accuracy, and this approach was used in our program to implement the potential function as shown in Eq. (5).

B. Numerical details

As it was outlined previously, the MCTDH approach is based on a two layer representation of the full-dimensional wave function. In our case, the wave function is expanded onto a configuration space obtained from the direct product of five sets of SPFs, one for each DoF of the system. Then, each of these SPFs is represented in a suitable time-independent basis. Four of the SPFs sets used in the present work (ρ, ϕ, x and y) are represented in a Fourier method grid. However, a particular issue appears when representing the orientation of the H_2, θ: due to the $\frac{1}{\sin^2\theta}$ term that appears in Eq. (3), a singularity arises in the Hamiltonian for $\theta = 0$, i.e., if the H_2 molecule is oriented parallel to the nanotube's axis. This singularity becomes specially important in the present case, due to the strong alignment of the confined molecule along the nanotube axis (z), $\theta = 0$. For this reason, the θ degree of freedom was represented in a cot-DVR scheme specially designed to avoid this singularity.[25]

The size of the primitive basis set itself, as well as the number of SPFs needed to represent each DoF, depends on the potential to which the hydrogen molecule is exposed. Hence, for the (8,0) nanotube, the number of SPFs for each degree

TABLE I. Numerical details of the basis set used for the calculations of the $H_2@(8,0)$ system. Magnitudes given in bohrs or radians, correspondingly.

Degree of freedom	Number of SPFs	Lower limit	Upper limit	Number of functions	Initial position
ρ	2	0.5	5.0	32	1.41
θ	7	0.0	π	64	$\pi/2$
ϕ	7	0.0	2π	64	0.0
x	5	−3.5	3.5	32	0.0
y	5	−3.5	3.5	32	0.0

of freedom was increased until the numerical convergence of more than 40 excited states was achieved. The detailed information about the parameters used for the representation of the wave function is given in Table I.

Due to the extreme tightness of the potential generated by narrower nanotubes, this basis had to be changed significantly in the case of the $H_2@(5,0)$ system: first of all, the range of the x and y coordinates was reduced to go just from −0.8 to 0.8 bohrs, since for larger distances from the nanotube's center, the potential was way too repulsive (see Figure 3). Then, once this range was set, the number of SPFs was adjusted to achieve the numerical convergence of up to 26 eigenstates. The converged parameters for the wave function representation are shown in Table II. Note that the number of SPFs needed to converge the calculation increases in the vibrational degree of freedom. This seems to indicate that the coupling between the internal and translational DoFs will be much more important for this system than for the previous one.

With these basis sets, the eigenstates for the $H_2@(8,0)$ and $H_2@(5,0)$ were computed following the SA-MCTDH approach explained above. A value of β = 525 a.u. was used in both systems for the Boltzmann operator.

In the case of the (8,0) nanotube, the 50 lower energy eigenstates were converged after 27 iterations. Energy values are listed in the second column of Table III. Two main features stand out in the energy spectrum. The first is its high zero point energy of 2580 cm^{-1}, which is 421 cm^{-1} larger than that of the free H_2. This feature was already pointed out in a previous work by some of us,[13] where it was argued that this increase of the Zero Point Energy (ZPE) appears not only because of the quantization of the translational degree of freedom, but it is also an evidence of the coupling between the different degrees of freedom. The second feature to highlight is that the eigenstate spectrum is radically densified under confinement conditions. The reason for this increase in the

TABLE II. Numerical details of the basis set used for the calculations of the $H_2@(5,0)$ system. Magnitudes given in bohrs or radians, correspondingly.

Degree of freedom	Number of SPFs	Lower limit	Upper limit	Number of functions	Initial position
ρ	4	0.5	5.0	32	1.45
θ	8	0.0	π	64	$\pi/2$
ϕ	6	0.0	2π	64	0.0
x	4	−0.8	0.8	32	0.0
y	4	−0.8	0.8	32	0.0

TABLE III. Relevant results of the qualitative assignation of the calculated eigenstates of the $H_2@(8,0)$ system. Energies are given in wavenumber units related to the ground state energy of 2580 cm^{-1}. See text for the meaning of the h label.

State	ΔE	n_x	n_y	l	$|m|$	k
0	0	0	0	0	0	0
1	59	0	0	1	0	0
2	171	0	0	1	1	0
3	171	0	0	1	1	0
4	265	1	0	0	0	0
5	265	0	1	0	0	0
6	310	1	0	1	0	0
7	310	0	1	1	0	0
8	343	0	0	2	0	0
9	346	0	0	2	1	0
10	346	0	0	2	1	0
11	428	h	h	2	2	0
12	429	0	0	2	2	0
13	429	0	0	1	1	0
14	462	h	h	2	2	0
15	462	h	h	2	2	0
16	503	h	h	2	2	0
17	550	(1,0)/(0,1)		0	0	0
18	550	(1,0)/(0,1)		0	0	0
19	572	(2,0)/(0,2)		0	0	0
20	580	(1,0)/(0,1)		1	0	0
21	580	(1,0)/(0,1)		1	0	0
22	590	h	h	2	1	0
23	597	(2,0)/(0,2)		1	0	0
24	615	1	0	0	0	0
25	615	0	1	0	0	0

density of eigenenergies is threefold: first of all, the confining potential quantizes the translational motion of H_2. Second, the cylindrical symmetry of the potential breaks the degeneracy of rotational eigenstates. And finally, mixed states are expected to appear in the spectrum due to the coupling between the internal and translational degrees of freedom.

Regarding the extremely confining (5,0) nanotube, 26 eigenstates were converged after 20 iterations. The corresponding eigenenergies are reported in Table IV. In this case, the ZPE for the system is outstandingly high (9273 cm^{-1}). An important part of this ZPE (4278 cm^{-1}) is due to the quantization of the translational degree of freedom, and its high value is consistent with the extreme tightness of the potential created by such a narrow nanotube. The remaining 4995 cm^{-1} comes from the combined effect of the vibrational and rotational ZPE (this latter is no longer 0, due to the hindrance to rotation) plus the energy due to the coupling between the degrees of freedom.

IV. EIGENSTATE ANALYSIS

In this section, we present our analysis of the eigenstates of the confined hydrogen system employing two schemes, one based on the graphical inspection of the nodal structure of the wave function and a more rigorous analysis consisting in the study of the overlap of the system's eigenfunctions with models of reduced dimensionality. The strengths and weaknesses of each approach will be discussed next.

TABLE IV. Results of the qualitative assignation of the different degrees of freedom for the $H_2@(5,0)$ system. Energies are relative to the ground state energy of 9273 cm^{-1}.

State	ΔE	n_x	n_y	l	$|m|$	k
0	0	0	0	1	0	0
1	0	0	0	1	0	0
2	3552	0	0	1	1	0
3	3552	0	0	1	1	0
4	3552	0	0	1	1	0
5	3552	0	0	1	1	0
6	3591	0	1	1	0	0
7	3591	0	1	1	0	0
8	3591	1	0	1	0	0
9	3591	1	0	1	0	0
10	4636	0	0	1	0	1
11	4636	0	0	1	0	1
12	6674	0	0	1	3	0
13	6674	0	0	1	3	0

A. Low-coupling limit: Assignment based on the nodal pattern

The first attempt in the description of the eigenstates of our system was to carry out a qualitative analysis of the wave functions. As it was discussed in Sec. I, for a fully separable Hamiltonian, the total wave function would be described as a product of individual wave functions, each being the solution for each degree of freedom in the Hamiltonian. If the Hamiltonian is not separable but the coupling between the internal and translational DoFs is small (*low-coupling limit*), one can still write the total wave function approximately as a direct product of a translational and a rovibrational wave function. Our approach is based on the mapping of the total 5-D function into subspaces corresponding to the translational (x and y), rotational (θ and ϕ), and vibrational (ρ) degrees of freedom, thus allowing a graphical representation of the reduced probability density in these subspaces. Then, these mappings can be directly compared with the solutions for a hypothetical separable system, which corresponds to direct products of a two-dimensional harmonic oscillator function ($H_{n_x,n_y}(x,y)$) accounting for the translational DoFs, a spherical harmonic ($Y_l^m(\theta,\phi)$) accounting for the rotation, and a Morse function ($M_k(\rho)$) to include vibration. Comparing the nodal pattern of the mapped probability densities with the different states of the separable problem, one tries to obtain a one-to-one correspondence between the confined and the free systems, and assigns a quantum number to each degree of freedom for a given state: n_x and n_y for the translation, l and $|m|$ for the angular momentum, and k for the vibration. The quantity $|m|$ is used instead of simply m because of the cylindrical symmetry of the system, which will force the degeneracy of the energy of states with equal l and $|m|$.

Some relevant results of the qualitative analysis for hydrogen confined in the wider nanotube are found in Table III. As it is seen in this table, no excitation is found in the vibrational degree of freedom, and therefore, the selection of the rigid rotor functions to study the internal degrees of freedom of the H_2 molecule seems justified for low energy eigenstates.

This graphical inspection was enough to relate most of the eigenstates of the system to a given pair of rotational and translational reference functions and assign the corresponding quantum numbers. The procedure is illustrated in Figure 4 for the first excited state. In the figure, the projection of the total wave function onto the rotational and translational subspaces is shown. For the translational projection, the absolute square value of the function is shown in the xy plane, while for the rotational subspace, the function is given in spherical coordinates. In this representation, the radius of the plot is related to the squared absolute value of the function for a given pair of θ and ϕ angles. The plane corresponding to a value of $\theta = \pi/2$, that is for the perpendicular orientation of the internuclear axis with respect to the carbon nanotube, is also given to ease the interpretation. One can observe that, in this state, this plane is precisely a nodal plane in the θ coordinate. This nodal plane in the θ dimension, together with the presence of no nodes in the ϕ degree of freedom, corresponds to a Y_1^0 spherical harmonic, so we assign the quantum numbers $l = 1$, $m = 0$ to the first excited state. Since there are no nodal planes in the xy plane of the translational subspace mapping, we also assign the quantum numbers $n_x = 0$ and $n_y = 0$. Finally, for the internuclear distance subspace, again no nodes are found and therefore the state is labeled as $k = 0$. However, although the study of the nodal pattern enables a one-to-one correspondence between most of the $H_2@(8,0)$ states and the free H_2 ones, a deeper study of Table III shows that this assignation is not consistent in all cases. This is evidenced by the fact that some of the states yield exactly the same quantum numbers under the nodal planes' criterion, even though they are clearly different functions with different energies. This is the case of the set formed by the 2nd, 3rd (degenerate), and 13th excited states, for instance. Oppositely, the 12th and 13th excited states are energetically degenerate despite the fact that the analysis of nodal planes tells us that they should have different values of $|m|$. A closer look to the functions shows us why this method is not good enough to establish a clear correspondence between the confined and free H_2 states. For instance, the ground state wave function mapped on the orientational subspace (θ, ϕ), shown in Figure 5, shows no nodal plane in this projection. In our qualitative approach, this means that this function corresponds to a $l = 0$, $m = 0$ state. However, a significant depression is found for values of the polar angle θ near to $\pi/2$, which indicates that there is a significant mixing of rigid rotor states in order to give rise to this function. A similar case is found in the translational mapping of the 11th, 14th, 15th, 16th, and 22nd excited states. These projections, shown in Figure 6 for the 11th excited state, present a minimum of probability in the $x = 0$, $y = 0$ point, which cannot be strictly considered a nodal point. This structure does not correspond to any eigenstate of an anharmonic oscillator, and therefore, an h state is used to label the n_x and n_y quantum numbers. Finally, a more subtle example is found in the translational projection of the remaining eigenstates: there are slight differences in the overall shape for many of the functions without any nodal plane that may be therefore labelled as $H_{0,0}$. These variations imply that again there is a significant coupling between rotation and translation.

As expected, the inaccuracies of the qualitative inspection method are even more noticeable in case of the narrower (5,0)
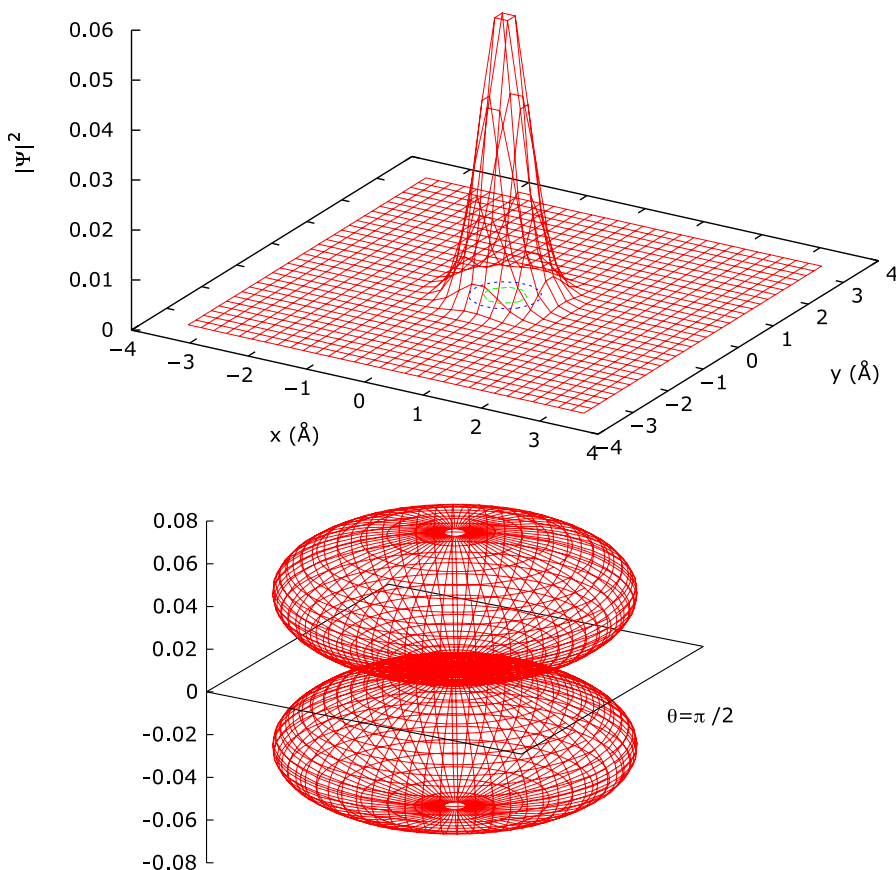
FIG. 4. Projection of the first excited state of the $H_2@(8,0)$ system in the translational (upper panel) and rotational (lower panel) subspaces. The ϕ plane shown corresponds to a θ value of $\pi/2$.

FIG. 5. Rotational projection of the total ground state wave function of H_2 in the (8,0) CNT. Note the significant depression for $\theta = \pi/2$.

nanotube: due to the tightness of the potential, all coordinates are even more coupled than they were in the wider (8,0) nanotube, which makes the study more difficult. The results of the qualitative analysis of the system are shown in Table IV. Note that, as predicted in the discussion about the potential energy surface, the energy pattern corresponds to that of a symmetric double-well system with a very high energy barrier: the eigenstates are numerically bidegenerate for all values of energy far below the top of the rotational barrier. This degeneracy is caused by a negligible tunnelling splitting. In the case of the ground state, the corresponding eigenfunctions are shown in

Fig. 7, projected on the rotational degree of freedom. These functions appear localized around $\theta = 0$ and $\theta = \pi$, with an amplitude restricted to an arc of about 0.5 rad, which clearly means that this distortion is far too large for this coordinate to be inspected by direct comparison to rigid rotor functions. However, some quantum numbers have been assigned in the ϕ degree of freedom to represent the nodal planes which appear in this dimension. Concerning the other degrees of freedom, it should be pointed that the excitation energies are much larger in this case than in the previously studied, again due to the tighter potential. Note however that, in spite of the tightness of the potential, translational excited states in x and y degrees of freedom are still degenerate. As a final remark, in this system we do see vibrational excitations, which were too high in energy to be seen in the previous case and are now of the order of translational and rotational excitations.

B. Quantitative description of the eigenstates

It has been seen that a qualitative description of the eigenstates is not suitable for the $H_2@SWCNT$ systems: even in the ground state, we find very significant deviations from the reference 2-D problem in the rotational degrees of freedom, and the translational functions also present variations between different energy levels which are not in a good agreement with a separable solution. Therefore, a quantitative analysis is desirable to truly obtain a meaningful correspondence between the eigenstates of the unbound and the confined molecule.
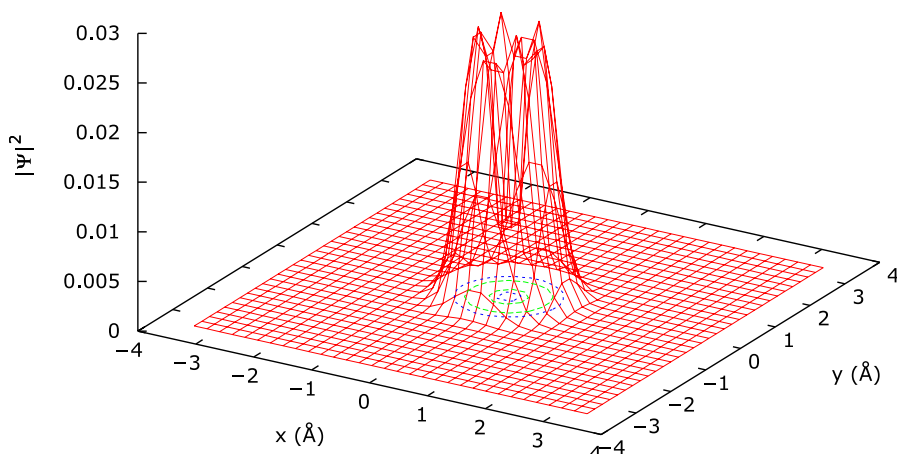
FIG. 6. Translational projection for the 11th excited state of the $H_2@(8,0)$ system.

In order to perform this more rigorous analysis of the eigenfunctions of the system, a basis set is built from the solutions of an hypothetical separable Hamiltonian. This means that each element of the basis will be a direct product of functions corresponding to the different degrees of freedom of the system under study. For our specific problem, where the degrees of freedom are the internuclear distance, rotation, and translation of the center of mass of the molecule in the CNT potential, these basis functions have the form

$$\Phi^{k,l,m,n_x,n_y}(\rho,\theta,\phi,x,y) = M_k(\rho)Y_l^m(\theta,\phi)\Xi_{n_x,n_y}(x,y),$$
(8)

where each function of the product corresponds to the solution of a model system or to a eigenstate of a separable part of the Hamiltonian. Therefore, the functions which represent the internuclear distance, $M_k(\rho)$, and the rotation of the molecule, $Y_l^m(\theta,\phi)$, were built from the solution of two well-known problems, namely, the Morse potential and the rigid rotor, respectively. On the other hand, the translational functions, $\Xi_{n_x,n_y}(x,y)$, are chosen to be the solutions corresponding to a structureless particle moving in the xy plane, subjected to the potential created by the specific CNT under study, which resemble two-dimensional anharmonic oscillators.

The basis set is then built by adding each time a quantum to each degree of freedom. Once this is done, the actual system's eigenfunction can be represented in this basis

$$\Psi^n = \sum_{k=0}^{k_{max}} \sum_{l=0}^{l_{max}} \sum_{m=-l}^{l} \sum_{n_x=0}^{n_x\,max} \sum_{n_y=0}^{n_y\,max} c_{k,l,m,n_x,n_y}^n \Phi^{k,l,m,n_x,n_y},$$
(9)

where the coefficients of the linear combination, c_{k,l,m,n_x,n_y}^n, can be obtained by performing the scalar product between a given function Ψ^n and each basis element

$$c_{k,l,m,n_x,n_y}^n = \langle \Psi^n \mid \Phi^{k,l,m,n_x,n_y} \rangle,$$
(10)

where m labels the basis element. These quantities give us a quantitative description of how much the actual eigenstate resembles that of the separable problem and therefore allows for a rigorous yet understandable interpretation of the quantum confinement phenomena.

The results for this analysis are given in Table V for the case of the $H_2(8,0)$ system. We can see that, except for the 1st excited state, all other eigenfunctions are not directly related to a single reference function, but rather with a linear combination of at least two of them. This agrees with the inconsistencies found during the interpretation of the wave function carried out in Sec. IV A: concerning the ground state, we see an important contribution of the $|02000\rangle$ function, which implies a contamination of the rotational subspace with the Y_2^0 function. Regarding the 11th excited state, whose projection we could not relate with any anharmonic oscillator function, its nature is also made clear by this analysis: the projection is just the result of a mixing of $(0,1)$ and $(1,0)$ states of the anharmonic oscillator. It should also be noted that, as the energy increases, the more reference functions are needed to represent accurately a given state.

For the case of the $H_2@(5,0)$ system, the results of the full dimensional integration shown in Table VI differ significantly from those corresponding to the $(8,0)$ nanotube: every state is a mixture of many more basis functions, even for the lowest energies. This means, as it was already pointed during the qualitative inspection of the mappings of the wave functions, that the distortions with respect to the free hydrogen case are much more important for the narrower nanotube.
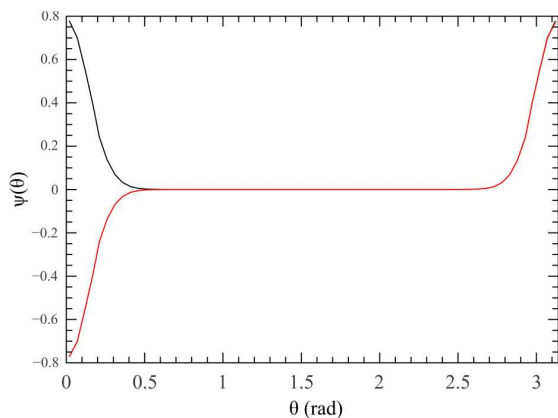

FIG. 7. Rotational projection of the degenerate ground state functions of the $H_2@(5,0)$ system along the θ dimension, with $\phi = 0$.

TABLE V. Representation of the H_2@(8,0) system's eigenfunctions in the basis of direct product functions. Energies in cm^{-1} units. See Table ST1 in the supplementary material[19] for a complete table with all converged eigenstates.

State	ΔE	Basis element ($|klmn_x n_y\rangle$)	$|c^n_{k,l,m,n_x,n_y}|$
0	0	$|00000\rangle$	0.92
		$|02000\rangle$	0.06
1	59	$|01000\rangle$	0.98
2	171	$|01100\rangle$	0.48
		$|01-100\rangle$	0.48
3	171	$|01100\rangle$	0.48
		$|01-100\rangle$	0.48
4	265	$|00001\rangle$	0.87
		$|02001\rangle$	0.11
5	265	$|00010\rangle$	0.85
		$|00030\rangle$	0.02
		$|02010\rangle$	0.10
6	310	$|01001\rangle$	0.95
		$|03001\rangle$	0.02
7	310	$|01010\rangle$	0.92
		$|01030\rangle$	0.04
8	343	$|00000\rangle$	0.06
		$|02000\rangle$	0.90
9	346	$|02-100\rangle$	0.48
		$|02100\rangle$	0.48
10	346	$|02-100\rangle$	0.48
		$|02100\rangle$	0.48
11	428	$|01-101\rangle$	0.23
		$|01-110\rangle$	0.25
		$|01110\rangle$	0.25
		$|01101\rangle$	0.23
12	429	$|00010\rangle$	0.02
		$|02-200\rangle$	0.48
		$|02200\rangle$	0.48
13	429	$|02200\rangle$	0.48
		$|02-200\rangle$	0.48
14	462	$|01110\rangle$	0.23
		$|01101\rangle$	0.23
		$|01-101\rangle$	0.23
		$|01-110\rangle$	0.23
15	462	$|01110\rangle$	0.23
		$|01101\rangle$	0.23
		$|01-101\rangle$	0.23
		$|01-110\rangle$	0.23
16	503	$|01110\rangle$	0.23
		$|01101\rangle$	0.23
		$|01-101\rangle$	0.23
		$|01-110\rangle$	0.23
17	550	$|00010\rangle$	0.74
		$|02110\rangle$	0.16
18	550	$|00002\rangle$	0.46
		$|00020\rangle$	0.27
		$|02002\rangle$	0.10
		$|02020\rangle$	0.06
19	572	$|00002\rangle$	0.30
		$|00020\rangle$	0.44
		$|02000\rangle$	0.03
		$|02002\rangle$	0.06
		$|02020\rangle$	0.08

TABLE VI. Representation of the H_2@(5,0) system's eigenfunctions in the basis of direct product functions. Energies in cm^{-1} units. See Table ST2 in the supplementary material[19] for a complete table with all converged eigenstates.

State	ΔE	Basis element ($|klmn_x n_y\rangle$)	$|c^n_{k,l,m,n_x,n_y}|$
0	0	$|00000\rangle$	0.072
		$|02000\rangle$	0.282
		$|12000\rangle$	0.032
		$|32000\rangle$	0.018
		$|04000\rangle$	0.096
		…	…
1	0	$|01000\rangle$	0.199
		$|03000\rangle$	0.309
		$|11000\rangle$	0.029
		$|13000\rangle$	0.030
		$|31000\rangle$	0.023
		$|33000\rangle$	0.020
		…	…
2	3552	$|02-100\rangle$	0.017
		$|02100\rangle$	0.065
		$|12100\rangle$	0.012
		$|04-100\rangle$	0.052
		$|04100\rangle$	0.196
		$|14100\rangle$	0.030
		$|34100\rangle$	0.014
		…	…
3	3552	$|02-100\rangle$	0.065
		$|02100\rangle$	0.017
		$|12-100\rangle$	0.012
		$|04-100\rangle$	0.196
		$|04100\rangle$	0.052
		$|14-100\rangle$	0.030
		$|34-100\rangle$	0.014
		…	…
4	3552	$|01100\rangle$	0.016
		$|03-100\rangle$	0.036
		$|03100\rangle$	0.134
		$|13100\rangle$	0.023
		…	…
5	3552	$|01-100\rangle$	0.016
		$|03-100\rangle$	0.134
		$|03100\rangle$	0.035
		$|13-100\rangle$	0.028
		…	…
6	3591	$|00010\rangle$	0.067
		$|02010\rangle$	0.264
		$|03010\rangle$	0.013
		$|12010\rangle$	0.031
		$|32010\rangle$	0.017
		$|04002\rangle$	0.091
		…	…
7	3591	$|01010\rangle$	0.186
		$|02010\rangle$	0.012
		$|03010\rangle$	0.291
		$|11010\rangle$	0.023
		$|13010\rangle$	0.031
		$|31010\rangle$	0.012
		$|33010\rangle$	0.019
		…	…

Table VI shows an important feature of the system: note that for some states, basis functions with both even and odd quantum numbers, l, have a relevant contribution in the final state. This feature is a result of the exceptionally large rotational barrier of the confined hydrogen molecule. This hindrance in the angular degree of freedom, as it was discussed earlier, forces a numerical bidegeneracy of the rotational energy levels of the hydrogen molecule. If symmetry conditions are not imposed for the eigenstates of the system, two possible solutions are equally valid: a delocalized representation of the wave function or a localized representation made from the linear combination of symmetric and antisymmetric states. In our case, the basis set employed is formed of functions without any parity, which favours (but does not force) the localized representation of the eigenstates. Finally, another important difference between the hydrogen molecules confined in the (8,0) or the (5,0) nanotube is found in the ρ degree of freedom: for the narrower CNT, vibrationally excited states contribute to the wave function already in the 3rd excited state, while no excitations were found during the analysis of the $H_2@(8,0)$ system's eigenstates.

The full dimensional overlap offers a direct and simple view of the total wave function as a combination of well-known reference states. Yet, it is still difficult to get an insight into the dynamics of the confined hydrogen molecule just by observing these quantities, since the actual wave function, which gives information about the probability of finding the molecule in a given position and orientation, is lost when performing the scalar products. Our aim here is to develop a representation of the wave function which allows an intuitive understanding of the motion of H_2 inside a confining structure, while maintaining a rigorous approach.

Following this idea, we computed a partial overlap function, $\sigma(\vec{x}_{red})$, between the full five-dimensional wave function corresponding to each eigenstate and a model function corresponding to a *logical* coordinates of the system. These *logical* coordinates are understood as strongly coupled degrees of freedom which cannot be straightforwardly separable. In our case, these will be rotation on one hand and translation of the center of mass on the other. Hence, the magnitudes that we will study will be

$$\sigma_{l,m}(\rho,x,y) = \langle \psi(\rho,\theta,\phi,x,y) \mid Y_l^m(\theta,\phi) \rangle$$

$$= \int_0^{2\pi} \int_0^{\pi} \psi(\rho,\theta,\phi,x,y)^* Y_l^m(\theta,\phi) \, sin\theta \, d\theta \, d\phi, \quad (11)$$

$$\sigma_{n_x,n_y}(\rho,\theta,\phi) = \langle \psi(\rho,\theta,\phi,x,y) \mid \Xi_{n_x,n_y}(x,y) \rangle$$

$$= \int_{-\infty}^{\infty} \int_{-\infty}^{\infty} \psi(\rho,\theta,\phi,x,y)^* \Xi_{n_x,n_y}(x,y) \, dx \, dy, \quad (12)$$

where the model functions for the rotational degrees of freedom are the same that were used for the definition of the full dimensional overlap. We will refer to these quantities as rotational and translational overlap functions, respectively.

Note that the magnitudes in Eqs. (11) and (12) are scalar products between functions of different dimensionalities. Hence, there are three features that must be taken into account for their correct interpretation:

1. Since we are integrating the functions in a 2-D subspace of the 5-D total space, this product is a function of the three

non-integrated degrees of freedom. This will allow us to see how the states corresponding to the reference problem change their contribution as the potential changes.

2. Both the total 5-D function and the reference 2-D ones are normalized in the space they span, and for that the scalar product will *not* be normalized, but rather depend on the norm of the total 5-D function in each point of the non-integrated space. This will allow us to focus on the region in which the total wave function is relevant.

3. For each point of the full 5-D space, the total wave function can be obtained through a direct product of the sum of partial overlaps for the different degrees of freedom. For a system divided in q logical coordinates, each containing k_q degrees of freedom

$$\Psi^n(\vec{x}) = \prod_q \left(\sum_{j_1} \cdots \sum_{j_{k_q}} \sigma_q(\vec{x}_q) \right). \quad (13)$$

In our specific case,

$$\Psi^n(\vec{x}) = \left(\sum_k \sigma_k(\theta,\phi,x,y) M_k(\rho) \right)$$

$$\times \left(\sum_l \sum_m \sigma_{l,m}(\rho,x,y) Y_l^m(\theta,\phi) \right)$$

$$\times \left(\sum_{n_x} \sum_{n_y} \sigma_{n_x,n_y}(\rho,\theta,\phi) \Xi_{n_x,n_y}(\theta,\phi) \right). \quad (14)$$

In short, from the study of the overlap function in the different subspaces, we obtain quantitative information of both the norm of the total wave function in a given point and about its shape, through the interpretation of the overlap as the coefficients of the linear combination of basis functions, which gives rise to the eigenstate. Then, the study of these functions allows a straightforward interpretation of the dynamics of the hydrogen molecule, since we can see directly how the coupling between different degrees of freedom affects the dynamics.

Still, the analysis of a three-dimensional object is not a trivial task; it is always easier to study the trends of one-dimensional functions. To further reduce the dimensionality of the problem, we take advantage of two characteristic features of the system: first, no vibrational excitations are observed within the first 50 calculated eigenstates. This feature will allow us to explore the behaviour of $\sigma_{n_x,n_y}(\rho,\theta,\phi)$ and $\sigma_{l,m}(\rho,x,y)$ for a fixed $\rho = 1.41$ bohrs, which corresponds to the internuclear distance with maximum probability density for the vibrational ground state. The second feature is the symmetry of the eigenfunctions studied: in the translational subspace, they are all either cylindrical or mainly located along two orthogonal axes, which we can consider as the x and y axes. Therefore, we can focus on the values of the functions along these axes. On the other hand, the rotational functions can be scanned along the range of θ from 0 to π for, in principle, any value of ϕ. However, in spite of the isotropy of the potential for the (8,0) nanotube, the rotational eigenfunctions will not be isotropic and may present several nodal planes in both θ or ϕ coordinates. Therefore, we do not have a preferred value of the coordinates to scan *a priori*, since any arbitrary value
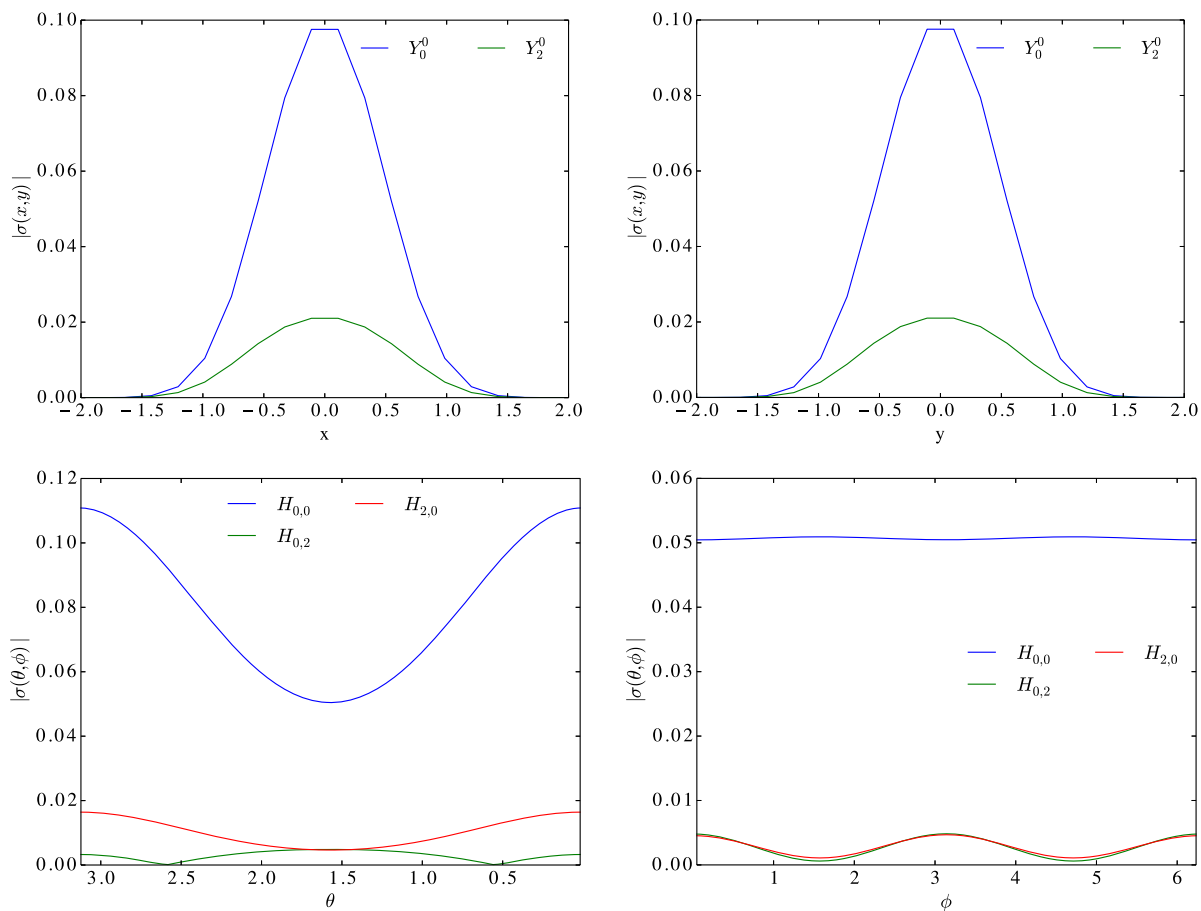
FIG. 8. Analysis of the ground state eigenfunction of the $H_2@(8,0)$ system. Upper panel: Radial overlap function along the x and y axes for the ground state function. Lower panel: Translational overlap function along θ for $\phi = 0$ and along ϕ for $\theta = \pi/2$.

of the angle may in principle correspond to a nodal plane for some eigenstate of the system. The pair of angles which will be scanned therefore will depend on the particular function under study. A general rule could be that the fixed value of

ϕ along which the θ dimension will be scanned may correspond to the point in which the translational overlap function, $\sigma_{n_x,n_y}(\rho,\theta,\phi)$, presents a maximum. The same can be used to select the fixed value of θ for which ϕ will be studied. Yet, this
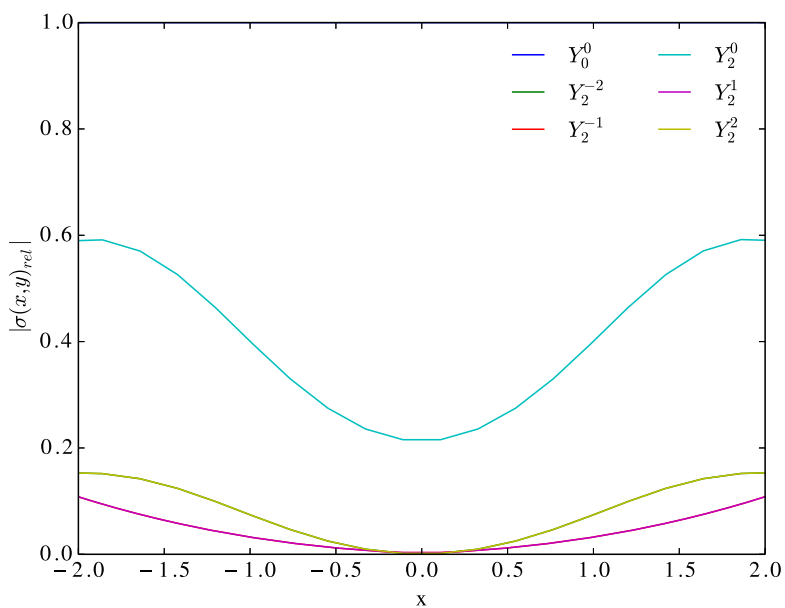

FIG. 9. Representation of the most relevant relative rotational overlap functions for the ground state in the $H_2@(8,0)$ system.
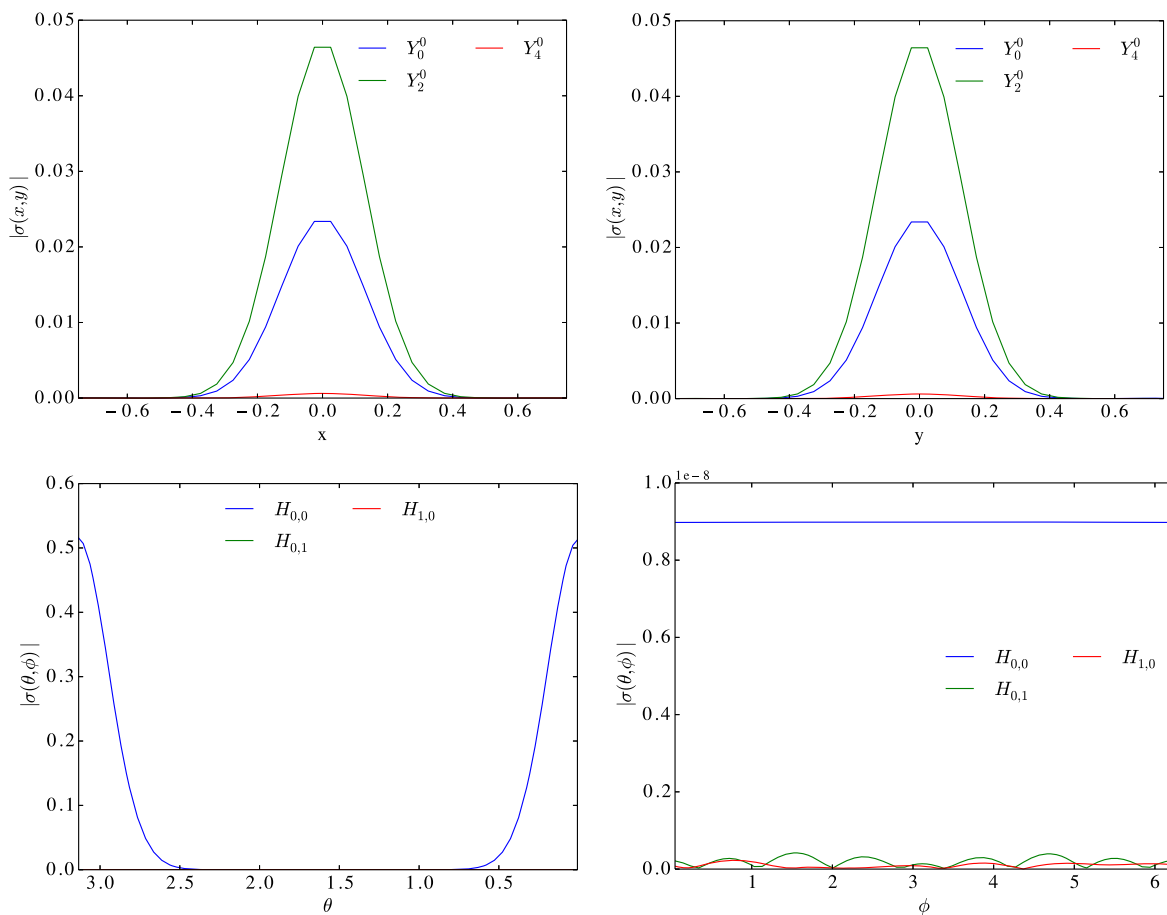
FIG. 10. Upper panel: Radial overlap function along the x and y axes for the ground state wave function in the H₂@(5,0) system. Lower panel: Translational overlap function along θ for $\phi = 0$ and along ϕ for $\theta = 0$.

criterion may be altered in favour of a more physically relevant pair.

It shall be noted that this reduction of the dimensionality is carried out only with the aim of easing the interpretation and gives a general overview of the H₂@SWCNT systems under study. The overlap functions in the different subspaces are obtained without calling on any approximation and therefore can be used to study any wave function in an arbitrary point of the space in a rigorous way.

Starting with the H₂@(8,0) system, we have obtained the three-dimensional overlaps with the rotational (Eq. (11)) and translational (Eq. (12)) model functions. As an example, in Figure 8, the absolute values of the rotational and translational overlap functions for the ground state with the most relevant test functions are shown along the four directions outlined previously (θ, ϕ, x and y). Each line in the plot corresponds to the overlap function related to a single reference state. It is readily seen that this state does not correlate with a single state of the free H₂ molecule, but it rather has many contributions. These contributions, as it was predicted, vary significantly depending on the orientation and position of the c.o.m of the H₂ molecule, thus confirming the strong coupling between the translational and internal degrees of freedom in all the eigenstates of the system. In particular, it can be seen how, although the major contribution to the ground state comes from

the Y_0^0 and $H_{0,0}$ states, there is a significant contribution of the Y_2^0 state in all the translational subspace. Similarly, we see an important contribution of the $H_{2,0}$ and $H_{0,2}$ states, which hits a maximum proportion in the region near $\theta = 0$.

Therefore, these plots allow us to determine the shape of the eigenstate at a given point. Furthermore, since the overlap function is *weighted* by the total norm of the wave function in a given point, non-relevant areas in the total sampling space simply do not appear, which is a great advantage. However, this feature introduces a problem in the interpretation for the translational degrees of freedom: since the probability density in these coordinates has a gaussian-like shape, it decreases rapidly when the molecule gets closer to the nanotube's walls. This makes it difficult to see how the relative contribution of the model states changes away from the center of the nanotube, which is the key to see if the system becomes more distorted as we approach the nanotube's wall. To overcome this difficulty, we plot the *relative* overlap function in the translational space, which results from dividing the rotational overlap for each reference function with the rotational overlap function of the dominant state, i.e., the state which has the maximum contribution to the total wave function, denoted $\sigma_{l^{dom}, m^{dom}}$,

$$\sigma_{l,m}^{rel}(\rho, x, y) = \frac{\sigma_{l,m}}{\sigma_{l^{dom}, m^{dom}}}, \tag{15}$$

TABLE VII. Results of the quantitative description of the eigenstates of the H$_2$@(8,0) system. Energies referred to the ground state energy of 2580 cm^{-1}, contribution of the reference functions referred to the point of maximum probability density in the 5D space. See Table ST3 in the supplementary material[19] for a complete table with all converged eigenstates.

State	ΔE	ρ	θ	ϕ	x	y	l,m	$|\sigma^n_{l,m}|$	n_x, n_y	$|\sigma^n_{n_x,n_y}|$
0	0	1.4	0.0	0.0	0.0	0.0	(0,0)	0.097	(0,0)	0.11
							(2,0)	0.021	(0,2)	0.02
1	59	1.4	π	0.0	0.0	0.0	(1,0)	0.096	(0,0)	0.14
							…	…	(0,2)	0.02
2	171	1.4	1.8	$\pi/2$	0.0	0.0	(1,1)	0.011	(0,0)	0.11
							(1,−1)	0.011	…	…
3	171	1.4	1.25	π	0.0	0.0	(1,1)	0.073	(0,0)	0.11
							(1,−1)	0.073	(2,0)	0.01
							…	…	(0,2)	0.01
4	265	1.4	π	$\pi/4$	0.55	0.0	(0,0)	0.084	(0,1)	0.12
							(2,0)	0.028	(1,2)	0.02
5	265	1.4	π	$3\pi/4$	0.0	0.55	(0,0)	0.084	(1,0)	0.12
							(2,0)	0.028	(0,3)	0.03
6	310	1.4	π	1.32	0.55	0.0	(1,0)	0.087	(0,1)	0.15
							…	…	(1,2)	0.02
7	310	1.4	π	2.90	0.0	0.55	(1,0)	0.087	(1,0)	0.15
							…	…	(0,3)	0.04
8	343	1.4	π	0.0	0.0	0.0	(0,0)	0.038	(0,0)	0.15
							(2,0)	0.092	(0,2)	0.03
							…	…	(2,0)	0.01
9	346	1.4	$3\pi/4$	$\pi/2$	0.0	0.0	(2,1)	0.070	(0,0)	0.14
							(2,−1)	0.070	(0,1)	0.01
10	346	1.4	$3\pi/4$	π	0.0	0.0	(2,1)	0.070	(0,0)	0.14
							(2,−1)	0.070	(0,2)	0.02
11	428	1.4	1.1	$\pi/2$	0.33	0.33	(1,−1)	0.048	(1,0)	0.08
							(1,1)	0.048	…	…
12	429	1.4	$\pi/2$	$\pi/4$	0.0	0.0	(2,2)	0.011	(0,0)	0.13
							(2,−2)	0.011	(1,1)	0.01
							…	…	(2,0)	0.01
							…	…	(0,2)	0.01
13	429	1.4	$\pi/2$	$\pi/2$	0.0	0.0	(2,2)	0.073	(0,0)	0.13
							(2,−2)	0.073	…	…
14	462	1.4	2.18	4.76	0.32	0.32	(1,1)	0.050	(1,0)	0.07
							(1,−1)	0.050	…	…
15	462	1.4	2.09	1.62	0.0	0.55	(1,1)	0.048	(0,1)	0.08
							(1,−1)	0.048	…	…
16	503	1.4	h.0	0.0	0.0	0.0	(1,1)	0.050	(1,0)	0.08
							(1,−1)	0.050	(0,3)	0.01
17	550	1.4	π	$\pi/4$	0.55	0.55	(0,0)	0.067	(1,1)	0.13
							(2,0)	0.031	…	…
18	550	1.4	π	0.54	−0.76	0.0	(0,0)	0.067	(0,0)	0.01
							(2,0)	0.031	(2,0)	0.11
							…	…	(0,2)	0.08
19	572	1.4	0.0	3.0	0.0	0.0	(0,0)	0.085	(0,0)	0.03
							(2,0)	0.051	(2,0)	0.08
							…	…	(0,2)	0.10
20	580	1.4	3.0	$\pi/4$	−0.55	0.55	(1,0)	0.075	(1,1)	0.15
							(3,0)	0.014	…	…

always considering only the space in which the total wave function has a relevant value, in order to have a well-behaved function.

The plot of the relative overlap functions corresponding to the upper left panel of Figure 8, corresponding to the rotational overlap function along the x coordinate for the ground state of the H$_2$@(8,0) system, is shown in Figure 9. It is readily seen that the percentage of contribution of high-energy reference states increases as we get close to the nanotube's walls, changing from a mixture of Y_0^0/Y_2^2 in a 5/1 proportion in the center of the nanotube to a mixture of 5 states, where the main one has less than a 50% of contribution. This fact illustrates the effects of the coupling on the overall function.

The general trends observed in the study are that the higher the energy of the studied state, the more eigenstates of the free molecule contribute to it, even though in general there is always a dominant contribution to a given state. This is consistent with the fact that in excited eigenstates, the maximum probability density is located in areas where the potential affects more strongly, thus further increasing the distortion with respect to the reference functions. Therefore, it is clear that the coupling between the different degrees of freedom forces us to study the whole subspaces in which the overlap function is represented in order to understand the system.

The quantitative study of the eigenstates of the H_2 molecule in the narrower (5,0) nanotube confirms what was expected from all the previous studies (qualitative analysis of both the PES and the projected eigenfunctions, as well as the full-dimensional overlap study): a tighter potential increases the couplings in the system, and therefore, the distortions away from the model states are even more noticeable. However, the partial overlap functions allow us to find how the different degrees of freedom are distorted. As seen in Figure 10, for the ground state of the system, the translational part of the wave function does not differ much from the structureless particle in the anharmonic potential. This apparent small coupling between the internal and translational degrees of freedom, which is surprising at first glance, can be understood in terms of the hindered rotation: for this system, the hydrogen molecule is forced to remain almost parallel to the nanotube's axis, which is the disposition that is more similar in energy to a structureless particle, in terms of the potential energy surface. Therefore, there is indeed a strong coupling between the

degrees of freedom, but it is not seen as a mixing of states, but rather as a localization of the wave function.

To obtain precise information of relevant points of the whole 5D space spanned by the systems under study, we can take advantage of Eq. (14), which expresses the wave function in a given point as a direct product of the linear combination of the different basis functions, with the coefficient of the combinations being the value of the overlap function in that point. This interpretation allows an intuitive understanding of the high dimensional wave function in a single point of the space in terms of the more familiar one or two dimensional model functions.

In Tables VII and VIII, the lowest energy states are shown for the $H_2@(8,0)$ and $H_2@(5,0)$, respectively, following this idea: for each function, the point in the 5D space with the highest probability density is selected. Then, for this point, the model functions which contribute the most to the system are listed together with the absolute value of their coefficient in the linear combination (i.e., the value of the corresponding overlap function). Note that, for the sake of clarity, the absolute value of the coefficient is given instead of the complex number, and therefore, the phase of the combination is disregarded.

Table VII offers a summary of the information obtained for the $H_2@(8,0)$ system. It can be seen that the results are in general consistent with the overlap with 5D basis functions and the overlap functions plots. However, we must take into account a conceptual difference between these two analyses: the full overlap carried out previously gave us information about the averaged wave function in all the spanned space, whereas these overlap functions focus on different points in a given

TABLE VIII. Results of the quantitative description of the eigenstates of the $H_2@(5,0)$ system. Energies referred to the ground state energy of 9273 cm^{-1}, contribution of the reference functions referred to the point of maximum probability density in the 5D space. See the supplementary material[19] (Table ST4) for a complete table with all converged eigenstates.

State	ΔE	ρ	θ	ϕ	x	y	l, m	$\lvert \sigma_{l,m}^n \rvert$	n_x, n_y	$\lvert \sigma_{n_x,n_y}^n \rvert$
									Model functions contribution	
0	0	1.3	π	0	0.025	0.025	(0, 0)	0.023	(0, 0)	0.52
							(2, 0)	0.046	…	…
							(4, 0)	0.027	…	…
1	0	1.3	0.0	5.7466	−0.025	−0.025	(1, 0)	0.039	(0, 0)	0.51
							(3, 0)	0.049	…	…
2	3552	1.3	0.22	$\pi/4$	−0.025	−0.025	(2, −1)	0.011	(0, 0)	0.41
							(2, 1)	0.022	(2, 0)	0.06
							(4, −1)	0.020	…	…
							(4, 1)	0.039	…	…
3	3552	1.3	0.22	π	0.025	0.025	(2, −1)	0.022	(0, 0)	0.41
							(2, 1)	0.011	(0, 1)	0.06
							(4, −1)	0.039	…	…
							(4, 1)	0.020	…	…
4	3552	1.3	2.91	$\pi/4$	−0.025	0.025	(1, −1)	0.006	(0, 0)	0.41
							(1, 1)	0.011	(2, 0)	0.06
							(3, −1)	0.016	…	…
							(3, 1)	0.032	…	…
5	3552	1.3	2.91	2π	0.025	−0.025	(1, −1)	0.011	(0, 0)	0.41
							(1, 1)	0.006	(2, 0)	0.06
							(3, −1)	0.032	…	…
							(3, 1)	0.016	…	…

subspace. The different natures of the analysis can lead to some inconsistencies. For instance, the translational contributions in 11th excited state indicate that only the $n_x = 1, n_y = 0$ function contributes to that point. This apparent inconsistency arises due to the cylindrical symmetry of this state in the xy subspace, since we have selected just a point as representative of a whole set of points which present the same density.

Table VIII summarizes an overview of the main contributions to the different wave functions calculated for the $H_2@(5,0)$ system. Oppositely from what was found for the previous system, in which most states where a combination of two or three functions of the model systems at most, what is found here is that the wave function has many more contributions. We refer to the supplementary material[19] Table ST2 for information about higher energy states. Note that in this case, the values of maximum probability on the internuclear distance change on some states, due to the presence of excited states in this DoF.

V. SUMMARY AND CONCLUSIONS

A novel view in the study of nuclear eigenstates of systems with important couplings between different degrees of freedom has been developed through the computation and analysis of different overlap functions rather than of the reduced probability density. This method allows to get an insight into how the system behaves in the different points of the space under study. Our approach has been applied to two nanoconfined systems, being the first a technologically relevant system in which confinement effects have been previously studied (a single hydrogen molecule confined in an (8,0) carbon nanotube) and the second an academic case in which the confining potential is still more hindering (the $H_2@(5,0)$ system). In both cases, the results extracted of a qualitative inspection of the reduced probability density of the system were compared with the results of our quantitative study made through overlap functions.

The analysis shows clearly that the qualitative inspection of reduced density functions can lead to erroneous interpretations, because the non-separability of the Hamiltonian prevents the assignation of the usual quantum numbers to the different degrees of freedom. The study of the overlap functions in suitable subspaces, on the other hand, offers an intuitive and rigorous image of the dynamics of the embedded molecule, allowing to see the changes of the wave function in the different points of the space.

ACKNOWLEDGMENTS

[1]M. Xu, L. Ulivi, M. Celli, D. Colognesi, and Z. Bačić, "Rigorous quantum treatment of inelastic neutron scattering spectra of a heteronuclear diatomic molecule in a nanocavity: HD in the small cage of structure II clathrate hydrate," Chem. Phys. Lett. **563**, 1–8 (2013).

[2]T. Rõõm, L. Peedu, M. Ge, D. Hüvonen, U. Nagel, S. Ye, M. Xu, Z. Bačić, S. Mamone, M. H. Levitt, M. Carravetta, J. Y.-C. Chen, X. Lei, N. J. Turro, Y. Murata, and K. Komatsu, "Infrared spectroscopy of small-molecule endofullerenes," Philos. Trans. Ser. A: Math., Phys. Eng. Sci. **371**, 20110631 (2013).

[3]Q. Wang, S. Challa, D. Sholl, and J. Johnson, "Quantum sieving in carbon nanotubes and zeolites," Phys. Rev. Lett. **82**, 956–959 (1999).

[4]S. Fatemi, M. Vesali-Naseh, M. Cyrus, and J. Hashemi, "Improving CO_2/CH_4 adsorptive selectivity of carbon nanotubes by functionalization with nitrogen-containing groups," Chem. Eng. Res. Des. **89**, 1669–1675 (2011).

[5]T. Lu, E. Goldfield, and S. Gray, "Quantum states of hydrogen and its isotopes confined in single-walled carbon nanotubes: Dependence on interaction potential and extreme two-dimensional confinement," J. Phys. Chem. B **110**, 1742–1751 (2006).

[6]T. Yildirim and A. Harris, "Quantum dynamics of a hydrogen molecule confined in a cylindrical potential," Phys. Rev. B **67**, 245413 (2003).

[7]I. Matanović, J. L. Belof, B. Space, K. Sillar, J. Sauer, J. Eckert, and Z. Bačić, "Hydrogen adsorbed in a metal organic framework-5: Coupled translation-rotation eigenstates from quantum five-dimensional calculations," J. Chem. Phys. **137**, 014701 (2012).

[8]S. Ye, M. Xu, S. FitzGerald, K. Tchernyshyov, and Z. Bacic, "H_2 in solid C_{60}: Coupled translation-rotation eigenstates in the octahedral interstitial site from quantum five-dimensional calculations," J. Chem. Phys. **138**, 244707 (2013).

[9]T. K. Nielsen, U. Bösenberg, R. Gosalawit, M. Dornheim, Y. Cerenius, F. Besenbacher, and T. R. Jensen, "A reversible nanoconfined chemical reaction," ACS Nano **4**, 3903–3908 (2010).

[10]C. I. Contescu, H. Zhang, R. J. Olsen, E. Mamontov, J. R. Morris, and N. C. Gallego, "Isotope effect on adsorbed quantum phases: Diffusion of H_2 and D_2 in nanoporous carbon," Phys. Rev. Lett. **110**, 236102 (2013).

[11]S. FitzGerald, T. Yildirim, L. Santodonato, D. Neumann, J. Copley, J. Rush, and F. Trouw, "Quantum dynamics of interstitial H2 in solid C60," Phys. Rev. B **60**, 6439–6451 (1999).

[12]T. Yildirim and A. Harris, "Rotational and vibrational dynamics of interstitial molecular hydrogen," Phys. Rev. B **66**, 214301 (2002).

[13]J. Suarez and F. Huarte-Larrañaga, "Hydrogen confined in single-wall carbon nanotubes: Anisotropy effects on ro-vibrational quantum levels," J. Chem. Phys. **137**, 064320 (2012).

[14]R. Dovesi, R. Orlando, B. Civalleri, C. Roetti, V. R. Saunders, and C. M. Zicovich-Wilson, "CRYSTAL: A computational tool for the *ab initio* study of the electronic properties of crystals," Z. Kristallogr. **220**, 571–573 (2005).

[15]R. Dovesi, V. R. Saunders, C. Roetti, R. Orlando, C. M. Zicovich-Wilson, F. Pascale, B. Civalleri, K. Doll, N. M. Harrison, I. J. Bush, P. D'Arco, and M. Llunell, *CRYSTAL09 User's Manual* (University of Torino, Torino, 2009).

[16]P. Morse, "Diatomic molecules according to the wave mechanics. II. Vibrational levels," Phys. Rev. **34**, 57–64 (1929).

[17]A. Novaco and J. Wroblewski, "Rotational states of H_2, HD, and D_2 on graphite," Phys. Rev. B **39**, 11364–11371 (1989).

[18]F. Huarte-Larrañaga and M. Albertí, "A molecular dynamics study of the distribution of molecular hydrogen physisorbed on single walled carbon nanotubes," Chem. Phys. Lett. **445**, 227–232 (2007).

[19]See supplementary material at http://dx.doi.org/10.1063/1.4913293 for complete tables and additional figures.

[20]U. Manthe, "The state averaged multiconfigurational time-dependent Hartree approach: Vibrational state and reaction rate calculations," J. Chem. Phys. **128**, 064108 (2008).

[21]H.-D. Meyer, U. Manthe, and L. Cederbaum, "The multi-configurational time-dependent Hartree approach," Chem. Phys. Lett. **165**, 73–78 (1990).

[22]*Multidimensional Quantum Dynamics*, edited by H.-D. Meyer, F. Gatti, and G. A. Worth (Wiley-VCH Verlag GmbH & Co. KGaA, Weinheim, Germany, 2009).

[23]H.-D. Meyer, F. Gatti, and G. A. Worth, "Kinetic energy operators," in *Multidimensional Quantum Dynamics*, edited by H.-D. Meyer, F. Gatti, and G. A. Worth (Wiley-VCH Verlag GmbH & Co. KGaA, 2009), pp. 91–110.

[24]"Correlation discrete variable representation (CDVR)," *Multidimensional Quantum Dynamics. MCTDH Theory and Applications*, edited by H.-D. Meyer, F. Gatti, and G. A. Worth (Wiley-VCH Verlag GmbH & Co. KGaA, 2009), pp. 73–80.

[25]J. Schiff and B. Poirier, "Communication: Quantum mechanics without wavefunctions," J. Chem. Phys. **136**, 031102 (2012).

Supplementary information for Publication 1: *5D quantum dynamics of the H$_2$@SWNT system: Quantitative study of the rotational–translational coupling*

Table ST1: Representation of the H$_2$@(8,0) system's eigenfunctions in the basis of direct product functions. The basis functions have a norm of 0.5. Energies in cm^{-1} units.

State	ΔE	Basis Element ($\lvert klmn_x n_y\rangle$)	$\lvert c^n_{k,l,m,n_x,n_y}\rvert$	State	ΔE	Basis Element ($\lvert klmn_x n_y\rangle$)	$\lvert c^n_{k,l,m,n_x,n_y}\rvert$	State	ΔE	Basis Element ($\lvert klmn_x n_y\rangle$)	$\lvert c^n_{k,l,m,n_x,n_y}\rvert$
0	0	$\lvert00000\rangle$	0.68	15	462	$\lvert01110\rangle$	0.34	25	614	$\lvert00002\rangle$	0.22
		$\lvert02000\rangle$	0.17			$\lvert01101\rangle$	0.34			$\lvert02002\rangle$	0.62
1	59	$\lvert01000\rangle$	0.70			$\lvert01{-}101\rangle$	0.34			$\lvert02030\rangle$	0.13
2	171	$\lvert01100\rangle$	0.49			$\lvert01{-}110\rangle$	0.34			$\lvert32002\rangle$	0.11
		$\lvert01{-}100\rangle$	0.49	16	503	$\lvert01110\rangle$	0.34	26	619	$\lvert02-101\rangle$	0.34
3	171	$\lvert01100\rangle$	0.49			$\lvert01101\rangle$	0.34			$\lvert02-102\rangle$	0.33
		$\lvert01{-}100\rangle$	0.49			$\lvert01{-}101\rangle$	0.34			$\lvert02101\rangle$	0.34
4	265	$\lvert00001\rangle$	0.66			$\lvert01{-}110\rangle$	0.34			$\lvert02102\rangle$	0.33
		$\lvert02001\rangle$	0.23	17	550	$\lvert00010\rangle$	0.61	27	619	$\lvert02-101\rangle$	0.34
5	265	$\lvert00010\rangle$	0.65			$\lvert02110\rangle$	0.28			$\lvert02-102\rangle$	0.34
		$\lvert00030\rangle$	0.11	18	550	$\lvert00002\rangle$	0.48			$\lvert02101\rangle$	0.34
		$\lvert02010\rangle$	0.22			$\lvert00020\rangle$	0.37			$\lvert02102\rangle$	0.34
6	310	$\lvert01001\rangle$	0.69			$\lvert02002\rangle$	0.22	28	649	$\lvert02-101\rangle$	0.34
		$\lvert03001\rangle$	0.10			$\lvert02020\rangle$	0.17			$\lvert02-102\rangle$	0.34
7	310	$\lvert01010\rangle$	0.68	19	572	$\lvert00002\rangle$	0.39			$\lvert02101\rangle$	0.34
		$\lvert01030\rangle$	0.14			$\lvert00020\rangle$	0.47			$\lvert02102\rangle$	0.34
8	343	$\lvert00000\rangle$	0.18			$\lvert02000\rangle$	0.12	29	695	$\lvert01-103\rangle$	0.12
		$\lvert02000\rangle$	0.67			$\lvert02002\rangle$	0.17			$\lvert01103\rangle$	0.12
9	346	$\lvert02{-}100\rangle$	0.49			$\lvert02020\rangle$	0.20			$\lvert03-100\rangle$	0.46
		$\lvert02100\rangle$	0.49	20	580	$\lvert01010\rangle$	0.67			$\lvert03100\rangle$	0.46
10	346	$\lvert02{-}100\rangle$	0.49			$\lvert03010\rangle$	0.12	30	695	$\lvert01-111\rangle$	0.11
		$\lvert02100\rangle$	0.49			$\lvert31010\rangle$	0.12			$\lvert01111\rangle$	0.11
11	428	$\lvert01{-}101\rangle$	0.34	21	580	$\lvert01003\rangle$	0.54			$\lvert03-100\rangle$	0.46
		$\lvert01{-}110\rangle$	0.35			$\lvert01011\rangle$	0.40			$\lvert03100\rangle$	0.46
		$\lvert01110\rangle$	0.35	22	590	$\lvert02-101\rangle$	0.35	31	701	$\lvert01003\rangle$	0.12
		$\lvert01101\rangle$	0.34			$\lvert02-102\rangle$	0.34			$\lvert01011\rangle$	0.14
12	429	$\lvert00010\rangle$	0.11			$\lvert02101\rangle$	0.35			$\lvert03000\rangle$	0.67
		$\lvert02{-}200\rangle$	0.49			$\lvert02102\rangle$	0.34			$\lvert33000\rangle$	0.12
		$\lvert02200\rangle$	0.49	23	597	$\lvert01003\rangle$	0.39	32	730	$\lvert00021\rangle$	0.12
13	429	$\lvert02200\rangle$	0.49			$\lvert01011\rangle$	0.50			$\lvert02-201\rangle$	0.34
		$\lvert02{-}200\rangle$	0.49			$\lvert03000\rangle$	0.18			$\lvert02-202\rangle$	0.33
14	462	$\lvert01110\rangle$	0.34			$\lvert03011\rangle$	0.11			$\lvert02201\rangle$	0.34
		$\lvert01101\rangle$	0.34	24	614	$\lvert00001\rangle$	0.21			$\lvert02202\rangle$	0.33
		$\lvert01{-}101\rangle$	0.34			$\lvert02001\rangle$	0.63				
		$\lvert01{-}110\rangle$	0.34			$\lvert32001\rangle$	0.11				

1

Table ST2: Representation of the H_2@(5,0) system's eigenfunctions in the basis of direct product functions. Energies in cm^{-1} units.

State	ΔE	Basis Element $(\lvert klmn_xn_y\rangle)$	$\lvert c^n_{k,l,m,n_x,n_y}\rvert$	State	ΔE	Basis Element $(\lvert klmn_xn_y\rangle)$	$\lvert c^n_{k,l,m,n_x,n_y}\rvert$	State	ΔE	Basis Element $(\lvert klmn_xn_y\rangle)$	$\lvert c^n_{k,l,m,n_x,n_y}\rvert$
0	0	$\lvert 00000\rangle$	0.072	5	3552	$\lvert 01{-}100\rangle$	0.016	9	3591	$\lvert 01001\rangle$	0.181
		$\lvert 02000\rangle$	0.282			$\lvert 03{-}100\rangle$	0.134			$\lvert 02001\rangle$	0.019
		$\lvert 12000\rangle$	0.030			$\lvert 03100\rangle$	0.036			$\lvert 03001\rangle$	0.283
		$\lvert 32000\rangle$	0.018			$\lvert 13{-}100\rangle$	0.023			$\lvert 11001\rangle$	0.023
		$\lvert 04000\rangle$	0.096			$\cdots$	$\cdots$			$\lvert 13001\rangle$	0.030
		$\cdots$	$\cdots$	6	3591	$\lvert 00010\rangle$	0.067			$\lvert 31001\rangle$	0.012
1	0	$\lvert 01000\rangle$	0.199			$\lvert 02010\rangle$	0.264			$\lvert 33001\rangle$	0.019
		$\lvert 03000\rangle$	0.309			$\lvert 03010\rangle$	0.013			$\cdots$	$\cdots$
		$\lvert 11000\rangle$	0.023			$\lvert 12010\rangle$	0.031	10	4636	$\lvert 10000\rangle$	0.065
		$\lvert 13000\rangle$	0.030			$\lvert 32010\rangle$	0.017			$\lvert 12000\rangle$	0.231
		$\lvert 31000\rangle$	0.013			$\lvert 04002\rangle$	0.091			$\lvert 22000\rangle$	0.015
		$\lvert 33000\rangle$	0.020			$\cdots$	$\cdots$			$\lvert 14000\rangle$	0.064
		$\cdots$	$\cdots$	7	3591	$\lvert 01010\rangle$	0.186			$\cdots$	$\cdots$
2	3552	$\lvert 02{-}100\rangle$	0.017			$\lvert 02010\rangle$	0.012	11	4636	$\lvert 11000\rangle$	0.174
		$\lvert 02100\rangle$	0.065			$\lvert 03010\rangle$	0.291			$\lvert 13000\rangle$	0.231
		$\lvert 12100\rangle$	0.012			$\lvert 11010\rangle$	0.023			$\lvert 21000\rangle$	0.013
		$\lvert 04{-}100\rangle$	0.052			$\lvert 13010\rangle$	0.031			$\lvert 23000\rangle$	0.014
		$\lvert 04100\rangle$	0.196			$\lvert 31010\rangle$	0.012			$\cdots$	$\cdots$
		$\lvert 14100\rangle$	0.030			$\lvert 33010\rangle$	0.019	12	6673	$\lvert 03{-}200\rangle$	0.032
		$\lvert 34100\rangle$	0.014			$\cdots$	$\cdots$			$\cdots$	$\cdots$
		$\cdots$	$\cdots$	8	3591	$\lvert 00001\rangle$	0.065	13	6673	$\lvert 04{-}200\rangle$	0.086
3	3552	$\lvert 02{-}100\rangle$	0.065			$\lvert 01001\rangle$	0.013			$\lvert 14{-}200\rangle$	0.019
		$\lvert 02100\rangle$	0.017			$\lvert 02001\rangle$	0.257			$\cdots$	$\cdots$
		$\lvert 12{-}100\rangle$	0.012			$\lvert 03001\rangle$	0.021	14	6673	$\lvert 03200\rangle$	0.031
		$\lvert 04{-}100\rangle$	0.196			$\lvert 12001\rangle$	0.030			$\cdots$	$\cdots$
		$\lvert 04100\rangle$	0.052			$\lvert 32001\rangle$	0.017	15	6673	$\lvert 04200\rangle$	0.084
		$\lvert 14{-}100\rangle$	0.030			$\lvert 04001\rangle$	0.088			$\lvert 14200\rangle$	0.019
		$\lvert 34{-}100\rangle$	0.014			$\cdots$	$\cdots$			$\cdots$	$\cdots$
		$\cdots$	$\cdots$					16	6833	$\lvert 00000\rangle$	0.073
4	3552	$\lvert 01100\rangle$	0.016							$\lvert 02000\rangle$	0.165
		$\lvert 03{-}100\rangle$	0.036							$\lvert 02020\rangle$	0.014
		$\lvert 03100\rangle$	0.134							$\lvert 14000\rangle$	0.014
		$\lvert 13100\rangle$	0.023							$\cdots$	$\cdots$
		$\cdots$	$\cdots$								

1

Table ST3: Results of the quantitative description of all the converged eigenstates of the H_2@(8,0) system. Energies referred to the ground state energy of 2580 cm^{-1}, contribution of the reference functions referred to the point of maximum probability density in the 5D space.

State	ΔE	ρ	θ	ϕ	x	y	Model Functions contribution
							l,m	$\left\|\sigma_{l,m}^n\right\|$	n_x,n_y	$\left\|\sigma_{n_x,n_y}^n\right\|$
0	0	1.4	3.1235	0.049087	-0.10938	-0.10938	$(0,0)$	0.097	$(0,0)$	0.11
							$(2,0)$	0.021	$(2,0)$	0.01
1	58	1.4	0.067494	2.1108	-0.10938	-0.10938	$(1,0)$	0.096	$(0,0)$	0.14
							$(3,0)$	0.008	$(2,0)$	0.02
2	171		1.8421	1.5217	-0.10938	-0.10938	$(1,-1)$	0.073	$(0,0)$	0.11
							$(1,1)$	0.073	-	-
							$(3,-1)$	0.006	-	-
							$(3,1)$	0.006	-	-
3	171	1.4	1.8915	3.0925	-0.10938	-0.10938	$(1,-1)$	0.073	$(0,0)$	0.11
							$(1,1)$	0.073	$(0,2)$	0.01
							$(3,-1)$	0.006	$(2,0)$	0.01
							$(3,1)$	0.006	-	-
4	265	1.4	3.1235	0.34361	-0.54688	-0.10938	$(0,0)$	0.083	$(0,1)$	0.12
							$(2,0)$	0.027	$(0,3)$	0.01
							-	-	$(2,1)$	0.01
5	265	1.4	0.018094	2.9943	-0.10938	0.54688	$(0,0)$	0.083	$(1,0)$	0.12
							$(2,0)$	0.028	$(3,0)$	0.03
6	310	1.4	3.0741	1.4235	-0.54688	-0.10938	$(1,0)$	0.086	$(0,1)$	0.15
							$(3,0)$	0.012	$(0,3)$	0.01
							-	-	$(2,1)$	0.02
7	310	1.4	3.0741	3.0925	-0.10938	0.54688	$(1,0)$	0.087	$(1,0)$	0.14
							$(3,0)$	0.012	$(3,0)$	0.03
8	342	1.4	3.1235	0.049087	-0.10938	0.10938	$(0,0)$	0.038	$(0,0)$	0.15
							$(2,0)$	0.092	$(0,2)$	0.01
							-	-	$(2,0)$	0.03
9	346	1.4	2.4339	1.5217	-0.10938	-0.10938	$(2,-1)$	0.070	$(0,0)$	0.14
							$(2,1)$	0.070	$(1,0)$	0.01
							-	-	$(2,0)$	0.01
10	346	1.4	2.4339	3.0925	-0.10938	-0.10938	$(2,-1)$	0.070	$(0,0)$	0.14
							$(2,1)$	0.070	$(0,1)$	0.01
							-	-	$(0,2)$	0.01
							-	-	$(2,0)$	0.01
11	428	1.4	2.0394	1.5217	-0.32812	-0.32812	$(1,-1)$	0.047	$(0,1)$	0.07
							$(1,1)$	0.047	-	-
12	429	1.4	1.5955	0.73631	-0.10938	-0.10938	$(2,-2)$	0.073	$(0,0)$	0.12
							$(2,2)$	0.073	$(0,2)$	0.01
							-	-	$(1,1)$	0.01
							-	-	$(2,0)$	0.01
13	429	1.4	1.5955	1.6199	-0.10938	0.10938	$(2,-2)$	0.073	$(0,0)$	0.12
							$(2,2)$	0.073	-	-
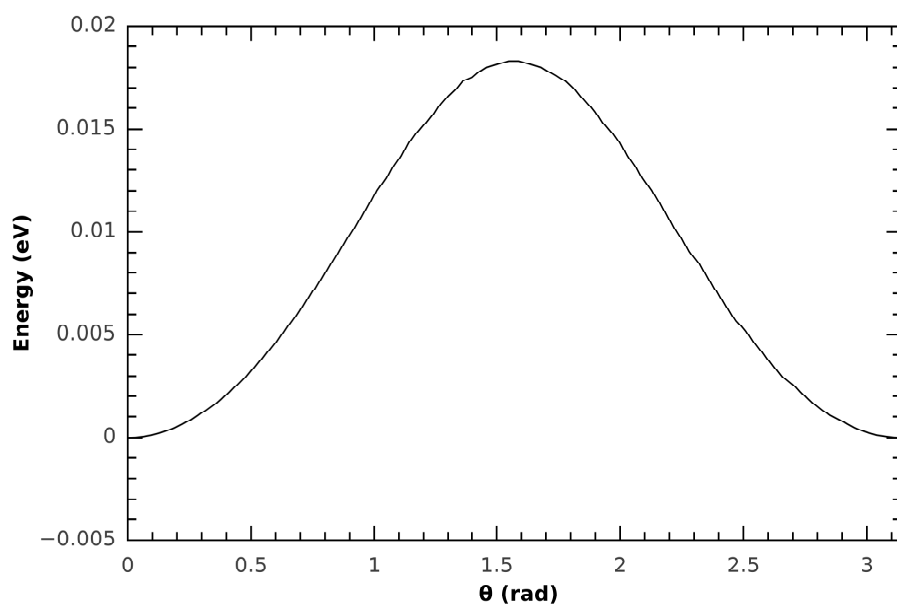
Figure SF1: Plot of the relaxed potential energy surface scanned along the θ coordinate for the H_2@(8,0) system.
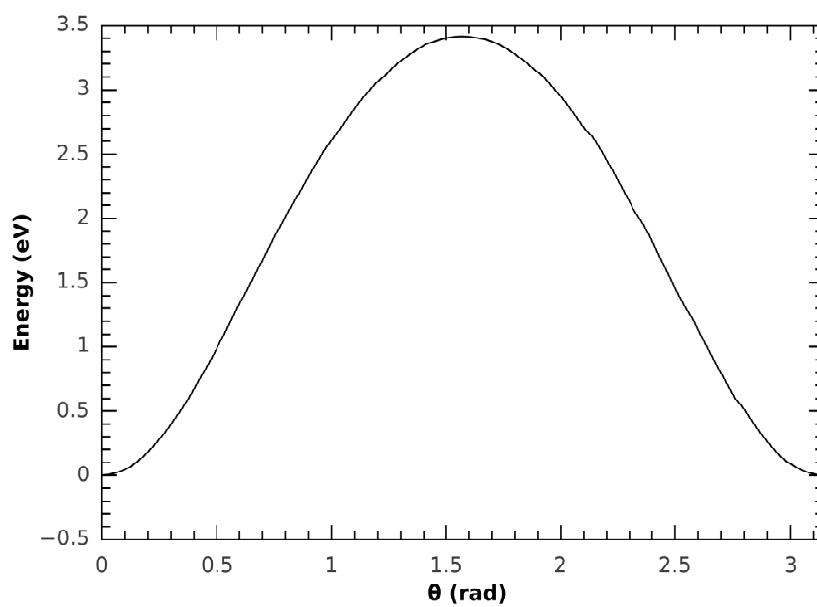
Figure SF2: Plot of the relaxed potential energy surface scanned along the θ coordinate for the H_2@(5,0) system. Note the significant increase of the barrier compared with the previous case, as well as its broadening.

5.4 Summary and Conclusions:

In this Chapter we have presented a detailed study of the H_2 molecule confined in a (8,0) SWNCT: first, the overall power spectrum of the system has been discussed, finding a great densification when compared with the spectrum of the free molecule. We have also taken advantage of the study to discuss the pros and cons of the computation of a power spectrum by Fourier transforming the Autocorrelation function of an arbitrary wave packet propagated for 1000 fs. Secondly, the first 50 individual eigenstates of the system have been computed using the SA-MCTDH approach, and analyzed in three distinct ways: by direct observation of the projected wave function, by computation of the scalar product with known 5D reference functions, and by performing partial overlaps with familiar functions only in relevant DOFs. The joint use of all these tools has significantly increased the understanding of the coupling between the different coordinates.

The main conclusions to be drawn from this Chapter are:

- It is possible to extract information of a system from both time–dependent and time–independent formalisms. However, each one focuses on different aspects of the problem.

- Power spectrum calculations allow us to have a general view of the system through the number of lines present. However, the intensity of those lines is in principle arbitrary and highly dependent on the initial state of the propagation. More detailed procedures in this regard exist in the literature[145, 146].

- The SA–MCTDH approach is excellent for the computation of nuclear eigenstates, even though the initial state to be propagated in imaginary time has an important effect on the efficiency of the convergence.

- The confinement inside a nanotube induces a coupling, which is specially noticeable between the translational DOFs, x and y, and the azimuthal angle of rotation, θ. This is seen both in the mixed contributions of several spherical harmonics to the ground state, and also in the clear dependence of this mixing on the actual position of the c.o.m in the molecule, illustrated through the partial overlap functions.

Chapter 6

Diffusion of H$_2$ along Single–walled Carbon Nanotubes

6.1 Diffusion and quantum sieving

Quantum sieving refers to the change in transport properties that different isotopologues exhibit when they are interacting with a nanostructured material. These molecules have the same electronic structure, and therefore are exposed to identical potential interactions with the nanostructure. Classically, this would imply that their dynamics would be slightly different, since the kinetic energy depends on their mass. However, the quantum mechanical nature of molecular systems is known to affect the dynamics of light atoms more strongly due to the effect of the mass on other properties such as the ZPE or the tunneling permeability. This is notorious in reaction dynamics under the name of *kinetic isotope effects* (KIE)[147], a term that refers to the changes in the reaction rate of a given process upon the isotopic substitution of one of the reactants. It has been seen that similar effects appear in nanoconfined systems, giving rise to different transport properties of isotopologues in nanostructured substrates and allowing to use these variations to separate isotopical mixtures of compounds, primarily H$_2$ from D$_2$.

Quantum sieving effects, just as KIE, appear due to the different ZPE of the isotopologues: even though the potential energy surface remains the same for the various species, their ZPE is proportional to $1/\sqrt{m}$, with m the mass of the particle. This is qualitatively illustrated in Figure 6.1, where the dissociation curve of the free H$_2$ molecule is represented together with hydrogen's and deuterium's ZPE. The difference in ZPE has a relevant effect in the dispersion of the wave function: in the previous example, the dispersion in the vibrational DOF will be larger in H$_2$ than in D$_2$. It is straightforward to understand quantum sieving taking this change of the wave function into account: heavier isotopologues (D$_2$) have a smaller effective size compared to lighter ones (H$_2$), and therefore they will experience more repulsion from the substrate's walls. Even though this effect was predicted in mesoporous silica[13], it becomes more critical as the size of the pore is reduced[22].

Quantum sieving effects appear in different processes: adsorption into a porous cavity, diffusion along a pore, or diffusion along a nanostructure itself. In general, depending on the specific process, quantum sieving effects can be classified two types: thermodynamic or kinetic. Thermodynamic sieving refers to the preferential adsorption of one of the isotopologues over the other on a nanostructured material. This can be understood in terms of the effective size of the adsorbate just discussed: since heavier molecules have a smaller effective size, they can pass more easily through a nanometric pore. Conversely, the larger dispersion in lighter species will cause the adsorption process to be less favorable, due to the larger repulsion with the cavity. On the other hand, kinetic quantum sieving regards the differences
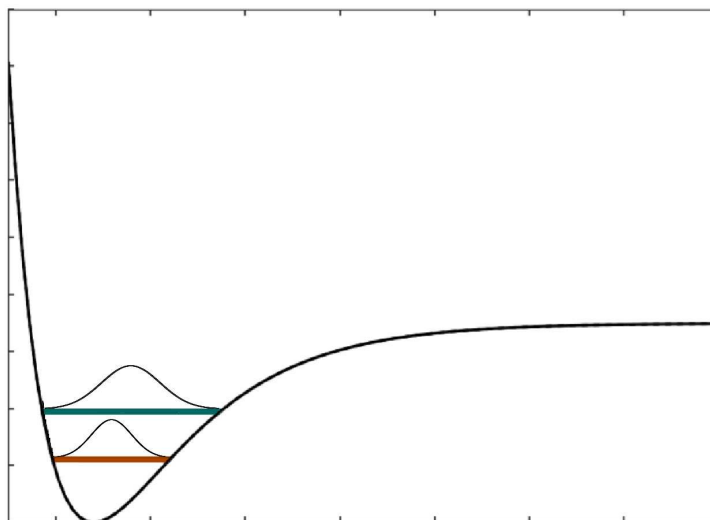
FIGURE 6.1: Schematic representation of the dissociation curve for
hydrogen (black) and the ZPE levels for H$_2$ (blue) and D$_2$ (brown).
Note how the expectation value of the internuclear distance is larger
for H$_2$ than it is for D$_2$.

in the diffusion dynamics of isotopologues, either when crossing a pore mouth or a longer portion of a nanomaterial. It was generally believed that the trend in these processes was similar to that of thermodynamic sieving: at low enough temperatures, heavier isotopologues should diffuse faster than lighter ones because their smaller effective size would generate lower diffusion barriers inside the nanostructure. This has been theoretically and experimentally confirmed for Carbon Molecular Sieves (CMS)[40, 42]. In our first work on this subject, which is presented in **Publication 2**, we wanted to check if this behavior was maintained for the diffusion of H$_2$ and D$_2$ along an (8,0) SWCNT. We did so by calculating the diffusion coefficient of both isotopologues in a fully quantum formalism using a 6D model for the adsorbate, so that all couplings and non–classical effects could be taken into account without any approximation. The approach used to obtain the diffusion coefficients will be the subject of Section 6.2. These first calculations, carried out on both the AH and FB PESs (see Chapter 4), yielded results in agreement with previous studies in CMSs: deuterium, the heavier isotopologue, diffused faster than hydrogen at temperatures below 50 K, when confinement effects become more noticeable. Moreover the thermodynamic sieving obtained with our full–dimensional Hamiltonian was also consistent with the calculations by Lu et al.[34] on the FB PES using a 4D model.

We will start this Chapter by reviewing the methodology needed to directly obtain diffusion rates from a set of propagations, namely the flux–correlation function approach, in Section 6.2 . Then the main results of **Publication 2** will be discussed in Section 6.3, followed by the paper itself. Finally, the results will be critically analyzed in Section 6.5, and the main conclusions of this Chapter drawn in Section 6.6 .

6.2 Diffusion kinetics from Time-dependent Quantum Dynamics: Flux Correlation Functions

Quantum dynamics, as pointed out in Chapter 2, is the microscopic foundation of the chemical reaction and its kinetics. Historically, phenomenological rate constants of chemical processes were determined by experimental procedures based on the concentration change of either reactants or products. Later, more evolved experiments allowed for the calculation of reaction rates of elementary reactions through crossed molecular beams set–ups. However, the thermal rate constant of a (elementary) chemical reaction can actually be computed from first principles, without resorting to experimental data.

The general expression for a reaction rate is given as a thermal average of its cumulative reaction probability (CRP), $N(E)$:

$$k(T) = \frac{1}{2\pi\hbar Q_r(T)} \int_{-\infty}^{\infty} dE e^{-E\beta} N(E), \tag{6.1}$$

with $\beta = 1/k_B T$. The mentioned quantity is in turn a sum of individual reactant state to product state reaction probabilities.The calculation of rate constants for chemical reactions by direct dynamics (that is, avoiding the calculation of the state-to-state reaction probabilities) was introduced in 1974 by Miller[148], while working to obtain a quantum mechanical equivalent of the classical transition state theory. In order to do this, he started by defining a dividing surface separating reactants from products through a Heaviside function, $h(s)$, so that $h(q) = 1$ for reactants ($q < s$) and $h(q) = 0$ for products ($q > s$). Then, he defined the flux of a wave function through this surface with the *flux operator*, $\hat{F}$:

$$\hat{F} = \frac{i}{\hbar} \left[\hat{H}, h(s) \right], \tag{6.2}$$

and showed that the reaction rate was directly related with the trace of this operator. Later, Miller et al. found that this trace could be computed as the integral of the *flux–flux autocorrelation function*, $C_{ff}(t, t', T)$; a result already pointed out by Yamamoto[149]:

$$k(T) = \frac{1}{2\pi\hbar Q_r(T)} \int_0^{\infty} dt C_{ff}(t, t', T_0). \tag{6.3}$$

It must be taken into account that the flux operator is singular, that meaning that its eigenfunctions do not belong to a Hilbert space. One is then forced to use its regularized version, the *thermal flux operator*, $\hat{F}_{T_0} = e^{-\beta\hat{H}/2}\hat{F}e^{-\beta\hat{H}/2}$, to build the function basis.The flux–flux autocorrelation function is then defined as:

$$C_{ff}(t, t', T_0) = \sum_{f_{T_0}} f_{T_0} \left\langle f_{T_0} | e^{i\frac{\hat{H}}{\hbar}t'} \hat{F} e^{-i\frac{\hat{H}}{\hbar}t} | f_{T_0} \right\rangle. \tag{6.4}$$

where f_{T_0} and $| f_{T_0} \rangle$ stand for the eigenvalues and eigenstates of the thermal flux operator, respectively.

The interpretation of these equations is more clear when one considers their classical equivalent. The quantum mechanical trace is equivalent to an integral over all the possible initial conditions spanned by the system. If we consider all possible trajectories as starting from the dividing surface, the rate of the reaction will be determined by how many of these trajectories end up in the reactant or the product
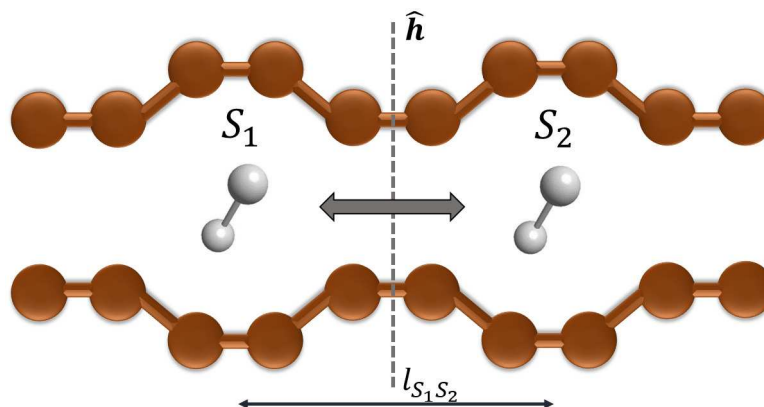
FIGURE 6.2: Schematic representation of the procedure to compute a diffusion rate from first principles in the single–hopping approach.

region of the space. The flux–correlation formalism evaluates this at a quantum mechanical level by the propagation of a series of *thermal flux eigenstates*, computed at the dividing surface. Each one of these states can be seen as a vibrational state of the *activated complex* of the reaction. Once the wave packets have abandoned the interaction area, the integral of the flux–flux autocorrelation function (Eq. (6.3)) converges and the cumulative reaction probability is obtained by a Fourier transform. See Ref. [150] for a complete discussion on this interpretation, and Ref. [151] for more specific mathematical details.

As it is readily seen in Eq. (6.4), obtaining $k(T)$ implies a summation over all thermal flux eigenfunctions. Fortunately, it is known that the flux operator has a limited number of non-zero eigenvalues, so the number of terms in the sum is low enough to make the equation computationally affordable. Within this representation, the cumulative reaction probability is:

$$N(E) = \frac{1}{2}e^{\beta E}\sum_{f_{T_0}} f_{T_0} \int_{-\infty}^{\infty} \mathrm{d}t \int_{-\infty}^{\infty} \mathrm{d}t' e^{\mathrm{i}Et}e^{-\mathrm{i}Et'}\langle f_{T_0} \mid e^{\mathrm{i}\frac{\hat{H}}{\hbar}t'}\hat{F}e^{\mathrm{i}\frac{\hat{H}}{\hbar}t} \mid f_{T_0}\rangle. \qquad (6.5)$$

Note that the sum runs over the different flux eigenstates. This allows us to define *individual state contributions* to the CRP. It is important to take into account that the regularization of the flux operator has an important effect on $N(E)$: the Boltzmann–distribution type exponentials appearing in Eq. (6.5) introduce numerical noise in energy values not populated according to statistical mechanics, which are translated in large oscillations which negatively affect the quality of rate's computation.

The methodology that we have just described was developed for the calculation of conversion rates in chemical reactions. Although diffusion is certainly not a chemical reaction, it is possible to establish a direct connection between such a process and diffusion: in both cases a certain initial atomic arrangement (reactants) must cross a potential barrier to reach a new configuration (products). In the case of diffusion, reactants and products will be the same chemical species, only adsorbed in different adsorption sites. If the pressure of the gaseous species is low enough, there will be no interaction between adsorbate molecules. Then, following Zhang et al.[152], we use the single–hoping and nearest neighbor approximations[153] to compute the diffusion rate. Figure 6.2 illustrates the idea of the whole process of computing a diffusion rate through this approach: once the adsorption sites S_1 and S_2 have been found, we set the dividing surface $h(s)$ and use the flux correlation functions formalism to obtain the rate of crossings from one adsorption site to the
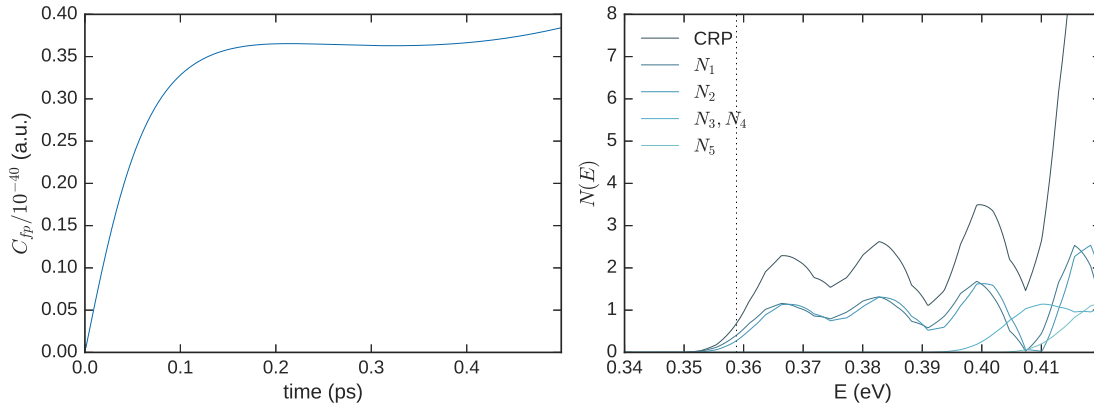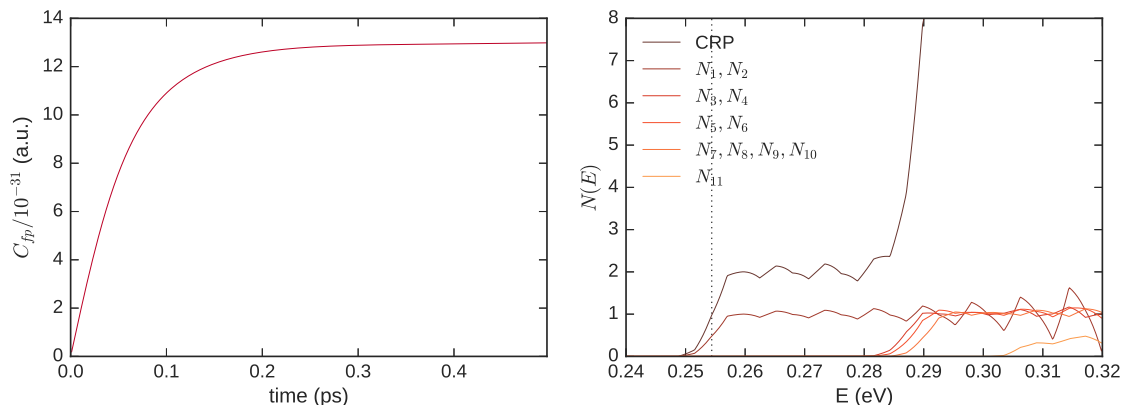
FIGURE 6.3: Left: flux–position autocorrelation function for the diffusion of H_2 (bottom) along an (8,0) SWCNT. Right: Cumulative Reaction Probability and individual contributions for the same process. Vertical dotted line identifies the adiabatic barrier for diffusion.

other, k_{hop}. Then, the diffusion coefficient is obtained by applying Eq. (6.6):

$$D(T) = \left(\frac{l^2}{2d} \right) k_{hop}(T),\tag{6.6}$$

with l the distance between adsorption sites, here equivalent to the length of the unit cell L, and d the symmetry number of the system, which in this case equals 2.

6.3 Result Discussion

6.3.1 Diffusion rates: first results and convergence issues

This Section contains a general overview of the main results found in **Publication 2**, Section 6.4.

The study contained in **Publication 2** represents, to the best of our knowledge, the first attempt to calculate diffusion rates for H_2 and D_2 through a fully quantum formalism and a 6D Hamiltonian considering all the DOFs of the adsorbate. Using the flux–flux correlation function formalism we obtained the $N(E)$ for both isotopologues, by propagating the thermal flux eigenstates obtained at different reference temperatures (75, 100 and 150 K) for a total time of 500 fs. Then the CRP (Eq. (6.5) was thermally averaged in order to obtain the transmission rate, from which the diffusion rate was obtained. This procedure was carried out for both the AH and the FB PESs presented in Chapter 4.Details on the results in the AH PES can be found in the main body of **Publication 2**.

It can be shown that the integral of $C_{ff}(t, t', T_0)$ (Eq. (6.3)) is formally equivalent to the limit of the *flux–position autocorrelation function*, $C_{fp}(t)$, as $t \to \infty$, an therefore this function is a useful visual guide to check convergence. The flux–position autocorrelation function and the resulting $N(E)$ obtained with the FB PES are shown for hydrogen and deuterium in Figures 6.3 and Figures 6.4, respectively. The energy range shown in the CRP figures comprehends all energies with a relevant population for temperatures up to 150 K for each system.

Since $C_{fp}(t)$ reaches a plateau at around 200 fs for both isotopologues, it would seem that the calculations are correctly converged. Hydrogen's cumulative reaction probability presents an energy threshold slightly above 0.35 eV for H_2 and slightly

FIGURE 6.4: Left: flux–position autocorrelation function for the diffusion of D_2 (bottom) along an (8,0) SWCNT. Right: Cumulative Reaction Probability and individual contributions for the same process. Vertical dotted line identifies the adiabatic barrier for diffusion.

under 0.25 eV for D_2. In both cases these energies are below the adiabatic barrier for diffusion, which is 0.369 eV and 0.254 eV for hydrogen and deuterium, respectively. This indicates the presence of some tunneling effects for the diffusion process, which are more important in the case of the lighter isotopologue. In addition to the total $N(E)$, both figures include the individual contributions of the different flux eigenstates to the total CRP. At this point it is worthwhile to discuss briefly the implications of the regularization of the flux operator at a certain value of T. Even though the flux operator has a virtually infinite spectrum, its regularized version only has a limited number of eigenstates with non–zero eigenvalues, each one weighted by a factor related with the population of the rovibrational eigenstates of the activated complex at the regularization temperature according to a Boltzmann distribution[46]. The eigenstates with lower weight introduce numerical error to $N(E)$, which negatively affects the quality of $k(T)$ at temperatures significantly higher or lower than T. Therefore, since we can only get numerically accurate results for a certain temperature range, it is convenient to limit the number of flux eigenstates considered to those with a relevant weight in this range in order to maximize the efficiency of the calculation. In our case, the number of flux eigenstates contributing to the diffusion process was of 5 for hydrogen and 11 for deuterium, significantly lower than the amount of flux eigenstates computed with the SA-MCTDH approach (50 in total). Since the size of the common SPFs basis needed is larger if we have to describe 50 eigenstates than it would be if we only required to compute 20 of them, the overall efficiency of the calculation was not optimal, even though we were able to obtain the diffusion rates in a reasonable time. It is noteworthy that the number of flux eigenstates contributing to deuterium's diffusion is significantly higher than that of hydrogen. This is consistent with the rovibrational spectrum of both isotopologues: test calculations carried out at a fixed z point showed that D_2 has a much denser eigenstate spectrum compared to H_2.

The diffusion coefficients for both hydrogen and deuterium are shown in Figure 6.5, together with the experimental data for diffusion of both isotopologues in a carbon molecular sieve obtained from Ref. [41]. There are two main conclusions to be extracted from this plot. First, the results obtained with both PESs suggest an inverse kinetic isotope effect, so that deuterium would start to diffuse faster than hydrogen at low temperatures. This could be explained in terms of the change in ZPE discussed in Section 6.1. Secondly, the turnover temperature is higher for the FB PES,
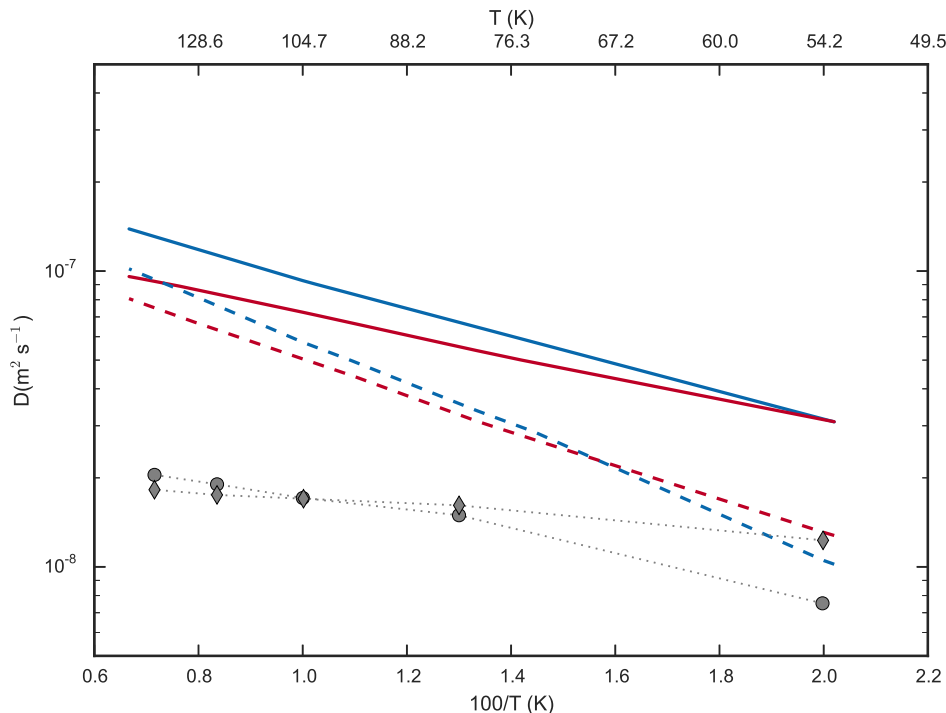
FIGURE 6.5: Diffusion rates for H_2 (blue) and D_2 (red), computed with the AH (solid line) and the FB PESs (dashed line). Experimental results for diffusion in CMS, extracted from Ref. [42], are shown as circles (H_2) and diamonds (D_2)

which is consistent with the analysis of the potential energy profiles: since this set of parameters generates a more confining potential than the AH set, the changes in ZPE are more relevant and they affect more deeply the diffusion process. These results were backed up by Transition State Theory (TST) computations, and agree qualitatively with the diffusion coefficients measured in a CMS, even though the structure of such materials consists on relatively large cavities connected through narrow and short pores rather than a single narrow cavity as it is the case of SWCNT.

6.3.2 Diffusion coefficients after time–extended propagation: resonance–enhanced tunneling

During further studies on the H_2@SWCNT system we developed an approach based on separating the confined DOFs from the diffusion coordinate due to the different characteristic times in these sets of coordinates. This development, which is thoroughly discussed in Chapter 7 and in **Publication 4**, allowed us to highly increase the efficiency of our calculations. The outstanding performance of the new approach permitted the propagation of the flux eigenstates for times up to 20 ps, thus revealing new insight of the system which was not grasped in the previous computations.

The overall shape of the integral of $C_{ff}(t, t', T_0)$, as it was mentioned previously, is a useful tool to asses convergence with respect to the propagation time, since it reaches a plateau when the wave packet has left the interaction region. However, the visual analysis of this function can lead to a misinterpretation of the results, since the existence of a plateau in a given time range is not a sufficient condition for convergence: it could be that the function stabilizes for a certain amount of time, only to start evolving again. Figure 6.6, adapted from **Publication 4** (to be discussed
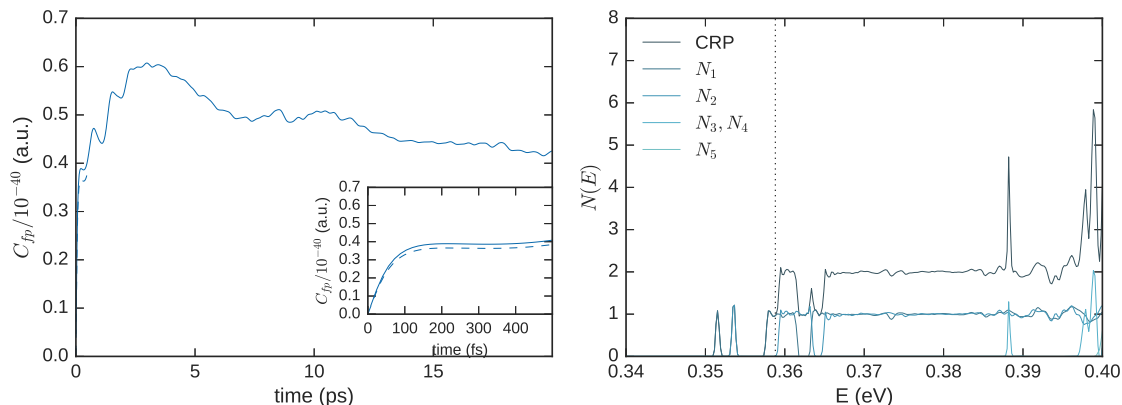
FIGURE 6.6: Left: flux–position autocorrelation function for the diffusion of H_2 along an (8,0) SWCNT. Inset: close up to the short–time region (dashed line corresponding to the 6D propagation). Right: Cumulative Reaction Probability for the same system after 20 ps propagation. Vertical dotted line marks the adiabatic diffusion barrier.

in the next Chapter), shows the flux–position autocorrelation function as a function of time using the 6D model and the time–scale separation approach for hydrogen's diffusion. It is straightforward to see that the propagation was not converged at 500 fs: although we detected a plateau in the first 500 fs of the propagation, for longer times we can see important oscillations in the function. These features (called *recurrences*) are a sign of the existence of resonant states. Resonances appear when a given quasi–bound state has an energy which coincides with another state beyond a potential energy barrier. When this happens, the wave function tunnels through the barrier very efficiently, giving rise to an increase of the transmission probability at almost discrete energy values. These resonances are clearly seen in the CRP obtained after 20 ps of propagation, shown again in Figure 6.6 for H_2, as narrow peaks in the cumulative reaction probability. A similar behavior appears in the case of D_2, whose $C_{fp}(t)$ and $N(E)$ are plotted in Figure 6.7. It should be mentioned that the propagations are not completely converged either after 20 ps of propagation, since the $C_{fp}(t)$ has not stabilized to a constant value. This is typical for resonant systems with a low potential energy barrier. Thus, to obtain smooth $N(E)$ functions a damping function had to be added to the flux–flux correlation function. However, we are confident of the results because the computed CRP did not change appreciably when increasing or decreasing the propagation times.

The possibility of running time–extended simulations offered the chance to revisit the diffusion coefficients of nanoconfined hydrogen and deuterium. Comparing the cumulative reaction probability for both H_2 and D_2, one can see two main differences. On one hand, the energy at which the first resonances appear relative to the adiabatic diffusion barrier, and their intensity, is significantly different for H_2 and for D_2. On the other, the density of the higher energy resonances is much larger for the heavier isotopologue. The former feature is probably the more critical point, since it will influence more heavily the behavior of the different molecules at low temperature. The two first resonances in $N(E)$ for the H_2 molecule are both strong and appear at energies significantly lower than the threshold. Moreover, a second–order resonance appears at E=0.36 eV, just above the diffusion threshold, thus contributing to increase the diffusion rate at all temperatures. On the contrary, for D_2 we find a quite negligible resonance at E=0.248 eV, while two strong resonances exist at energies just below the energy threshold. Being that close to the diffusion threshold,
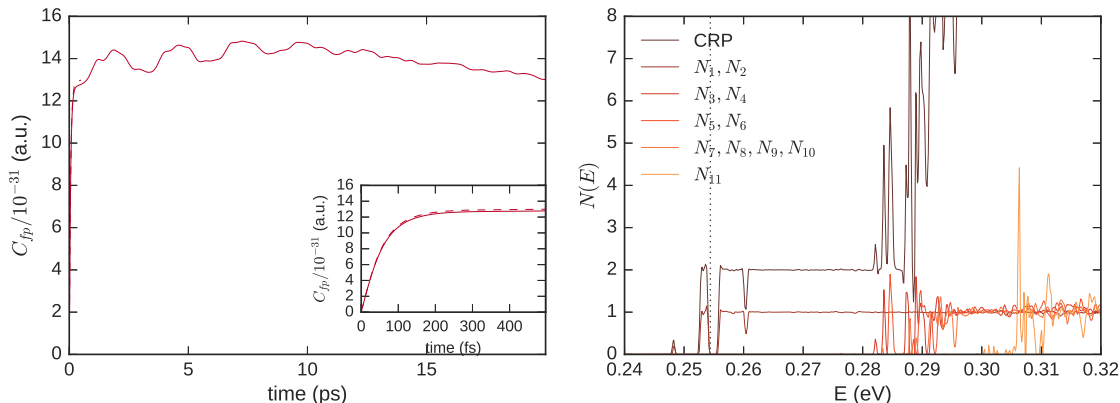
FIGURE 6.7: Left: flux–position autocorrelation function for the diffusion of D_2 along an (8,0) SWCNT. Inset: close up to the short–time region (dashed line corresponding to the 6D propagation). Right: Cumulative Reaction Probability for the same system after 20 ps propagation. Vertical dotted line marks the adiabatic diffusion barrier.

these resonances will have a smaller effect on D_{diff} at low temperatures than those present in H_2. Regarding the denser resonance spectrum of D_2 at higher energies, its effect on the diffusion rate is minimal, since most of the contribution to the transition probability comes from lower energy states.

These resonances prove to be of critical importance and change the qualitative picture of kinetic sieving pictured by the previous results, as it can be seen by comparing the results of the first publication (500 fs propagation), Transition State Theory calculations, and the converged diffusion rate (20 ps propagation). The diffusion rates computed with the three approaches are all plotted in Figure 6.8 for comparison. It is clearly seen that the results after 500 fs propagation lie between the converged and TST calculations. Since TST is a semiclassical theory, based on classical assumptions, it is known that it cannot reproduce some pure quantum effects such as tunneling. The Figure confirms that the issue in the first calculations was that they were not able to fully resolve the resonances. This is true for both H_2 and D_2. However, the relative importance of tunneling is larger for the former than for the latter, which makes a qualitative difference in the results of our study: resonance enhanced tunneling overcomes the ZPE energy effects at low temperatures, and thus H_2 diffuses faster than D_2 in the whole the temperature range studied (and presumably at all temperatures). This is seen in Figure 6.9, where the diffusion rates for both isotopologues is shown as a function of T. The results concerning hydrogen are extracted from **Publication 4**, while the ones for deuterium are new results that we expect to submit for publication shortly.

As a final note, these new results do not change the previous conclusions regarding the thermodynamic sieving: the preferential adsorption of D_2 in front of H_2 is still expected. This quantity is an *equilibrium* property depending only on the partition functions of H_2 and D_2, and therefore was not affected by the unconverged propagations in the first work. Neither are they necessarily in conflict with previous works, which focused mainly on diffusion along CMS: both kind of nanostructures are inherently different, and thus the behavior of confined molecules might also differ. However, the presence of tunneling remarks the importance to take into account all quantum effects in dynamic studies.
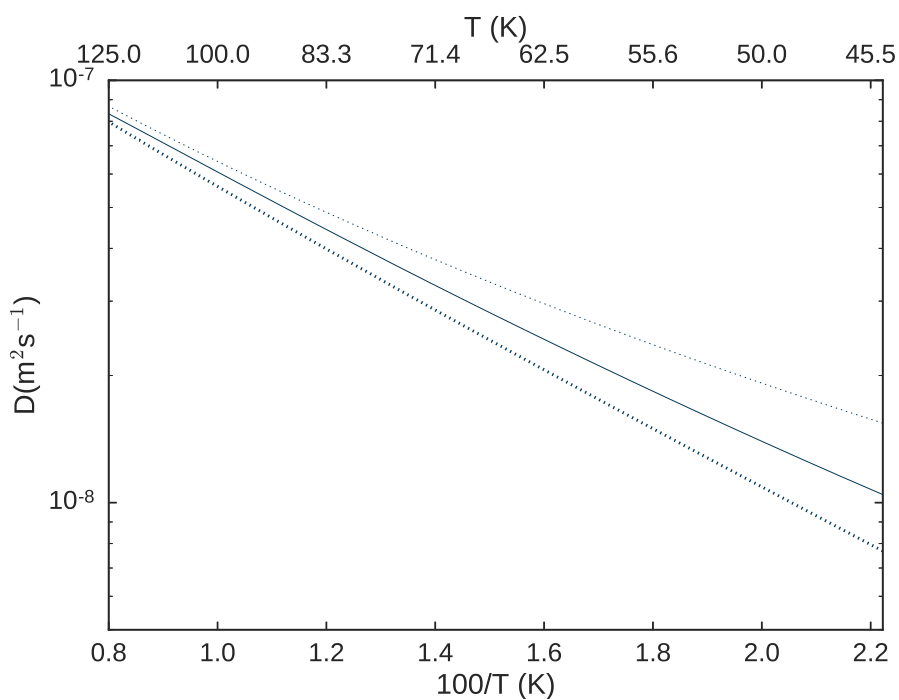
FIGURE 6.8: Diffusion rates for H$_2$ computed with flux correlation function approach after 500 fs propagation (solid) and after 20 ps propagation (dotted line), and using TST (dashed line).
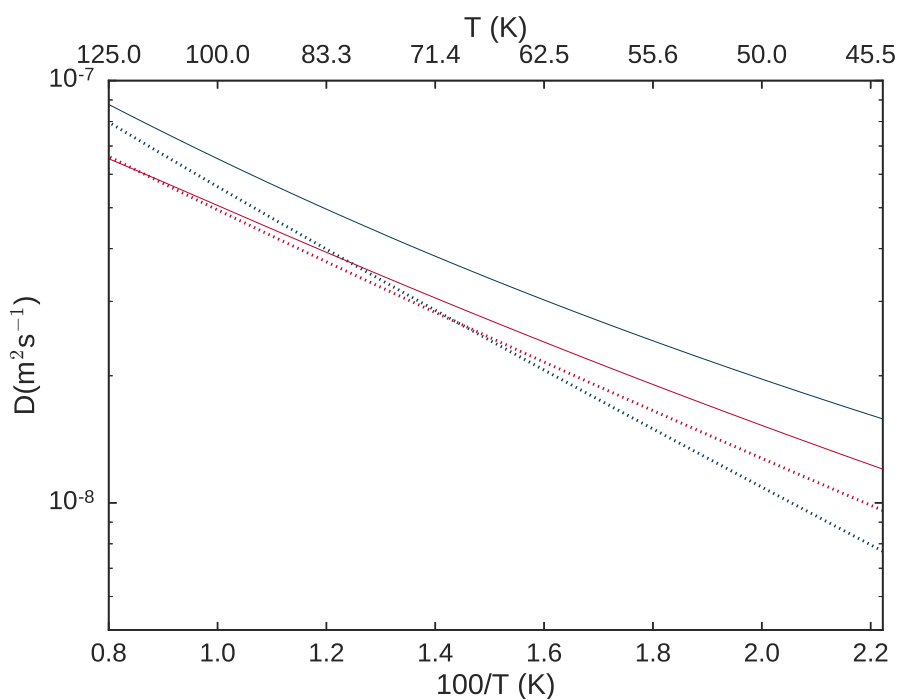

FIGURE 6.9: Diffusion rates for H$_2$ (blue line) and D$_2$ (red line) obtained with converged quantum calculations (solid line) and TST (dotted line).

6.4 **Publication 2:** *Diffusion of H$_2$ and D$_2$ Confined in Single-Walled Carbon Nanotubes: Quantum Dynamics and Confinement Effects*

Diffusion of H₂ and D₂ Confined in Single-Walled Carbon Nanotubes: Quantum Dynamics and Confinement Effects

Manel Mondelo-Martell and Fermín Huarte-Larrañaga*

Department of Materials Science & Physical Chemistry and Institute of Theoretical and Computational Chemistry (IQTCUB), Universitat de Barcelona, 08028 Barcelona, Spain

Ⓢ *Supporting Information*

ABSTRACT: We present quantum dynamics calculations of the diffusion constant of H_2 and D_2 along a single-walled carbon nanotube at temperatures between 50 and 150 K. We calculate the respective diffusion rates in the low-pressure limit by adapting well-known approaches and methods from the chemical dynamics field using two different potential energy surfaces to model the C−H interaction. Our results predict a usual kinetic isotope effect, with H_2 diffusing faster than D_2 in the higher temperature range but a reverse trend at temperatures below 50−70 K. These findings are consistent with experimental observation in similar systems and can be explained by the different effective size of both isotopes resulting from their different zero-point energy.
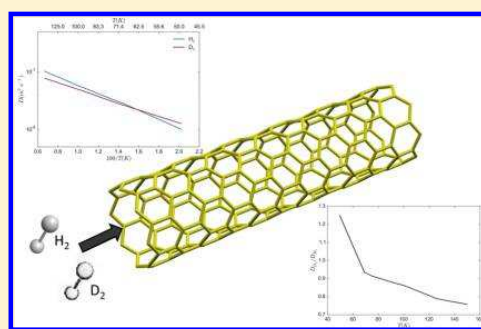
1. INTRODUCTION

Nanostructured materials have received much attention in the last years due to their unique properties in fields such as mechanics, electronics, fluidics, and storage technologies.[1−8] In particular, their suitability as storage devices for small gaseous molecules has comprised a great deal of the research in the field due to its direct environmental impact. For instance, dangerous pollutants or greenhouse effect compounds can be kept off the atmosphere, or clean fuels such as hydrogen can be transported from production to consumption sites, thus spreading its use.[1,9−16] The study of these substrate−gas systems has led to the discovery of quantum confinement effects, distortions of the molecular structure arising from the encapsulation in cavities of the order of the nanometer.[17] These effects have opened a new field of research that tries to understand them to design novel and better storage devices[18−26] and find new technological applications. These applications include isotopic separation of compounds, either by selective adsorption[17,27] or kinetic effects,[28] to nanoconfined tailored reactions.[29−31]

Among all relevant molecules studied in the field of nanomaterial−gas interactions, hydrogen and its isotopologues have been the most studied since the seminal work of Dillon et al.[14] The reason for this is 2-fold: First, there is obvious economical interest in hydrogen, which is regarded as a potential fuel for the near future and is much more efficient and environmentally sustainable than current fossil fuels. However, its low density makes its storage in conventional devices highly inefficient, and this has pushed the research toward the study of novel devices to make the storage and transport feasible (See ref 11 and references therein). Second, hydrogen stands as an interesting molecule itself due to its low mass, which makes quantum effects much more highly noticeable and important

than in the case of heavier atoms. An especially interesting effect appearing when these molecules are confined in nanostructures is the so-called quantum sieving, a large difference in the adsorption properties of two isotopologues due to their different zero-point energy (ZPE). This effect has been posited as a potential separation method between hydrogen and deuterium molecules.[17,27] Inspired by this discovery, several theoretical works have been performed studying the dynamics of a hydrogen molecule in different nanometric cavities such as carbon nanotubes,[23] zeolites,[32] or metal−organic frameworks (MOFs),[21,33] most of them focusing on the study of a rigid molecule with motion confined to a single unit cell of the material. Some of the milestones in the field are the work of Beenakker et al.,[17] which first described the quantum sieving effect, and the work of Lu et al.[23] in which *extreme confinement* is presented. More recently, Bačić and coworkers have made important advances in this field through the use of modern potential energy surfaces to study new systems and compare their results with experimental data,[20,21] thus providing new evidence and explanations of the quantum confinement effects. However, only a few works have considered so far the motion of the molecule along the periodic dimensions of the different nanomaterials at full quantum level, with the two most recent by Skouteris and Laganà[34] and ourselves.[19] The dynamics of the diffusion process are important to explain an additional effect, the kinetic molecular sieving predicted by Kumar and Bhatia[35] and experimentally confirmed by Nguyen et al.[36] and Contescu et al.,[37] which involves a faster diffusion of D_2 in front

of H$_2$ when confined in certain nanostructured materials. This trend, which opposes the usual kinetic isotope effect, could improve the separation of isotopologues. Although the quantum sieving effect on carbon nanotubes has been previously studied by several groups from a stationary point of view,[23,38] focusing on the selective adsorption of D$_2$ in front of H$_2$, a simulation of the actual dynamics of the diffusion in these materials at a quantum level is still missing.

In the present work, we make our first attempt to compute diffusion rates of molecular hydrogen inside a carbon nanotube using quantum dynamics approaches. Although diffusion is known to be one of the processes most affected by quantum confinement effects, full quantum simulations in nanoconfined systems are still missing. On the contrary, diffusion has been theoretically studied on heterogeneous gas-surface systems for a long time, and diffusion rates have been calculated with quantum dynamics methods, which provides a solid theoretical ground for similar studies on nanostructures. These methods range from the development of specific master kinetic equations specific for diffusion processes[39,40] to the adaptation of chemical kinetics formalisms.[41,42] Thus, our work focuses on the rigorous quantum mechanical calculation of the diffusion rate constant for a single hydrogen or deuterium molecule inside an (8,0) single-walled carbon nanotube (SWCNT) through the adaptation of the work of Zhang et al., who successfully reproduced the experimental behavior of a single H atom on a copper surface using a fully quantum-mechanical approach. In addition to this, the comparison of H$_2$ and D$_2$ diffusion rates inside carbon nanotubes could provide some additional insight into the sieving mechanism in other devices such as carbon molecular sieves.

The paper is structured as follows. In the first section the theoretical background of the study is described, including the approach used to calculate diffusion rates, an overview of the flux correlation function formalism, and the calculation of partition functions. Also, a brief discussion on the model of the system and on the calculation method (the multiconfigurational time-dependent Hartree method) is presented. Section 3 is devoted to the discussion of the actual results of the study, focusing on the computed diffusion coefficients. The selectivity factor for the isotopologues' adsorption is also calculated. Our results are summarized in Section 4, where the main conclusions are drawn.

2. THEORETICAL METHODS

2.1. Diffusion Rate Calculation. The process of the diffusion of a gas in a condensed phase, for low temperatures and low concentration of adsorbate, can be described by a hopping model.[43,44] In this model, the diffusion rate $D(T)$ is considered to depend exclusively on the probability of a single-molecule crossing from one binding site i to another binding site j

$$D(T) = (1/2d) \sum_{j \neq i} k_{i \rightarrow j}(T) l_{ij}^2 \tag{1}$$

where $k_{i \rightarrow j}$ is the hopping frequency from site i to j, l_{ij} is the distance between binding sites, and d is the symmetry number of the system. A parallelism between this model of diffusion and a chemical reaction can be established: In both cases we are concerned with the probability to go from a given thermal equilibrium configuration (reactants) to another (products), with both configurations separated by a potential energy barrier.

There are nevertheless differences, one of them being that in diffusion one has several equivalent sites at different distances, while in a chemical reaction one is mainly concerned with one minimum of the potential energy surface (PES). However, as pointed out in ref 43, usually the most important hops occur between adjacent binding sites, and eq 1 can be simplified, obtaining

$$D(T) = (l^2/2d) k_{\text{hop}}(T) \tag{2}$$

The problem of diffusion is then reduced to the calculation of the hopping frequency between two adjacent binding sites, k_{hop}.

Several methods are found in the literature to compute k_{hop}, either classically or using quantum mechanics. Within the classical mechanics framework, molecular dynamics (MD) and grand canonical Monte Carlo (GCMC) provide methods for calculating either k_{hop} or even directly the diffusion rate via velocity correlation functions. Taking advantage of the similarities already outlined between chemical reactions and diffusion, other tools such as transition state theory (TST) can also be used. This latter approach implicitly implies two related approximations: The first one is the nearest neighbor approximation already discussed, and the other is the uncorrelated hopping approximation, which implies that once the substrate crosses the dividing surface it is directly considered as belonging to the product channel. This means, as it is well known, that the TST hopping frequency is an upper bound to the real k_{hop} because no recrossing is allowed. On the contrary, specific models have been proposed to find k_{hop} in the quantum dynamics formalism (see ref 43 and references therein). In the present work we follow the work of Light and coworkers,[41] in which they calculated the hopping frequency using the transition state wave packet method.[45] This approach is based on the use the flux correlation function formalism first introduced by Miller.[46] Even though we will use the same basic concepts, our calculation of k_{hop} will rely on the calculation and propagation of the thermal flux operator eigenstates.

2.2. Description of the System. The model proposed for describing the diffusion of the hydrogen (or deuterium) molecule along a nanotube consists of a full dimensional representation of a single diatomic molecule, confined in the hollow cavity of a rigid (8,0) carbon nanotube made up from the concatenation of 20 unit cells to be able to disregard edge effects. The unit cell's geometry was obtained from a CRYSTAL09[47] optimization using the B3LYP functional and a 6-21G basis set in a periodic model, obtaining a unit-cell length and diameter of 8.07 and 12.08 bohrs, respectively. Although the interaction between the structure phonons and the diffusion is known to be an important factor in diffusion,[43,44] we consider that the frozen structure model is a reasonable assumption for a first approach to the problem.

The system's Hamiltonian is therefore a 6D operator with the form

$$\hat{H}_{6D} = -\frac{\hbar^2}{2\mu_{H_2}} \left(\frac{\partial^2}{\partial \rho^2} + \frac{2}{\rho} \frac{\partial}{\partial \rho} + \frac{1}{\rho^2} \frac{\partial^2}{\partial \theta^2} + \frac{1}{\rho^2} \frac{1}{\sin^2 \theta} \frac{\partial^2}{\partial \phi^2} \right)$$
$$- \frac{\hbar^2}{2m_{H_2}} \left(\frac{\partial^2}{\partial x^2} + \frac{\partial^2}{\partial y^2} + \frac{\partial^2}{\partial z^2} \right) + \hat{V}(\rho, \theta, \phi, x, y) \tag{3}$$

where ρ stands for the internuclear distance between the atoms in the diatomic molecule, θ and ϕ represent, respectively, the polar and azimuthal angles of the molecular axis with respect to

The Journal of Physical Chemistry A

the nanotube's axis, and x, y, and z are the coordinates of the center of mass of the molecule, where z is coincident with the nanotube's axis. The 6D PES is given by a sum of Lennard-Jones (LJ) pair interaction terms between the carbon and the hydrogen (or deuterium) atoms to represent the dispersion forces and a Morse potential to take into account the covalent bond in the molecule

$$\hat{V}_{6D} = V_{H-H}(\rho) + V_{C-H}(\rho, \theta, \phi, x, y, z) \tag{4}$$

$$\hat{V}_{C-H}(\rho, \theta, \phi, x, y, z) = \sum_{i=1}^{2} \sum_{j=1}^{NC} V_{i,j}^{LJ}(d_{H_i - C_j}) \tag{5}$$

The parameters used to model the covalent interaction are well known (D_e = 0.1746 hartree, a = 1.0271 bohr^{-1}, and R_e = 1.4 bohrs). Instead, several sets of LJ parameters have been used in the past to model the C−H interactions in a nanotube. Among the available LJ parameters, we have first selected a set used by us in our recent work,[18,22,48] with σ = 2.82 Å and ϵ = 0.0605 kcal/mol (this potential will referenced as ref 48 PES). Additionally, motivated by the large differences between the different potentials reported by Garberoglio et al.,[38] we have also used a second potential for our calculations. We have chosen the Frankland−Brenner potential, with σ = 3.08 Å and ϵ = 0.0549 kcal/mol (FB PES). This potential was employed in refs 23 and 38, predicting a remarkable quantum sieving.

Relaxed projections of the two potential energy surfaces used in the present work are shown in Figure 1. The FB PES presents a tighter profile on the x dimension, which is consistent with the higher barriers for both rotation (θ) and diffusion (z). This feature suggests a slower diffusion when using the FB PES rather than the ref 48 PES. Note, however, the energy scale of the potential energy cut along the z coordinate, which is on the order of a few millielectronvolts.

2.3. Flux Correlation Functions and Direct Rate Constant Calculation. The methodology used to calculate the hopping frequency in this work is explained in the present section. Note that atomic units are assumed throughout this section. For a complete discussion on the method in the context of chemical reactions, the reader is referred to ref 49.

The general expression for a reaction rate is given as a Boltzmann thermal average of its cumulative reaction probability (CRP), $N(E)$

$$k(T) = \frac{1}{2\pi Q_r(T)} \int_{-\infty}^{\infty} dE \, e^{-E\beta} N(E) \tag{6}$$

with β = $1/k_B T$. The calculation of this quantity through direct dynamics methods is based on the correlation function formalism introduced by Miller and coworkers.[46,50] In the present work we use the approach by Matzkies and
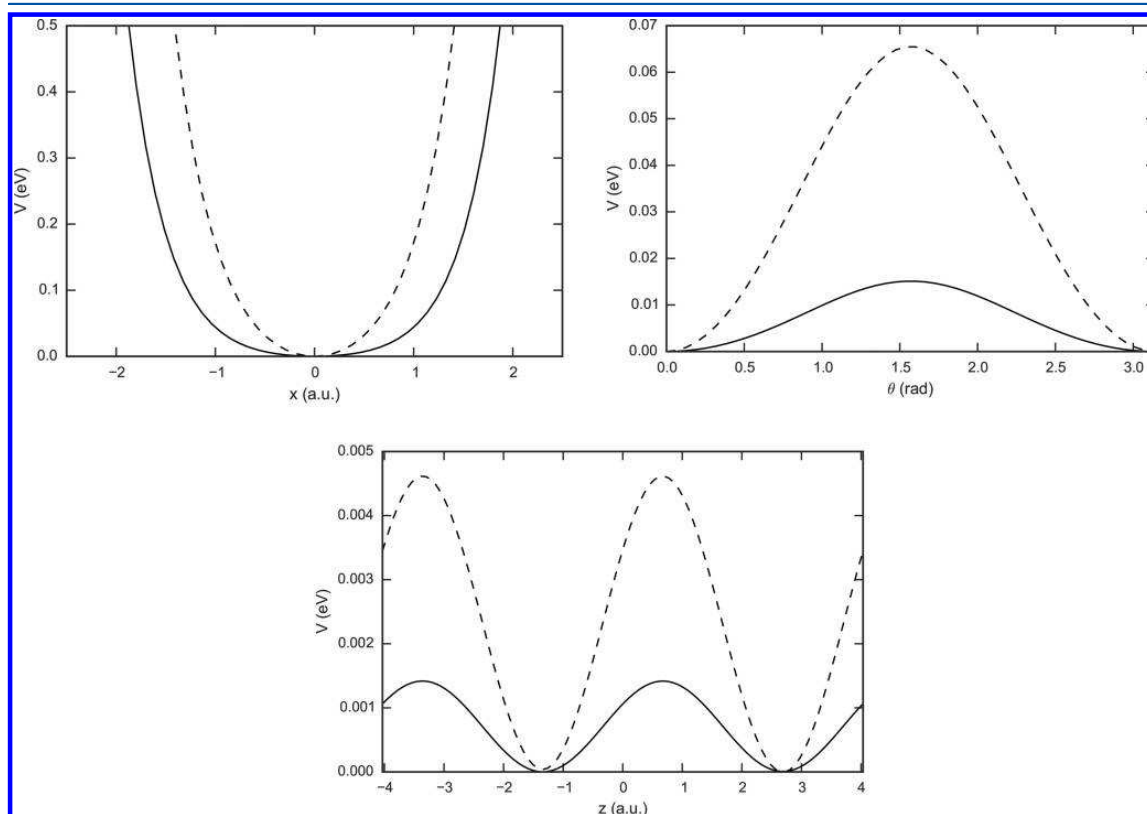

Figure 1. Relaxed projection of the ref 48 (solid) and FB (dashed) potential energy surfaces along the x (top left), θ (top right), and z (bottom) DOFs.

The Journal of Physical Chemistry A   Article

Manthe,[51,52] where the cumulative reaction probability is obtained as

$$N(E) = \frac{1}{2} e^{\beta E} \sum_{f_{T_0}} f_{T_0} \int_{-\infty}^{\infty} dt \int_{-\infty}^{\infty} dt' \, e^{iEt} e^{-iEt'} \langle f_{T_0} | e^{i\hat{H}t'} \hat{F} e^{-i\hat{H}t} | f_{T_0} \rangle$$

(7)

or, alternatively, as

$$N(E) = \frac{1}{2} e^{\beta E} \sum_{f_{T_0/2}} \sum_{f'_{T_0/2}} f_{T_0} f'_{T_0} \left| \int_{-\infty}^{\infty} dt \, e^{iEt} \langle f_{T_0/2} | e^{i\hat{H}t} | f'_{T_0/2} \rangle \right|^2$$

(8)

In eqs 7 and 8, f_{T_0} and $|f_{T_0}\rangle$ stand, respectively, for the eigenvalues and eigenstates of the thermal flux operator, $\hat{F}_{T_0} = e^{-\beta\hat{H}/2} \hat{F} e^{-\beta\hat{H}/2}$, and $\hat{F}$ is, in turn, the flux operator, defined as

$$\hat{F} = i[h, \hat{H}]$$

(9)

where $\hat{H}$ is the system's Hamiltonian and h is a Heaviside function, which separates reactants from products. Note that in eq 8 the reference temperature of the thermal flux operator is divided by a factor of 2. This equation may be used when the same flux operator is employed to obtain the flux eigenstates and analyze their propagation, and it implies that for a value of $\beta = 1/kT_0$ we obtain information for temperatures equivalent to $T_0/2$. Regarding the Heaviside function, because we do not have a real chemical reaction but a diffusion process, the dividing surface is placed at a value of the diffusion coordinate corresponding to a saddle point of the PES separating two neighbor unit cells. Hence, we arbitrarily define the geometries at one side of this dividing surface as reactants, and the remaining as products. Then, to take into account diffusion on both directions, we must multiply $k(T)$ by a factor of 2 to obtain the hopping frequency k_{hop}.

Equation 9 can be rewritten in terms of the flux–flux correlation function, $C_{ff}(t, t') = \sum_{f_{T_0}} f_{T_0} \langle f_{T_0} | e^{i\hat{H}t'} \hat{F} e^{-i\hat{H}t} | f_{T_0} \rangle$

$$N(E) = \frac{1}{2} e^{\beta E} \int_{-\infty}^{\infty} dt \int_{-\infty}^{\infty} dt' \, e^{iEt} e^{iEt'} C_{ff}(t, t')$$

(10)

This quantity and its time integral, the flux-position correlation function, C_{fp}, are central because their shape and limits can be used as convergence criteria for the computation of $N(E)$. In our case, the following scheme has been used to compute a hopping frequency for a diffusion problem

1. Set a dividing surface at a maximum of the PES along the diffusing coordinate (the nanotube's axis).
2. Calculate the eigenstates of the thermal flux operator on this dividing surface at a given reference temperature, $|f_{T_0}\rangle$.
3. Propagate the eigenstates and Fourier transform the matrix elements of the flux operator to obtain the CRP. In this step, each flux eigenstate contribution is weighted by its corresponding degeneracy number depending on its rotational parity and whether it is D$_2$ or H$_2$.
4. Obtain the hopping frequency by thermal averaging of $N(E)$.

In the present work all of these steps are carried out using the state-averaged multiconfigurational time-dependent Hartree (SA-MCTDH) method by Manthe[53] using the Bielefeld MCTDH software package, which is briefly discussed in Section 2.5.

2.4. Partition Function Calculation. Once the CRP is obtained, according to eq 6, the second term needed to calculate a rate constant is the reactant partition function, $Q(T)$. To compute this term we have relied on the assumption of separability of this system[19] into a 1D *diffusing* degree of freedom (DOF) and a set of five confined DOFs

$$Q(T) = q_{dif}(T) q_{con}(T)$$

(11)

The diffusing term in eq 11 is then evaluated following the standard quasiclassical approximation for translational motion

$$q_{dif} = \left(\frac{2\pi m k_B T}{h^2} \right)^{1/2} L$$

(12)

where L is the length of the unit cell of the nanotube.

The calculation of the $q_{con}(T)$ can be carried out either with a semiclassical or a fully quantum approach. Even though the semiclassical approximation is usually considered accurate enough for diatomic molecules, either free or adsorbed on surfaces, for a confined system it is not clear whether this model is reliable enough. For instance, the model relies on the full separability of all the DOFs, which is known to be too harsh an assumption on nanoconfined systems.[18,22,23] For this reason, q_{con} is actually calculated as the trace of the Boltzmann operator of the confined 5D Hamiltonian, $\hat{H}_{con}(\rho, \theta, \phi, x, y)$. This operator is equivalent to the one in eq 3, but fixes the position along z at -1.36 bohr, corresponding to an energy minimum. To take into account the total symmetry of the system with respect to particle exchange, the eigenstates of $\hat{H}_{con}$ are classified according to their rotational parity and multiplied by the corresponding degeneracy number

$$q_{conf} = g_e \sum_{\forall n} e^{-\beta E_n^e} + g_o \sum_{\forall n} e^{-\beta E_n^o}$$

(13)

where E_n^e and E_n^o stand, respectively, for the energies of the eigenstates with even and odd parity with respect to rotation, placing the energy origin at the bottom of the PES. As discussed in the Results section, a comparison between the semiclassical and quantum partition functions reveals a difference of several orders of magnitude, so the use of the latter is fully justified in the present context.

2.5. MCTDH. As mentioned above, the SA-MCTDH method has been employed in the thermal flux eigenstate calculation and corresponding time propagation. In the standard MCTDH method,[54] a single wave function is represented as a sum of configurations *Ansatz* with the form

$$\Psi(Q_1, ..., Q_p, t) = \sum_{j_1=1}^{n_1} \cdots \sum_{j_p=1}^{n_p} A_{j_1 \cdots j_p}(t) \prod_{k=1}^{p} \varphi_{j_k}^{(k)}(Q_k, t)$$

(14)

where each degree of freedom (DOF) k is represented by a set of low-dimensional time-dependent basis functions $\varphi_{j_k}^{(k)}$ known as single particle functions (SPFs). These SPFs are, in turn, represented on a time-independent (primitive) basis set, usually consisting on DVR or FFT grids, thus giving rise to the two-layer representation of the total wave function, which is behind the outstanding numerical efficiency of the MCTDH algorithm. The propagation is then carried out by integration of a set of coupled equations of motion derived from the Dirac−Frenkel variational principle.

The state-averaged multiconfigurational time-dependent Hartree (SA-MCTDH) is a modification of the MCTDH method

Article

Table 1. Quantum Dynamics of H$_2$ Confined in a (8,0) SWCNT at 150 K and Using Ref 48 PES[a]

| DOF | number of SPFs | | primitive grid | | |
	eigenstates	propagation	number points	type	range
ρ	2	2	32	FFT	0.5−5.0 a_0
θ	5	5	64	cot-DVR	0−π/2
ϕ	7	7	64	FFT	0−2π
x	3	4	32	FFT	−3.5−3.5 a_0
y	3	4	32	FFT	−3.5−3.5 a_0
z	2	6	256	FFT	−28.033−28.033 a_0

[a]Basis set and grid MCTDH representation for the calculation of thermal flux eigenstates and time propagation.
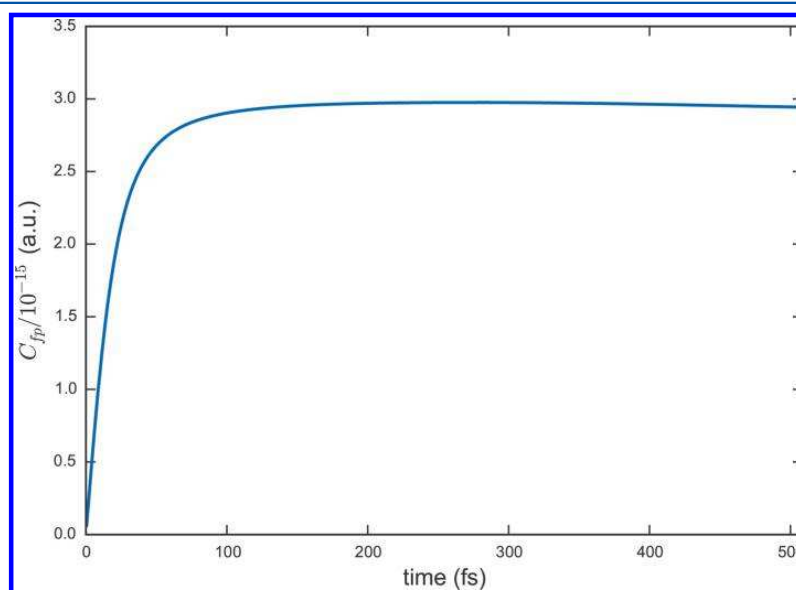
Figure 2. Total flux-position correlation function for the diffusion of H$_2$ along an (8,0) carbon nanotube at T = 150 K using the ref 48 PES.

that represents a set of wave functions using a common SPFs set, which adapts at each time step to provide the best basis for the *average* of the wave functions represented. This means that more SPFs will be needed than if the wave functions were represented independently but has the advantage that the effort to propagate a set of wave functions is then roughly independent of the number of wave functions in the set. Moreover, overlap operations between these functions are straightforwardly performed because they do not require projections on the SPF basis. This advantage is exploited to calculate eigenstates of general operators by iterative diagonalization, and it has been effectively used in high dimension systems.[55]

2.6. Simulation Details. Three kinds of calculation were needed to obtain the diffusion rates for either the H$_2$ or D$_2$: (1) calculation of the 5D Hamiltonian eigenstates at a minimum of the PES to compute the reactant partition function, (2) calculation of the thermal flux operator eigenstates with a dividing surface set at a maximum of the PES and, finally (3) the propagation of the latter for a time long enough to ensure convergence of the results. To be able to span a large temperature range, the thermal flux eigenstates were calculated and propagated for three different reference temperatures, namely, 75, 100, and 150 K, so a total of seven calculations were carried out on each PES. The wave function representation parameters (number of SPFs, primitive functions, and grid

parameters for each degree of freedom) were employed for the calculation and propagation of the thermal flux eigenstates at 150 K for the hydrogen molecule using the ref 48. PES are found in Table 1. The details regarding the numerical convergence and the basis used for the remaining calculations are given in the Supporting Information. Note that the primitive grid is maintained in all sets of thermal flux eigenstates calculation and propagation, but the number of SPFs changes. This is particularly noticeable in the z coordinate, associated with the diffusion motion. A complex absorbing potential (CAP) was placed at both edges of the z coordinate grid, with a length of 9 bohr, to avoid aliasing during the propagation step.

It is worthwhile to point out that the grid on the z coordinate is large. This is done to allow a good description of the dynamics before the wave packet is absorbed by the CAP. This differs from the work in ref 41, where the CAP was placed just in the first minimum after the dividing surface, thus making an uncorrelated hopping approximation somewhat equivalent to a classical TST.

3. RESULTS AND DISCUSSION

The calculation of the 50 eigenstates for the H$_2$ molecule, using the ref 48 PES at a reference temperature of 150 K, required 10 h of calculation in a 32-core Intel Xeon E5-4620 0 @ 2.20 GHz processor, while 9 h was needed for D$_2$ under the same conditions.
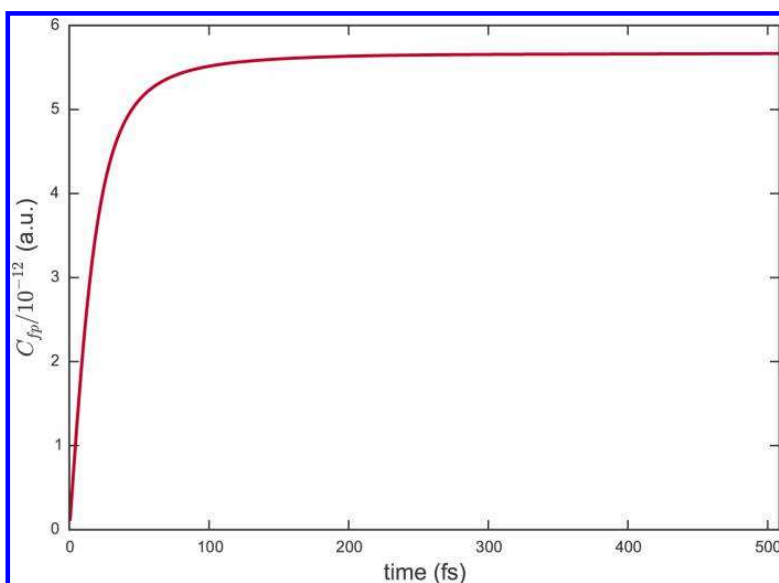
Figure 3. Total flux-position correlation function for the diffusion of D₂ along an (8,0) CNT at T = 150 K using the ref 48 PES.
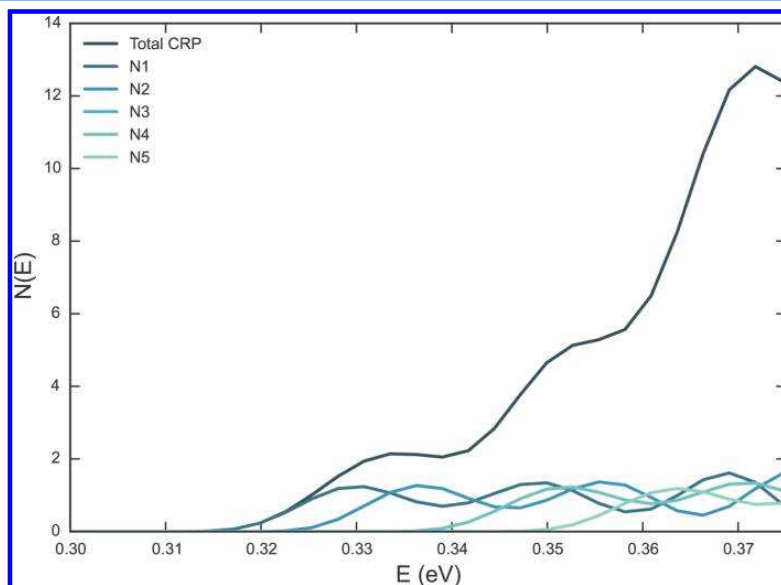

Figure 4. Total (darkest) and the five lower-energy individual reaction probabilities for the diffusion process of H₂ along an (8,0) carbon nanotube at a reference temperature of 150 K using the ref 48 PES. Symmetry numbers due to the rotational parity of H₂ are not taken into account in the curves.

With this number of eigenstates, the last (50th) eigenvalue was, in all cases, at most 5 orders of magnitude smaller than the first one. This guarantees that all relevant flux contributions were taken into account for the calculation of $N(E)$. The subsequent propagation of these flux eigenstates for 500 fs took 105 h for H₂ and 76 h for D₂ in the same machine for a reference temperature of 150 K. Similar times were required for the calculation carried out under the remaining reference temperatures and with the FB PES.

For the sake of clarity, we focus the following discussion on the results obtained using the ref 48 PES. The detailed results

corresponding to the FB PES can be found in the Supporting Information, and here only the final diffusion coefficients and selectivities will be discussed.

The flux-position correlation function obtained for the H₂ diffusion simulation at T = 150 K is shown in Figure 2. Note that a plateau is reached at ∼200 fs, although a small decrease can be observed after 300 fs. This could be due to recrossing effects at very large times, but nevertheless we consider that the function is smooth enough to obtain relevant information. On the contrary, C_{fp} for the deuterium molecule in the same conditions is shown in Figure 3. Note the difference in scale
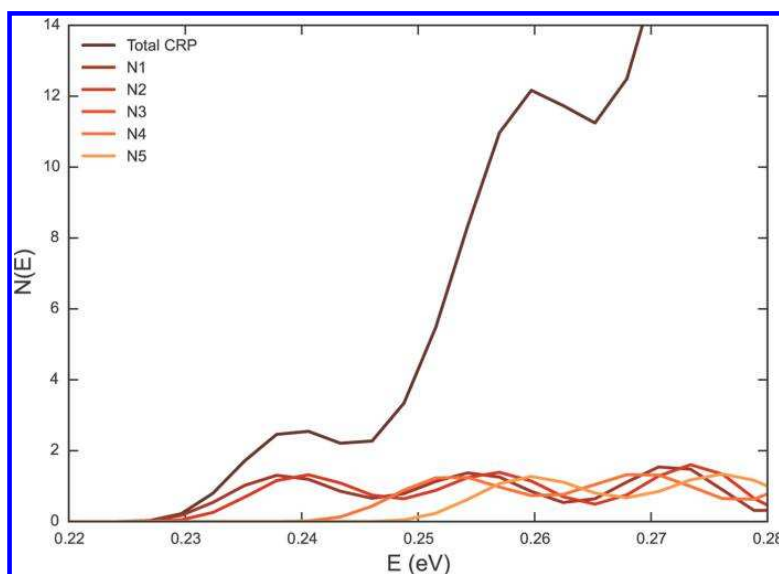
Figure 5. Total (darkest) and the five lower-energy individual probabilities for the process of diffusion of D_2 inside an (8,0) carbon nanotube at a reference temperature of 150 K using ref 48 PES. Symmetry numbers due to the rotational parity of D_2 are not taken into account in the curves.

between both figures, with the flux-position correlation function for D_2 being three orders of magnitude larger than the one for H_2. In this case there is no sign of decreasing of the function, which remains flat at $t > 200$ fs.

A Fourier transform of the flux−flux correlation function yields the cumulative reaction probability, $N(E)$ (see eq 7). This function is plotted as a function of the total energy for the hydrogen and deuterium systems in Figures 4 and 5, respectively. The total cumulative reaction probability, in the darkest color at each figure, increases gradually starting from a certain energy threshold. At first glance a higher energy threshold is identified in the case of H_2 diffusion with respect to D_2. However, given the low-energy barrier (11 cm^{-1} in ref 48 PES and 37 cm^{-1} in FB PES) the different energy threshold observed in the CRP plots can be mainly attributed to the different ZPE of the reactants (2534 cm^{-1} ∼ 0.31 eV for H_2 and 1820 cm^{-1} ∼ 0.22 eV for D_2 in the ref 48 PES). Nevertheless, calculating the adiabatic energy barrier (i.e., considering the ZPE of both reactant and activated complex) reveals that this quantity is slightly higher in the case of H_2 (58 cm^{-1}) than in the case of D_2 (45 cm^{-1}). This difference in the adiabatic energy barrier can be related to the different vibrational amplitude of both isotopologues' wave function. A smaller vibrational amplitude for D_2 (lower ZPE) compared with that of H_2 results in a less corrugated potential for the heavier molecule as it diffuses along the nanotube. A similar reasoning has been employed by Kumar and Bhatia when studying the quantum confinement effects affecting H_2 and D_2 adsorption and diffusion inside a ρ zeolite.[35]

Another difference between both systems is the rate of increase in $N(E)$, which is steeper for D_2 than for H_2. This issue can be explained by decomposing the total CRP into individual probabilities resulting from the flux eigenpairs contributing to the process (25 in this case). In the Figures, the individual contribution corresponding to the first five flux eigenstates is depicted together with the CRP, showing the reason for the different pattern between both isotopologues: The density of

states participating in deuterium is much larger than that in hydrogen, thus explaining the faster increase in the total CRP. The individual contributions oscillate around a probability of ∼1, which may be an indication of recrossing effects. It must be pointed out that these contributions are not weighted by the ortho/para symmetry degeneration numbers. The CRPs obtained at the three reference temperature values sampled are essentially the same, as can be seen in Figures 6 and 7. In these Figures the total $N(E)$ is shown for
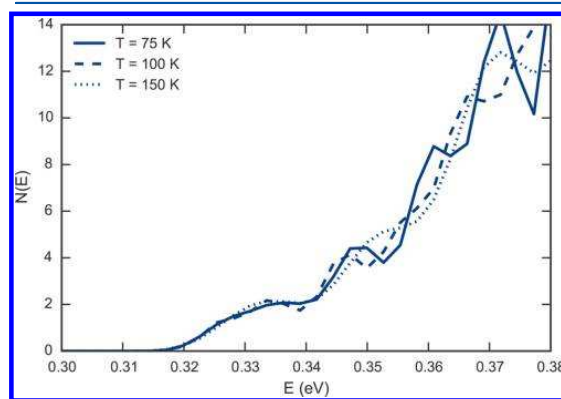

Figure 6. CRP for the $H_2@(8,0)$ system at the different temperatures sampled: $T = 75$ (solid line), 100 (dashed line), and 150 K (dotted line). Symmetry numbers due to the rotational parity of H_2 are not included.

the three values of β. Note, however, that the oscillations in the CRP at high energies are more important for the calculation employing a lower reference temperature, which indicates an increasing numerical error. This is the reason why several reference temperatures must be sampled to span a larger temperature interval.
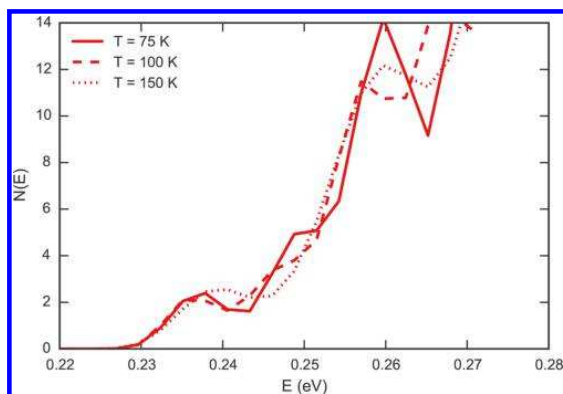
Figure 7. CRP for the D$_2$@(8,0) system at the different temperatures sampled: $T = 75$ (solid line), 100 (dashed line), and 150 K (dotted line). Symmetry numbers due to the rotational parity of D$_2$ are not included.

The partition functions were initially calculated using both a semiclassical and a quantum approach. The results obtained with both methodologies were not consistent, with differences of several orders of magnitude in their values even at low temperatures. This fact can be explained by the different ZPE resulting from both approaches: To calculate a semiclassical partition function, one relies on the full separability of the system. Considering this assumption, the total ZPE is the sum of the vibrational ZPE and the ZPE appearing due to the confining potential in x and y, which, in our case, is modeled as a harmonic oscillator. However, as it is seen in Figure 1, the potential along x and y is significantly anharmonic. In addition to this, as it was reported by one of us,[22] the coupling between the rotational and translational degrees of freedom has a relevant

effect on the ZPE of a nanoconfined system. These differences are enough to significantly change the value of the partition function at low temperatures, and for this reason only the results obtained with the quantum approach are shown hereafter.

After thermal averaging of the CRP to obtain the hopping probability, diffusion rates are obtained for both H$_2$ and D$_2$ according to eq 1. The results are shown in Figure 8 as an Arrhenius plot. The data obtained at three reference temperatures using eqs 7 and 8 is merged to span a broader temperature range from 50 to 155 K. No attempt has been made to go below this temperature because it is expected that intermolecular interactions become increasingly important below this point. Additionally, the same diffusion rates have been calculated using TST, obtaining similar results to those calculated by rigorous quantum dynamics. The TST results can be found in the Supporting Information (SI).

Similarly to what has just been discussed, we have computed the corresponding partition functions, CRPs, and hopping frequencies for the self-diffusion of H$_2$ and D$_2$ along an (8,0) CNT using the FB potential. Detailed results are available in the SI, and the final diffusion coefficient values are shown in Figure 8. Concerning the intermediate data (SI), we would like to mention that there are noticeable differences between the CRPs obtained from both surfaces, presenting a slightly larger energy threshold and a much lower density of states in the case of the FB potential. Nevertheless, the final diffusion rates obtained with both PES are comparable, with a difference of less than an order of magnitude. This seems to imply that even though the PES affects the calculation of the CRP and the partition functions, the effects compensate one another, thus providing a similar final result.

The activation energy for the diffusion process is estimated from the slope of the diffusion constant values plotted in Figure 8. The calculated values, shown in Table 2, show that this activation
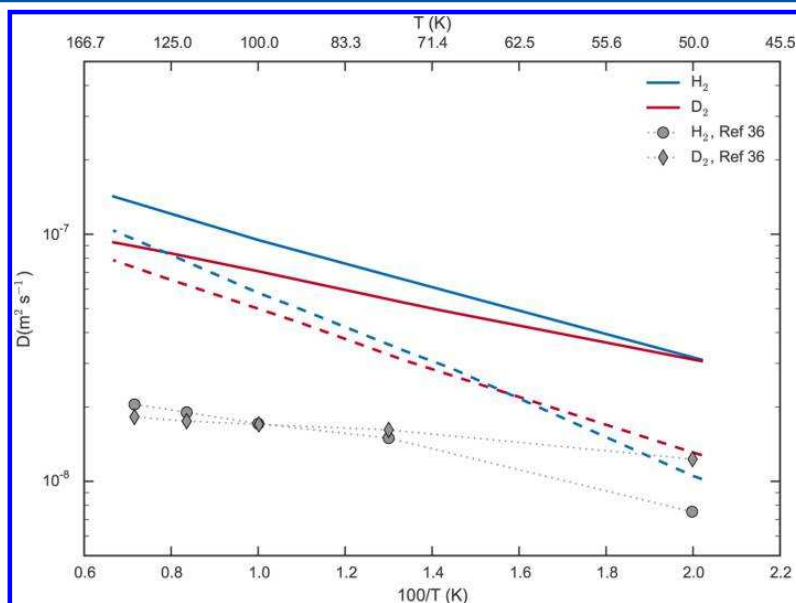

Figure 8. Calculated diffusion rates for hydrogen (blue) and deuterium (red) along an (8,0) carbon nanotube for ref 48 (solid) and FB (dashed) PES. The data obtained using different reference temperatures of 75, 100, and 150 K are combined to span the 50−155 K temperature range. Gray markers correspond to the experimental H$_2$/D$_2$ diffusion data in a CMS, extracted from ref 36.

Table 2. Activation Energies, in cm^{-1}, for the Diffusion of H$_2$ and D$_2$ inside an (8,0) CNT for the Two PESs Employed

	ref 48 PES	FB PES
H$_2$	77	107
D$_2$	60	94

energy is higher for H$_2$ than for D$_2$ for both PESs studied. This supports our discussion on the reaction probability plots and the corresponding adiabatic energy barriers. As a consequence of this difference in E_a, a reverse kinetic isotope effect appears at low temperatures; that is, even though at high temperatures H$_2$ diffuses faster than D$_2$, at a certain point in the cold temperature range, this trend is inverted and D$_2$ starts to diffuse faster than H$_2$. This point is located at ~50 K for the ref 48 PES and at ~62 K for the FB PES. At the lowest temperature reached by our calculations, deuterium diffusion rate is just slightly larger than hydrogen's, but the difference is expected to increase at even lower temperatures. To illustrate this effect, we plot the ratio of diffusion rates (D_{D_2}/D_{H_2}) in Figure 9 as a function of temperature for both PES objects of study. This function evidences an increasingly faster D$_2$ diffusion with respect to H$_2$ as the temperature is lowered, until for temperatures below 60−50 K the ratio is inverted. The effect is particularly more noticeable in the case of the FB-PES. This trend is consistent with the experimental diffusion rates obtained by Nguyen et al. in a Takeda 3A carbon molecular sieve (CMS).[36] The experimental data are shown in Figure 8 only for qualitative comparison purposes. Comparing the results obtained on both ref 48 and FB PESs, the larger sieving effects and the higher temperature at which the inversion of the diffusion rates ratio takes place are consistent with the fact that the potential energy barrier is ~4 times larger in the FB PES than in the ref 48. Despite the quantitative differences, the fact that two inherently different systems such as a CMS and an SWCNT present such a similar qualitative behavior regarding the diffusion of H$_2$ and D$_2$ is promising for the development of new molecular sieves taking advantage of the kinetic separation.

At this point it is interesting to consider again the selective adsorption mentioned in the Introduction. The quantum sieving effect between isotopologues has been traditionally related with the selective adsorption of the heavier species (D$_2$) over the lighter (H$_2$) due to the difference in ZPE for both species.[17,23,38] This magnitude is represented by the selectivity factor, S_0, defined as a ratio of equilibrium constants for the adsorption process of both species implicated

$$S_0(2/1) = \frac{K_2}{K_1} = \frac{Q_{ads,2} Q_{free,1}}{Q_{ads,1} Q_{free,2}} \tag{15}$$

We have calculated this quantity using our partition functions as explained before. The resulting selectivity factor is shown in Figure 10 for the both ref 48 (top panel) and FB PESs (bottom panel). The latter is compared with the results from ref 23 on the same PES. Note that there is a significant difference between both PESs, with the FB-PES predicting a larger adsorption selectivity. This finding was also reported by Garberoglio et al. in ref 38. Focusing on the FB potential, our S_0 is in good agreement with the one reported by Lu et al. The difference at lower temperatures can be related with the different Hamiltonian model used: While they considered a 4D Hamiltonian, freezing the internuclear distance, we treat all DOFs, thus allowing all couplings to appear. Additionally, the slightly different structure of our optimized nanotube with respect to the one used in previous works may lead to subtle changes in the global PES, further explaining the differences between our calculations.

4. SUMMARY AND CONCLUSIONS

In the present work we have calculated the diffusion constant for two isotopologues of molecular hydrogen (H$_2$ and D$_2$) inside a SWCNT using, for the first time, full-dimensional quantum dynamics methods within the single hopping and rigid structure approximations. Two different sets of LJ parameters have been used to model the H−C interaction potential. The diffusion constants obtained by quantum dynamics are similar regardless of the PES used, even though the electronic barriers
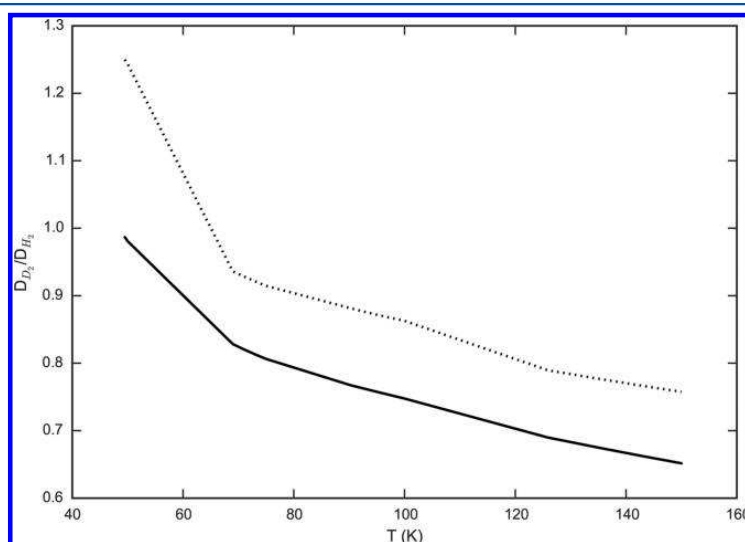
Figure 9. Ratio between the diffusion rates of D$_2$ and H$_2$ inside an (8,0) carbon nanotube calculated using ref 48. PES (solid line) and the FB PES (dotted line).
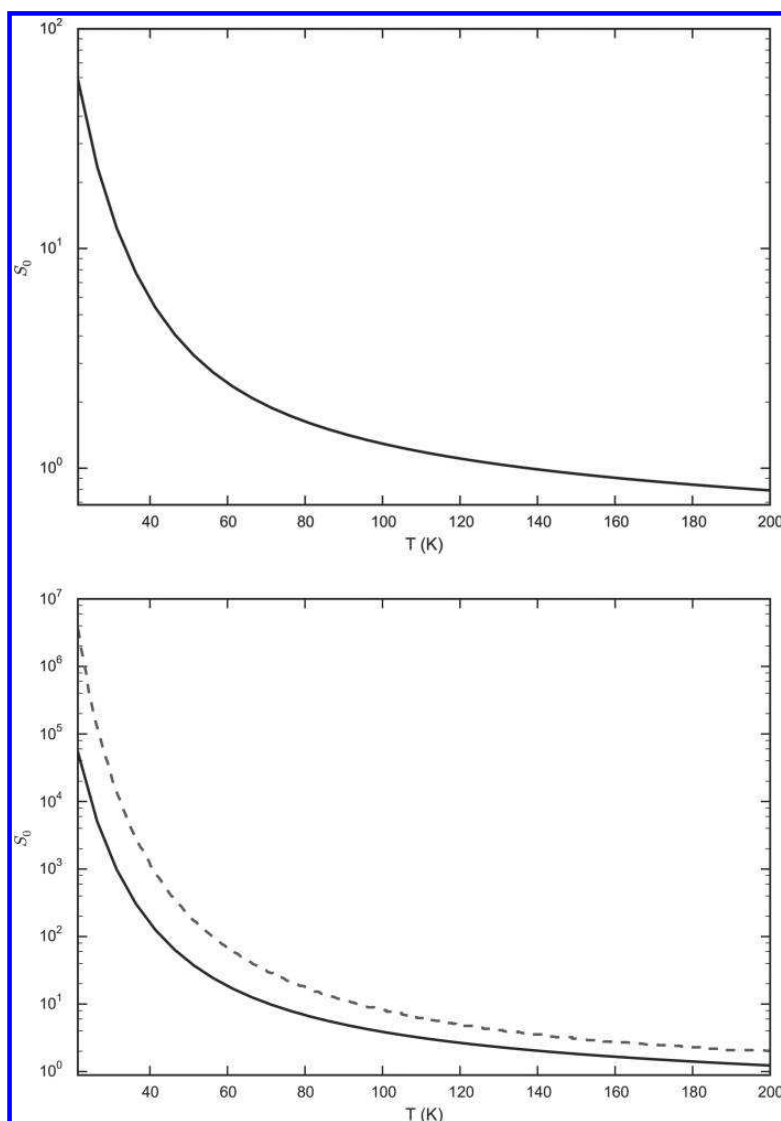
Figure 10. Selectivity factor, S_0, as a function of temperature for the ref 48 (upper panel) and the FB (lower panel) PES. The latter coincides greatly with the one obtained by Lu et al.[23] (dashed line).

for diffusion differ by a factor of 4. The general trend is a faster self-diffusion of H$_2$ in front of D$_2$ at high temperatures, with this tendency being inverted below 60 K. This difference can be explained in terms of the activation energy, which is higher for hydrogen, in part due to its larger effective size resulting from a higher ZPE.

It is also found that the computed diffusion rates qualitatively agree with experimental results obtained in carbon molecular sieves,[36] even though CMS and CNTs are not strictly comparable systems due to their different structures. The FB PES gives results more similar to experimental data obtained in similar nanostructured materials, which suggests that this potential parameters might be more reliable. We do reproduce previously reported quantum sieving effects in the selectivity factor, S_0, showing a preferred adsorption of D$_2$ with respect to H$_2$.

The full quantum dynamics formalism used here provides reliable results and gives insight into the diffusion process of light molecules and its isotopologues with valuable detail. Investigation should now be focused on the improvement of the interaction model between the nanotube and the confined molecule to see further effects.

■ ASSOCIATED CONTENT

ⓢ Supporting Information

The Supporting Information is available free of charge on the ACS Publications website at DOI: 10.1021/acs.jpca.6b00467.

Numerical details regarding the convergence of the different sets of calculations performed. Intermediate results obtained for the Frankland−Brenner potential. Final results obtained by transition state theory. (PDF)

AUTHOR INFORMATION

Corresponding Author

*E-mail: Fermin.huarte@ub.edu. Phone: +34 93 4031341. Fax: +34 93 4021231.

Notes

The authors declare no competing financial interest.

This paper was originally submitted for the Piergiorgio Casavecchia and Antonio Laganà Festschrift, "Forty Years of Crossed Molecular Beams and Computational Chemical Dynamics at Perugia: A Festschrift for Piergiorgio Casavecchia and Antonio Laganà", published as the July 14, 2016, issue of *J. Phys. Chem. A* (Vol. 120, No. 27).

REFERENCES

(1) Ioannatos, G. E.; Verykios, X. E. H_2 Storage on Single- and Multi-Walled Carbon Nanotubes. *Int. J. Hydrogen Energy* **2010**, *35*, 622−628.

(2) Ren, X.; Chen, C.; Nagatsu, M.; Wang, X. Carbon Nanotubes as Adsorbents in Environmental Pollution Management: A Review. *Chem. Eng. J.* **2011**, *170*, 395−410.

(3) Gibson, R. F.; Ayorinde, E. O.; Wen, Y.-F. Vibrations of Carbon Nanotubes and their Composites: A Review. *Compos. Sci. Technol.* **2007**, *67*, 1−28.

(4) Santamaría-Holek, I.; Reguera, D.; Rubi, J. M. Carbon-Nanotube-Based Motor Driven by a Thermal Gradient. *J. Phys. Chem. C* **2013**, *117*, 3109−3113.

(5) Jain, P. K.; Huang, X.; El-Sayed, I. H.; El-Sayed, M. A. Noble Metals on the Nanoscale: Optical and Photothermal Properties and Some Applications in Imaging, Sensing, Biology, and Medicine. *Acc. Chem. Res.* **2008**, *41*, 1578−1586.

(6) Aricò, A. S.; Bruce, P.; Scrosati, B.; Tarascon, J.-M.; van Schalkwijk, W. Nanostructured Materials for Advanced Energy Conversion and Storage Devices. *Nat. Mater.* **2005**, *4*, 366−377.

(7) Wang, J. Carbon-nanotube Based Electrochemical Biosensors: A Review. *Electroanalysis* **2005**, *17*, 7−14.

(8) Eijkel, J. C. T.; van den Berg, A. Nanofluidics: What Is It and What Can We Expect from It? *Microfluid. Nanofluid.* **2005**, *1*, 249−267.

(9) Millward, A. R.; Yaghi, O. M. Metal-Organic Frameworks with Exceptionally High Capacity for Storage of Carbon Dioxide at Room Temperature. *J. Am. Chem. Soc.* **2005**, *127*, 17998−9.

(10) Fatemi, S.; Vesali-Naseh, M.; Cyrus, M.; Hashemi, J.; et al. Improving CO_2/CH_4 Adsorptive Selectivity of Carbon Nanotubes by Functionalization with Nitrogen-Containing Groups. *Chem. Eng. Res. Des.* **2011**, *89*, 1669−1675.

(11) Schlapbach, L.; Züttel, A. Hydrogen-Storage Materials for Mobile Applications. *Nature* **2001**, *414*, 353−358.

(12) Cheng, H.-M.; Yang, Q.-H.; Liu, C. Hydrogen Storage in Carbon Nanotubes. *Carbon* **2001**, *39*, 1447−1454.

(13) Morris, R. E.; Wheatley, P. S. Gas Storage in Nanoporous Materials. *Angew. Chem., Int. Ed.* **2008**, *47*, 4966−4981.

(14) Dillon, A. C.; Jones, K. M.; Bekkedahl, T. A.; Kiang, C. H.; Bethune, D. S.; Heben, M. J. Storage of Hydrogen in Single-Walled Carbon Nanotubes. *Nature* **1997**, *386*, 377−379.

(15) Atwood, J. L.; Barbour, L. J.; Jerga, A. Storage of Methane and Freon by Interstitial Van der Waals Confinement. *Science (Washington, DC, U. S.)* **2002**, *296*, 2367−2369.

(16) Mueller, U.; Schubert, M.; Teich, F.; Puetter, H.; Schierle-Arndt, K.; Pastré, J. Metal-Organic Frameworks−Prospective Industrial Applications. *J. Mater. Chem.* **2006**, *16*, 626−636.

(17) Beenakker, J.; Borman, V.; Krylov, S. Molecular Transport in Subnanometer Pores: Zero-Point Energy, Reduced Dimensionality and Quantum Sieving. *Chem. Phys. Lett.* **1995**, *232*, 379−382.

(18) Mondelo-Martell, M.; Huarte-Larrañaga, F. 5D Quantum Dynamics of the H_2@SWNT System: Quantitative Study of the Rotational-Translational Coupling. *J. Chem. Phys.* **2015**, *142*, 084304−15.

(19) Mondelo-Martell, M.; Huarte-Larrañaga, F. Six Dimensional Propagation of the H_2 Molecule Confined in a Single-Walled Carbon Nanotube. *Chem. Phys.* **2015**, *462*, 41−50.

(20) Xu, M.; Ye, S.; Lawler, R.; Turro, N. J.; Bačić, Z. HD In C_{60}: Theoretical Prediction of the Inelastic Neutron Scattering Spectrum and its Temperature Dependence. *Philos. Trans. R. Soc., A* **2013**, *371*, 20110630−15.

(21) Matanović, I.; Belof, J. L.; Space, B.; Sillar, K.; Sauer, J.; Eckert, J.; Bačić, Z. Hydrogen Adsorbed in a Metal Organic Framework-5: Coupled Translation-Rotation Eigenstates from Quantum Five-Dimensional Calculations. *J. Chem. Phys.* **2012**, *137*, 14701−13.

(22) Suarez, J.; Huarte-Larranaga, F. Hydrogen Confined in Single-Wall Carbon Nanotubes: Anisotropy Effects on Ro-Vibrational Quantum Levels. *J. Chem. Phys.* **2012**, *137*, 064320−13.

(23) Lu, T.; Goldfield, E. E. M.; Gray, S. S. K. Quantum States of Hydrogen and its Isotopes Confined in Single-Walled Carbon Nanotubes: Dependence on Interaction Potential and Extreme Two-Dimensional Confinement. *J. Phys. Chem. B* **2006**, *110*, 1742−1751.

(24) Yildirim, T.; Harris, A. Quantum Dynamics of a Hydrogen Molecule Confined in a Cylindrical Potential. *Phys. Rev. B: Condens. Matter Mater. Phys.* **2003**, *67*, 245413−15.

(25) Yim, W.-L.; Byl, O.; Yates, J. T.; Johnson, J. K. Vibrational Behavior of Adsorbed CO_2 on Single-Walled Carbon Nanotubes. *J. Chem. Phys.* **2004**, *120*, 5377−5386.

(26) Valdés, Á; Arismendi-Arrieta, D. J.; Prosmiti, R. Quantum Dynamics of Carbon Dioxide Encapsulated in the Cages of the Si Clathrate Hydrate: Structural Guest Distributions and Cage Occupation. *J. Phys. Chem. C* **2015**, *119*, 3945−3956.

(27) Wang, Q.; Challa, S.; Sholl, D.; Johnson, J. Quantum Sieving in Carbon Nanotubes and Zeolites. *Phys. Rev. Lett.* **1999**, *82*, 956−959.

(28) Hankel, M.; Zhang, H.; Nguyen, T. X.; Bhatia, S. K.; Gray, S. K.; Smith, S. C. Kinetic Modelling of Molecular Hydrogen Transport in Microporous Carbon Materials. *Phys. Chem. Chem. Phys.* **2011**, *13*, 7834−44.

(29) Inokuma, Y.; Kawano, M.; Fujita, M. Crystalline Molecular Flasks. *Nat. Chem.* **2011**, *3*, 349−358.

(30) Nielsen, T. K.; Bösenberg, U.; Gosalawit, R.; Dornheim, M.; Cerenius, Y.; Besenbacher, F.; Jensen, T. R. A Reversible Nano-confined Chemical Reaction. *ACS Nano* **2010**, *4*, 3903−3908.

(31) Martinez de la Hoz, J. M.; Balbuena, P. B. Small-Molecule Activation Driven by Confinement Effects. *ACS Catal.* **2015**, *5*, 215−224.

(32) Kumar, A. V. A.; Jobic, H.; Bhatia, S. K. Quantum Effects on Adsorption and Diffusion of Hydrogen and Deuterium in Micro-porous Materials. *J. Phys. Chem. B* **2006**, *110*, 16666−71.

(33) Garberoglio, G. Quantum Sieving in Organic Frameworks. *Chem. Phys. Lett.* **2009**, *467*, 270−275.

(34) Skouteris, D.; Laganà, A. MCTDH Calculations on the Rigid OH Radical Moving Along a (10,0) Carbon Nanotube. *Chem. Phys. Lett.* **2013**, *575*, 18−22.

(35) Kumar, A. V. A.; Bhatia, S. K. Quantum Effect Induced Reverse Kinetic Molecular Sieving in Microporous Materials. *Phys. Rev. Lett.* **2005**, *95*, 1−4.

(36) Nguyen, T. X.; Jobic, H.; Bhatia, S. K. Microscopic Observation of Kinetic Molecular Sieving of Hydrogen Isotopes in a Nanoporous Material. *Phys. Rev. Lett.* **2010**, *105*, 085901.

(37) Contescu, C. I.; Zhang, H.; Olsen, R. J.; Mamontov, E.; Morris, J. R.; Gallego, N. C. Isotope Effect on Adsorbed Quantum Phases: Diffusion of H$_2$ and D$_2$ in Nanoporous Carbon. *Phys. Rev. Lett.* **2013**, *110*, 236102−5.

(38) Garberoglio, G.; DeKlavon, M. M.; Johnson, J. K. Quantum Sieving in Single-Walled Carbon Nanotubes: Effect of Interaction Potential and Rotational-Translational Coupling. *J. Phys. Chem. B* **2006**, *110*, 1733−1741.

(39) Pouthier, V.; Light, J. C. Surface Self-Diffusion of Hydrogen on Cu(100): A Quantum Kinetic Equation Approach. *J. Chem. Phys.* **2000**, *113*, 1204−1216.

(40) Firmino, T.; Marquardt, R.; Gatti, F.; Dong, W. Diffusion Rates for Hydrogen on Pd(111) from Molecular Quantum Dynamics Calculations. *J. Phys. Chem. Lett.* **2014**, *5*, 4270−4274.

(41) Zhang, D. H.; Light, J. C.; Lee, S.-Y. Y. Transition State Wave Packet Study of Hydrogen Diffusion on Cu(100) Surface. *J. Chem. Phys.* **1999**, *111*, 5741−5753.

(42) Jaquet, R.; Miller, W. H. Quantum Mechanical Rate Constants Via Path Integrals: Diffusion of Hydrogen Atoms on a Tungsten(100) Surface. *J. Phys. Chem.* **1985**, *89*, 2139−2144.

(43) Doll, J. D.; Voter, A. F. Recent Developments in the Theory of Surface Diffusion. *Annu. Rev. Phys. Chem.* **1987**, *38*, 413−431.

(44) Barth, J. Transport of Adsorbates at Metal Surfaces: From Thermal Migration to Hot Precursors. *Surf. Sci. Rep.* **2000**, *40*, 75−149.

(45) Zhang, D. H.; Light, J. C. Cumulative Reaction Probability Via Transition State Wave Packets. *J. Chem. Phys.* **1996**, *104*, 6184−6191.

(46) Miller, W. H. Quantum Mechanical Transition State Theory and a New Semiclassical Model for Reaction Rate Constants. *J. Chem. Phys.* **1974**, *61*, 1823−1834.

(47) Dovesi, R.; Orlando, R.; Civalleri, B.; Roetti, C.; Saunders, V. R.; Zicovich-Wilson, C. M.; Pascale, F.; Doll, K.; Harrison, N. M.; Bush, I. J.; et al. *Crystal 09 User's Manual*, 2009.

(48) Huarte-Larrañaga, F.; Albertí, M. A Molecular Dynamics Study of the Distribution of Molecular Hydrogen Physisorbed on Single Walled Carbon Nanotubes. *Chem. Phys. Lett.* **2007**, *445*, 227−232.

(49) Huarte-Larrañaga, F.; Manthe, U. Thermal Rate Constants for Polyatomic Reactions: First Principles Quantum Theory. *Z. Phys. Chem.* **2007**, *221*, 171−213.

(50) Miller, W. H.; Schwartz, S. D.; Tromp, J. W. Quantum Mechanical Rate Constants for Bimolecular Reactions. *J. Chem. Phys.* **1983**, *79*, 4889−4898.

(51) Matzkies, F.; Manthe, U. Accurate Quantum Calculations of Thermal Rate Constants Employing MCTDH: H$_2$+OH→H+H$_2$O and D$_2$+OH→D+DOH. *J. Chem. Phys.* **1998**, *108*, 4828−4836.

(52) Manthe, U.; Matzkies, F. Quantum Calculations of Thermal Rate Constants and Reaction Probabilities: H$_2$+CN→H+HCN. *Chem. Phys. Lett.* **1998**, *282*, 442−449.

(53) Manthe, U. The State Averaged Multiconfigurational Time-Dependent Hartree Approach: Vibrational State and Reaction Rate Calculations. *J. Chem. Phys.* **2008**, *128*, 64108−12.

(54) Meyer, H.-D.; Manthe, U.; Cederbaum, L. The Multi-Configurational Time-Dependent Hartree Approach. *Chem. Phys. Lett.* **1990**, *165*, 73−78.

(55) Hammer, T.; Manthe, U. Iterative Diagonalization in the State-Averaged Multi-Configurational Time-Dependent Hartree Approach: Excited State Tunneling Splittings in Malonaldehyde. *J. Chem. Phys.* **2012**, *136*, 54105−17.

Supplementary information for Publication 2: *Diffusion of H$_2$ and D$_2$ Confined in Single-Walled Carbon Nanotubes: Quantum Dynamics and Confinement Effects*

Supporting information for:

Diffusion of H$_2$ and D$_2$ Confined in Single-Walled Carbon Nanotubes: Quantum Dynamics and Confinement Effects.

Manel Mondelo-Martell and Fermín Huarte-Larrañaga[*]

Department of Materials Science & Physical Chemistry and Institute of Theoretical and Computational Chemistry (IQTCUB), Universitat de Barcelona, 08028 Barcelona, Spain

E-mail: fermin.huarte@ub.edu

Phone: +34 93 4031341. Fax: +34 93 4021231

---
[*]To whom correspondence should be addressed

Numerical details and convergence

Here we present the wavefunction representation parameters used for carrying out the calculations detailed in the main text. For each molecule and PES, these are:

- Flux eigenstates calculation, at reference temperature 75, 100 and 150 K.

- Flux eigenstates propagation, at the same reference temperatures.

The Multiconfigurational Time-dependent Hartree (MCTDH) approach used in the present work relies in a double layer representation of the wavefunction. Both levels are considered in the following to discuss the numerical convergence of the results.

Primitive grid

The primitive grid is kept the same for all the calculations. The most critical step regarding convergence at this level is the absence of aliasing or reflections at the edges of the non-periodic coordinate grids. In a DVR or FFT basis, this is checked by looking at the population of the primitive function at the limiting points the direct (position) and inverse (momentum) spaces: if it is low enough in both, the grid is well balanced and it should not pose convergence issues. Note that, in the case of periodic coordinates such as ϕ, aliasing appears naturally and is not related with numerical errors. Table S1 contains the population at the grid edges for the calculations carried out in this work. The θ coordinate is omitted due to its special characteristics. Observing the data in the table it can be seen that probability density does not exceed 10^{-9} in any of the ρ, x, y, z coordinates.

Single Particle Functions

The single particle functions (SPFs) constitute the time dependent basis set for the MCTDH calculations. Within the Correlation Discrete Variable Representation (CDVR), they also become the basis set used to evaluate the potential energy matrix elements. This allows

Table S1: Order of magnitude of the primitive function population at the first and last point of the coordinate grid. FB stands for the Frankland–Brenner PES, *eig* and *prp* label eigenstate calculation or propagation, respectively, and the number indicates the reference temperature for the calculation.

	ρ		ϕ		x		y		z	
	min	max	min	max	min	max	min	max	min	max
FB-eig-75K	10^{-9}	10^{-12}	10^{-2}	10^{-2}	10^{-25}	10^{-26}	10^{-17}	10^{-14}	10^{-23}	10^{-23}
FB-eig-100K	10^{-9}	10^{-12}	10^{-2}	10^{-2}	10^{-22}	10^{-23}	10^{-17}	10^{-18}	10^{-25}	10^{-21}
FB-eig-150K	10^{-9}	10^{-12}	10^{-2}	10^{-2}	10^{-20}	10^{-21}	10^{-13}	10^{-16}	10^{-12}	10^{-11}
FB-prp-75K	10^{-9}	10^{-12}	10^{-2}	10^{-2}	10^{-13}	10^{-13}	10^{-11}	10^{-11}	10^{-8}	10^{-7}
FB-prp-100K	10^{-9}	10^{-12}	10^{-2}	10^{-2}	10^{-12}	10^{-12}	10^{-10}	10^{-9}	10^{-9}	10^{-9}
FB-prp-150K	10^{-9}	10^{-12}	10^{-2}	10^{-2}	10^{-11}	10^{-11}	10^{-12}	10^{-13}	10^{-9}	10^{-8}
48-eig-75K	10^{-9}	10^{-11}	10^{-2}	10^{-2}	10^{-25}	10^{-27}	10^{-24}	10^{-24}	10^{-14}	10^{-13}
48-eig-100K	10^{-9}	10^{-11}	10^{-2}	10^{-2}	10^{-23}	10^{-24}	10^{-24}	10^{-24}	10^{-24}	10^{-24}
48-eig-150K	10^{-9}	10^{-12}	10^{-2}	10^{-2}	10^{-19}	10^{-21}	10^{-22}	10^{-22}	10^{-19}	10^{-21}
48-prp-75K	10^{-9}	10^{-12}	10^{-2}	10^{-2}	10^{-13}	10^{-13}	10^{-12}	10^{-13}	10^{-12}	10^{-12}
48-prp-100K	10^{-9}	10^{-12}	10^{-2}	10^{-2}	10^{-12}	10^{-12}	10^{-13}	10^{-13}	10^{-14}	10^{-13}
48-prp-150K	10^{-9}	10^{-11}	10^{-2}	10^{-2}	10^{-11}	10^{-11}	10^{-12}	10^{-12}	10^{-11}	10^{-11}

the utilization of general PES without the requirement of being expressed in product form, but also makes the overall method non–variational, so the balance in the number of SPFs in each degree of freedom becomes very important: a too large basis set can be as bad as a too small one. Here we present, for each one of the calculations carried out in this work, the results obtained using three different basis sets: a minimal basis set with at most 2 SPFs in each DOF, and two differently balanced SPFs sets. For the flux eigenstates calculation the eigenvalues obtained are shown, while for the propagations, the flux-position autocorrelation functions, $C_{fp}(t)$, illustrate the results.

Flux eigenstates calculation

Tables S2 to S13 show the absolute value for the 6 first flux eigenvalues obtained for the each calculations, *i.e.* for each molecule (H_2 or D_2) at three different reference temperatures (75, 100 and 150 K) and for each PES. Each table contains the results obtained using three different basis. The basis sets are labeled according to the number of SPFs in each degree of freedom, ordered as ρ,θ,ϕ,z,x,y.

Table S2: Absolute value for the first six eigenvalues for H$_2$ calculated at 75 K, with Ref 48 PES.

Basis	$\mid f_1\rangle$	$\mid f_2\rangle$	$\mid f_3\rangle$	$\mid f_4\rangle$	$\mid f_5\rangle$	$\mid f_6\rangle$
133222	1.2×10^{-26}	2.2×10^{-27}	5.7×10^{-28}	4.9×10^{-28}	9.7×10^{-29}	2.2×10^{-29}
145244	1.5×10^{-26}	4.6×10^{-27}	5.6×10^{-28}	5.6×10^{-28}	9.3×10^{-29}	9.3×10^{-29}
257233	1.5×10^{-26}	4.6×10^{-27}	6×10^{-28}	6×10^{-28}	9×10^{-29}	8.9×10^{-29}

Table S3: Absolute value for the first six eigenvalues for H$_2$ calculated at 100 K, with Ref 48 PES.

Basis	$\mid f_1\rangle$	$\mid f_2\rangle$	$\mid f_3\rangle$	$\mid f_4\rangle$	$\mid f_5\rangle$	$\mid f_6\rangle$
133222	4.3×10^{-21}	1×10^{-21}	3.8×10^{-22}	3.6×10^{-22}	1.2×10^{-22}	6.8×10^{-23}
145244	4.5×10^{-21}	1.9×10^{-21}	3.8×10^{-22}	3.8×10^{-22}	9.9×10^{-23}	9.9×10^{-23}
256233	4.6×10^{-21}	1.9×10^{-21}	4×10^{-22}	4×10^{-22}	9.7×10^{-23}	9.5×10^{-23}

Table S4: Absolute value for the first six eigenvalues for H$_2$ calculated at 150 K, with Ref 48 PES.

Basis	$\mid f_1\rangle$	$\mid f_2\rangle$	$\mid f_3\rangle$	$\mid f_4\rangle$	$\mid f_5\rangle$	$\mid f_6\rangle$
133222	1.5×10^{-15}	5×10^{-16}	3×10^{-16}	2.9×10^{-16}	1.4×10^{-16}	9.5×10^{-17}
145244	1.6×10^{-15}	9.1×10^{-16}	3×10^{-16}	3×10^{-16}	1.2×10^{-16}	1.2×10^{-16}
257233	1.5×10^{-15}	5×10^{-16}	3×10^{-16}	2.9×10^{-16}	1.4×10^{-16}	9.5×10^{-17}

Table S5: Absolute value for the first six eigenvalues for D$_2$ calculated at 75 K, with Ref 48 PES.

Basis	$\mid f_1\rangle$	$\mid f_2\rangle$	$\mid f_3\rangle$	$\mid f_4\rangle$	$\mid f_5\rangle$	$\mid f_6\rangle$
145233	1.5×10^{-20}	1.1×10^{-20}	1.7×10^{-21}	1.7×10^{-21}	5.7×10^{-22}	5.5×10^{-22}
155244	1.5×10^{-16}	1.2×10^{-16}	2.9×10^{-17}	2.9×10^{-17}	1.3×10^{-17}	1.3×10^{-17}
256233	1.5×10^{-16}	1.2×10^{-16}	2.9×10^{-17}	2.9×10^{-17}	1.3×10^{-17}	1.3×10^{-17}

Table S6: Absolute value for the first six eigenvalues for D$_2$ calculated at 100 K, with Ref 48 PES.

Basis	$\mid f_1\rangle$	$\mid f_2\rangle$	$\mid f_3\rangle$	$\mid f_4\rangle$	$\mid f_5\rangle$	$\mid f_6\rangle$
145233	1.5×10^{-16}	1.2×10^{-16}	2.8×10^{-17}	2.8×10^{-17}	1.3×10^{-17}	1.2×10^{-17}
155244	1.5×10^{-16}	1.2×10^{-16}	2.9×10^{-17}	2.9×10^{-17}	1.3×10^{-17}	1.3×10^{-17}
256233	1.5×10^{-16}	1.2×10^{-16}	2.9×10^{-17}	2.9×10^{-17}	1.3×10^{-17}	1.3×10^{-17}

Table S7: Absolute value for the first six eigenvalues for D$_2$ calculated at 150 K, with Ref 48 PES.

Basis	$\mid f_1\rangle$	$\mid f_2\rangle$	$\mid f_3\rangle$	$\mid f_4\rangle$	$\mid f_5\rangle$	$\mid f_6\rangle$
145233	1.7×10^{-12}	1.4×10^{-12}	5.5×10^{-13}	5.5×10^{-13}	3.2×10^{-13}	3.2×10^{-13}
155244	1.7×10^{-12}	1.4×10^{-12}	5.6×10^{-13}	5.6×10^{-13}	3.3×10^{-13}	3.3×10^{-13}
257233	1.7×10^{-12}	1.4×10^{-12}	5.6×10^{-13}	5.6×10^{-13}	3.3×10^{-13}	3.3×10^{-13}

Table S8: Absolute value for the first six eigenvalues for H$_2$ calculated at 75 K, with FB PES.

Basis	$\mid f_1\rangle$	$\mid f_2\rangle$	$\mid f_3\rangle$	$\mid f_4\rangle$	$\mid f_5\rangle$	$\mid f_6\rangle$
133222	4.1×10^{-29}	2.5×10^{-29}	1×10^{-31}	1×10^{-31}	7.4×10^{-34}	4.3×10^{-36}
153244	5.1×10^{-29}	4.1×10^{-29}	1.4×10^{-32}	1.4×10^{-32}	1.2×10^{-32}	1.2×10^{-32}
245233	5.3×10^{-29}	4.2×10^{-29}	1×10^{-31}	1×10^{-31}	2.2×10^{-32}	2.2×10^{-32}

Table S9: Absolute value for the first six eigenvalues for H$_2$ calculated at 100 K, with FB PES.

Basis	$\mid f_1\rangle$	$\mid f_2\rangle$	$\mid f_3\rangle$	$\mid f_4\rangle$	$\mid f_5\rangle$	$\mid f_6\rangle$
133222	4.9×10^{-23}	2.9×10^{-23}	5.6×10^{-25}	5.6×10^{-25}	1.4×10^{-26}	2.6×10^{-28}
143244	6.3×10^{-23}	5.3×10^{-23}	5×10^{-25}	1.7×10^{-25}	1.4×10^{-25}	1.3×10^{-25}
248233	6.5×10^{-23}	5.4×10^{-23}	5.5×10^{-25}	5.5×10^{-25}	1.9×10^{-25}	1.9×10^{-25}

Table S10: Absolute value for the first six eigenvalues for H$_2$ calculated at 150 K, with FB PES.

Basis	$\mid f_1\rangle$	$\mid f_2\rangle$	$\mid f_3\rangle$	$\mid f_4\rangle$	$\mid f_5\rangle$	$\mid f_6\rangle$
133222	8.7×10^{-17}	3.9×10^{-17}	3.6×10^{-18}	3.5×10^{-18}	1.6×10^{-18}	1.1×10^{-18}
156244	9×10^{-17}	8.1×10^{-17}	3.7×10^{-18}	3.7×10^{-18}	1.8×10^{-18}	1.8×10^{-18}
245233	9.2×10^{-17}	8.2×10^{-17}	3.6×10^{-18}	3.6×10^{-18}	1.8×10^{-18}	1.8×10^{-18}

Table S11: Absolute value for the first six eigenvalues for D$_2$ calculated at 75 K, with FB PES.

Basis	$\mid f_1\rangle$	$\mid f_2\rangle$	$\mid f_3\rangle$	$\mid f_4\rangle$	$\mid f_5\rangle$	$\mid f_6\rangle$
145233	4.5×10^{-22}	4.4×10^{-22}	3.3×10^{-24}	3.3×10^{-24}	2.8×10^{-24}	2.8×10^{-24}
143244	4.4×10^{-22}	4.4×10^{-22}	3.5×10^{-24}	3.4×10^{-24}	2.9×10^{-24}	2.8×10^{-24}
255233	4.6×10^{-22}	4.5×10^{-22}	3.7×10^{-24}	3.7×10^{-24}	2.7×10^{-24}	2.7×10^{-24}

Table S12: Absolute value for the first six eigenvalues for D$_2$ calculated at 100 K, with FB PES.

Basis	$\mid f_1\rangle$	$\mid f_2\rangle$	$\mid f_3\rangle$	$\mid f_4\rangle$	$\mid f_5\rangle$	$\mid f_6\rangle$
133222	1×10^{-17}	5×10^{-18}	2.7×10^{-19}	2.6×10^{-19}	1.8×10^{-19}	1.4×10^{-19}
243244	1.1×10^{-17}	1×10^{-17}	2.7×10^{-19}	2.7×10^{-19}	2.3×10^{-19}	2.3×10^{-19}
255233	1.1×10^{-17}	1×10^{-17}	2.8×10^{-19}	2.8×10^{-19}	2.2×10^{-19}	2.2×10^{-19}

Table S13: Absolute value for the first six eigenvalues for D$_2$ calculated at 150 K, with FB PES.

Basis	$\mid f_1\rangle$	$\mid f_2\rangle$	$\mid f_3\rangle$	$\mid f_4\rangle$	$\mid f_5\rangle$	$\mid f_6\rangle$
145233	2.8×10^{-13}	2.8×10^{-13}	2.4×10^{-14}	2.4×10^{-14}	2.2×10^{-14}	2.2×10^{-14}
148244	2.8×10^{-13}	2.8×10^{-13}	2.4×10^{-14}	2.4×10^{-14}	2.2×10^{-14}	2.2×10^{-14}
255233	2.9×10^{-13}	2.8×10^{-13}	2.5×10^{-14}	2.5×10^{-14}	2.2×10^{-14}	2.2×10^{-14}

Flux eigenstates propagation

The flux–position autocorrelation functions obtained with the different basis sets described previously are shown in Figures S1 and S2 for the Ref. 48 and the FB PES, respectively. Note that, of the three basis sets used for each calculation, two of them agree very well, pointing to a good convergence of the results.

Taking all these data into account, we selected the basis sets for H$_2$ (Table S14) and D$_2$ (Table S15).

Table S14: SPF basis size for the two sets of simulations carried out: calculation of thermal flux eigenstates and time propagation.

T	PES Ref 48		FB PES	
	Eigenstates	Propagation	Eigenstates	Propagation
75 K	257233	257633	245233	257744
100 K	256233	257644	248233	257844
150 K	257233	257633	245233	257844
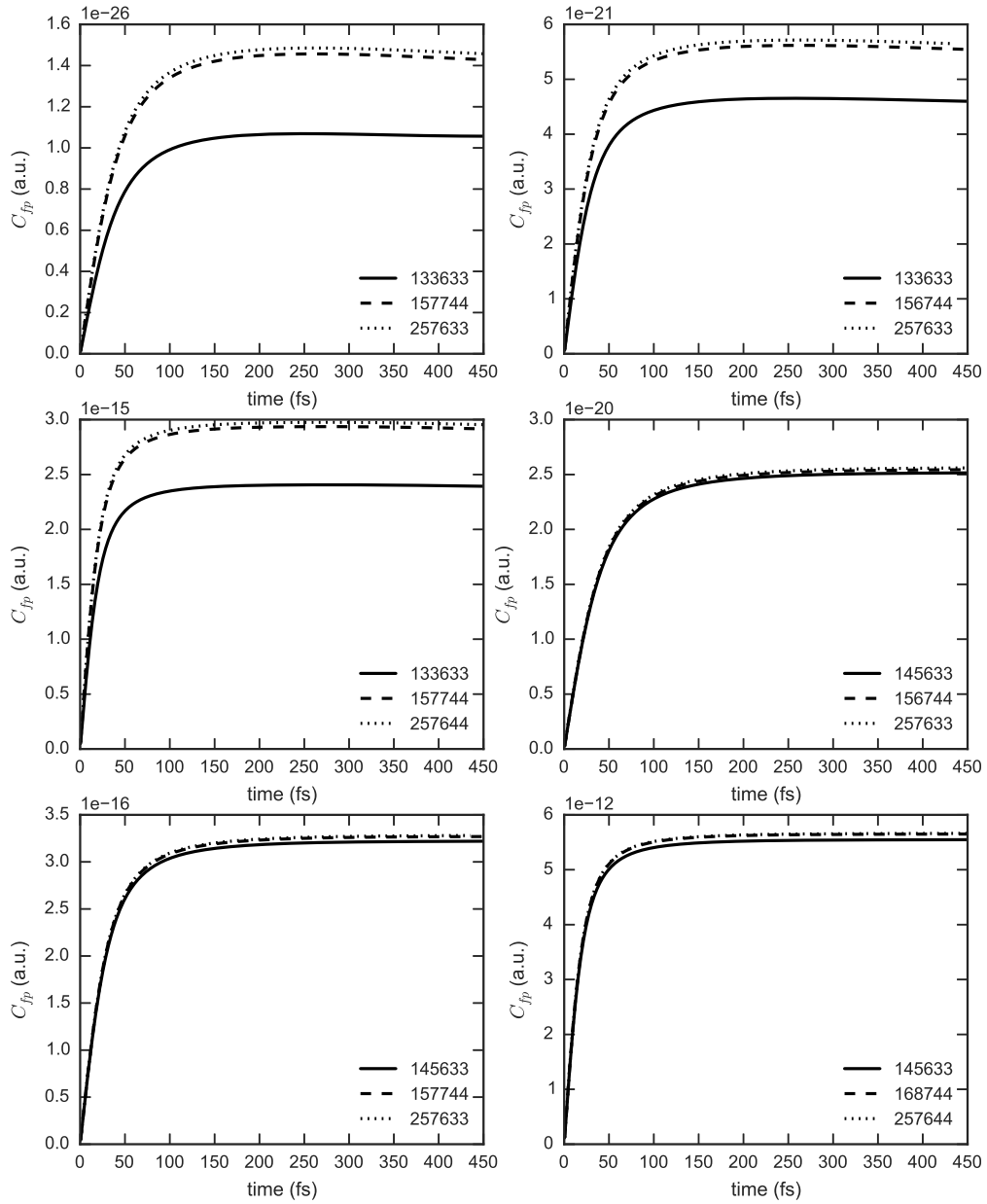
Figure S1: $C_{fp}(t)$ for the different calculations carried out on Ref. 48 PES. First column correspond to the H_2 molecule, second column to D_2. The rows contain the data at reference temperatures of 75, 100 and 150 K from top to bottom
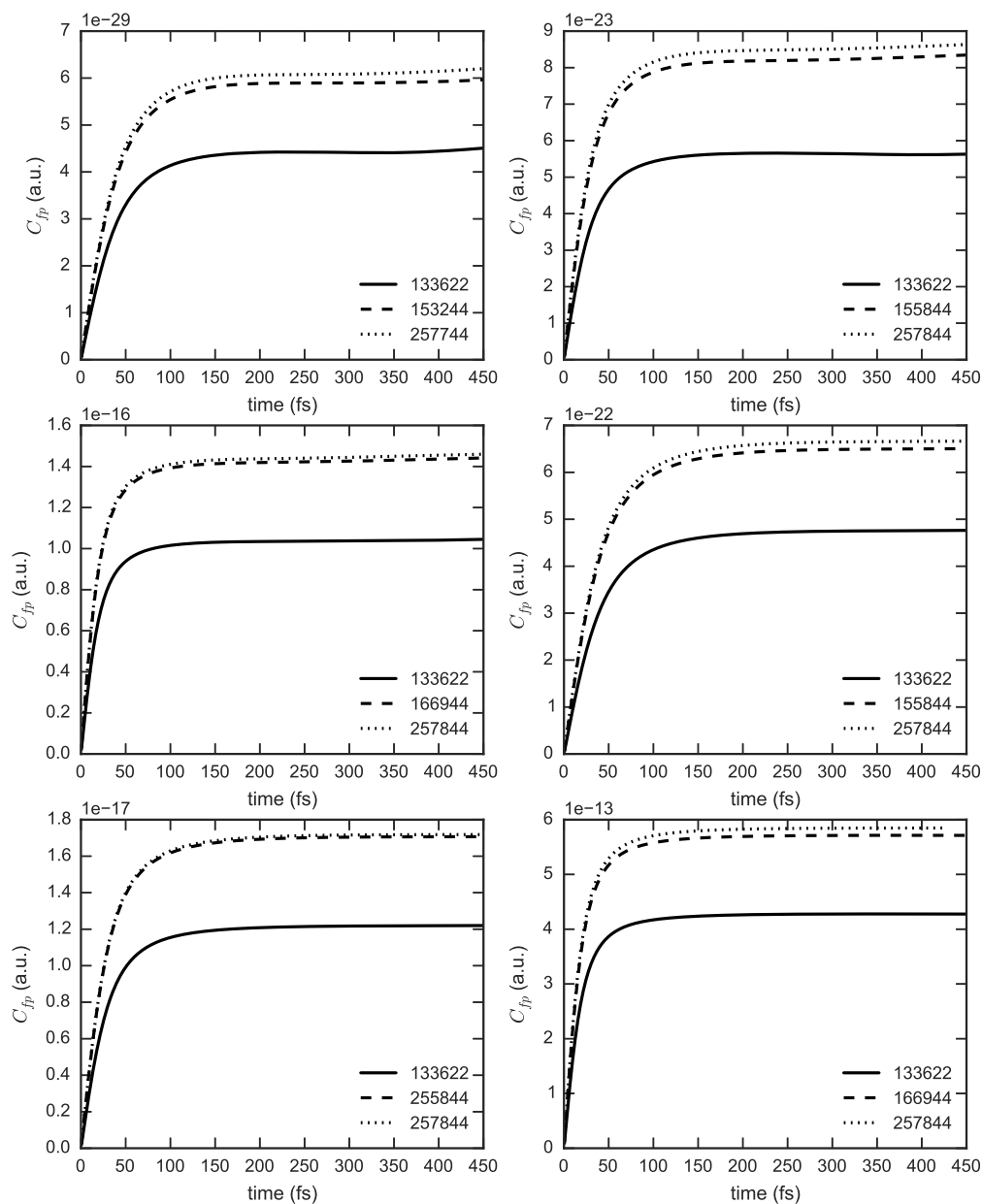
Figure S2: $C_{fp}(t)$ for the different calculations carried out on FB PES. First column corresponds to the H$_2$ molecule, second column to D$_2$. The rows contain the data at reference temperatures of 75, 100 and 150 K from top to bottom

S8

Table S15: SPF basis size for the two sets of simulations carried out: calculation of thermal flux eigenstates and time propagation.

T	PES Ref 48		FB PES	
	Eigenstates	Propagation	Eigenstates	Propagation
75 K	256233	257633	255233	257844
100 K	256233	257633	255233	257844
150 K	257233	257644	255233	257844

Quantum Dynamics on the Frankland-Brenner PES

Here we briefly discuss some qualitative aspects of the intermediate results obtained using the Frankland-Brenner PES, which were omitted in the main text for the sake of clarity.

The number of flux eigenstates was sufficient to guarantee that no relevant states were neglected in the calculation of the hopping probability, k_{hop}. It is worthwhile to mention that the pairs of eigenvalues of the flux operator follow a pattern very similar to the one existing in the energies of the 5D Hamiltonian, with relatively large gaps, as well as degeneracies. The flux–position autocorrelation function, $C_{fp}(t)$, at a reference temperature of 150 K ,is shown in Figures S3 and S4 for H_2 and D_2, respectively. The behavior is similar to the one shown in the main text for the Ref 48 PES: a steep increase of the function, reaching a plateau at arround 200 fs. Note that this is more clear for D_2 than for H_2. Also, there is a difference between one (for D_2) to three (for H_2) orders of magnitude when compared with the results on the Ref. 48 PES. This is given by the value of the flux eigenstates and may be related to the energy difference in the reaction barrier between both surfaces.

Regarding the cumulative reaction probability, $N(E)$, and the corresponding contribution from the most significant flux eigenstates, the results for the FB PES at a reference temperature of 150 K are shown in Figures S5 and S6 for H_2 and D_2, respectively. There are two main differences between both PES: first, the energy threshold to start the diffusion process changes. This is directly related with the different ZPE obtained with both sets of Lennard-Jones parameters. Secondly, the structure of the individual contributions to the CRP is significantly different: $N(E)$ computed on the Ref 48 PES increases with energy
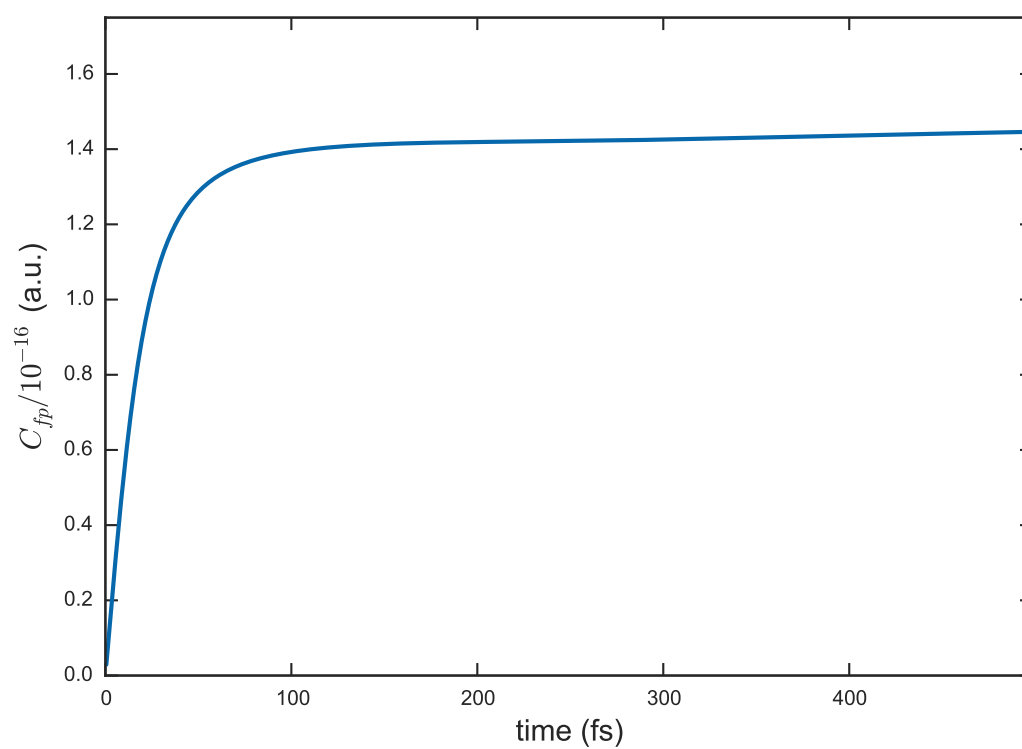
Figure S3: Flux–position autocorrelation function, C_{fp}, for H$_2$ confined in an (8,0) carbon nanotube at a reference temperature of 150 K.
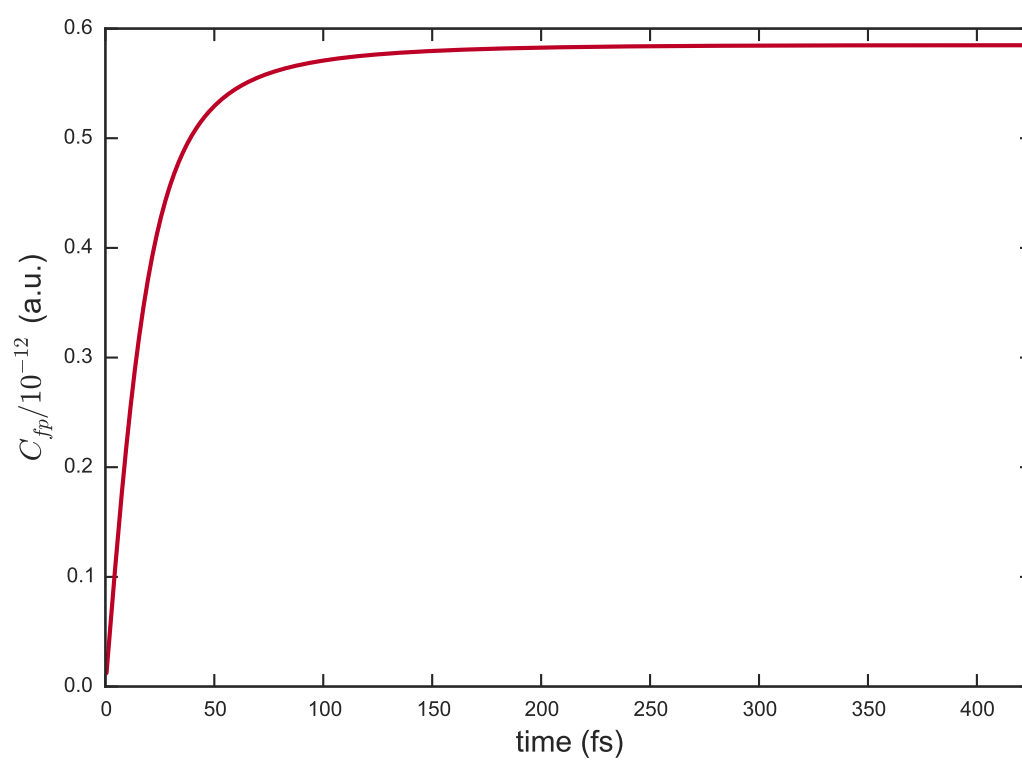
Figure S4: Flux–position autocorrelation function, C_{fp}, for D_2 confined in an (8,0) carbon nanotube at a reference temperature of 150 K.

in a relatively smooth fashion. Instead, using the FB PES we find first a rather steep rise of the CRP followed by a wide flat region. This is related with the structure of the flux eigenvalues, which appear more *clustered* in this PES. We think the reason for this behavior lies on the different profile of the potential energy surface, which is steeper for the FB PES, and therefore causes the energy levels to split differently than in the other PES.
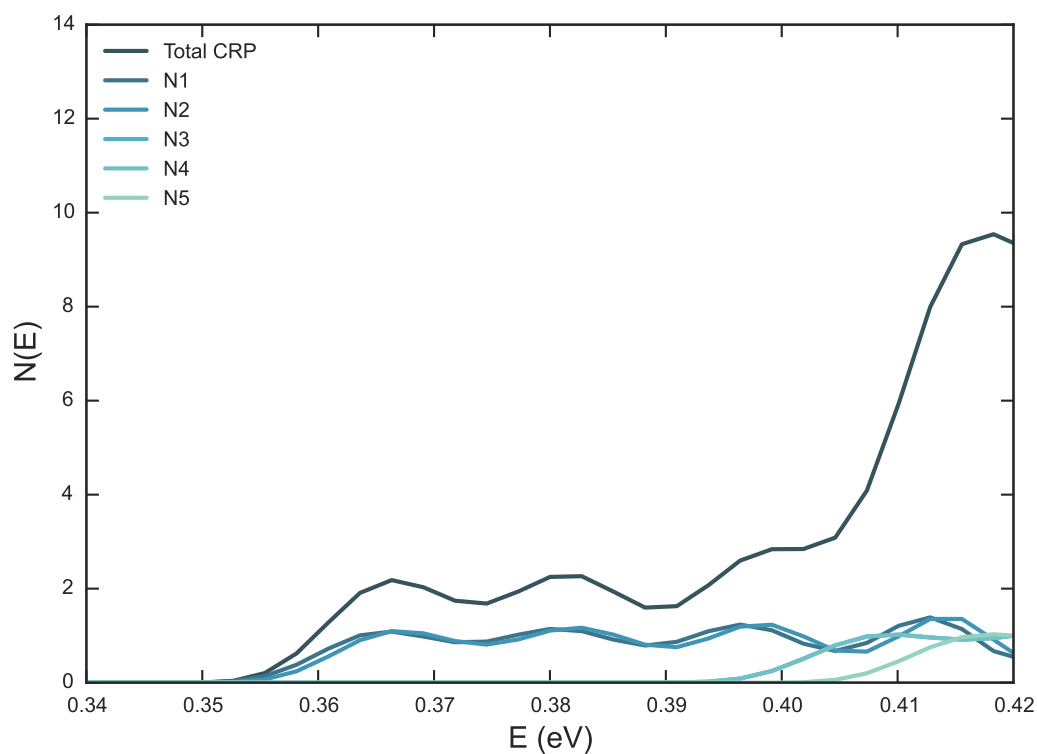
Figure S5: N(E) and the first five individual contributions to the CRP, for H$_2$ confined in an (8,0) carbon nanotube. Symmetry numbers from the rotational symmetry are not included.

Diffusion rates and adsorption selectivities are shown in the main text for both this and the Ref 48 PES.
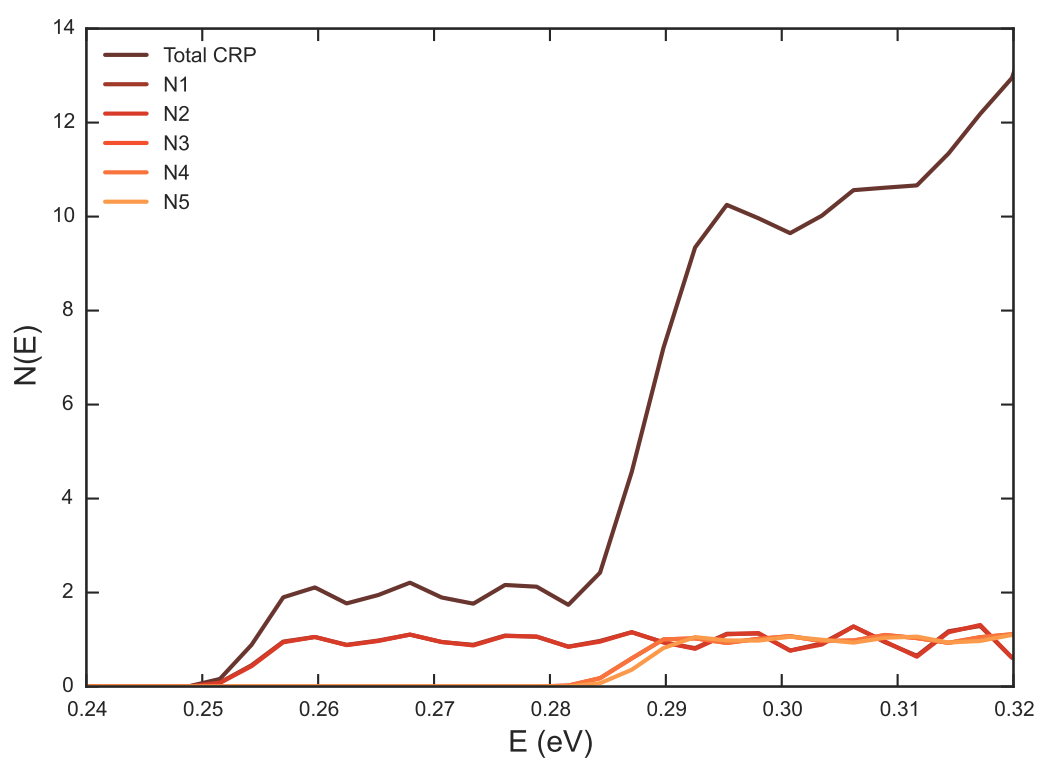
Figure S6: N(E) and the first five individual contributions to the CRP, for D_2 confined in an (8,0) carbon nanotube. Symmetry numbers from the rotational symmetry are not included.

Transition State Theory results

Transition state theory (TST) is a useful tool to obtain preliminary results concerning chemical kinetics. The rate for a chemical process within these approach is given by:

$$k^{TST}(T) = \frac{kT}{h} \frac{Q^{\dagger}(T)}{Q_r(T)}, \tag{1}$$

where $Q^{\dagger}$ is the partition function of the transition state structure, neglecting the reaction coordinate DOF, and Q_r is the full partition function for the reactants. The diffusion rates for H_2 and D_2, calculated with TST employing both Ref. 48 and FB PES, are shown in Figures S7 and S8.   The similarity of this results when compared with the quantum
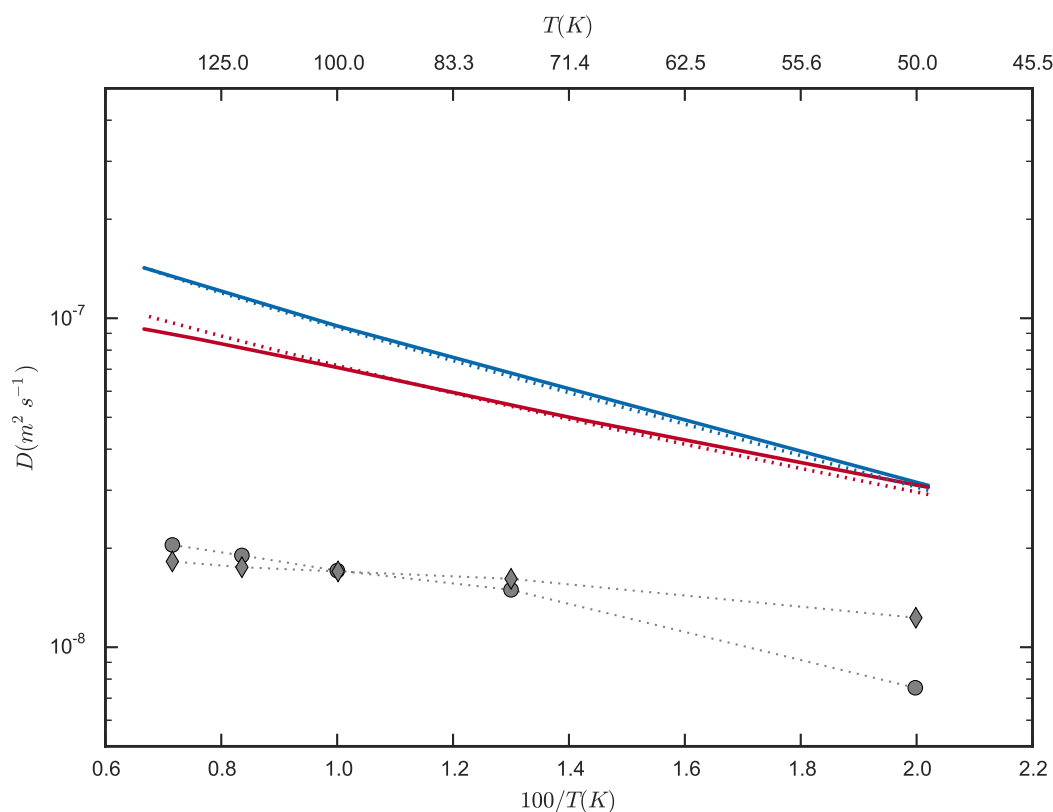
Figure S7: Diffusion rate constants for H_2 (blue) and D_2 (red) in an (8,0) CNT, computed with the Flux correlation function formalism (solid) and TST (pointed) in the Ref. 48 PES. Grey points correspond to experimental results in Ref 36.

dynamical calculations indicate a fairly low recrossing and tunneling effects in the diffusion
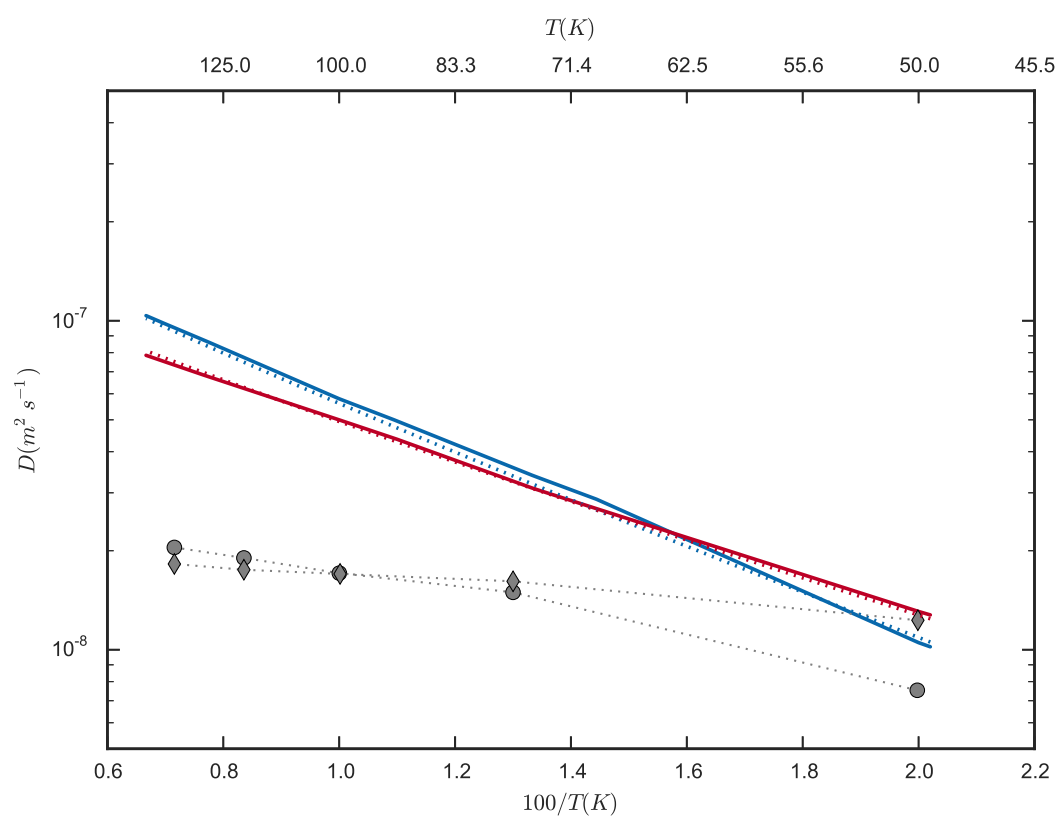
Figure S8: Diffusion rate constants for H_2 (blue) and D_2 (red) in an (8,0) CNT, computed with the Flux correlation function formalism (solid) and TST (pointed) in the FB PES. Grey points correspond to experimental results in Ref 36.

dynamics of this system.

6.5   Summary and Conclusions

The presented Chapter has included the study of the diffusion of H_2 and D_2 along an (8,0) SWCNT. Diffusion rates have been computed by using the flux correlation function approach and the single hopping approximation. A first set of results using a full dimensional Hamiltonian to define the adsorbate has been presented which seemed to support the claim of the existence of an Inverse Kinetic Isotope Effect in nanostructured materials. However, further calculations with a new representation of the Hamiltonian allowed for extended propagations, thus improving the results obtained in the first set of propagations. These new results have shown that the lighter isotopologue diffuses faster than the heavier at all the studied temperature values. This has been seen to be a consequence of sharp resonances in the tunneling regime, which favor the diffusion of H_2 at energies below the classical diffusion threshold.

The main conclusions extracted from this Chapter are:

- The flux–flux correlation function formalism, together with the single–hopping model for diffusion, can be used to compute diffusion rates in the low–pressure limit in a full–quantum manner.

- Time–extended simulations are particularly necessary to simulate the diffusion process, due to the low corrugation present in these systems.

- The ZPE effect enhances the diffusion of heavy isotopologues, as shown by the TST and quantum unconverged calculations.

- Tunneling effects, including resonances, are more important for lighter molecules.

- The final effect is that resonance enhanced tunneling overcompensates ZPE effects, and inverse kinetic sieving does not appear in this particular system.

- These results illustrate the importance of a quantum description of light atoms in chemical dynamics.

Chapter 7

Separation of time–scales in the H$_2$@SWCNT system

7.1   Coupling in the 6D model and adiabatic theorem

The cylindrical shape of a carbon nanotube gives the confined molecules some special properties that do not appear in most other nanostructured materials: in contrast with zeolites, CMS or most MOFs, in the case of nanotubes we have two confining dimensions of space (x and y), while the potential energy barriers along the nanotube's axis (z) are very low. Due to this particular shape, one can divide the degrees of freedom describing the adsorbate in two sets: five of them (ρ, θ, φ, x, and y) are considered the *confined* degrees of freedom (hereby referred collectively as q), while the sixth (z) is an *unbound* or *quasi–free* DOF. As it was already said in Chapter 5, it is generally accepted that the coupling between these two sets of coordinates is low enough so that one can just worry about the confining degrees of freedom, and therefore make studies keeping the molecule fixed at a certain z value. This however limits the possible studies that can be carried out on this system, preventing for instance the diffusion rates calculations presented in Chapter 6. To the best of our knowledge, the first work treating a diatomic molecule moving along a SWCNT in a full quantum framework was the study of the rigid OH radical along a (10,0) SWCNT by Skouteris and Laganà in 2013, but that line of research was not further explored. Here we present two methodological works which explicitly include motion along the nanotube's axis. The first study consists on the assessment of the coupling between the diffusion coordinate, z, and the remaining DOFs of the confined molecule. The results obtained led us to a second work which we develop a scheme to perform quantum dynamics propagations beyond 20 ps.

The work presented in **Publication 3** conforms the first study in which a full–dimensional Hamiltonian is used to simulate the motion of a H$_2$ molecule along a SWCNT. The main objective of such work was to confirm the assumption of negligible coupling between confined and unbound degrees of freedom by taking advantage of the overlap function tools (Chapter 5). In order to do so, we built a set of initial wave functions by diagonalizing the adsorbate's Hamiltonian in a harmonic trapping potential, so that they were restricted to a certain region of space. Then gave them a certain amount of linear momentum, propagated them in time without the trapping potential, and studied the outcome of such propagations. The idea behind this setup was to see how the shape of the wave function changed between two equivalent points of the nanotube: if the system were perfectly separable into confined and unbound degrees of freedom, then the wave function after the propagation would be equivalent to the initial state. The quantitative assessment of the coupling between the two sets of DOFs was made by taking advantage of the overlap function

tools developed previously, and presented in Chapter 5 and computing the convolution function of the propagated functions with the initial static eigenstates at different points along z. The results of this first study confirmed the quasi–separability of the system, and therefore the possibility to develop a time–scale separation of the variables based on the adiabatic theorem. This theorem states that, in case of smooth changes in a PES, the quantum numbers of a given state are maintained after a propagation. This paves the way to applying a Born–Oppenheimer–like scheme to the case of a confined molecule diffusing in a nanocavity, separating the fast, short amplitude motion in the confined degrees of freedom from the low–amplitude diffusion motion. After following this idea, we obtained the two Hamiltonian representations presented in **Publication 4**: a numerically exact *diabatic Hamiltonian*, and an approximate but very accurate *adiabatic approach* for the propagation. Both schemes proved to be successful in reproducing and improving diffusion rates calculations carried out previously, as it has been seen in Chapter 6. For this reason they have been used in further developments aiming at the inclusion of the phonons of the nanotube in the description of the system, which will be the subject of Chapter 8.

7.2   Result Discussion

7.2.1   Study of the coupling between confined and unbound degrees of freedom

This Section summarizes the contents of **Publication 3**, included in this Thesis as Section 7.3.

Following a philosophy similar to the work presented in Chapter 5 and **Publication 1**, the aim of this work was to qualitative and quantitatively measure the amount of coupling between the set of confined DOFs (hereby denoted by q) and the z coordinate. As already explained in the previous Section, the correlation between q and z was examined by building particular wave functions and analyzing their shape during their propagation along the nanotube.

The generation of the initial states was made by mimicking an experimental laser trapping setup. In this technique, a laser beam would fix the position of a given molecule at a certain point of the nanotube. This was simulated by the addition of a harmonic potential only in the z dimension which prevented the motion along the structure. The force constant of the trapping potential was chosen so that 10 eigenstates could be computed without generating translational excitations in the z coordinate. With this setup, the resulting stationary states were close to the direct product of the 5D eigenstates already studied in Chapter 5, times a ground state harmonic oscillator function in the unbound coordinate. Once the initial states were obtained, the harmonic potential was removed and the functions were propagated in time according to the 6D Hamiltonian of Section 4.2. In order to accelerate the propagations, we artificially added a certain linear momentum in the z and x coordinates by means of a vector with impinging angle α with respect to the nanotube's axis. The module of the vector was chosen to be of 25.6 meV, so that it coincided with the most probable velocity value of a particle, according to a Maxwell–Boltzmann distribution, at a reference temperature of 298 K.

The qualitative measure of the correlation between q and z was made by direct observation of the time evolution of wave function projected in each of the confined DOFs: if the coupling were low, then the wave function would not change significantly in the different confined coordinates, regardless of the changes in z. This is indeed the case, as it is seen in Figure 7.1, where the projection of the ground state
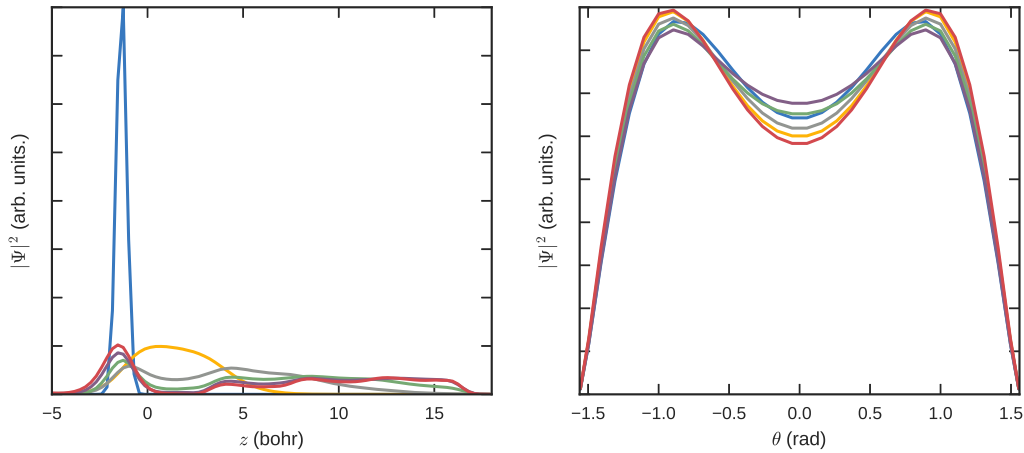
FIGURE 7.1: Projection of the 6D wave function onto the z (left) and θ coordinates (right) for times t=0 (blue), 100 (yellow), 200 (grey), 300 (green), 400 (purple) and 500 fs (red).

wave function of H_2 onto θ and z is shown at different propagation times, with an added momentum of 25.6 meV and an impinging angle of 45°. It is clear from this Figure that the motion along the z coordinate has only a very limited effect on the rotational distribution of the wave function. The other DOFs where checked, leading to similar or even lower levels of distortion. In the case of coaxial motion along the nanotube ($\alpha = 0°$) the distortions were still less noticeable than in the case of an impinging angle of $\alpha = 45°$. In all cases there was a clear and direct correspondence between wave packet at any propagation time and its initial states, which reinforced the idea that the coupling between the confined and unbound degrees of freedom was small.

The qualitative study of the coupling already hints at the quasi–separability of the system in q and z. However, the setup of the propagation allows us to go further an perform a quantitative analysis on this matter by adapting the overlap functions tools developed in **Publication 1**. Let us denote a set of functions computed in a trapping potential centered at z_0 as $\Phi_{z_0}(q, z)$. Since the potential is periodic, it is clear that the eigenstates would be exactly equivalent if the trapping potential were centered at a symmetric point z_0'. Let $\Psi_{z_0,n}(q, z, t)$ be the nth function of the set $\{\Phi_{z_0}\}$, propagated to a time t, so that $\Psi_{z_0,n}(q, z, t = 0) = \Phi_{z_0}(q, z)$. If there was no coupling between z and the remaining DOFs, after a propagation the q components of $\Psi_{z_0,n}(q, z, t)$ at z_0' would be the same as at $t = 0$ and $z = z_0$. It is then possible to quantitatively evaluate the amount of coupling by computing the convolution function of a propagated wave function $\Psi_{z_0,n}(q, z, t)$ with a set of static eigenstates centered at z_0', as schematically represented in Figure 7.2. These convolution functions, termed σ, are time–dependent functions yielding the overlap between the propagated wave packet, $\Psi_{z_0,n}(q, z, t)$, and the static functions $\Phi_{z_0}(q, z)$:

$$\sigma^{n,n'}(t, z_0) = \left\langle \Psi_{z_0,n}(q, z, t) | \Phi_{z_0',n'}(q, z) \right\rangle$$
$$= \int \Phi_{z_0'}(q, z, t)^* \Psi_{z_0}(q, z) \, \mathrm{d}q \, \mathrm{d}z. \tag{7.1}$$

They allow us to quantify the mixing between different eigenstates, and through it the correlation between the degrees of freedom: if the coupling were negligible,
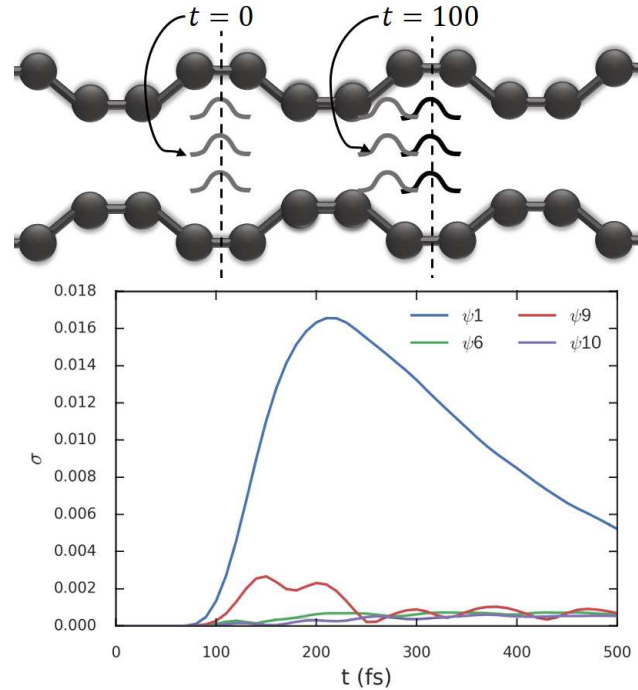
FIGURE 7.2: Schematic representation of the convolution functions calculation: a set of wave packets $\Psi_{z_0}(q,z,t)$ (grey) are computed at a certain point z_0 and evolved in time. The convolution function $\sigma^{n,n'}(t,z)$ is defined as the overlap of the $\Psi_{z_0}(q,z,t)$ functions with a set of static functions computed at $z = z'_0$, $\left\{ \Phi_{z'_0} \right\}$ (black).

all overlaps would be zero except for the one corresponding to the initial state of the wave packet. Conversely, high coupling would imply high mixing of the eigenstates, and the increase of the value of the overlaps with other eigenstates. The convolution functions computed at a distance of one unit cell from the initial center of the wave packet showed that the interstate mixing was minimal in case of coaxial linear momentum, as it is shown in **Publication 3**. On the other hand, increasing the impinging angle also increased the amount of mixing, specially for long propagation times. The comparison of convolution functions computed at different points along the z coordinate also seemed to confirm that the coupling was low, although it increased as the wave packet reached regions further away from the initial point. Finally, we also computed $\sigma(t;z'_0)$ for wave packets propagated without addition of initial lineal momentum. The resulting functions showed a mixing significantly higher than in the case of adding momentum with $\alpha = 0°$, albeit also much lower than in the case of $\alpha = 45°$, indicating that the correlation becomes more important at lower temperatures. However, all the results confirmed that the supposition of negligible coupling between the confined and unbound degrees of freedom is valid, thus justifying the time–scale separation developed in the next Section.

7.2.2   Time–scale separation between confined and unbound DOFs in the H_2@SWCNT system

The following Section presents a review of **Publication 4**, included in this Thesis as Section 7.4.

Once the coupling between the set of confined DOFs and z was shown to be small, we started to develop an approach to take advantage of this feature to reduce

the dimension of the system by the separation of time scales. The arguments used here are similar to those generally applied when deriving the Born–Oppenheimer approximation (See Section 2.1.1), namely the different characteristic times of both sets of DOFs and the adiabatic theorem.

We start by defining the z–parametrized 5D Hamiltonian, $\hat{H}^{5D}(q;z)$. The eigenstates of this operator fixed at $z = z_0$, $\xi(q;z_0) \equiv \xi^{z_0}$, correspond to the confined eigenstates analyzed in Chapter 5. We can use these eigenstates as a basis set to expand the total wave function of the system as:

$$\Psi(q, z, t) = \sum_j \psi_j(z, t) \xi_j(q; z_0). \tag{7.2}$$

Then, if we rewrite the full–dimensional Hamiltonian as:

$$\hat{H} = \hat{T}_z + \sum_{k=1}^{N_z} \left(\hat{T}_q + V_{5D}(q; z_k) \right) |z_k\rangle\langle z_k| = \hat{T}_z + \sum_{k=1}^{N_z} \hat{H}_{5D}(z_k)|z_k\rangle\langle z_k|, \tag{7.3}$$

and use Eq. (7.2), after some manipulation, one gets the *diabatic representation* of the Hamiltonian:

$$
\begin{aligned}
\hat{H}_{ij} &= \left\langle \xi_i^{z_0} | \hat{H} | \xi_j^{z_0} \right\rangle \\
&= \hat{T}_z \delta_{ij} + \sum_{k=1}^{N_z} \left\langle \xi_i^{z_0} \left| \hat{H}_{5D}(z_k) \right| \xi_j^{z_0} \right\rangle |z_k\rangle\langle z_k| \\
&= (\hat{T}_z + \varepsilon_i(z_0))\delta_{ij} + \sum_{k=1}^{N_z} \left\langle \xi_i^{z_0} | V_{5D}(q; z_k) - V_{5D}(q; z_0) | \xi_j^{z_0} \right\rangle |z_k\rangle\langle z_k|.
\end{aligned}
\tag{7.4}
\tag{7.5}
$$

Note that we have used the fact that the basis in q is z–independent, so that we can focus only on the effect of the 5D Hamiltonian, but otherwise no approximation has been made.

In this representation we can distinguish two types of operator terms. On one hand we have a 1D kinetic energy operator acting on the z coordinate, corrected with the ith eigenvalue of the 5D Hamiltonian at the reference point z_0. The representation of this corrected kinetic energy operator will therefore be a diagonal matrix. On the other hand, we have a sum of N_z terms, each one consisting on a matrix which contains all information about the coupling between the set of confined coordinates, q, and the diffusion coordinate, z, at a certain point z_k. These matrices are somehow comparable to the coupling operators appearing in the right–hand side of Eq. (2.8), seen in the context of the BO approximation. They contain the information about the non–adiabatic transitions between different 5D eigenstates. By observing these matrices we see that the coupling appears as a result of the differences in the 5D potential at each representation point z_k and at the reference point, z_0. If the 5D potential would not depend on z, then the potential energy difference matrix would become zero and the system would become separable in q and z. Otherwise we can consider two extreme cases: if there was a strong dependence of V_{5D} on z, we would have dense potential difference matrices at different z_k points which we would have to take fully into account. Conversely, in the case the dependence of the 5D potential with z was relevant, but still a smooth function (meaning that there are no points onto which the steepness of the function is large), the potential energy difference matrices would be quasi–diagonal, and we could apply the *adiabatic approximation* to our Hamiltonian. The latter is indeed the case for our system.

To apply the adiabatic approximation it is convenient to rewrite Eq. (7.2) in an

adiabatic representation, which is based on using a basis of z–dependent 5D eigenstates, $\{\xi(q; z_k) \equiv \xi^{z_k}\}$. The expansion of the total wave function then reads:

$$\Psi(q, z, t) = \sum_j \tilde{\psi}_j(z, t) \xi_j(q; z). \tag{7.6}$$

The z–dependence of the 5D eigenstates basis prevents us from factorizing the Hamiltonian operator and thus focusing on the 5D basis as in Eq. (7.5). This correlation appears as a set of derivative coupling operators, so that the adiabatic representation of the Hamiltonian therefore becomes:

$$H_{ij} = \left\langle \sum_j \tilde{\psi}_j(z, t) \xi_i(q; z) | \hat{H} | \sum_j \tilde{\psi}_j(z, t) \xi_j(q; z) \right\rangle \tag{7.7}$$

The derivative coupling terms are analogous to the potential energy difference matrices in the diabatic representation: they contain the information about the coupling between q and z. If the dependence of the adiabatic basis with z is a smooth function, then the derivative coupling terms will be close to zero. If we neglect them, we obtain the *adiabatic approximation* representation of the Hamiltonian:

$$\hat{H}_j^{(ad)} = \hat{T}_z + \sum_{k=1}^{N_z} \varepsilon_j(z_k) |z_k\rangle\langle z_k| \ . \tag{7.8}$$

We have termed the set of z–dependent eigenvalues, $\varepsilon_j(z_k)$, as *confined eigenstates Potential Energy Surface* (cePES), due to their analogy with the electronic PES. The adiabatic approximation yields an straightforward understanding of the resonance mediated diffusion discussed in Chapter 6: each cePES generates a certain number of translational eigenstates in a given unit cell, each one with a given energy. These levels are in resonance with the equivalent states in the neighboring unit cells, and thus tunneling is extremely efficient in this system. This can be seen in Figure 7.3 (adapted from **Publication 4**), where the energies of the 6D eigenstates appear as vertical lines superimposed to the CRP for the diffusion of hydrogen. The explanation is confirmed when observing that the eigenenergies of the 6D Hamiltonian are perfectly coincident with the resonance peaks appearing in $N(E)$: dotted lines represent flux 6D states without a node along the diffusion coordinate (symmetric), which resonate between the different energy minima and increase the transmission probability. Conversely, dotted lines represent states with nodal patterns between the PES critical points (antisymmetric), which when in resonance result in a decrease in $N(E)$. We can also detect non-resonant transmission states, which are those which contribute constantly to the CRP, such as the ones appearing at ≈ 36.8 and ≈ 36.5 eV, and even two Feshbach resonances around 37.5 eV. The details of the analysis of the structure of the resonances can be found in Section 7 (**Publication 4**).

Regarding the accuracy of the adiabatic approximation, our calculations show that the results obtained through this approach were in almost perfect agreement with those obtained with the formally exact diabatic representation. The $N(E)$ functions calculated using both formalism are compared in Figure 7.4. There, it becomes clear that the final results are essentially the same in both cases: resonances appear at the same energies and with similar intensities. However, it is also evidenced that the results in the diabatic representation have a significant amount of numerical noise that does not exist in the $N(E)$ obtained using the adiabatic approximation. This
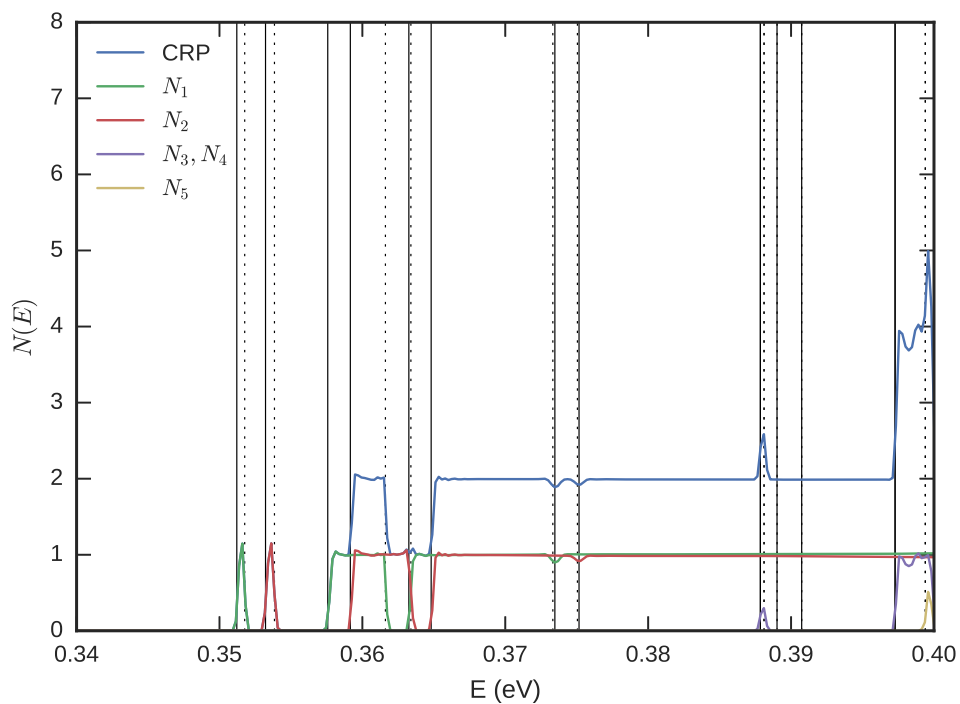
FIGURE 7.3: CRP and individual contributions of the first 5 flux eigenstates for H_2 diffusion along a (8,0) SWCNT. Vertical lines label the eigenergies of flux eigenstates symmetric (solid) and antisymmetric (dotted) along the diffusion coordinate.
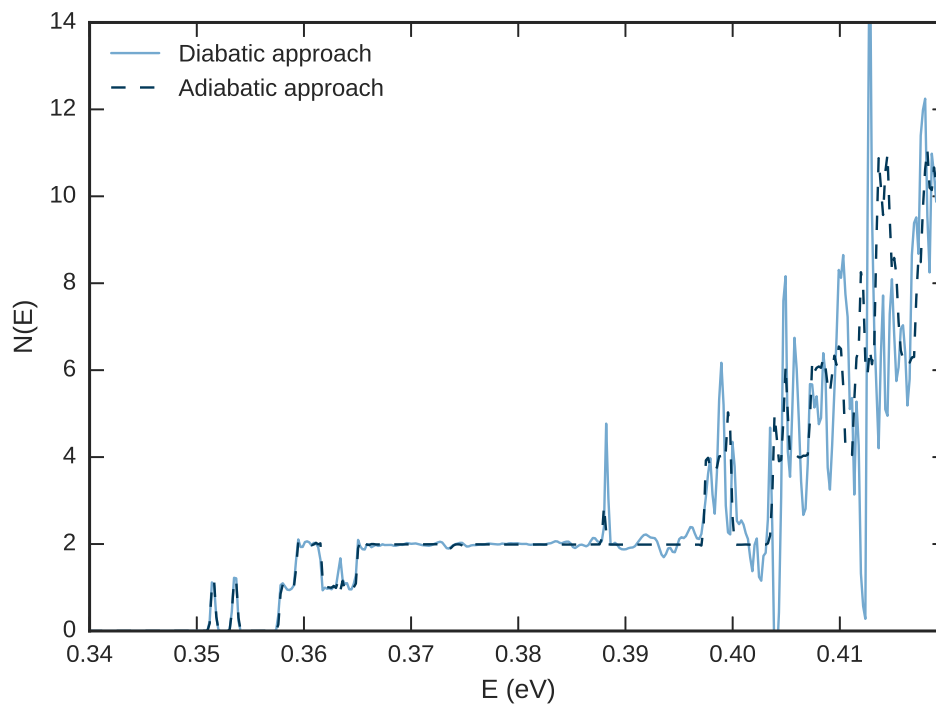

FIGURE 7.4: CRP for the diffusion of H_2 along a (8,0) SWCNT, computed through the diabatic (solid) and adiabatic (dashed) representations of the Hamiltonian.

noise tells us that the convergence of the propagation is still slightly incomplete after 20 ps This fact seems to indicate that the non–adiabatic couplings between the confined eigenstates, even though minimal, have a certain effect on the propagation of the flux eigenstates. This is not a surprising result, considering the observations summarized in Section 7.2.1, where we saw that the coupling between confined and unbound degrees of freedom began to become relevant at long propagation times. Nevertheless, the numerical noise appears at high energies, and essentially vanishes after Boltzmann averaging $N(E)$ in the whole temperature range studied, up to 150 K. For this reason, the diffusion rates obtained using either the diabatic representation of the Hamiltonian or the adiabatic approximation are numerically equivalent.

7.3   Publication 3: *Six dimensional propagation of the H$_2$ molecule confined in a Single-walled Carbon Nanotube*
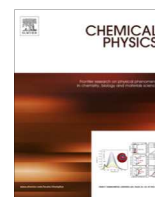
Six dimensional propagation of the H$_2$ molecule confined in a Single-walled Carbon Nanotube

Manel Mondelo-Martell, Fermín Huarte-Larrañaga *

Universitat de Barcelona, Departament de Química Física & Institut de Química Teòrica i Computacional, Spain

A R T I C L E I N F O

Article history:
Available online 3 August 2015

Keywords:
Hydrogen
Carbon Nanotubes
Storage devices
Quantum dynamics
Confinement effects

A B S T R A C T

A study on the quantum dynamics of the hydrogen molecule embedded in the hollow cavity of a Single-walled Carbon Nanotube is presented, taking into account for the first time all six degrees of freedom of the confined molecule. A set of initial eigenstates of the trapped H$_2$ molecule are propagated for 500 fs using the State Average Multiconfigurational Time-dependent Hartree approach. An initial linear momentum is added to the hydrogen molecule in order to mimic high temperature behavior, forming an angle of 0° and 45° with respect to the nanotube's axis; an additional propagation is carried out without adding any extra momentum. The wave packet dynamics are analyzed using projections and overlap functions in the appropriate degrees of freedom. The study reveals little correlation between the translation of the confined molecule along the nanotube and the remaining degrees of freedom.

© 2015 Elsevier B.V. All rights reserved.

1. Introduction

In the last few years the development of new storage devices for low-density gaseous species has become a field of intensive research. Their interest arises with two basic objectives in mind: to store large amounts of potential fuels in order to make their transport from the production centers feasible, and to capture known pollutants from the atmosphere to prevent, for instance, the greenhouse effect [1]. A paradigmatic case of potential fuel for the near future, due to its high efficiency and low impact in the environment, is hydrogen. Nanostructured materials, such as Carbon Nanotubes (CNTs) or some Metal–organic Frameworks (MOFs) show the potential to be used for this purpose [1–4]. A paradigmatic case is the research on hydrogen storage in nanostructured materials, such as Carbon Nanotubes (CNTs) or Metal–organic Frameworks (MOFs) [3,5–11], given the potentiality of this gas a fuel for the near future. Due to its large economical interest, the storage of hydrogen in nanostructured materials has been largely studied both theoretically and experimentally, specially in the last few years. The research carried out in this kind of systems has shown the effectiveness of some of these materials as storage devices. A collateral effect of gas adsorption in nanostructures is the distortion of the confined molecules at the molecular level when the cavities in which they are trapped are of the order of the nanometer. These distortions, which are changes of the

electronic structure and the dynamics of confined species, were first studied by Beenakker [12] et al. in the middle 90s. In the early 2000s relevant studies of the hydrogen molecule in confining environments, including a quantum treatment of the nuclei, were carried out by Yildirim et al. [7,13,14] in different carbon structures. Gray and co–workers latter calculated the distortions in the rotation and translation of hydrogen in narrow Carbon Nanotubes using a four–dimensional model [15]. Lately, more complex studies have appeared on similar systems: the first 5–D quantum study of hydrogen in a Carbon Nanotube was carried out by one of us [16], and Bazic and co–workers have studied H$_2$ confined in different nanostructures such as metal–organic frameworks (MOFs) and endofullerenes. More recently, we carried out a rigorous analysis of the hydrogen molecule confined in different Carbon Nanotubes correlating the eigenstates of the trapped molecule with those of the free molecule [17]. The importance of these studies lies in the fact that they would not only allow a better understanding of the affinity of the confined molecules by the adsorbent, but they may also allow the discovery of new potential applications for nanostructured materials. A particularly interesting example of these novel applications are quantum sieves, which allow the separation of isotopomers of a given molecule, like H$_2$ and D$_2$, due to the different Zero-point energy (ZPE) of molecules with different mass [4,18–20]. Also, some investigations point to the possibility of controlling chemical reactions at the molecular level using nanostructured materials [21].

Our aim in this work has been to go one step further with respect to previous simulations and carry out full dimensional

---

* Corresponding author.
   E-mail address: fermin.huarte@ub.edu (F. Huarte-Larrañaga).

(6D) propagations for a single hydrogen molecule confined in an $(8, 0)$ Single walled Carbon Nanotube. Unlike Refs [7,15–17], the hydrogen molecule is here able to diffuse along the CNT axis. This is done in a fully quantum mechanical approach in order to gain insight of the quantum confinement effects at an intimate level. In spite of the number of studies in this kind of confined systems, to our knowledge few have been made which take into account the diffusion of a molecule along a nanotube [22], and this is the first one to take into account all possible degrees of freedom of the adsorbate. In order to see the coupling between the degrees of freedom when a hydrogen molecule is diffusing along the nanotube we employ the following strategy. First, a set of functions is obtained simulating the eigenstates of a trapped H₂ molecule. These eigenstates are then given a linear impulse along the nanotube axis with different impingement angles and propagated in time. The outcome of these propagations is analyzed using several tools based on wave functions projections and overlap functions to see whether the nature of the eigenstates is conserved when the confined wave packet travels along the nanotube axis.

The work is therefore structured as follows. In Section 2 the model used to describe the system is presented. Then the relevant features of the computational tools are outlined in Section 3, focusing first on the Multiconfigurational Time-dependent Hartree approach. The remainder of Section 3 describes the procedure followed in the dynamics simulation: the preparation of the set of initial states, the simultaneous propagation and the description of the tools used to analyze them. The results of the study are discussed in Section 4 and our conclusions summarized in Section 5.

2. Description of the model

Our system of study (hereafter, H₂@SWNT) consists on a single hydrogen molecule confined in the hollow cavity of a $(8, 0)$ Single-walled Carbon Nanotube. We implemented a 6–dimensional (6D) Hamiltonian within the rigid nanotube approximation, that is, we take into account explicitly all degrees of freedom (DOFs) of the hydrogen molecule, but neglect the vibration of the carbon atoms. To obtain the structure of the nanotube, a geometrical optimization of its unit cell was carried out using a B3LYP functional and a 6-21G basis set with the Crystal09 software [23,24]. The full nanotube is then represented by the concatenation of 20 unit cells, each one with a length of 8 bohr, in order to mimic an infinitely large structure and therefore minimize any edge effects.

Regarding the hydrogen molecule, the six DOFs are chosen as the internuclear H–H distance (ρ), the polar angle of the diatomic vector with respect to the nanotube's axis (θ), the azimuthal angle (ϕ), and the Cartesian coordinates of the c.o.m. of the diatom (x, y and z, being z collinear with the nanotube's axis) (Fig. 1). The 6D Hamiltonian reads:

$$\widehat{H}_{6D} = -\frac{\hbar^2}{2\mu_{H_2}} \left(\frac{\partial^2}{\partial \rho^2} + \frac{2}{\rho} \frac{\partial}{\partial \rho} + \frac{1}{\rho^2} \frac{\partial^2}{\partial \theta^2} + \frac{1}{\rho^2} \frac{1}{\sin^2 \theta} \frac{\partial^2}{\partial \phi^2} \right)$$
$$- \frac{\hbar^2}{2m_{H_2}} \left(\frac{\partial^2}{\partial x^2} + \frac{\partial^2}{\partial y^2} + \frac{\partial^2}{\partial z^2} \right) + \widehat{V}(\rho, \theta, \phi, x, y, z), \quad (1)$$

with μ_{H_2} and m_{H_2} being respectively the reduced mass and the total mass of the hydrogen molecule. Hence, all degrees of freedom are explicitly defined and all couplings allowed.

The potential energy term is a 6 dimensional function of the coordinates of the hydrogen molecule. Since the Van der Waals interactions are the ones ruling the behavior of the system, we represent the potential energy surface (PES) as a sum of Lennard–Jones pair potentials — as done in previous studies on similar systems [15–17]—. Additionally, the covalent interaction between the
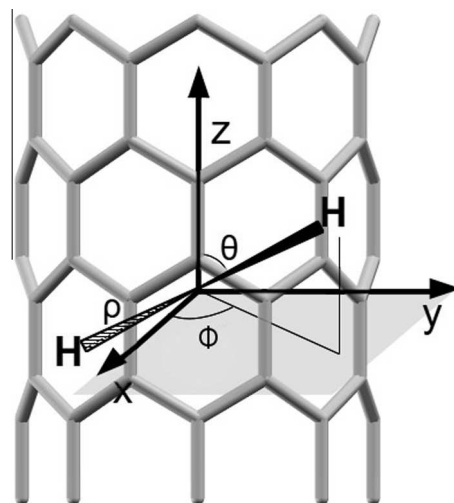

Fig. 1. Scheme of the DOFs considered in the present work.

hydrogen atoms is represented by a Morse potential [25]. The PES then has the form:

$$\widehat{V}_{6D} = V_{H-H}(\rho) + V_{C-H}(\rho, \theta, \phi, x, y, z), \quad (2)$$

$$\widehat{V}_{C-H}(\rho, \theta, \phi, x, y, z) = \sum_{i=1}^{2} \sum_{j=1}^{Nc} V_{i,j}^{IJ}(d_{H_i-C_j}), \quad (3)$$

with parameters $D_e = 0.1746$ Hartree, $a = 1.0271$ bohr^{-1} and $R_e = 1.4$ bohrs for the Morse potential, and $\epsilon = 2.82$ Å and $\sigma = 0.0605$ kcal/mol for the Lennard–Jones interaction. See Ref. [17] for a discussion about the suitability of these parameters.

3. Simulation details

3.1. Wave function representation

The propagations have been carried out using the Multiconfigurational Time-dependent Hartree (MCTDH) approach [26,27]. This method allows an efficient propagation of multidimensional wave packets due to the use of a two-layer representation for the wave functions: a relatively small basis set of time-dependent, low-dimensional basis functions, known as Single-Particle Functions (SPFs, $\varphi_{j_k}^{(k)}(Q_k, t)$), which in turn are expanded in a time-independent basis of primitive functions. The *Ansatz* is then constructed as a sum of configurations, each one being a Hartree product of SPFs:

$$\Psi(Q_1, \ldots, Q_p, t) = \sum_{j_1=1}^{n_1} \cdots \sum_{j_p=1}^{n_p} A_{j_1 \cdots j_p}(t) \prod_{k=1}^{p} \varphi_{j_k}^{(k)}(Q_k, t). \quad (4)$$

And the representation of the SPFs on the primitive basis of time-independent functions reads:

$$\varphi_j^{(k)}(Q_k) = \sum_{l=1}^{N_k} a_{l_j}^{(k)} \chi_l^{(k)}(Q_k), \quad (5)$$

where the χ functions are usually a Discrete Variable Representation (DVR) or Fast Fourier Transform (FFT) grid. Eq. 4, in combination with the Dirac-Frenkel variational principle, yields a system of coupled equations of motion for the system which must be integrated to solve the dynamics of the problem. This two-layer approach allows an important decrease of the size of the matrices during the integration of the equations of motion.

Another conceptual advantage of the MCTDH approach is that, since the wave function is represented as a sum of configurations, the correlation between the degrees of freedom is readily seen by the coefficients of the linear combination: for a separable system without correlation between the degrees of freedom, a single Hartree product would be enough to describe the whole system. This tool can therefore be used to analyze qualitatively the coupling between the degrees of freedom.

In the present work we have used a particular variant of the MCTDH approach: the State Averaged MCTDH method (SA-MCTDH) developed by Manthe [28]. This scheme allows the simultaneous propagation of several independent wave packets under a orthogonality constraint in a way that, in general, this simultaneous propagation is more efficient than the propagation of the individual wave packets. This method is particularly useful to obtain nuclear eigenstates of a given system by successive application of the Boltzmann operator [28,29]. In our calculations we have taken advantage of both particularities: the Boltzmann operator has been used to obtain a set of physically meaningful states, and these states are next propagated simultaneously –this simultaneous propagation being more efficient than the individual propagation of multiple wave packets–.

In our model, each degree of freedom is represented by a set of 1D SPFs. The primitive basis sets, listed in Table 1, are chosen as a FFT equidistant grid for the ρ, ϕ, x, y and z DOFs. For the remaining degree of freedom (θ) the cot–DVR [30] is used in order to avoid a singularity in the $\frac{1}{\sin\theta}$ term of the Hamiltonian (see Eq. 1).

Regarding the SPF basis two comments ought to be made. First, comparing the size of the primitive and SPF basis, the computational saving introduced by MCTDH with respect to standard wave packet approaches is evident. Secondly, the degrees of freedom with more correlation require a higher SPFs basis in order to take all this effects into account. Thus, from our converged MCTDH basis it can be predicted that the most correlated DOFs are the x, y translations and the rotational coordinates while vibration remains essentially uncoupled in our simulations.

Finally, a quartic complex absorbing potential (CAP) with length 4 Å has been added in the z coordinate in order to prevent any aliasing of the wave packet when it reaches the edge of the simulation grid.

3.2. Initial state calculation

Since solving the Time-dependent Schrödinger equation is an initial value problem, it is important to obtain physically meaningful initial states in order to extract correct information from a propagation. This initial state could be constructed, following the approach in Ref [22], as a direct product of the eigenstates of a free hydrogen molecule for the internal coordinates (ρ, θ and ϕ) and Gaussian functions for the c.o.m coordinates (x, y and z). However, as shown in a previous study [17], there are important deviations from this separable model when the hydrogen molecule

is confined in a (8,0) CNT. Therefore, in order to obtain more realistic initial states for the propagation, the initial states were calculated directly as eigenstates of the H_2 confined molecule. Given that the potential is essentially unbound along z, a virtual harmonic potential was added in this degree of freedom, centered in the center of a unit cell, where the potential energy is a minimum (Fig. 2). This potential allows us to artificially *trap* the gas molecule and obtain eigenstates, with only small dispersion along the z dimension but taking into account all possible distortions due to the effect of the confining potential and the coupling between the degrees of freedom. Based on the results of the 5D calculations on the same system found in Refs [16,17], the force constant for the virtual *trapping* potential was chosen to be 200 cm^{-1}, in a way that there were no excitations in the z coordinate for the first 10 excited states of the trapped system. The details on the SPF basis set used to compute these eigenstates is shown in the first column of Table 2. Note that due to the large force constant used in the trapping potential, a single SPF can be used in the z coordinate. Employing this basis set, the SA-MCTDH scheme was applied to diagonalize the Boltzmann operator at a reference temperature of 300 K. After 20 iterations the energies of a total of 11 states were converged. These are all eigenstates significantly populated at 298 K according to a Boltzmann thermal distribution.

3.3. Propagation of the initial states

The states obtained as reported above have a very low initial linear momentum in the z coordinate and are therefore not well suited for time propagation. In order to simulate the diffusion of the hydrogen molecule inside the nanotube, the linear momentum distribution of H_2's c.o.m in the z coordinate was shifted to match a mean value of 25.6 meV, with an indetermination of 9.39 meV. This energy value corresponding to the most probable kinetic energy of a particle with mass m_{H_2} following a Maxwell–Boltzmann distribution at a temperature of 298 K.

Two sets of propagations were run with different impinging angles α between the linear momentum vector and the nanotube axis: 0° and 45°. For each set, the propagation of the set of initial wave packets was carried out simultaneously during a total of 500 fs. For angles α significantly larger than 45°, the repulsion coming from the nanotube walls proved to be too large for a satisfactory convergence of the calculation, and therefore no propagations were carried out beyond this limiting value.

Although one may naively employ the same MCTDH basis employed in the eigenstate calculation, we expect distortions of the wave functions as it evolves along the nanotube axis. This will basically the case in the z coordinate where the potential energy landscape changes drastically but also in the x and y DOFs for the $\alpha = 45°$ case. For this reason the SPFs basis set used to generate the initial states was expanded in order to provide a flexible enough basis and allow for the convergence of the calculations. See in Table 2 the MCTDH basis set representation in the $\alpha = 0°$ (second column) and $\alpha = 45°$ (third column).

3.4. Analysis of the wave packets

The dynamics propagation of the H$_2$@CNT eigenstates is studied following two different and complementary approaches. Since the direct observation of the full wave function evolution is not possible due to the high dimensionality of the wave packets, the first tool at our disposal is the projection onto relevant subspaces. This projection allows us to reduce the dimensionality of the functions, yielding a result which can be plotted and visualized:

$$|\Psi|^2(\vec{r}, t) = \langle \Psi(\vec{R}; \vec{r}, t) | \Psi(\vec{R}; \vec{r}, t) \rangle, \tag{6}$$

Table 1
Numerical details of the MCTDH wave function basis set: n_i labels the SPF basis set size, N_i the primitive basis set size, (q_{min}, q_{max}) correspond to the representation grid edges and $\langle q_i \rangle_0$ the initial position expectation value. Magnitudes are given in bohr or radians, correspondingly.

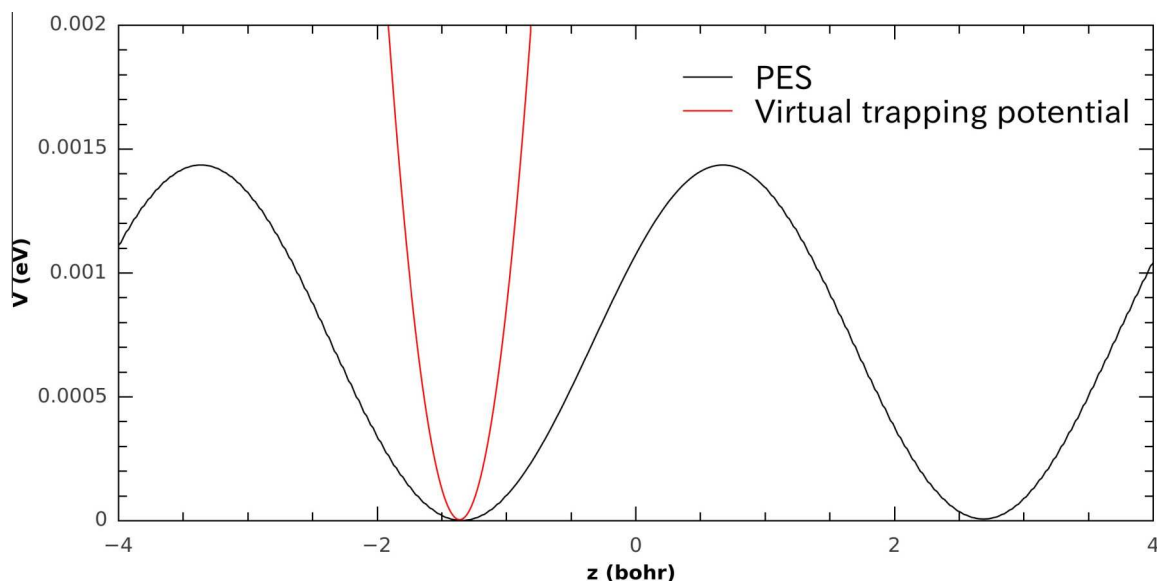| q_i	n_i	q_{min}	q_{max}	N_i	$\langle q_i \rangle_0$
ρ	2	0.5	5.0	32	1.41
θ	5	0.0	π	64	$\pi/2$
ϕ	6	0.0	2π	64	0.0
x	4	−3.5	3.5	32	0.0
y	4	−3.5	3.5	32	0.0
z	5	−18.0	18.0	128	−1.36

Fig. 2. Representation of the projection of the PES in the z dimension (black) and the virtual trapping potential (red). (For interpretation of the references to color in this figure legend, the reader is referred to the web version of this article.)

Table 2
Basis set size (n_i) in the different degrees of freedom (q_i) for the three calculations in the present work: initial state calculation with trapping potential, and propagation of a set of wave packets with $\alpha = 0°$ and $\alpha = 45°$ initial conditions.

	Iterative diagonalization	Collinear propagation	$\alpha = 45°$ propagation
q_i	n_i	n_i	n_i
ρ	2	2	2
θ	4	5	5
ϕ	6	6	6
x	4	4	5
y	4	4	5
z	1	5	5

where $\vec{R}$ and $\vec{r}$ represent the integrated and the projection subspaces, respectively.

Through this method we are able to extract relevant information about particular degrees of freedom of the system, but on the other hand it may also cause the loss of detailed information regarding, for instance, the coupling between the different degrees of freedom. In order to overcome this limitation and be able to gain insight on the coupling and how energy is transferred among the DOFs, we have analyzed how the character of the H_2 initial eigenstates is conserved throughout the propagation, by calculating the overlap, $\theta(z)$, between the propagated functions, Ψ, and a set of *static* H_2 eigenstates computed at several points along the nanotube axis, Φ:

$$\sigma(z,t) = \langle \Psi(\vec{R};z,t) | \Phi(\vec{R};z,t) \rangle$$
$$= \int \Psi(\rho,\theta,\phi,x,y,z,t)^* \Phi(\rho,\theta,\phi,x,y,z,t) d\rho d\theta d\phi dx dy \quad (7)$$

where $\vec{R}$ stands for the degrees of freedom taken into account for the overlap. The Φ eigenstates are obtained following the same procedure described in Section 3.2 only the value of z_0 in the trapping potential is changed. The overlap between the propagated wave packet and these reference functions tells us about the distortions of the wave packets when they travel along the nanotube: if a one-to-one correspondence between the wave packets and the bound states was found, that would mean that there are no distortions of the eigenstates due to the propagation along the nanotube, and therefore that the coupling of the z DOF with the remaining 5 is

negligible. Oppositely, a large coupling would lead to a strong mixing of states during the propagation. It should be mentioned that we calculate a partial overlap function, since we integrate only in the subspace complementary to the z DOF, and therefore the overlap will depend on the total value of the wave function in that point, thus allowing us to focus the analysis on the relevant areas of the propagated wave packet at each time step. This analysis is done at several points along the z coordinate to detect how the H_2 states are distorted as they evolve along the nanotube.

4. Discussion

Employing the SA-MCTDH approach and the parameters details in Sections 3.2 and 3.3 the first 11 eigenstates of the H_2@SWCNT system were converged for a z value of the trapping potential, $z = -1.36$ bohr, corresponding to the center of a nanotube unit cell. The corresponding eigenenergies relative to the ground state are listed in Table 3. The reported energy values are in complete agreement with those of previous 5D calculations shown in Refs [16,17]. Table 3 also contains the energies of the eigenstate calculations at values of $z = 0.73$, 2.73, 4.73 and 6.74 bohr, corresponding to alternating minima and maxima. As expected, due to the small

Table 3
Computed eigenenergies (cm^{-1} units) of the H_2@SWNT system with the H_2 trapped with an harmonic potential centered at different points along the z coordinate. Ground state energies given in the first row, energy increments given for the remaining of states.

State	ΔE (cm^{-1})				
	$z = -1.36$	$z = 0.73$	$z = 2.73$	$z = 4.73$	$z = 6.74$
0	2744	2798	2744	2798	2798
1	71	58	58	58	71
2	157	175	175	175	157
3	157	175	175	175	157
4	253	270	270	270	253
5	253	270	270	270	253
6	396	434	434	434	396
7	409	435	435	435	409
8	409	436	436	436	409
9	428	443	448	448	428
10	430	472	468	468	430

corrugation of the potential along the z coordinate, the eigenenergies calculated at several points of the nanotube present only minor differences among them in terms of energy (tenths of wave numbers between calculations at maxima and minima). Note that the zero point energy for this eigenstates includes ~ 200 cm^{-1} corresponding to the ZPE of the harmonic trapping potential added.

As detailed in Section 3.3 the resulting initial eigenstates are next prepared for the time propagation. In order to do that, first a linear impulse is given in the z DOF and second the SPF basis of the MCTDH wave function is expanded. Two sets of propagation have been carried out here, one simulating a set of confined H$_2$ eigenstates traveling collinearly along the nanotube axis ($\alpha = 0°$) and an average thermal translational energy of 298 K, and second set with same energy content but an impinging angle of $\alpha = 45°$. In both cases, the MCTDH wave function was propagated during 500 fs. In the case of the $\alpha = 0°$ propagation, the calculation implied 216 h of clocktime in a 12 core processor. For the $\alpha = 45°$ propagation, the required time was 190 h.

4.1. Projection analysis

The projection of the wave packet sets on the z coordinate shows that the corrugation of the nanotube, even though it is quite small, has a deep effect on the dynamics of the system: the wave packet does not advance as it would for a free particle, even with a considerably high kinetic energy (26 meV), but has to overcome periodic potential barriers (~ 8 meV) which give a clear structure to the function. As an illustrative example, Fig. 3 displays four snapshots of the z-projection of the ground state wave packet for $\alpha = 0°$ at 0, 100, 200, and 500 fs superimposed to a schematic projection of the PES is also given (dashed line). The initially localized wave packet spreads as the propagation goes on, gaining structure due to the presence of the periodic potential. The projections also show that this propagation time is enough to separate the whole the wave packet in two fractions: the one which has enough energy to overcome the potential energy barrier created by the corrugation of the nanotube, and the one which does not have the necessary energy. The fraction of the wave packet trapped in the initial potential energy well can be estimated integrating over the region of the z coordinate which delimitates this well (from -3.34 to 0.74 bohr). In the case of the collinear ground state, we find that approximately a 23% of the initial wave packet remains trapped in the initial potential energy well after 500 fs. The amount of wave packet trapped after the propagation is related to the overall shape of the initial wave packet, since the probability distribution in the different coordinates will affect the potential felt by the whole hydrogen molecule (Table 4). This means that some wave packets, with a higher probability density in areas of the PES which are more strongly repulsive, will have to overcome higher potential barriers than others. In this respect, note for instance that the first excited state, whose wave function presents a node in the $\theta = \pi/2$ plane, is the one with less fraction remaining trapped in the well. On the other hand, for other states with a high probability density in this region the fraction of wave function remaining in the well becomes much higher.

Concerning the remaining coordinates of the system, the respective projections show a very small variation in time, which points to a low coupling between the z coordinate and the other five DOFs. This is explained by the small corrugation of the potential along the Carbon Nanotube: unlike the barrier posed for the rotation along θ and the confining potential in x and y, which are large enough to generate a coupling between the degrees of freedom [17], the changes of the PES in z are not strong enough. This lack of correlation is further confirmed by studying at the population of the last occupied natural SPF in the different DOFs as a
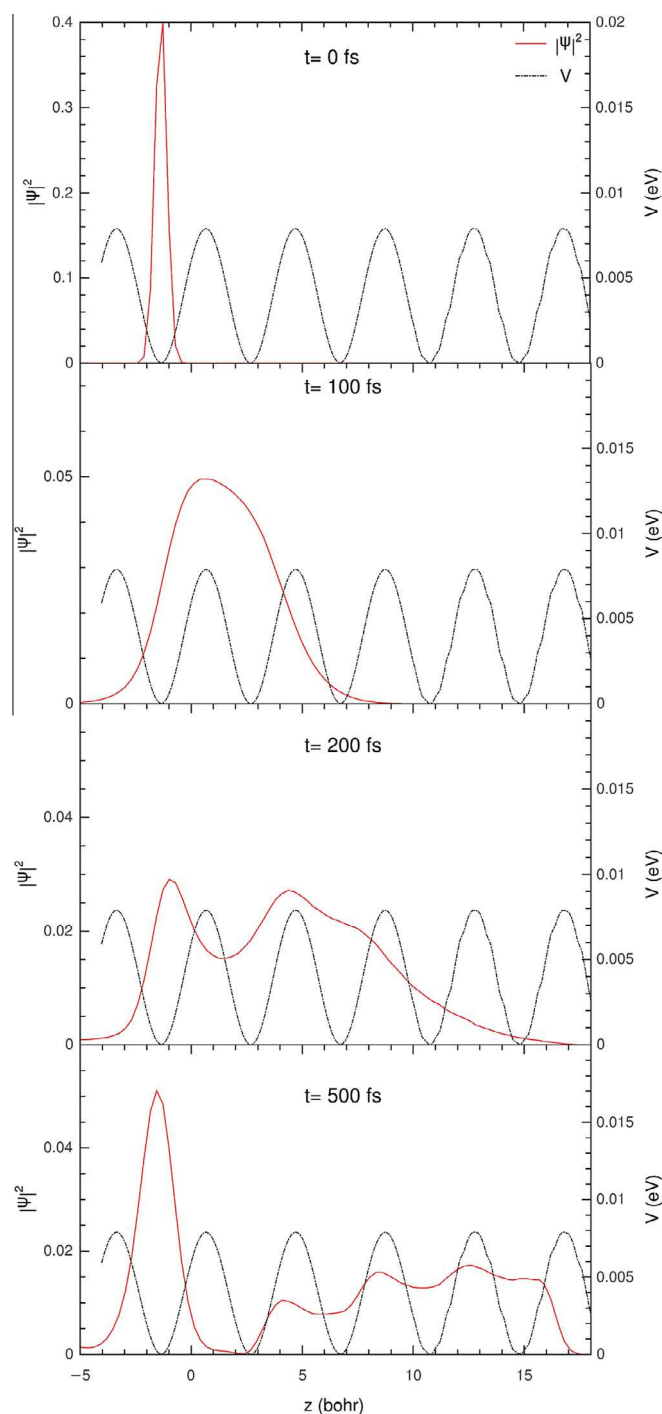

Fig. 3. Several snapshots of the propagation using the bound ground state as the initial state, projected on the z coordinate. The wave packet gains structure as time advances. Note the change of scale on the axis corresponding to the probability density.

function of time: we see clearly that the changes are of the order of 10^{-3}, which is pretty much insignificant.

Increasing the impinging angle to 45° changes significantly the outcome of the propagation to what the projection on the z coordinate is concerned. This projection is shown in Fig. 4 together with the projection of the PES for 4 different time instants. As expected, since there is less effective linear momentum along the z coordinate, the amount of wave packet which remains trapped is significantly higher: around 36% for the ground state, and up to 43% for

Table 4
Percentage of the probability density of the different wave packets that remains in the initial potential energy well after 500 fs of propagation.

α = 0°				α = 45°			
State	% in well	State	% in well	State	% in well	State	% in well
0	23	5	26	0	36	5	41
1	20	6	32	1	32	6	37
2	27	7	28	2	43	7	36
3	27	8	28	3	43	8	40
4	26	9	33	4	42	9	35

some excited states. Moreover, the distortions observed in the remaining degrees of freedom are much stronger in this case than in the previous one. The initial wave packet has a linear momentum partially pointing to the nanotube wall, and explores a region of the PES with much more corrugation along the z axis. In this new landscape, the correlation between the different degrees of freedom, mainly z, x and θ, is increased. In Fig. 5 we can see the projection of the ground state wave packet with impinging angle 45 in the θ dimensions at four different time instants. These projections show how the probability distribution in θ changes in time due to the coupling with z.

4.2. Overlap study

As discussed earlier, the projection of the projected wave packets in different coordinates allows for an intuitive qualitative interpretation of the propagation, but misses more detailed information about the couplings between the degrees of freedom and the energy exchange between them. This information can be obtained by comparing the projection of the wave packets at different times with a set of static eigenstates. These states are obtained using the same trapping potential as in Section 3.2, but centered at different z values.

The overlap between the propagated wave packet and this set of static eigenstates is analyzed from two different points of view. In the first place, we focus our attention on how crossing a complete unit cell of the nanotube affects the wave packets. In order to do this, the static eigenstates are computed at $z = 6.74$ bohr, which is an equivalent point to the initial position of the wave packet ($z = -1.36$ bohr) in the neighboring unit cell. On the other hand, we are also interested on how the possible changes in the wave packets are produced. To study this, we perform the same overlap calculation with static eigenstates corresponding to several points along the z coordinate. These analysis points were selected at the critical points of the unit cell, *i. e.* the potential maxima ($z = 0.74$ and 4.73 bohr) and minima ($z = 2.73$ and 6.74 bohr). Through this approach we intend to see if the mixing occurs mainly in certain points along the nanotube, or if it is a gradual change.

The changes on a wave packet after crossing a whole unit cell are shown in Figs. 6 and 7, where we show the overlap functions between the ground state wave packet and the most relevant elements of the set of static eigenstates, computed at the point $z = 6.74$ bohr. Again, we take the ground state propagation as a representative case, and discuss the changes between the different impinging angles, $\alpha = 0°$ and $45°$. Note that for both figures there is a clearly dominant overlap function, corresponding to the overlap between the wave packet and the reference function most similar to the initial state (upper panels), while the overlap with other eigenstates is comparatively much smaller. This trend is maintained for all the initial states propagated, and confirms the idea of small coupling discussed in Section 4.1. However, in spite of this common trend, we find significant differences between the collinear and the $\alpha = 45°$ propagation. The first difference between the propagations carried out at different conditions is seen in the
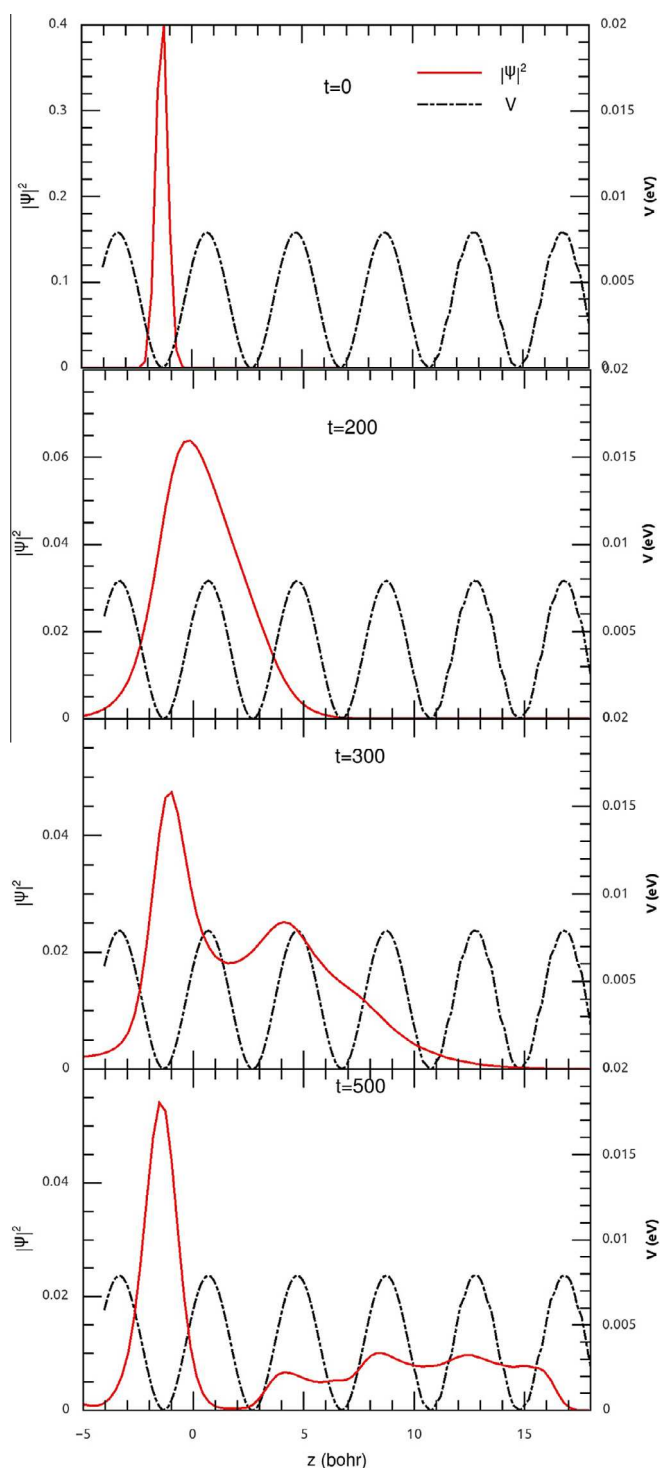

Fig. 4. Snapshots of the projection of the ground state wave packet for *t* = 0, 100, 200 and 500 fs on the *z* subspace.

overall shape of the dominant overlap function. It is readily seen that the decrease on this function is much sharper for the $\alpha = 0°$ propagation. This is again related with the effective linear momentum along the z coordinate, which is higher for this initial configuration. Regarding the remaining overlap functions, the differences between the collinear ($\alpha = 0°$) and the deviated ($\alpha = 45°$) propagations are even more noticeable. The collinear case presents almost no mixing of states in any of the states propagated, the most significant contributions arises from states 8 and 10 but in both cases is
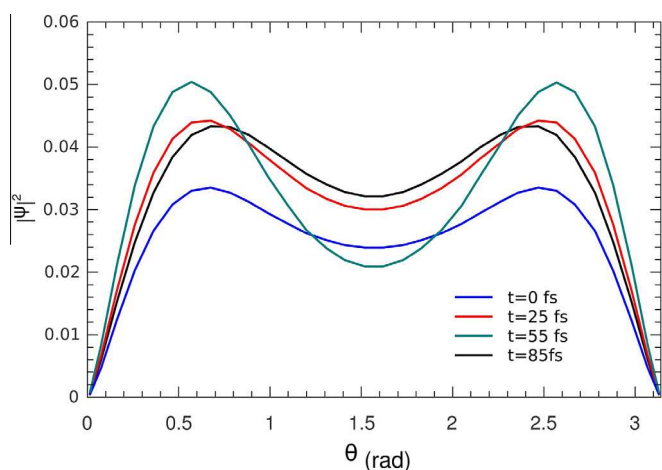
Fig. 5. Projection on the θ subspace for the ground state wave packet at $t = 0$, 25, 55 and 85 fs.
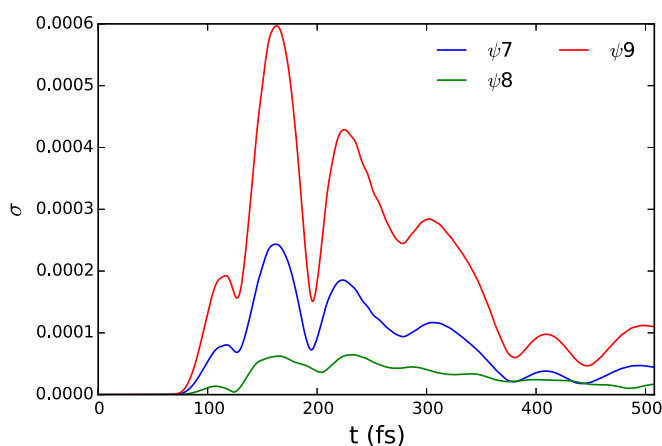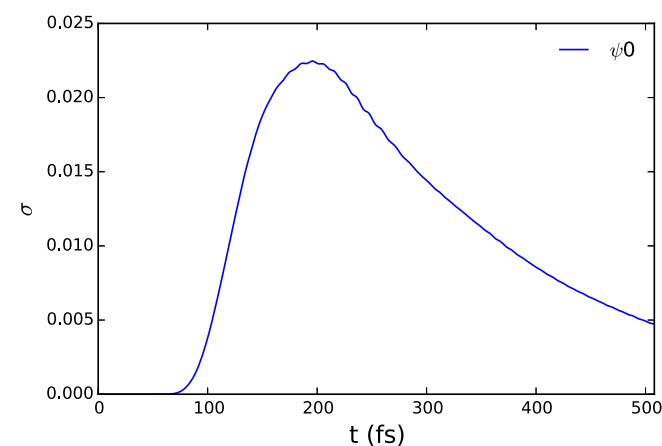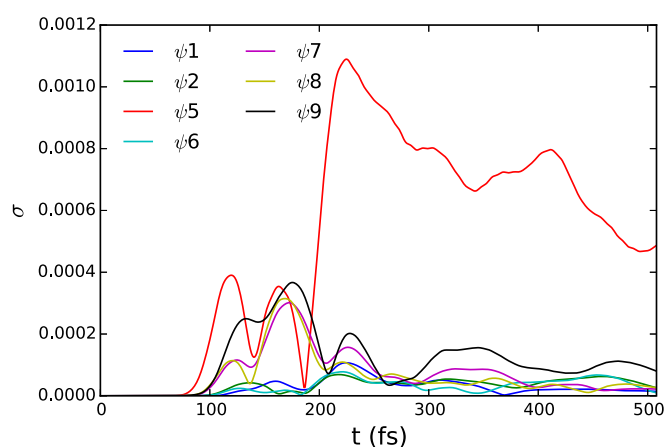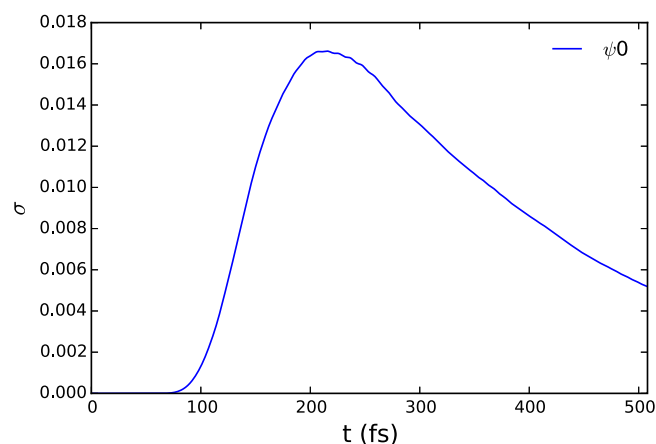

Fig. 7. Value of the overlap function of the lowest energy wave packet, with $\alpha = 45°$, with 10 reference functions at $z = 6.74$ bohr. Upper panel: main overlap function, corresponding to the ground bound state. Lower panel: overlaps of the remaining relevant overlap functions.

comparable to the GS overlap. This indicates a higher dynamical coupling and exchange of energy between the different degrees of freedom. Additionally, this coupling increases in time, as it can be seen by the fact that the main overlap function decreases, while the overlap with other states remains basically constant; t the final steps of the propagation, the proportion of mixed states reaches almost a 20%. These results are again consistent with the analysis of the projections of the wave packet.

The second part of the overlap functions' analysis, carried out at several points along the z coordinate of the nanotube, is shown in Figs. 8 and 9, again, for the ground state with both impinging angles. There, the two most relevant overlap functions are plotted as a function of time for several z values (0.73, 2.73, 4.73 and 6.75 bohr). Note again the difference in scale: the primary overlap function (upper panel) is much more relevant than the secondary (lower panel). For the primary overlap, the changes in the function seem to be mainly related with the different shape of the wave packet when it crosses the different analysis points. However, if we take a look to the secondary overlap, we see a trend not noticed before: although the shape of the function is similar in all the analysis points, the overlaps at the points corresponding to a maximum in the PES ($z = 0.73$ and $z = 4.73$ bohr) are significantly higher than the ones computed in the minima ($z = 2.73$ and $z = 6.74$ bohr). Therefore, it could be argued that the positive gradients in the PES increase the mixing of states, whether the negative gradients favor a partial recovery of the initial properties of the wave packet. Therefore, for longer propagation times and farther analysis points,
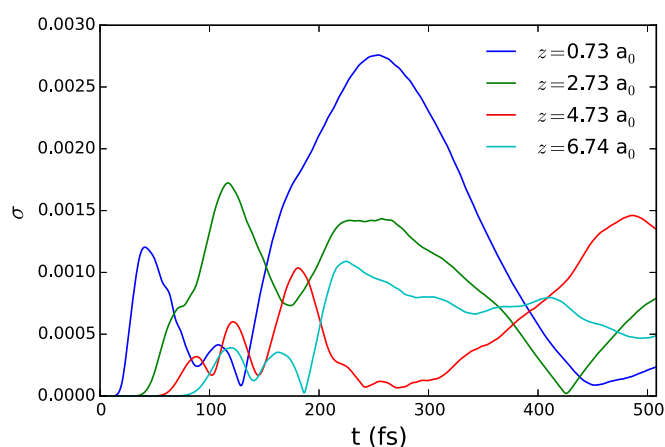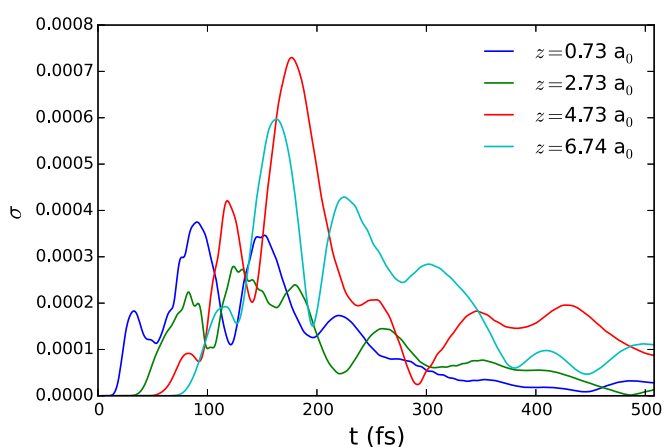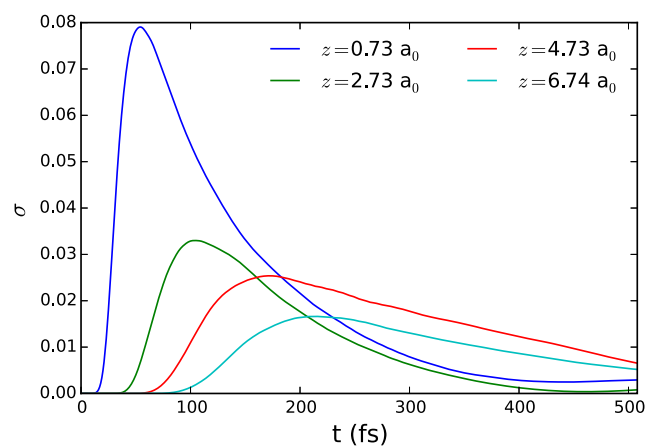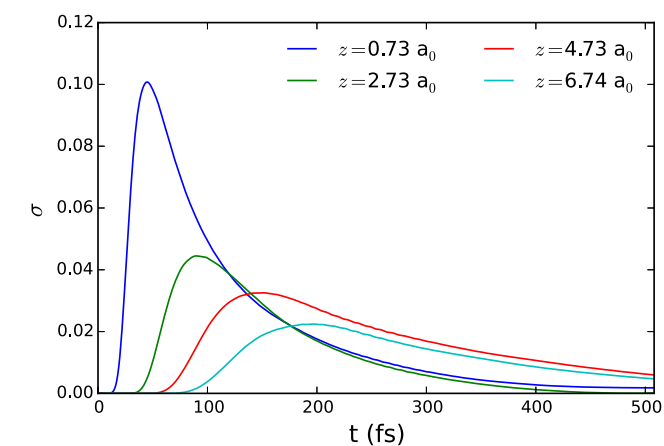

Fig. 6. Value of the overlap function of the lowest energy wave packet, with $\alpha = 0°$, with 10 reference functions at $z = 6.74$ bohr. Upper panel: main overlap function, corresponding to the ground bound state. Lower panel: overlaps for the remaining relevant overlap functions.

two orders of magnitudes smaller than the ground state contribution. This is in complete agreement with the observations made on the base of the projections in different degrees of freedom. On the other hand, in the $\alpha = 45°$ case there is a higher overlap between the wave packet and several other static eigenstates. In particular the 5th excited state at approximately 200 fs reaches a value

Fig. 8. Value of the overlap function of the lowest energy wave packet, with $\alpha = 0°$, at 4 different points along the z coordinate. Upper panel: most relevant overlap function –see Fig. 6–. Lower panel: second most important overlap function.

Fig. 9. Value of the overlap function of the lowest energy wave packet, with $\alpha = 45°$, at 4 different points along the z coordinate. Upper panel: most relevant overlap function –see Fig. 7–. Lower panel: second most important overlap function.

we should see an increase in the mixing of states, since as the wave packet travels through the nanotube, the cumulative effect of maxima and minima might blur the properties of the initial state of the propagation.

On the other hand, for the $\alpha = 45°$ propagation we see a different behavior. This can be seen in Fig. 9, which shows the two most important overlap functions for the ground state propagated with impinging angle of 45°. Note that for the final instants of the propagation the primary overlap function decreases, while the overlap with the 5th excited state, although oscillating, maintains its value. This is again prove of a higher coupling and mixing of states with respect to the collinearly diffusing H$_2$. However, the maxima-minima pattern observed for the collinear propagation is not clear anymore, probably due to the fact that there is a strong coupling between the x and θ DOFs induced by the linear momentum added to the x dimension: since this changes the area of the PES explored by the wave packet, it may result in a different potential energy landscape in which the analysis points do not correspond to critical points anymore.

Note that our simulations correspond to a high temperature frame. In these conditions, the kinetic energy of the molecules is, as we have already seen, enough to overcome the corrugation of the nanotube quite easily (even though not completely). Quantum confinement effects are known to be more noticeable at low temperatures [15,18,19]. In order to confirm this fact, we have tried to mimic an experimental setup which would allow to follow the diffusion of a single hydrogen molecule in the nanotube. This setup would use laser light to trap a molecule in a certain

region of space (as does our virtual trapping potential). Then, once the laser would be turned off (we remove our trap), the molecule would evolve freely and diffuse. To reproduce computationally this experiment, we carried out a calculation letting the system evolve freely, without modifying the momentum of the individual wave packets. Therefore, the linear momentum of the initial functions is centered at 0 eV and the simulation would correspond to the free diffusion of an eigenstate. This simulation was carried out using the same basis set as for the collinear propagation with increased initial linear momentum.

The analysis of this last propagation allows some final details of the interpretation previously presented to be discussed. Figs. 10 and 11 correspond to the same analysis of the overlap functions as the one made for translationally excited wave packets: Fig. 10 shows the main overlap functions for the propagation of the ground state at $z = 6.74$ bohr, and Fig. 11 gathers the two main overlap functions at the same four analysis points presented before. Regarding Fig. 10, we see that the shape of the main overlap function differs significantly from those of Figs. 6 and 7: it is much broader and starts to be relevant at larger time values. This is clearly a result of the smaller kinetic energy of the wave packet. This difference is even more noticeable when comparing the profiles of the overlap functions at different z points: whilst in the case of increased initial linear momentum the overall shape of the main overlap function seemed to decay smoothly, in Fig. 11 we see that it changes significantly. This shows again that the structure that the wave packets acquire during the propagation, as shown in
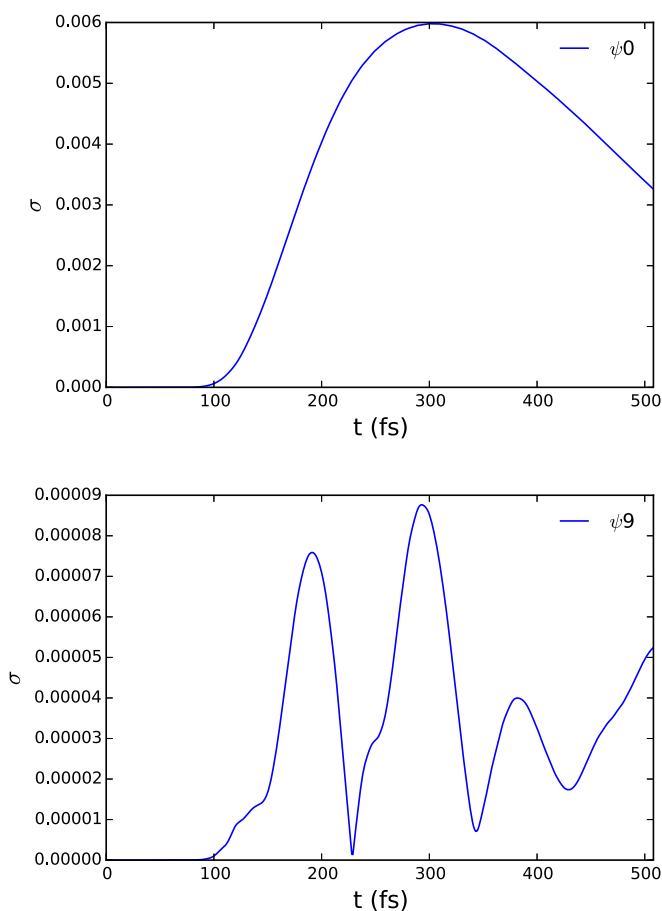
Fig. 10. Value of the overlap function of the lowest energy wave packet with 0 group velocity. Upper panel: primary overlap function, corresponding to the ground bound state. Lower panel: relevant secondary overlap function corresponding the the 9th excited state. Note the difference in the maximum of probability with respect to previous states with increased initial linear momentum.

Fig. 11. Value of the overlap function of the lowest energy wave packet, with $\alpha = 45°$, at 4 different points along the z coordinate.

Section 4.1, is much more important in this case. This is still more noticeable in some excited states like the 9th. This fact makes difficult to establish a trend in the secondary overlap functions, but in general and comparing with the systems studied with different initial conditions, the coupling is significantly higher in this case than in the collinear propagation, although not as large as in the $\alpha = 45°$ one (Fig. 10). This indicates that an increased initial linear momentum helps the wave packet to overcome the barriers with enough kinetic energy, so that the coupling is less important. On the other hand, when the wave packet has no net initial linear momentum it explores areas with less kinetic energy, which are more affected by the potential, and therefore the coupling between the DOFs is stronger.

5. Summary and conclusions

In the present work we have presented a 6D study of the hydrogen molecule confined in Single-walled Carbon Nanotubes. The system is modeled within the rigid nanotube approach, taking into account the full coupling among all of hydrogen DOFs. The use of a virtual trapping potential to compute eigenstates highly localized in the z coordinate has provided a set of 11 physically meaningful initial states for the propagation, and in full agreement with previous studies with 5D models [16,17]. The simultaneous propagation of these states using the SA-MCTDH approach has proved both efficient and rigorous.
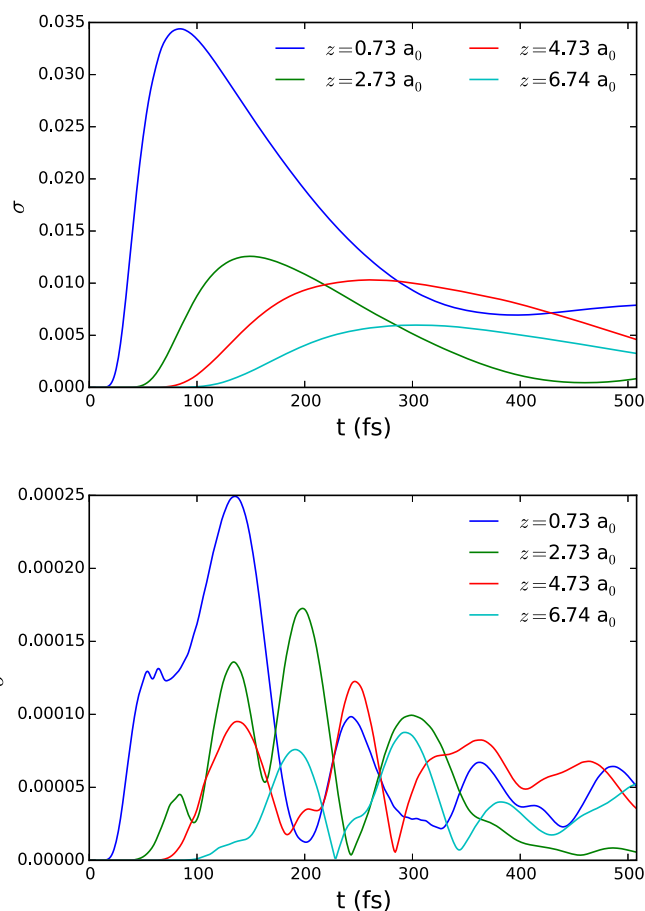
We have carried out three propagations with different initial conditions. In two of them we have added a linear momentum to the center of mass of the molecule to account for a translationally excited molecule, with average kinetic energy corresponding to 298 K. In one case, the initial momentum was directed along the z coordinate, in the other one, the momentum vector formed a 45° angle with the nanotube's axis. Finally, a propagation was made without shifting the momentum distribution, in order to mimic an experimental assembly of molecular hydrogen trapping by laser cooling. The wave function projections of the three propagations reveal a probability density structured in the z dimension, whereas the distortions on the remaining DOFs are very weak in comparison. This is taken as a first indication of the conservation throughout the propagation of the nature of each initial eigenstate. The complementary analysis relying on the calculation of the partial overlap between the propagated wave packet and sets of eigenstates calculated at different points along the Carbon Nanotube axis, allows us to quantify the coupling between the degrees of freedom, and shows that the wave packets with increased initial momentum collinear to the nanotube's axis are the ones with the smallest coupling, whether the ones with an initial momentum directed partially towards the nanotube's walls present a much higher mixing of states, although still not extremely high. The wave packets with zero group velocity lie somewhere in between the previous cases, showing that quantum effects are stronger at lower temperatures due to the lower kinetic energy of the particles.

The low coupling, in agreement with studies on similar systems [22], suggests that a mean-field scheme could be used in this

context. Its development would allow an improvement of the model by being able to find more complex and accurate potential energy surfaces and leaving the rigid nanotube approximation behind.

Conflict of interest

The authors declare no conflict of interest.

Acknowledgements

References

[1] X. Ren, C. Chen, M. Nagatsu, X. Wang, Chem. Eng. J. 170 (2011) 395.
[2] U. Mueller, M. Schubert, F. Teich, H. Puetter, K. Schierle-Arndt, J. Pastré, J. Mater. Chem. 16 (2006) 626.
[3] R.E. Morris, P.S. Wheatley, Angew. Chem. Int. Ed. Engl. 47 (2008) 4966.
[4] J.-R. Li, R.J. Kuppler, H.-C. Zhou, Chem. Soc. Rev. 38 (2009) 1477.
[5] A.C. Dillon, K.M. Jones, T.A. Bekkedahl, C.H. Kiang, D.S. Bethune, M.J. Heben, Nature 386 (1997) 377.
[6] H.-M. Cheng, Q.-H. Yang, C. Liu, Carbon 39 (2001) 1447.
[7] T. Yildirim, A. Harris, Phys. Rev. B 67 (2003) 245413.
[8] D. Henwood, J.D. Carey, Phys. Rev. B 75 (2007) 245413.
[9] J.L. Belof, A.C. Stern, B. Space, J. Phys. Chem. C 113 (2009) 9316.
[10] G.E. Ioannatos, X.E. Verykios, Int. J. Hydrogen Energy 35 (2010) 622.
[11] I. Matanovi, J.L. Belof, B. Space, K. Sillar, J. Sauer, J. Eckert, Z. Bači, J. Chem. Phys. 137 (2012) 014701.
[12] J.J.M. Beenakker, V.D. Borman, S.Y. Krylov, Phys. Rev. Lett. 72 (1994) 514.
[13] S. FitzGerald, T. Yildirim, L. Santodonato, D. Neumann, J. Copley, J. Rush, F. Trouw, Phys. Rev. B 60 (1999) 6439.
[14] T. Yildirim, A. Harris, Phys. Rev. B 66 (2002) 214301.
[15] T. Lu, E. Goldfield, S. Gray, J. Phys. Chem. B 110 (2006) 1742.
[16] J. Suarez, F. Huarte-Larranaga, J. Chem. Phys. 137 (2012) 064320.
[17] M. Mondelo-Martell, F. Huarte-Larrañaga, J. Chem. Phys. 142 (2015) 084304.
[18] C.I. Contescu, H. Zhang, R.J. Olsen, E. Mamontov, J.R. Morris, N.C. Gallego, Phys. Rev. Lett. 110 (2013) 236102.
[19] Q. Wang, S. Challa, D. Sholl, J. Johnson, Phys. Rev. Lett. 82 (1999) 956.
[20] G. Garberoglio, Chem. Phys. Lett. 467 (2009) 270.
[21] T.K. Nielsen, U. Bösenberg, R. Gosalawit, M. Dornheim, Y. Cerenius, F. Besenbacher, T.R. Jensen, ACS Nano 4 (2010) 3903.
[22] D. Skouteris, A. Laganà, Chem. Phys. Lett. 575 (2013) 18.
[23] R. Dovesi, R. Orlando, B. Civalleri, C. Roetti, V.R. Saunders, C.M. Zicovich-Wilson, Zeitschrift für Kristallographie 220 (2005) 571.
[24] R. Dovesi, R. Orlando, B. Civalleri, C. Roetti, V.R. Saunders, C.M. Zicovich-Wilson, F. Pascale, K. Doll, N.M. Harrison, I.J. Bush, P. DArco, M. Llunell, Crystal 09 user's manual, 2009.
[25] P. Morse, Review 34 (1929) 57.
[26] H.-D. Meyer, U. Manthe, L. Cederbaum, Chem. Phys. Lett. 165 (1990) 73.
[27] M. Beck, A. Jäckle, G.A. Worth, H.-D. Meyer, Phys. Rep. 324 (2000) 1.
[28] U. Manthe, J. Chem. Phys. 128 (2008) 064108.
[29] T. Hammer, U. Manthe, J. Chem. Phys. 136 (2012) 054105.
[30] G. Schiffel, U. Manthe, Chem. Phys. 374 (2010) 118.

7.4 Publication 4: *Quantum dynamics of H$_2$ in a carbon nanotube: Separation of time scales and resonance enhanced tunneling*

Quantum dynamics of H₂ in a carbon nanotube: Separation of time scales and resonance enhanced tunneling

Manel Mondelo-Martell,[1] Fermín Huarte-Larrañaga,[1] and Uwe Manthe[2]

[1]*Departament de Ciència de Materials i Química Física and Institut de Química Teòrica i Computacional, Universitat de Barcelona, C/ Martí i Franquès 1, 08028 Barcelona, Spain*
[2]*Theoretische Chemie, Fakultät für Chemie, Universität Bielefeld, Universitätsstr. 25, D-33615 Bielefeld, Germany*

Quantum confinement effects are known to affect the behavior of molecules adsorbed in nanostructured materials. In order to study these effects on the transport of a single molecule through a nanotube, we present a quantum dynamics study on the diffusion of H₂ in a narrow (8,0) carbon nanotube in the low pressure limit. Transmission coefficients for the elementary step of the transport process are calculated using the flux correlation function approach and diffusion rates are obtained using the single hopping model. The different time scales associated with the motion in the confined coordinates and the motion along the nanotube's axis are utilized to develop an efficient and numerically exact approach, in which a diabatic basis describing the fast motion in the confined coordinate is employed. Furthermore, an adiabatic approximation separating the dynamics of confined and unbound coordinates is studied. The results obtained within the adiabatic approximation agree almost perfectly with the numerically exact ones. The approaches allow us to accurately study the system's dynamics on the picosecond time scale and resolve resonance structures present in the transmission coefficients. Resonance enhanced tunneling is found to be the dominant transport mechanism at low energies. Comparison with results obtained using transition state theory shows that tunneling significantly increases the diffusion rate at T < 120 K. *Published by AIP Publishing.* [http://dx.doi.org/10.1063/1.4995550]

I. INTRODUCTION

Nanostructured materials stand as one driving force in current research, both for their interesting fundamental properties and for their potential technological applications.[1,2] Among the different phenomena appearing in the nanoscale, the structural and dynamical changes experienced by molecules adsorbed in nanometric cavities, known as *quantum confinement effects*, are of particular interest since they allow to store light gases, achieve chemical and isotopical separation of gaseous mixtures,[3,4] and even tailor the reactivity of chemical species using specific materials.[5] The understanding of these effects is of key importance when trying to design such devices.

Since the first prediction of quantum confinement by Beenakker,[6] there has been intensive research both theoretically and experimentally on systems expected to present these effects. As a result of this, the available knowledge on these systems has increased steadily in the last years. Hydrogen adsorbed in carbon-based nanostructured materials, such as fullerenes and carbon nanotubes, was among the first systems to be studied and still remain the most relevant in the literature.[3,7–22] More recently, studies have appeared focusing on different adsorbates, such as CO, CH₄, CO₂, SO₂, or H₂O, and different substrates such as zeolites and metal-organic frameworks.[7,23–28]

One particular feature present in single-walled carbon nanotubes (SWCNTs) that makes them especially interesting materials is their cylindrical shape, which gives rise to the coexistence of a 2D confinement in the space perpendicular to the nanotube's axis and unbound motion along this latter coordinate. Even though 2D confinement has been relatively studied and reviewed in the literature,[12,16,29,30] only few studies have treated both the confined and the quasi-free coordinates in a fully quantum formalism. To the best of our knowledge, only Skouteris and Laganá,[31] treating the motion of an OH radical along a (10,0) SWCNT, and some of the present authors,[32,33] dealing with the H₂ molecule in a (8,0) SWCNT, have performed such studies. The most relevant conclusion drawn from these two studies is that the quasi-free coordinate of the diatomic molecule is only weakly coupled to the set of confined coordinates. This was shown quantitatively in the case of H₂[32] through the analysis of the convolution functions of a set of 6D propagated wave packets and a set of 5D eigenstates calculated at different points along the nanotube's axis. In that study, it was seen that the state mixing between different initial states was small as the diatomic molecule progressed along the nanotube's axis. This low mixing, together with different characteristic times in the sets of confined and unbound coordinates, suggests that the fast motions of the confined degrees of freedom (DOFs) could be adiabatically separated from the slow large amplitude motions in the quasi-free coordinate.

The present work exploits the idea of separation of time scales in different ways. First, a numerically exact scheme is introduced which employs the separation of time scales to reduce the numerical effort. In this scheme, first "diabatic" basis functions describing the dynamics in the

five confined coordinates are constructed. In the wave packet dynamics calculation, the total wave function is then expanded in this discrete basis and only the motion in the unbound coordinate is described using a grid representation. Second, an adiabatic approximation which separates the dynamics in the unbound and the constrained coordinates is investigated.

The increased numerical efficiency offered by both approaches facilitates a detailed investigation of the dynamics on a longer time scale not considered by previous work by some of the authors,[32] in which the diffusion rate of H$_2$ in a (8,0) SWCNT was computed using a full 6D quantum dynamics formalism for the first time. Interestingly, the energy resolution provided by these long time simulations allows one to identify resonances corresponding to metastable states residing in the shallow potential wells along the unbound coordinate. These resonances are found to crucially enhance the transport through the carbon nanotube at low energies.

This paper is organized as follows. In Sec. II, the theoretical modeling of the H$_2$@SWCNT system is reviewed first. Then a diabatic representation of the system's Hamiltonian, which allows one to efficiently compute numerically exact results, is introduced (Sec. II B) and an adiabatic approximation separating the confined coordinates and the unbound coordinate describing motion along the nanotube's axis is discussed (Sec. II C). The description of the methodology used to simulate the wave packet dynamics and to compute the cumulative reaction probabilities (CRPs) (Sec. II E) completes Sec. II. Finally, the resulting flux correlation functions and cumulative reaction probabilities are discussed and analyzed and used to compute the diffusion rate of H$_2$ along the nanotube (Sec. III) and the main conclusions of the work are drawn (Sec. IV).

II. THEORY AND METHODS

A. The H$_2$@SWCNT system

Our system consists of a single H$_2$ molecule trapped inside the hollow cavity of a single-walled carbon nanotube (SWCNT). The nanotube, aligned along the z axis, is treated within the frozen structure approximation, i.e., the positions of the carbon atoms are fixed and vibrations are not allowed. The geometry of the CNT is obtained from quantum chemistry calculations using the Crystal09[34] software with a B3LYP functional, yielding a unit cell with 8.1 bohrs length and 12 bohrs diameter. On the other hand, we treat the hydrogen molecule inside the nanotube as a six-dimensional system, taking into account all the molecular degrees of freedom (DOFs): vibration of the H–H bond (ρ), orientation with respect to the nanotube's axis (θ), an azimuthal angle of rotation (ϕ), and translation of the center of mass (c.o.m.) of the molecule in Cartesian coordinates (x, y, and z). This coordinate system is depicted in Fig. 1. Note that, since a spherical coordinate system is used for ρ, θ, and ϕ, the volume element related to this coordinate system, dV, is

$$dV = \rho^2 \sin\theta \, d\theta \, d\phi \, d\rho \, dx \, dy \, dz.$$
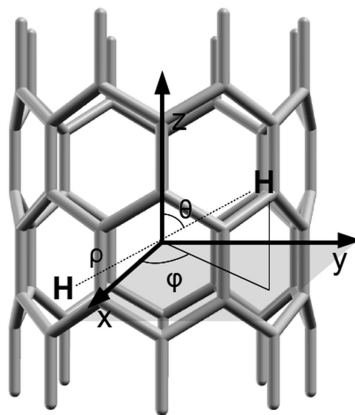
The full Hamiltonian, $\hat{H}_{6D}$, thus reads

FIG. 1. Scheme of the coordinate system used in the present work.

$$
\hat{H}_{6D} = -\frac{1}{2\mu_{H_2}} \left(\frac{\partial^2}{\partial \rho^2} + \frac{2}{\rho}\frac{\partial}{\partial \rho} + \frac{1}{\rho^2}\frac{\partial^2}{\partial \theta^2} + \frac{1}{\rho^2}\frac{1}{\sin^2\theta}\frac{\partial^2}{\partial \phi^2} \right)
$$
$$
- \frac{1}{2m_{H_2}} \left(\frac{\partial^2}{\partial x^2} + \frac{\partial^2}{\partial y^2} + \frac{\partial^2}{\partial z^2} \right) + \hat{V}(\rho, \theta, \phi, x, y, z). \quad (1)
$$

(Note that atomic units are used throughout this paper, and therefore $\hbar = 1$.)

With the idea in mind of separating the motion of the confined and the unbound coordinates, Eq. (1) can be rewritten in a compact form, taking advantage of the separability of the Kinetic Energy Operator (KEO),

$$\hat{H}_{6D} = \hat{T}_z + \hat{T}_q + \hat{V}, \quad (2)$$

with $\hat{T}_z$ being the z-dependent KEO term and $\hat{T}_q$ gathering the remaining KEO terms related with the set of confined coordinates, ρ, θ, ϕ, x, and y. For the sake of clarity, we will refer collectively to the set of confined coordinates as q.

The potential energy term, on the other hand, is not separable and couples all the DOFs. Following previous studies, the overall H$_2$-SWCNT potential is divided into a Morse term, to account for the H–H bond, and a sum of Lennard-Jones pair interactions that model the van der Waals interactions between C and H,

$$\hat{V} = V_{H-H}(\rho) + V_{C-H}(\rho, \theta, \phi, x, y, z), \quad (3)$$

$$\hat{V}_{C-H}(\rho, \theta, \phi, x, y, z) = \sum_{i=1}^{2} \sum_{j=1}^{N_C} V_{i,j}^{LJ}(d_{H_i-C_j}). \quad (4)$$

The set of parameters used in $V_{i,j}^{LJ}$ correspond to the Frankland-Brenner (FB) potential[9] with $\sigma = 5.82$ bohrs and $\epsilon = 0.0549$ hartree. This function has been used previously to define H$_2$ adsorption and confinement in carbon nanotubes by several authors.[16,19,33] Standard parameters are used in the Morse function V_{H-H}: $D_e = 0.1746$ hartree, $a = 1.0271$ bohr^{-1}, and $R_e = 1.4$ bohrs.

B. Diabatic representation of the Hamiltonian

In order to introduce a diabatic representation of our system, we start by defining a basis of states $\{z_k\}$ approximately

localized at the points z_k to represent the wave function along the z coordinate. Applying the resolution of the identity generated by this basis set onto the last two terms of Eq. (2), we obtain

$$\hat{H}_{6D} = \hat{T}_z + \sum_{k=1}^{N_z} \left(\hat{T}_q + V_{5D}(q; z_k) \right) |z_k\rangle \langle z_k|$$

$$= \hat{T}_z + \sum_{k=1}^{N_z} \hat{H}_{5D}(z_k)|z_k\rangle \langle z_k|, \qquad (5)$$

where we have introduced a *reduced 5D* Hamiltonian, $\hat{H}_{5D}(z)$, which parametrically depends on the value of z and operates on the five coordinates q describing bound motion. We can define an eigenvalue equation for this operator at a given point z_k and obtain a set of eigenstates $\xi_j(q; z_k)$ and eigenvalues, $\epsilon_j(z_k)$,

$$\hat{H}_{5D}(q; z_k)\xi_j(q; z_k) = \varepsilon_j(z_k)\xi_j(q; z_k). \qquad (6)$$

These $\xi_j(q; z_k)$ functions form a complete basis set in the reduced five-dimensional space. If the eigenstates of $H_{5D}(q; z)$ at a fixed point z_0, $\xi_j(q; z_0)$, are used as a basis to described the wave function's dependence on q, a *diabatic representation* is obtained,

$$\Psi(q, z, t) = \sum_j \psi_j(z, t)\xi_j(q; z_0). \qquad (7)$$

Here the vector of z-dependent functions $\psi_j(z, t)$ represents the motion along the quasi-free coordinate. Since the basis functions $\xi_j^{z_0} = \xi_j(q; z_0)$ are z independent, the corresponding matrix representation of the Hamiltonian operator reads

$$\hat{H}_{ij} = \left\langle \xi_i^{z_0} | \hat{H} | \xi_j^{z_0} \right\rangle$$

$$= \hat{T}_z \delta_{ij} + \sum_{k=1}^{N_z} \left\langle \xi_i^{z_0} \left| \hat{H}_{5D}(z_k) \right| \xi_j^{z_0} \right\rangle |z_k\rangle \langle z_k|$$

$$= (\hat{T}_z + \varepsilon_i(z_0))\delta_{ij} + \sum_{k=1}^{N_z} \langle \xi_i^{z_0} | V_{5D}(q; z_k)$$

$$- V_{5D}(q; z_0)|\xi_j^{z_0}\rangle |z_k\rangle \langle z_k|. \qquad (8)$$

It is useful to take a closer look at Eq. (8) in order to understand some of its properties. First of all, note that we have not included any additional approximation to go from the general Hamiltonian, Eq. (1), to its diabatic form, Eq. (5). Therefore, Eq. (8) is exact in the complete basis set limit ($N_z \rightarrow \infty$). The coupling between the confined and unbound coordinates is contained in the 5D Hamiltonian matrix. Since $z = z_0$ has been used as reference point to obtain the diabatic basis, the matrix representation of the 5D Hamiltonian is diagonal at $z = z_0$ but non-diagonal elsewhere. However, due to the low coupling between the confined (q) and unbound (z) sets of degrees of freedom, it is expected that the non-diagonal elements of the matrix will be rather small, and thus a relatively low number of $\xi_i^{z_0}$ basis functions will be enough to yield numerically accurate results.

C. Adiabatic representation of the Hamiltonian

Although the diabatic approach just presented is rigorous and numerically exact, its physical interpretation neither is straightforward nor offers us a clear picture about the

separability of the confined and unbound degrees of freedom beyond the number of basis functions needed to achieve convergence. The *adiabatic* approximation, on the other hand, can shed light on the physics of the system while, under certain circumstances, providing a reasonably accurate description of the system's dynamics.

An adiabatic representation is obtained by employing the z-dependent eigenstates of $H_{5D}(q; z)$ as a basis for the expansion of the wave function,

$$\Psi(q, z, t) = \sum_j \tilde{\psi}_j(z, t)\xi_j(q; z). \qquad (9)$$

The corresponding matrix representation of the Hamiltonian operator contains derivative couplings due to the action of the kinetic energy operator $\hat{T}_z$ on the z-dependent basis functions $\xi_j(q; z)$. To avoid the complications resulting from derivative coupling terms, numerically accurate wave packet calculations typically avoid the use of adiabatic representations.

If the adiabatic approximation is invoked and non-adiabatic transitions between the different adiabatic states $\xi_j(q; z)$ are neglected, the motion of the one-dimensional $\tilde{\psi}_j(z, t)$ can be given (approximately) by

$$i\frac{\partial}{\partial t}\tilde{\psi}_j(z, t) = \hat{H}_j^{(ad)}\tilde{\psi}_j(z, t), \qquad (10)$$

where the one-dimensional adiabatic Hamiltonian $\hat{H}_j^{(ad)}$ takes the simple form

$$\hat{H}_j^{(ad)} = \hat{T}_z + \sum_{k=1}^{N_z} \varepsilon_j(z_k) |z_k\rangle \langle z_k|. \qquad (11)$$

The above equations provide a simple physical picture: the dynamics in each *confined eigenstates*, $\left\{\xi_j(q; z)\right\}$, evolves independently on a *confined eigenstate potential energy surface* (cePES), $\varepsilon_j(z)$ onto which a quasi-particle with a single DOF, $\psi(z, t)$, evolves. Furthermore, it should be noted that the adiabatic dynamics described by these equations can be simulated with negligible numerical effort once the cePESs have been determined.

The value of cePESs at all grid points z_k can efficiently be computed by diagonalizing the 5D Hamiltonian in the diabatic representation at these grid points,

$$\sum_{n,m} U_{jn}^*(z_k) \left\langle \xi_n^{z_0} | \hat{H}_{5D}(z_k) | \xi_m^{z_0} \right\rangle U_{mi}(z_k) = \delta_{ji}\varepsilon_j(z_k). \qquad (12)$$

The unitary transformation matrix $\mathbf{U}(z_k)$ in the above equation defines the transformation from the diabatic to the adiabatic representation. The z-dependent wave packets in diabatic representation, $\psi_j(z, t)$, and the z-dependent wave packets $\tilde{\psi}_j(z, t)$ obtained from a rigorous simulation in the adiabatic basis, which can deviate from the wave packets calculated within the adiabatic approximation, are related via

$$\psi_j(z, t) = \sum_i U_{ji}(z)\tilde{\psi}_i(z, t). \qquad (13)$$

It should be noted that the only difference in the implementation of both approaches is whether the Hamiltonian matrix computed at the different grid points along z is diagonalized (adiabatic) or not (diabatic). Thus, the scheme to carry out a calculation in our system using both approaches consists of three steps:

1. Calculation of the 5D eigenstates at a chosen point along the z dimension, $z = z_0$.
2. Evaluation (and diagonalization, in the case of the adiabatic approach) of the reduced 5D Hamiltonian operator at the different values of the z coordinate grid, using the basis previously obtained. After this step, we obtain a set of 5D-Hamiltonian matrices (diabatic) or cePESs (adiabatic) at all the grid points z_k.
3. Propagation of the wave packets using the Hamiltonian matrices or the confined eigenstates potential energy surfaces.

Both the 5D eigenstates and the Hamiltonian matrices (or cePES) can be stored so that steps 1 and 2 need only to be performed just once at the beginning of the study. The stored eigenstates can be used as long as $\hat{H}_{5D}$ remains unchanged (i.e., neither the electronic potential energy nor the KEO is modified) and the grid in the unbound coordinate is maintained. The storage of the 5D eigenfunctions is particularly important, since this step is usually the most computationally demanding.

D. Time dependent quantum dynamics: Diffusion rates

Diffusion and adsorption rates stand among the most relevant observables in nanoconfined substance studies, due to the interest in the development of efficient storage devices. In the present work, we will focus on obtaining diffusion rates for the H_2 molecule inside the hollow cavity of a narrow (8,0) nanotube. Following the work of Zhang and Light,[35] diffusion rates are obtained directly from the transition rate between two potential minima through the single hopping approximation, $k_{hop}(T)$,

$$D(T) = \frac{l^2}{2d} k_{hop}(T), \qquad (14)$$

where l is the distance between adjacent potential minima and d is the dimension of the system, which equals 1 in the present work. This equation implies that thermalization due to coupling to degrees of freedom not explicitly considered in the dynamical simulations is fast compared to the hopping rate $k_{hop}(T)$. Furthermore, the hopping rate will be approximated by the rate of transition through a dividing surface separating two adjacent minima.

The transition rate through a dividing surface is calculated by the thermal averaging of the corresponding energy dependent Cumulative Reaction Probability (CRP), $N(E)$,

$$k(T) = \frac{1}{2\pi Q(T)} \int_{-\infty}^{\infty} e^{-\beta E} N(E) dE, \qquad (15)$$

where $\beta = 1/k_B T$ and k_B is the Boltzmann constant. The partition function, $Q(T)$, has been computed as the trace of the 5D Boltzmann operator of the system, $e^{\beta \hat{H}_{5D}}$, and then multiplied by the contribution of the unbound coordinate, z, obtained through the semiclassical expression for a particle in a periodic potential, $L \left(\frac{mT}{2\pi}\right)^{1/2}$ (here, L stands for the length of the unit cell and m stands for the mass of the diatom). The CRP is the sum of all (energy-dependent) transition coefficients corresponding to open channels describing passage through the barrier separating two adjacent potential minima.

The cumulative reaction probability will be computed following the *flux correlation function* approach[36–38] employing the scheme described in Refs. [39] and [40]. As a starting point, one defines the *flux operator*, $\hat{F} = i[\hat{H}, h]$, where h is a Heaviside dividing surface discriminating reactant and product geometries, and the thermal flux operator, $F_T = e^{-\beta \hat{H}/2} \hat{F} e^{-\beta \hat{H}/2}$. In the first step of the calculation, the eigenvalues f_n and eigenstates $|f_n\rangle$ of the thermal flux operator,

$$F_{T_0} = \sum_n |f_n\rangle f_n \langle f_n|, \qquad (16)$$

for a conveniently chosen reference temperature T_0 are computed. Then $N(E)$ is calculated via a Fourier transform of the correlation function obtained from the time propagation of the thermal flux eigenstates,

$$N(E) = \frac{1}{2} e^{2\beta_0 E} \sum_n \sum_m f_n f_m \left| \int_{-\infty}^{\infty} dt e^{iEt} \langle f_n | e^{-i\hat{H}t} | f_m \rangle \right|^2. \qquad (17)$$

It should be pointed out that when the dividing surface is placed at the top of the potential barrier separating both configurations, a straightforward interpretation of the nature of the flux eigenstates can be found: they correspond to the vibrational states of the activated complex of the reaction.[41,42]

If the system's dynamics shows long-living resonances, the flux correlation function $\langle f_n | e^{-i\hat{H}t} | f_n' \rangle$ converges only very slowly. To avoid excessively large propagation times, then it is preferable to compute the cumulative reaction probability with limited energy resolution. The limited resolution CRP $\bar{N}(E)$ is defined as the convolution of $N(E)$ with a Gaussian function of width ΔE,

$$\bar{N}(E) = \int_{-\infty}^{\infty} dE' \, N(E') \, \frac{e^{-\frac{1}{2} \frac{(E-E')^2}{\Delta E^2}}}{\sqrt{2\pi} \Delta E}. \qquad (18)$$

$\bar{N}(E)$ can directly be computed using the flux-correlation function present in Eq. (17),

$$\bar{N}(E) = \frac{1}{2} e^{2\beta_0 E} \sum_n \sum_m f_n f_m$$
$$\times \left| \int_{-\infty}^{\infty} dt e^{iEt} e^{-\frac{1}{8\pi^2} \Delta E^2 t^2} \langle f_n | e^{-i\hat{H}t} | f_m \rangle \right|^2. \qquad (19)$$

Here an additional damping factor appears in the Fourier integral which determines the required propagation time. If the energy resolution ΔE is significantly smaller than $k_B T$ for all temperatures considered, one can substitute $N(E)$ by $\bar{N}(E)$ in Eq. (15) without causing significant errors.

E. The Multiconfigurational Time-dependent Hartree (MCTDH) approach

The Multiconfigurational Time-dependent Hartree (MCTDH) approach[43] has been used to represent the wave function in the different quantum dynamical calculations reported in this work. The efficiency of this method lies to a great extent on the structure of the ansatz. In the MCTDH approach, the f-dimensional wave function, $\Psi(Q_1, \ldots, Q_f, t)$, is represented as a sum of Hartree products of time-dependent basis functions called Single Particle Functions (SPFs),

$$\Psi(Q_1, \ldots, Q_f, t) = \sum_{j_1=1}^{n_1} \cdots \sum_{j_f=1}^{n_f} A_{j_1 \cdots j_f}(t) \prod_{k=1}^{f} \varphi_{j_k}^{(k)}(Q_k, t), \quad (20)$$

where Q_i represent the DOFs of the system. The SPFs are in turn represented in a time-independent or *primitive* basis set, typically consisting of Discrete Variable Representation (DVR) or Fast Fourier Transform (FFT) functions,

$$\varphi_{j_k}^{(k)}(Q_k, t) = \sum_{i=1}^{N_k} c_i(t) \chi_i^{(k)}(Q_k). \quad (21)$$

One can straightforwardly see that, due to the time-dependent nature of the SPF basis set, the number of basis functions, $\prod_{k=1}^{f} n_k$, required in Eq. (20) to achieve numerical convergence will be significantly lower than $\prod_{k=1}^{f} N_k$, the corresponding number of basis functions used in a standard wave packet propagation scheme. The efficient implementation of the MCTDH approach requires a specific representation of the Hamiltonian. Preferably, the Hamiltonian is written as a sum of products of operators acting only on a single Q_k.[43,44] While kinetic energy operator can almost always be written as a sum of products of one-dimensional operators, multidimensional PESs usually are not given in this form. Currently there are two main approaches to address this problem within the MCTDH framework: the fitting of the PES to product form (e.g., using the *potfit* algorithm)[45,46] or the Correlation DVR (CDVR) approach.[47] The latter approach, which uses a time-dependent quadrature corresponding to the SPF basis and allows the use of general potentials without fitting them to product form, has been used in this work for the calculation of the eigenvalues of the reduced 5D Hamiltonian. However, once the diabatic basis is built, CDVR is no longer needed, since the diabatic potential energy matrix depends only on a single coordinate.

Besides the regular real-time propagations, the MCTDH approach can also be used to obtain eigenvalues and eigenfunctions of certain relevant operators which imply imaginary-time propagations. In the present work, block relaxation of state-averaged MCTDH (SA-MCTDH) wave functions[40] is used to obtain the eigenstates and eigenvalues of the 5D Hamiltonian operator, $\hat{H}_{5D}(q; z)$. Furthermore, the eigenvalues and eigenstates of thermal flux operator are calculated by the iterative diagonalization of $\hat{F}_T$ within the state-averaged MCTDH approach.[40]

III. RESULTS AND DISCUSSION

In Sec. II B it was argued that the diabatic approach is formally exact in the limit of a complete basis set. In the case of a quasi-separable system, with a very small coupling between confined and unbound coordinates, convergence will be achieved with few eigenfunctions. Furthermore, an adiabatic approximation which separates the motion of the fast confined degrees of freedom from that of the slower unbound ones will yield good results. In Sec. III, we will first discuss the validity of the model by studying the cePESs obtained with the adiabatic approach and the 5D Hamiltonian matrix in the diabatic representation. Then the approach will be used to rigorously compute CRPs using the diabatic representation.

The accuracy of the adiabatic approximation will be studied by comparison with full-dimensional Hamiltonian results. Finally, the diffusion rates of H_2 into the hollow cavity of the nanotube will be computed.

A. Diabatic Hamiltonian matrices and adiabatic cePESs

In the present work, a total of 50 confined 5D eigenstates were used as a basis for the diabatic (and adiabatic) representation of q. To ensure convergence of the 50 $\xi_j(z_0)$ basis functions, a higher number of states was calculated in the SA–MCTDH diagonalization, namely, 80. The numerical parameters for the MCTDH wave function representation used to calculate the confined eigenstates are given in Table I: SPF basis size and primitive's grid type, number of points, and the span of the representation. Note that the primitive's grid type is a FFT grid, except for the angular coordinate θ, for which a Cotangent DVR (cot-DVR)[48] was chosen. This representation was constructed specifically to avoid the singularity appearing due to the term $\frac{1}{\sin \theta}$ in the Hamiltonian, Eq. (1). See Ref. 48 for more details. The calculation of the 5D eigenstates at a value of $z = -1.36\, a_0$, corresponding to a minimum in the electronic PES, took 14 h in a 16 core Intel Xeon E5-4620 0@2.20 GHz machine. The subsequent calculation of the diabatic Hamiltonian matrix and the adiabatic cePESs for 512 equidistant values in the $z \in [-56.066, 56.066]\, a_0$ range—corresponding to the length of 14 (8,0)-SWCNT unit cells—took only few seconds in the same machine.

Through the analysis of the adiabatic surfaces, one can detect regions where avoided crossings appear, and therefore the coupling between states could be stronger. The adiabatic surfaces $\{\varepsilon_j(z)\}$ of the H_2 molecule inside the CNT are plotted in Fig. 2 as a function of the diffusion coordinate, z. It should be noted that only states transforming according to the same irreducible representation of the system's symmetry group can interact. cePESs corresponding to states of different symmetry can thus cross without giving rising to any coupling. In Fig. 2, cePESs corresponding to states which are symmetric with respect to the permutation of the two hydrogen atoms are displayed by full lines while cePESs of antisymmetric states are shown as dashed lines.

In Fig. 2, it is readily seen that the lower cePESs are well-behaved, smooth functions and therefore the coupling between them is expected to be negligible. However, as one goes up in energy, the density of states is largely increased and avoided crossings appear. This is seen in the higher energy surfaces in Fig. 2. Considering the z-dependence, one finds that near

TABLE I. Basis set and grid MCTDH representation used in the calculation of the 5D eigenstate basis for H_2.

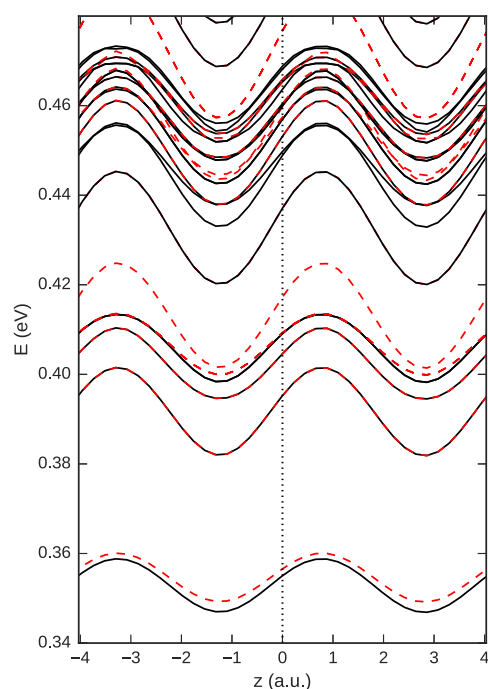| DOF	Number of SPFs	Primitive grid		
		Number of points	Type	Range
ρ	2	32	FFT	0.5–5.0 a_0
θ	7	64	cot-DVR	0–$\pi/2$
ϕ	8	64	FFT	0–2π
x	5	32	FFT	−3.5–3.5 a_0
y	5	32	FFT	−3.5–3.5 a_0

FIG. 2. Adiabatic cePESs generated by the 30 lowest energy eigenstates of the H$_2$@SWCNT system. cePESs corresponding to confined eigenstates which are symmetric with respect to permutation of the two hydrogen atoms are displayed by black solid lines while cePESs corresponding to antisymmetric states are shown as red dashed lines.

the minima of the cePESs all surfaces are well distinguishable. No avoided crossings are found in this region and the coupling between the different cePESs can be expected to be negligible. However, in the steep regions of the PES and near the maxima, avoided crossings are visible. The coupling between different confined eigenstates is potentially significant in these areas.

Following the analysis of the cePESs, we can graphically represent the 5D Hamiltonian matrix of Eq. (8) at different points of z, paying special attention to the areas where avoided crossings appear in the cePESs. This representation will provide further information about which confined states, if any, are significantly coupled: large off-diagonal matrix elements would indicate significant couplings and a breakdown of the adiabatic approximation. On the other hand, if the couplings are small and H_{5D} is quasi-diagonal, the adiabatic approximation can be expected to yield good results.

Furthermore, in this case just a few basis functions will be required in the diabatic representation in order to obtain accurate results.

Figure 3 shows a representation of the H_{5D} matrix for H$_2$, using fifty 5D eigenstates as a basis for q, at two points along the PES: a minimum of the PES ($z = -1.36$ bohr), and at $z = 0$ bohr (indicated by the vertical dotted line in Fig. 2), a point where many avoided crossings of the cePESs appear and the largest couplings can be expected. The matrix elements are represented in logarithmic scale for the sake of clarity. As it was expected, the off-diagonal terms at $z = -1.36$ bohr, the reference point used for the definition of the diabatic basis, effectively vanish. More interesting are the results obtained at a point in the strong coupling region at $z = 0$ bohr. Even here, the largest off-diagonal terms are roughly 50–100 times smaller than the diagonal elements. This finding indicates a very low coupling between the unbound motion in z and the dynamics in the confined DOFs q. It strongly suggests the suitability of an adiabatic separation of the time scales in studies of the quantum dynamics of nanoconfined species.

B. Dynamics of H$_2$ diffusion

The two approaches described in Secs. II B and II C were used to run quantum dynamics simulations of H$_2$ diffusion inside the SWCNT. Cumulative reaction probabilities were obtained at a reference temperature of 100 K and the diffusion rate was computed by thermal averaging of $N(E)$. Additional calculations were preformed at a reference temperature of 1000 K to confirm the accuracy of the results.

In order to obtain converged results in the diabatic and adiabatic schemes, several parameters need to be optimized, namely: the primitive basis set used in both q and z, the propagation time, the complex absorbing potential (CAP), and the number of flux eigenstates contributing to $N(E)$ in the chosen temperature range. Using the relation between flux eigenstates and eigenstates of the confined Hamiltonian, we can get an approximate threshold for the number of relevant flux eigenstates at a given temperature: they will correspond to approximately twice the number of confined eigenstates relevantly populated at that temperature. In our case, for the highest temperature considered, 1000 K, up to 11 confined eigenstates would be significantly populated. For the sake of numerical accuracy, 26 flux eigenstates were obtained by the iterative diagonalization of the thermal flux operator. These eigenstates were propagated in real time to finally obtain $N(E)$. Regarding
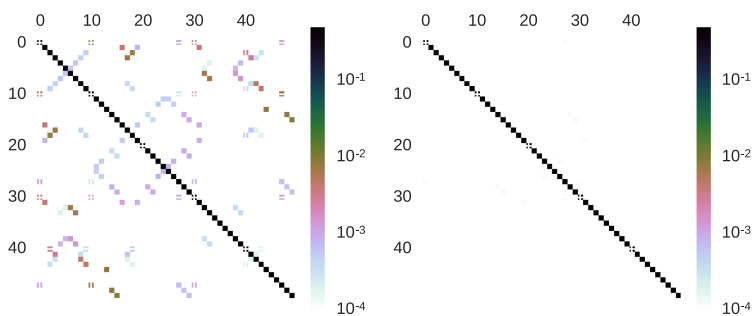

FIG. 3. Graphic representation of the Hamiltonian matrix in the basis of SPFs at the point of minimum (right) and maximum (left) coupling. Energy scale is in eV.

the primitive basis, converged results were obtained using 50 diabatic basis functions in the q coordinate and 20 SPFs in the unbound DOF z. The different basis sets used in the diabatic and adiabatic calculations are given in Table II.

Finally, both time convergence and CAP optimization required a special treatment due to the very low energies involved in the diffusion process. Regarding the CAP, it was seen that regular polynomial forms of the imaginary potential failed to avoid both reflexions and transmissions of the wave packets in the energy range involved. To overcome this issue, a transmission-free absorbing potential[49,50] was used. This potential has the advantage that no transmission of the wave packet is possible. Hence, one could in principle reduce the amount of reflexion arbitrarily by increasing the length of the imaginary potential. In our case, to avoid all possible reflections, a length of 20 Å was required. The thermal flux eigenstates were propagated for 10 ps which allows one to obtain the symmetric flux correlation in Eqs. (17) and (19) for times up to 20 ps.[41]

As seen in Eq. (17), the cumulative reaction probability is obtained as the Fourier transform of a flux autocorrelation function. Although an infinite propagation time is in principle needed to obtain $N(E)$, generally convergence is achieved at relatively short times, as the wave packet leaves the interaction region. A measure to qualitatively check the convergence of a quantum dynamics calculation is given by the flux-flux correlation function,

$$C_{ff}(t;T) = tr\left(e^{-i\hat{H}t}\hat{F}_T e^{i\hat{H}t}\hat{F}_T\right)$$
$$= \sum_m f_n f_m \left|\langle f_n | e^{-i\hat{H}t} | f_m \rangle\right|^2, \quad (22)$$

an its time integral, the flux-position correlation function,

$$C_{fp}(t;T) = \int_0^t C_{ff}(t;T). \quad (23)$$

Generally, this function increases and potentially oscillates while the wave packet remains in the interaction region, but asymptotically reaches a constant value. The total C_{fp} for both approaches developed in the present work, together with the full dimensional data obtained from a previous work,[33] is shown in Fig. 4 for the reference temperature of 100 K.

There are several conclusions to be drawn from the exploration of this quantity. First, focusing in the short-time region (see the inset of Fig. 4), it is seen that the results obtained using the three different approaches agree almost perfectly. The agreement between the data from our previous 6D work and the new results obtained using the diabatic approach described in Sec. II B confirms that both numerically exact calculations (6D
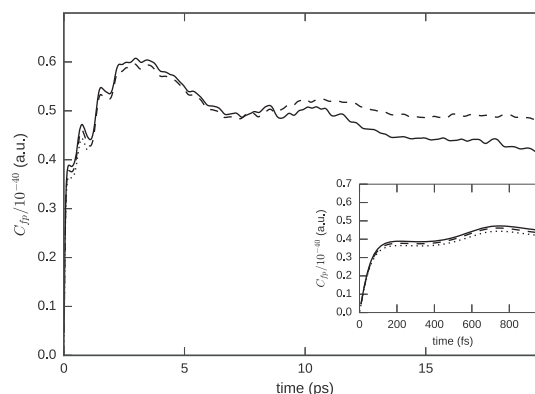
TABLE II. Basis set and grid MCTDH representation used in the propagations.

DOF	Number of SPFs	Primitive grid		
		Number of points	Type	Range
q	25	50	Discrete	...
z	20	512	FFT	-56.066–$56.066\ a_0$

FIG. 4. Flux-position correlation function at $T_0 = 100$ K for the diffusion of H_2 in an (8,0) CNT obtained with a 6D model (dotted), a diabatic approach (solid), and an adiabatic approach (dashed). Inset: Close-up to the short-time region.

and diabatic representation) are numerically converged. Furthermore, it is found that the adiabatic approximation yields very accurate results at this time scale. This finding confirms the separation of time scales of the dynamics in the unbound and constrained DOFs.

Second, one notes the complex, long-living structures in the flux-position correlation function which does not reach to a constant value even at 20 ps. This behavior indicates the existence of long-living resonances. Due to the long propagation times required, these structures were not studied in a previous work. Their investigation in the present study is facilitated by the numerical efficiency of the diabatic approach described in Sec. II B.

Finally, it must be noted that C_{fp} resulting from the diabatic and adiabatic propagations are very similar until about 10 ps but differ significantly beyond this value. The differences indicate that the coupling between the motion in unbound and constrained DOFs becomes relevant at about 10 ps. This time scale corresponds to coupling constants of about 0.06 meV. It should be noted that the gradual decay of accuracy resulting from the assumption of separability of time scales in the adiabatic calculation is consistent with the results reported in a previous work by some of the authors.[32] Here it was shown that the coupling between unbound and confined degrees of freedom increased each time a wave packet crossed a maximum of the PES.

To investigate the resonances giving rise to the long-living structures in the flux-correlation function in more detail, the limited resolution CRP was computed as defined in Eq. (18), $\bar{N}(E)$, with a resolution of $\Delta E = 0.12$ meV, and is displayed in Fig. 5. Comparing the rigorous results obtained by the diabatic approach with the results of the adiabatic approximation, one immediately finds that the resonance structures are well described within the adiabatic approach. The agreement between the results of the diabatic and adiabatic calculations is perfect at low energies, almost perfect at energies up to about 0.4 eV, and reasonably good at higher energies. It should be noted that the results of diabatic calculation show a slightly more noisy behavior at higher energies indicating remaining numerical inaccuracies due to imperfect convergence.
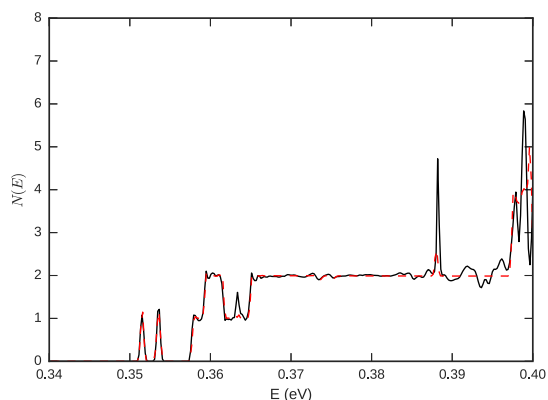
FIG. 5. Comparison of the total N(E) for the diffusion of H$_2$ in an (8,0) CNT obtained through the diabatic (solid, black) and adiabatic (dashed, red) approaches.

FIG. 7. Diffusion rate for H$_2$ in an (8,0) CNT computed using the diabatic approach (solid line) and the adiabatic approximation (dashed). TST results (dotted) are also given for comparison.

As it was hinted by the complex shape of the flux-position correlation function, N(E) presents a number of structures, specially in the lowest energy region. These can be nicely explained studying Fig. 6, where the CRP obtained in adiabatic approximation is plotted together with the individual contributions arising from the first five flux eigenstates. In order to investigate the resonant character of the peaks found in the CRP, we have calculated the eigenstate spectrum of H$_2$ confined to a single unit cell of the carbon nanotube, i.e., applying the periodic boundary condition at the limits of the box displayed in Fig. 2. The computed eigenenergies are plotted in Fig. 6 as vertical lines. These eigenstates appear in pairs corresponding to eigenstates which are either symmetric or antisymmetric with respect to reflection in z-planes located at the top of the potential barriers. In Fig. 6, solid vertical lines correspond to symmetric eigenstates while dotted ones are used for anti-symmetric ones.

The connection between the eigenenergies and the resonances is clearly visible in the figure: the contribution of a given flux eigenstate to the CRP, N_i, rises to unity whenever the total energy coincides with the value of a symmetric eigenstate. On the other hand, it decays again to zero when the energy
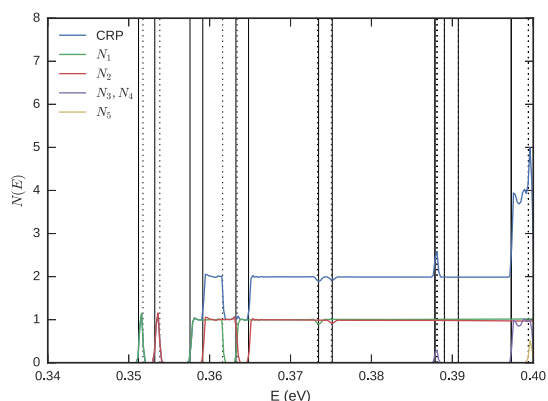
corresponding to an anti-symmetric eigenstate is reached. In the energy interval between the two eigenenergies, resonance enhanced tunneling through the barrier is possible. Comparing the resonance positions in Fig. 6 with the cePESs in Fig. 2, the low-lying resonances in the CRP can be straightforwardly assigned. The two prominent resonances below 0.355 eV result from resonance enhanced tunneling on the two lowest cePESs. The corresponding resonance wave function is mainly localized in the potential wells and shows no nodes in this region. The corresponding tunneling splitting is in the meV range. The next eigenstates appear about 5 meV above the first ones. Comparing this excitation energy with the barrier height of about 10 meV on the lowest cePESs, one would expect a much larger tunneling splitting. Actually the corresponding tunneling splittings seen in Fig. 6 are about 4 meV, which confirms this expectation. The two overlapping CRP contributions resulting from these states give rise to the interesting feature seen at about 0.36 eV. At even higher energies, the available energy exceeds the barrier height and both channels corresponding to the two lowest cePESs are completely open. Therefore the CRP settles at a value of two until the first resonance states located on the higher cePES appear between 0.38 and 0.39 eV.

After Boltzmann averaging and integration of the CRP at different temperatures, we first obtain $k(T)$ and then, using Eq. (14), the diffusion rate. This quantity, computed by both approaches developed in this work, is shown in Fig. 7 for the H$_2$ molecule in an (8,0) CNT. Transition state theory results are also plotted for comparison. As it was expected from the study of the different $N(E)$, the results obtained with the diabatic and adiabatic formalisms agree perfectly, both showing a significant tunneling contribution below 125 K.

IV. SUMMARY AND CONCLUSIONS

The differences in the time scales of the fast motion in the confined DOFs and the slow motion along the nanotube's axis in the H$_2$@(8,0) SWCNT system were exploited to devise efficient numerical methods to study the system's quantum dynamics. In the rigorous, numerically exact approach,

FIG. 6. Total N(E) and the first five individual contributions to the CRP obtained with the adiabatic approach at a reference temperature T_0 of 100 K. N_3 and N_4 come from degenerate states. Vertical lines correspond to the eigenstates of the 6D Hamiltonian computed in a unit cell with periodic boundary conditions (see text for details).
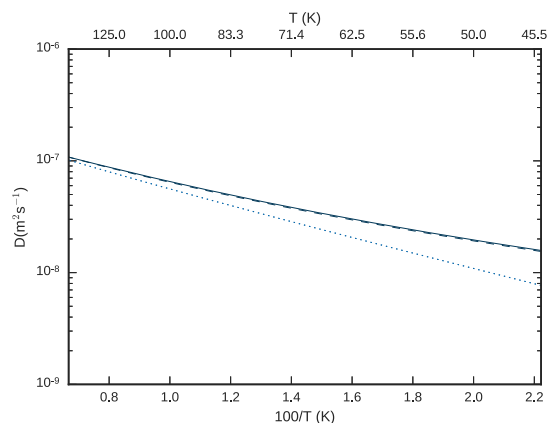
first a diabatic basis and a corresponding Hamiltonian matrix describing the motion in the confined coordinates is constructed. The resulting diabatic Hamiltonian matrix only depends on the z-coordinate describing the unbound motion of H_2 along the nanotube. Thus, the 6D Schrödinger equation is turned into a 1D equation describing the motion on a set of coupled diabatic potential energy surfaces. Due to the small size of the couplings, converged results can be obtained with a small number of diabatic basis states. The resulting scheme is extremely numerically efficient and allows one to study the system's dynamics on a time scale which could not be accessed in previous studies.[32,33]

Invoking an adiabatic approximation to decouple the slow and fast motions, the description of the system's dynamics can be further simplified. In the adiabatic approximation, the dynamics precede on uncoupled adiabatic potential energy curves. Comparison with rigorous results shows that the adiabatic approximation works very well for the present system. The adiabatic picture is then successfully utilized to interpret the system's dynamics.

The investigation of the long-time dynamics in the H_2@(8,0) SWCNT system facilitated by this methodological development yielded interesting new insights. It was found that the motion of H_2 along the nanotube axis at low energies can occur via resonance enhanced tunneling. Corresponding structures are clearly visible in the computed energy-dependent transmission coefficients. The resonance can be assigned to quantum states localized in the wells of the adiabatic PESs. This result is particularly interesting as it suggests that tunneling might be the dominant mechanism for the motion of individual H_2 molecules trough narrow CNTs a low temperature. The consequences of this finding should be investigated more deeply, since it might affect potential applications of carbon nanotubes, such as their usefulness as quantum sieves.

ACKNOWLEDGMENTS

[1]S. L. Candelaria, Y. Shao, W. Zhou, X. Li, J. Xiao, J. G. Zhang, Y. Wang, J. Liu, J. Li, and G. Cao, "Nanostructured carbon for energy storage and conversion," Nano Energy **1**, 195 (2012).

[2]R. B. Getman, Y.-S. Bae, C. E. Wilmer, and R. Q. Snurr, Chem. Rev. **112**, 703 (2012).

[3]Q. Wang, S. Challa, D. Sholl, and J. Johnson, Phys. Rev. Lett. **82**, 956 (1999).

[4]M. Hankel, H. Zhang, T. X. Nguyen, S. K. Bhatia, S. K. Gray, and S. C. Smith, Phys. Chem. Chem. Phys. **13**, 7834 (2011).

[5]T. K. Nielsen, F. Besenbacher, and T. R. Jensen, Nanoscale **3**, 2086 (2011).

[6]J. J. M. Beenakker, V. D. Borman, and S. Y. Krylov, Phys. Rev. Lett. **72**, 514 (1994).

[7]I. Holleman, G. von Helden, E. H. T. Olthof, P. J. M. van Bentum, R. Engeln, G. H. Nachtegaal, A. P. M. Kentgens, B. H. Meier, A. van der Avoird, and G. Meijer, Phys. Rev. Lett. **79**, 1138 (1997).

[8]S. A. FitzGerald, T. Yildirim, L. J. Santodonato, D. A. Neumann, J. R. D. Copley, J. J. Rush, and F. Trouw, Phys. Rev. B **60**, 6439 (1999).

[9]S. J. V. Frankland and D. W. Brenner, Chem. Phys. Lett. **334**, 18 (2001).

[10]S. R. Challa, D. S. Sholl, and J. K. Johnson, Phys. Rev. B **63**, 245419 (2001).

[11]T. Yildirim and A. B. Harris, Phys. Rev. B **66**, 214301 (2002).

[12]T. Yildirim and A. B. Harris, Phys. Rev. B **67**, 245413 (2003).

[13]A. V. A. Kumar and S. K. Bhatia, Phys. Rev. Lett. **95**, 245901 (2005).

[14]H. Tanaka, H. Kanoh, M. Yudasaka, S. Iijima, and K. Kaneko, J. Am. Chem. Soc. **127**, 7511 (2005).

[15]A. V. A. Kumar, H. Jobic, and S. K. Bhatia, J. Phys. Chem. B **110**, 16666 (2006).

[16]T. Lu, E. M. Goldfield, and S. K. Gray, J. Phys. Chem. B **110**, 1742 (2006).

[17]T. X. Nguyen, H. Jobic, and S. K. Bhatia, Phys. Rev. Lett. **105**, 085901 (2010).

[18]A. J. Horsewill, S. Rols, M. R. Johnson, Y. Murata, M. Murata, K. Komatsu, M. Carravetta, S. Mamone, M. H. Levitt, J. Y. C. Chen, J. A. Johnson, X. Lei, and N. J. Turro, Phys. Rev. B **82**, 081410 (2010).

[19]G. Garberoglio and J. K. Johnson, ACS Nano **4**, 1703 (2010).

[20]S. Mamone, J. Y.-C. C. Chen, R. Bhattacharyya, M. H. Levitt, R. G. Lawler, A. J. Horsewill, T. Rõõm, Z. Bačić, and N. J. Turro, Coord. Chem. Rev. **255**, 938 (2011).

[21]C. I. Contescu, H. Zhang, R. J. Olsen, E. Mamontov, J. R. Morris, and N. C. Gallego, Phys. Rev. Lett. **110**, 236102 (2013).

[22]P. M. Felker, J. Chem. Phys. **141**, 184305 (2014).

[23]M. Johnson, S. Rols, P. Wass, M. Muris, M. Bienfait, P. Zeppenfeld, and N. Dupont-Pavlovsky, Chem. Phys. **293**, 217 (2003).

[24]I. Matanović, J. L. Belof, B. Space, K. Sillar, J. Sauer, J. Eckert, and Z. Bačić, J. Chem. Phys. **137**, 014701 (2012).

[25]C. Beduz, M. Carravetta, J. Y.-C. Chen, M. Concistrè, M. Denning, M. Frunzi, A. J. Horsewill, O. G. Johannessen, R. Lawler, X. Lei, M. H. Levitt, Y. Li, S. Mamone, Y. Murata, U. Nagel, T. Nishida, J. Ollivier, S. Rols, T. Rõõm, R. Sarkar, N. J. Turro, and Y. Yang, Proc. Natl. Acad. Sci. U. S. A. **109**, 12894 (2012).

[26]J.-R. Li, Y. Ma, M. C. McCarthy, J. Sculley, J. Yu, H.-K. Jeong, P. B. Balbuena, and H.-C. Zhou, Coord. Chem. Rev. **255**, 1791 (2011).

[27]A. Valdés, D. J. Arismendi-Arrieta, and R. Prosmiti, J. Phys. Chem. C **119**, 3945 (2015).

[28]T. Pham, K. A. Forrest, E. H. L. Falcão, J. Eckert, and B. Space, Phys. Chem. Chem. Phys. **18**, 1786 (2016).

[29]J. Suarez and F. Huarte-Larrañaga, J. Chem. Phys. **137**, 064320 (2012).

[30]M. Mondelo-Martell and F. Huarte-Larrañaga, J. Chem. Phys. **142**, 084304 (2015).

[31]D. Skouteris and A. Laganà, Chem. Phys. Lett. **575**, 18 (2013).

[32]M. Mondelo-Martell and F. Huarte-Larrañaga, Chem. Phys. **462**, 41 (2015).

[33]M. Mondelo-Martell and F. Huarte-Larrañaga, J. Phys. Chem. A **120**, 6501 (2016).

[34]R. Dovesi, B. Civalleri, R. Orlando, C. Roetti, and V. R. Saunders, Rev. Comput. Chem. **21**, 1 (2005).

[35]D. H. Zhang, J. C. Light, and S.-Y. Y. Lee, J. Chem. Phys. **111**, 5741 (1999).

[36]T. Yamamoto, J. Chem. Phys. **33**, 281 (1960).

[37]W. H. Miller, J. Chem. Phys. **61**, 1823 (1974).

[38]W. H. Miller, S. D. Schwartz, and J. W. Tromp, J. Chem. Phys. **79**, 4889 (1983).

[39]F. Matzkies and U. Manthe, J. Chem. Phys. **108**, 4828 (1998).

[40]U. Manthe, J. Chem. Phys. **128**, 064108 (2008).

[41]F. Matzkies and U. Manthe, J. Chem. Phys. **106**, 2646 (1997).

[42]F. Huarte-Larrañaga and M. Albertí, Chem. Phys. Lett. **445**, 227 (2007).

[43]M. Beck, A. Jäckle, G. A. Worth, and H.-D. Meyer, Phys. Rep. **324**, 1 (2000).

[44]U. Manthe, H. Meyer, and L. S. Cederbaum, J. Chem. Phys. **97**, 3199 (1992).

[45]A. Jäckle and H. Meyer, J. Chem. Phys. **104**, 7974 (1996).

[46]*Multidimensional Quantum Dynamics*, edited by H.-D. Meyer, F. Gatti, and G. A. Worth (Wiley-VCH Verlag GmbH & Co. KGaA, 2009), pp. 81–89.

[47]U. Manthe, J. Chem. Phys. **105**, 6989 (1996).

[48]G. Schiffel and U. Manthe, Chem. Phys. **374**, 118 (2010).

[49]D. E. Manolopoulos, J. Chem. Phys. **117**, 9552 (2002).

[50]T. Gonzalez-Lezana, E. J. Rackham, and D. E. Manolopoulos, J. Chem. Phys. **120**, 2247 (2004).

7.5   Summary and Conclusions

During this Chapter we have investigated the relation between the *confined* degrees of freedom, namely ρ, θ, ϕ, x and y, and the *unbound* or *quasi–free* coordinate, z, of a hydrogen molecule confined in an (8,0) SWCNT. This distinction arises due to the cylindrical shape of the nanotube, which imposes a tight confining potential in two dimensions of space (x and y) and a low corrugation along the third (z). The first 6D simulations on this system have been reported, based on the preparation of bound states in a particular position along z by the addition of a trapping potential, and their posterior propagation (Publication 3). With this setup it was possible to assign each wave packet to a confined 5D eigenstate. The analysis of the propagated wave packets was made by computing convolution functions of the propagated wave packet and different 5D eigenstates, showing a low mixing between them during the propagation. This is a prove of the low coupling between the two sets of coordinates, and has motivated the development of a representation of the Hamiltonian based on a time–scale separation between confined and unbound degrees of freedom (Publication 4). An exact *diabatic* approach was developed by using the eigenstates of the 5D Hamiltonian fixed at an arbitrary z point as a basis set for the matrix representation of $\hat{H}$, and tested by applying it to the problem of diffusion of H_2 along the nanotube. Its increased numerical efficiency allowed us to propagate flux eigenstates up to 20 ps, thus providing with the converged cumulative reaction probabilities for the process already discussed in Chapter 6. Then, an adiabatic approximation, which was possible due to the smooth dependence of $\hat{H}_{5D}$ with z, proved to be as accurate as the exact approach and slightly reduce the numerical noise.

The work presented here allows us to collect a set of conclusions:

- The particular shape of the nanostructure into which the adsorbates are confined affects to the relative amount of coupling in the different DOFs. In the particular case of the H_2@(8,0) system, the z coordinate is only weakly coupled with the remaining 5 DOFs.

- A correct design of the simulations can lead us to straightforward ways to analyze our results: in this particular case, the previous preparation of the wave packets and their relation to 5D eigenstates made possible the assessment of the coupling by convolution functions.

- It is possible to take advantage of these particularities to develop more efficient Hamiltonians without a significant lose of accuracy.

- The diabatic approach and the adiabatic approximation give accurate results efficiently. Without these tools it would have been extremely expensive to converge $N(E)$ for this particular system, characterized by resonances and a very low diffusion barrier.

Chapter 8

Phonon coupling in the H$_2$@SWCNT system

8.1 Phonons and dispersion

The collective vibrations of the atoms in a material, its *phonons*, have a critical importance in diffusion processes, since they act as a thermal bath which excites or dampens the motion and vibrations of the adsorbates[153], and thus introduce *dissipation* effects in the system. However, the inclusion of phonons in quantum mechanical calculations is not straightforward, since one must design a suitable model containing the coupling between the adsorbate and the substrate, and possible dissipation effects. For this reason, most of the theoretical works on quantum dynamics are based on the frozen substrate assumption, as explained in Chapter 4. There are notable exceptions of this, such as the work of Andrianov and Saalfrank[155], who studied the effects of substrate vibration on the adsorption of a H atom on a Si (100) surface. More recently Bonfanti et al.[156, 157], studied the sticking process of the same atom on graphene, and Meng and Meyer[158] found vibrational states of CO on a Cu (100) surface including surface vibrations. Note that these works are limited to surface diffusion, and to the best of our knowledge there are no similar theoretical studies for nanoconfined systems. For this reason, in this Chapter we present our approach to include the phonon coupling to the quantum dynamics of a H$_2$ molecule confined in the hollow cavity of an (8,0) carbon nanotube. This represents a highly relevant milestone of this Thesis, and is expected to have an impact on the available insight on quantum confinement effects.

This Chapter is organized as follows: first, the different portions of the model Hamiltonian are discussed. Once the Hamiltonian is defined, the coupling model between the molecule and the nanostructure is tested by using time–dependent perturbation theory to compute lifetimes of pure system states introduced in the phonon bath. Finally, the main results and conclusions of the study are summarized.

8.2 The System–bath Coupling model

There are several ways to describe dissipative systems as the one which occupies us: from using a density matrix–based formalism, to include some new terms into regular Hamiltonians[159]. In this Chapter we will focus on the well–known system–bath coupling model, based on the partition of the Hamiltonian in three terms: a system, a bath, and a third term to account for the coupling between them:

$$\hat{H} = \hat{H}_{sys} + \hat{H}_{bath} + \hat{H}_{coupl}. \tag{8.1}$$

In our case, the *system* will be the hydrogen molecule embedded in a rigid (8,0) carbon nanotube, as defined in Chapter 4. Hereafter we will indistinctly refer to this portion of the model as *system*, *adsorbate*, or *frozen model*. The system will be coupled to a *bath* of harmonic oscillators representing the *phonons* of the nanotube, and the third term will be the one responsible of modeling such coupling.

There are three important changes in the description of the system with respect to the model specified in Chapter 4. First, for practical reasons regarding the calculation of the phonon dispersion, in this Chapter the nanostructure used was optimized using the VASP package[160–163] instead of Crystal09, as it will be discussed later. Secondly, in order to increase the numerical efficiency and to ease the interpretation of the results, we use the adiabatic approximation to the Hamiltonian presented in Chapter 7 instead of the full–dimensional version. The third and final modification of the system's Hamiltonian is related with the need to define the linear momentum of the hydrogen molecule, k_{mol}: the exchange of this quantity with the phonon bath is one of the most relevant effects of the dispersion, so to correctly quantify it we need to have it perfectly defined for any adsorbate eigenstate. In order to turn this quantity into a quantum number of the system to label the different eigenstates, we Fourier transform the kinetic energy operator in the periodic dimension, $\hat{T}_z$, by applying the unitary transform $e^{\frac{-ik_{mol}z}{L}}$. Thus, we obtain:

$$e^{\frac{-ik_{mol}z}{L}}\hat{T}_z e^{\frac{ik_{mol}z}{L}} = -\frac{\hbar^2}{2m}\frac{\partial^2}{\partial z^2} - \frac{i\hbar}{m}\frac{k_{mol}}{L}\frac{\partial}{\partial z} + \frac{\hbar^2}{2m}\frac{k_{mol}^2}{L^2} \equiv \hat{\tilde{T}}_{z,k_{mol}}. \tag{8.2}$$

Then we can substitute $\hat{T}_z$ in Eq. (7.8) by its transformed version, Eq. (8.2). With this we can define the momentum–labeled Hamiltonian of the adsorbate as:

$$\hat{\tilde{H}}_j^{(ad)} = \hat{\tilde{T}}_{z,k_{mol}} + \sum_{l=1}^{N_z} \varepsilon_j(z_l)\,|z_l\rangle\langle z_k|\ . \tag{8.3}$$

We will now discuss the bath and coupling terms of the Hamiltonian.

8.2.1 The Phonon Bath

In condensed matter physics, phonons are usually treated in the harmonic approximation, similarly to what is done for normal modes of vibration in molecules. As discussed in Chapter 5, however, crystalline systems are characterized by their periodicity in some dimension of space. This periodicity implies some particularities when performing the normal mode analysis which differ from what is usually seen in molecular contexts, and will be reviewed in this section.

The first step in the computation of the phonons of a structure is to optimize the geometry of its unit cell, as defined in Chapter 5. Since a single–walled carbon nanotube is periodic only along the z dimension, we need to find a single cell parameter, and can restrict the analysis of the phonons to this particular coordinate. In this case we used the VASP package, since coupled with another third–party software for computing phonon dispersion called *Phon*[164], was more suitable for our purposes than Crystal09, as it will be discussed later in this Section. The unit cell was optimized with a PBE functional, using a set of plane waves with an energy cutoff of 400 eV as basis, which yielded a cell parameter $L = 8.071\ a_0$ and a tube's diameter $d = 12.049\ a_0$.

Once the unit's cell geometry has been optimized, one can perform the phonon analysis. Phonons imply the collective motion of all atoms in the system, and therefore the analysis cannot be restricted to a single unit cell: an infinite number of them

should in principle be taken into account. We have therefore the same problem as in the case of the electronic Hamiltonian discussed in Chapter 4: we cannot work with an infinite number of atoms. As in that particular case, we can take advantage of Bloch's Theorem, Eq. (4.3), which since we are working with a solid periodic only along the z–coordinate, we can rewrite as:

$$\Psi(z + L; k) = e^{ikL}\Psi(z; k),\tag{8.4}$$

where the 3–D vector quantities $\vec{r}$, $\vec{R}$ and $\vec{k}$ have become their scalar equivalents in 1–D: z, L, and k, respectively. We will maintain this 1–D notation throughout this whole Chapter. Then, after applying the Born–von Karman PBCs, Eq. (4.4), for N unit cells, we are able again to factor an infinite–dimensional differential equation in the direct space into N finite–dimensional problems in the reciprocal space.

The number of unit cells considered will determine the sampling of the k–vector, and therefore of reciprocal space. This is at the core of the *supercell* approach used to compute phonon dispersion relations. If we consider a single unit cell, we will be sampling a single point of the reciprocal space, which by convention is labeled Γ and corresponds to $k = 0$. According to Bloch's theorem, this means that all equivalent atoms in all unit cells of the infinite solid we are representing will be moving in phase. This implies that a translation of a unit cell will become a translation of the whole crystal, and therefore this phonon will have frequency 0. The phonons with frequency 0 at the Γ point are called *acoustic phonons*. In the particular case of nanotubes, there are 4 of such acoustic phonons: two degenerate modes accounting for the translation perpendicular to the nanotube's axis, a 3rd mode describing the longitudinal translation (the *translation* modes), and a final mode that characterizes the rotation of the whole structure around its axis (the *twisting* mode). The remaining $3N_{atoms} - 4$ phonon modes are known as *optical phonons*, and correspond to actual vibrations of the atoms in the unit cell. However, it is clear that the motions defined by the phonons with $k = 0$ are not enough to describe all possible motions of a nanotube. Let us introduce a second unit cell in our model. With this representation we are sampling two points of the reciprocal space: $k = 0$ and $k = \pi/L$, which by Bloch's theorem implies that we will have completely in–phase motion for the atoms of consecutive cells in Γ point, and completely out–of–phase motion of in the second sampling point. This is illustrated in Figure 8.1: we are breaking the symmetry of the system, and therefore we allow equivalent atoms of contiguous unit cells to move *out of phase*. It is important to note that for $k = \pi/L$ the acoustic phonons are no longer zero–frequency translations, but actual vibrations of the solid. By increasing the number of unit cells we are able to reproduce the phonon dispersion spectrum, which contains the dependence of the phonon's frequency with the different k points. In general, the relation between the number of unit cells included in the Born–von Karman model, N, and the k points of the reciprocal space implied that the k points allowed by the Bloch Theorem are given by:

$$k = \frac{2\pi}{L}\frac{m}{N},\tag{8.5}$$

for m integer between 0 and N, therefore we will have as many k points sampled as unit cells considered. Note that this is a 1D version of Eq. (4.5).

Mathematically, the supercell approach we have just illustrated is translated into the diagonalization of the *dynamical matrix*, $\boldsymbol{D}(k)$[137, 138]. For our set of N_{atoms} atoms in a unit cell we can define a vector $\vec{u}$ of $3N_{atoms}$ dimensions containing the Cartesian coordinates of each atom of the unit cell at the equilibrium geometry.
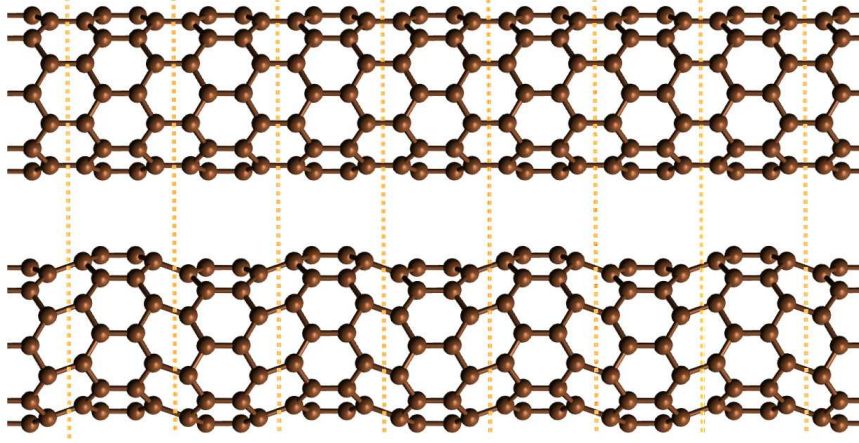
FIGURE 8.1: Scheme of the *supercell* approach for the calculation of phonon dispersion. Unit cells are separated by dotted lines. If one unit cell is considered, all atoms move in phase and we only sample $k = 0$ (top). If two unit cells are included, we include out–of–phase motion of consecutive cells and can sample $k = 0$ and $k = \pi/L$ (bottom).

Then, the dynamical matrix is defined as:

$$D_{\alpha i}^{\beta j}(k) = \sum_{m=1}^{N} e^{-i(r_m - r_n)kL} \left[\frac{\partial^2 V}{\partial u_{n\alpha i} \partial u_{m\beta j}} \right], \tag{8.6}$$

with m ranging from 0 to the number of unit cells N, r_m a lattice point of unit cell m and $u_{n\alpha i}$ the ith coordinate of the atom α of the unit cell n. Upon diagonalization of $D_{\alpha i}^{\beta j}(k)$, a set of eigenvalues $M_j \omega_j^2(k)$ and eigenvectors $c_{ij}(k)$ are found for each value of k:

$$\mathbf{M}\boldsymbol{\omega}^2(k)\mathbf{D}(k) = \mathbf{c}(k)\mathbf{D}(k), \tag{8.7}$$

with M_j and $\omega_j(k)$ the reduced mass and frequency of the jth phonon at the point k, respectively, and $c_{ij}(k)$ the eigenvectors which unitarily transform the u vector to the phonon coordinates, $Q_{j,k}$:

$$Q_{j,k} = \frac{1}{\sqrt{N}} \sum_{i,n} \sqrt{M_j} c_j^i(k) e^{inkL} \Delta u_{i,n}. \tag{8.8}$$

The calculation of the phonon's frequencies and eigenvectors has been done using the *Phon* software together with the VASP package. Although Crystal09 worked flawlessly for geometry optimizations and phonon calculations at the Γ point, we were not able to obtain phonon dispersion relations due to problems with the basis set and the reciprocal space representation. This was due to the impossibility to build the whole dynamical matrix: in order to rigorously sample the reciprocal space, one should include more and more unit cells in the supercell, and calculate the Hessian for these ever larger problems in order to obtain the dynamical matrix at a given k point. Conversely, the *Phon* program uses the *small displacement method*[165, 166], which is based on setting a cutoff distance for the interaction of two atoms in the supercell. This is done by building a relatively small supercell, and assuming that all relevant atom–atom interactions can be restricted to the length of that small
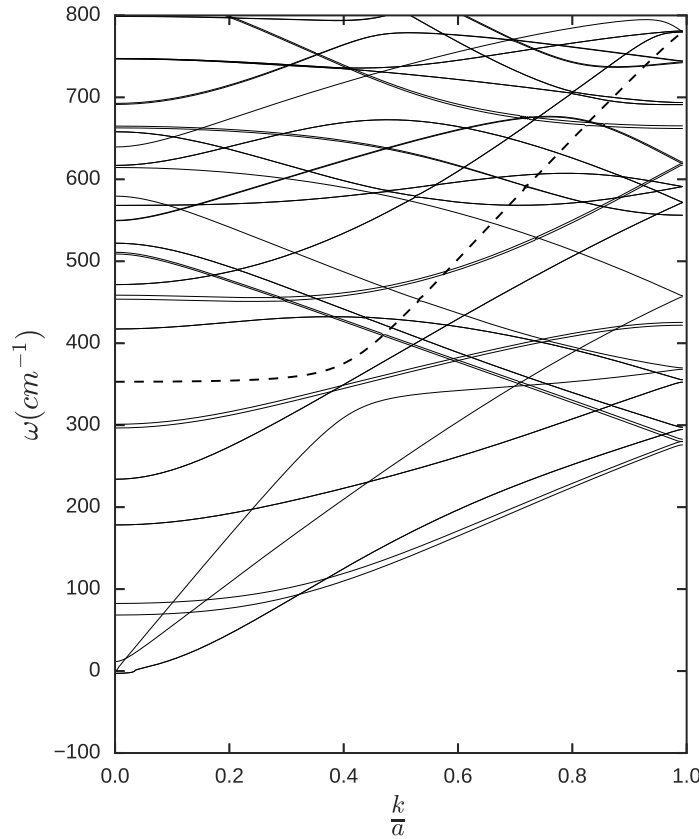
FIGURE 8.2: Phonon spectrum for an isolated (8,0) Carbon Nanotube. The first (doubly degenerated) and second branches are the translational acoustic phonons, the third corresponds to the twisting mode. The breathing mode is marked as a dashed line among the remaining optical phonons.

supercell. One then finds the minimum number of displacements in that structure to obtain the Hessian matrix appearing in Eq. (8.7). This matrix is then obtained through single–point calculations in the small supercell with the VASP code, which works with a plane wave basis set instead of Bloch functions build from localized basis functions centered on the atoms. Once the force constants in this system are build, the full dynamical matrix is built at arbitrary k points, considering that the interactions between atoms at a distance larger than that defined in the small supercell are negligible. The resulting phonon spectrum for the (8,0) CNT using the PBE functional and a basis set with an energy cutoff of 400 eV are shown in Figure 8.2. Acoustic phonons can be identified as the branches with frequency 0 at $k = 0$. For symmetry reasons, the first of such branches is degenerated and contains the two transversal translation phonons, and the more energetic one corresponds to the longitudinal translation. The twisting mode appears, due to numerical error, at frequencies slightly over 0, completing the set of four acoustic phonons. Of the different optical phonons, it is interesting to highlight the *breathing mode*, shown as a dashed line in Figure 8.2. This mode corresponds to a change of the nanotube's diameter due to the expansion and contraction of the unit cell's rings. This mode is expected to be relevant in the coupling with the adsorbate, but it is not sufficiently populated at the temperatures sampled here to have important effects.

Once the phonon spectrum is defined, we can build the bath Hamiltonian within the harmonic approximation as a set of Harmonic Oscillators with the required

masses, M_j, and frequencies, $\omega_{j,k}$:

$$\hat{H}_{bath} = \sum_{j=1}^{3N} \sum_k -\frac{\hbar^2}{2M_j} \frac{\partial^2}{\partial Q_{j,k}^2} + \frac{1}{2} M_j \omega_{j,k}^2 Q_{j,k}^2. \tag{8.9}$$

Each oscillator being associated with a phonon coordinate $Q_{j,k}$.

8.2.2   System–bath coupling

The system–bath coupling term will be the one connecting the two fragments involved in the problem. In order to build it, we perform a first order Taylor expansion of the interaction potential, $V(q,z)$, about the equilibrium geometry of the nanotube along the phonon coordinates $Q_{j,k}$:

$$V(q,z) \approx V(q,z,Q_{j,k}=0) + \sum_{j,k} \left| \frac{\partial V(q,z)}{\partial Q_{j,k}} \right|_{Q_{j,k}=0} Q_{j,k} + O^2(Q). \tag{8.10}$$

The truncation of the series to account only for linear coupling implies that only 1–phonon transitions will be taken into account in this model[155].

The derivative term is cumbersome and computationally demanding. However, by using the definition of the phonon coordinates, Eq (8.8), the chain rule:

$$\frac{\partial V(q,z)}{\partial Q_{j,k}} = \sum_{n=1}^{N} \sum_{i=1}^{3N_{at}} \frac{\partial V(q,z)}{\partial x_{i,n}} \frac{\partial x_{i,n}}{\partial Q_{j,k}}, \tag{8.11}$$

and the identity relation:

$$\sum_{n=1}^{N} \sum_{i=1}^{3N_{at}} \frac{\partial Q_{j,k}}{\partial x_{i,n}} \frac{\partial x_{i,n}}{\partial Q_{j,k}} = 1 , \tag{8.12}$$

we can turn the derivative term into a Cartesian coordinate–dependent derivative, which is easier to compute efficiently:

$$\frac{\partial V(q,z)}{\partial Q_{j,k}} = \sqrt{N} \sum_{n=1}^{N} \sum_{i=1}^{N_{at}} \frac{\partial V(q,z)}{\partial x_{in}} c_{ij}^{\dagger} e^{-iknL} \equiv \hat{f}_{j,k}(q,z), \tag{8.13}$$

where we have defined the *coupling operator*, $\hat{f}_{j,k}(q,z)$, which quantifies the coupling of the system at coordinates (q,z) with the jth phonon at the point k of the reciprocal space. Each operator is then a 6D function, and we have a total number of operators equal to $3N_{atoms} \times N$, with N the number of unit cells an therefore the number of k points.

We can represent the coupling operators in an adiabatic basis consisting of S eigenstates of the 5D Hamiltonian, $\{\xi(z)\}$ (see Chapter 7), and write each coupling operator as an $S \times S$ matrix with elements:

$$\left(\hat{f}_{j,k} \right)_{s,s'}(z) = \sqrt{N} \sum_{n=1}^{N} \sum_{i=1}^{N_{at}} c_{ij}^{\dagger} e^{-iknL} \left\langle \xi_s \left| \frac{\partial V(z)}{\partial x_{i,n}} \right| \xi_{s'} \right\rangle. \tag{8.14}$$

These z–dependent matrices give us information about which adiabatic 5D eigenstates are coupled by which phonons of the nanostructure, and which k momentum transfer is more efficient.

8.3 Transition rates through Time–dependent Perturbation Theory

If we neglect the coupling term in Eq (8.1) we obtain a separable Hamiltonian, whose functions will be a direct product of the frozen model functions, $\psi_{v,n_v,k_{mol}}$, and bath (SWCNT phonons) functions, $\Phi_{\nu_j,k_{ph}}$:

$$\Psi_{v,n_v,\nu_j,k_{mol},k_{ph}} = \psi_{v,n_v,k_{mol}}\Phi_{\nu_j,k_{ph}}. \tag{8.15}$$

The quantum numbers employed in the previous expressions label: the 5D rovibrational state of the confined molecule (v), the translational excitations within the cePES generated by that state (n_v), the excitation state in each phonon coordinate j, (ν_j), the momentum of the hydrogen molecule along the z axis (k_{mol}), and the crystal momentum of the nanotube (k_{ph}).

A good quantitative measure of the coupling between the adsorbate and the substrate's vibration is given by the lifetime of pure H_2 eigenstates obtained in the frozen model, $\psi_{v,n_v,k_{mol}}$, when we introduce the coupling term as a perturbation to the separable system–bath Hamiltonian. Using Time–dependent perturbation theory we can calculate the probability of an adsorbate eigenstate to make a transition to another state. Within this framework, the general expression for the transition rate from an initial state $\Psi^i_{v,n_v,\nu_j,k_{mol},k_{ph}}$ to a final state $\Psi^f_{v',n'_v,\nu'_j,k'_{mol},k'_{ph}}$ is given by:

$$w_{i \to f} = \frac{2\pi}{\hbar} \left| \left\langle \Psi^f | \hat{H}_{coupl} | \Psi^i \right\rangle \right|^2 \delta(E_f - E_i). \tag{8.16}$$

However, we are not interested in individual transitions between phonon states, because they act as a bath for the system. Therefore, in order to obtain transition rates between adsorbate states we must thermally average the contribution of the phonon states:

$$w_{v,n_v,k_{mol} \to v',n'_v,k'_{mol}} = \frac{2\pi}{\hbar} \sum_{\nu'_j,k'_{ph}} \left| \left\langle \Psi^f_{v',n'_v,\nu'_j,k'_{mol}} | \hat{f}_{j,k_{ph}} \hat{Q}_{j,k_{ph}} | \Psi^i_{v,n_v,\nu_j,k_{ph}} \right\rangle \right|^2$$
$$\times \rho_{\Phi_i} \, \delta(E_f - E_i), \tag{8.17}$$

with ρ_{Φ_i} the thermal distribution of the phonon bath, according to Bose–Einstein statistics, and $\hbar\omega_{jk_{ph}}$ the energy of the jth phonon with momentum k_{ph}. This Equation can be rearranged as:

$$w_{v,n_v,k_{mol} \to v',n'_v,k'_{mol}} = \frac{2\pi}{\hbar} \sum_{\nu'_j,k'} \left| \left\langle \psi^f_{v',n'_v,k'_{mol}} | \hat{f}_{j,k'_{ph}} | \psi^i_{v,n_v,k_{mol}} \right\rangle \right|^2$$
$$\times \left| \left\langle \Phi_{v',n'_v,k'_{ph}} | \hat{Q}_{j,|k-k'|} | \Phi_{v,n_v,k_{ph}} \right\rangle \right|^2 \rho_{\Phi_i} \tag{8.18}$$
$$\times \delta(E - E \pm \hbar\omega_{jk_{ph}}).$$

After thermally averaging the phonon contributions, integrating all bath degrees of freedom, and summing for all possible final states, we obtain the decay rate of an

adsorbate state, $\psi_{v,n_v,k_{mol}}$:

$$
\begin{aligned}
w_{v,n_v,k_{mol}} = \pi \sum_{v',n'_v} \Biggl[&\int_0^{2\pi} \sum_j \frac{\langle n_j \rangle}{\omega_{j,k_{ph}} N} \left| \left\langle \psi_{v',n'_v,k_{mol}} | \hat{f}_{j,k_{ph}} | \psi_{v,n_v,k_{mol}} \right\rangle \right|^2 \\
&\times \delta(E_f - \hbar\omega_{j,k_{ph}} - E_i) \, \mathrm{d}k_{ph} \\
&+ \int_0^{2\pi} \sum_j \frac{\langle n_j \rangle + 1}{\omega_{j,k_{ph}} N} \left| \left\langle \psi_{v',n'_v,k_{mol}} | \hat{f}_{j,k_{ph}} | \psi_{v,n_v,k_{mol}} \right\rangle \right|^2 \\
&\times \delta(E_f + \hbar\omega_{j,k_{ph}} - E_i) \, \mathrm{d}k_{ph} \Biggr],
\end{aligned}
\tag{8.19}
$$

with $\langle n_j \rangle = \frac{1}{e^{\beta\omega_{j,k_{ph}}} - 1}$ the average number of excitations in a phonon mode j at a temperature T given by $\beta = \frac{1}{k_B T}$, and E_i and E_f the energies of the system's Hamiltonian. Through this equation we can see that the transition probability essentially depends on the matrix representation of the coupling operator, $\hat{f}_{j,k_{ph}}$, on the average occupation of the phonon levels, $\langle n_j \rangle$, and on the energy difference between initial and final state. Note that in Eq (8.19) the one–phonon adsorption or emission condition appears naturally through the matrix elements and the Dirac deltas. In order to represent these functions, a normalized bump function is used:

$$
\delta\left(E_f - E_i \pm \hbar\omega_{j,k_{ph}}\right) \approx
\begin{cases}
\frac{1}{\Delta E} e^{-\frac{1}{1-x'}} & \text{if } |\,x'\,| \le 1 \\
0 & \text{if } |\,x'\,| > 1
\end{cases}
\tag{8.20}
$$

with $x' = \left(E_f - E_i \pm \hbar\omega_{j,k_{ph}}\right)\Delta E^{-1}$.

A final constraint must be taken into account: the crystal momentum of the total adsorbate–nanotube system must be conserved, so any momentum gained by the molecule must be subtracted from the phonon bath, and vice versa. Therefore, we can impose:

$$
k_{total} = k_{mol} + \sum_j k_{ph_j} = k'_{mol} + \sum_j k'_{ph_j},
\tag{8.21}
$$

and since only one–phonon transitions are allowed in this model, the values of k_{ph} in Eqs (8.18) and (8.19) are restricted to:

$$
k_{ph} = \left| k_{mol} - k'_{mol} \right|.
\tag{8.22}
$$

With this condition, Eq. (8.19) becomes:

$$
\begin{aligned}
w_{v,n_v,k_{mol}} = \pi \sum_{v',n_v'} \Bigg[&\int_0^{2\pi} \sum_j \frac{\langle n_j \rangle}{\omega_{j,|k_{mol}-k_{mol}'|} N} \left| \left\langle \psi_{v',n_v',k_{mol}} \left| \hat{f}_{j,|k_{mol}-k_{mol}'|} \right| \psi_{v,n_v,k_{mol}} \right\rangle \right|^2 \\
&\times \delta(E_f - \hbar\omega_{j,|k_{mol}-k_{mol}'|} - E_i)\, \mathrm{d}|k_{mol} - k_{mol}'| \\
&+ \int_0^{2\pi} \sum_j \frac{\langle n_j \rangle + 1}{\omega_{j,k_{ph}} N} \left| \left\langle \psi_{v',n_v',k_{mol}} \left| \hat{f}_{j,|k_{mol}-k_{mol}'|} \right| \psi_{v,n_v,k_{mol}} \right\rangle \right|^2 \quad\quad (8.23) \\
&\times \delta(E_f + \hbar\omega_{j,|k_{mol}-k_{mol}'|} - E_i)\, \mathrm{d}|k_{mol} - k_{mol}'| \Bigg],
\end{aligned}
$$

which will be the equation used to obtain the decay rates of any adsorbate initial state caused by the coupling with the phonons of the nanostructure.

8.4 Results and discussion

8.4.1 Adiabatic basis and system eigenstates

In this study we have used the adiabatic representation of the Hamiltonian, as presented in Chapter 7, to compute the adsorbate 6D eigenstates, $\psi_{v,n_v,k_{mol}}$. First, a set of 5D eigenstates of the H_2 molecule within the frozen nanotube approximation, $\{\xi(z)\}$, was computed in order to obtain the cePESs, $\varepsilon_v(z)$. Then the k_{mol}–labeled adiabatic Hamiltonian, Eq. (8.3), was used to obtain the 6D eigenstates for different values of k_{mol} using the SA–MCTDH approach. Recall, k_{mol} accounts for the linear momentum of the adsorbate's c.o.m. A total of 50 wave packets were propagated for 200 values of k_{mol} between 0 and $\frac{2\pi}{L}$, obtaining approximately 40 converged adsorbate eigenstates for each k_{mol} value. These states were found to be distributed among the first five cePES. The energies of the first 22 eigenstates, as well as the associated cePES, are shown in Table 8.1 for $k_{mol} = 0$. These eigenstates correspond to the ones significantly populated at $T = 100\ K$, according to a thermal Boltzmann distribution.

The matrix representation of the coupling operators ($\hat{f}_{j,k}(z)$), given in Eq. (8.14), can be used to extract qualitative information about which phonon modes couple the different cePESs more efficiently. Large matrix elements will point out to strong coupling and therefore a more probable transition between adsorbate states, mediated by the jth phonon. Although these matrix representations are not included in the Thesis for the sake of clarity, some representative examples are highlighted. For instance, the two–fold degenerate lower energy acoustic modes, which correspond to zero–frequency translation modes at the gamma point, $k_{phon} = 0$, couple efficiently cePESs with $v = 0$ and $v = 6$, as well as the $v = 1$ and $v = 8$ cePESs. However, the most efficient coupling appears for the momentum exchange within the same cePES, i.e. transitions of the type $\omega_{(v,n_v,k_{mol}) \to (v,n_v',k_{mol}')}$. These are mediated more strongly by the acoustic modes, and by the optical breathing mode (shown as a dashed line in Figure 8.2). Overall, no clear selection rules apply for these coupling operators.

TABLE 8.1: Eigenenergies of the first 22 eigenstates of the H$_2$ molecule confined in a frozen (8,0) CNT. Energies referred to a Zero–point Energy of 2821.031 cm^{-1}. v labels the cePES, and n_v the adiabatic state within the cePES.

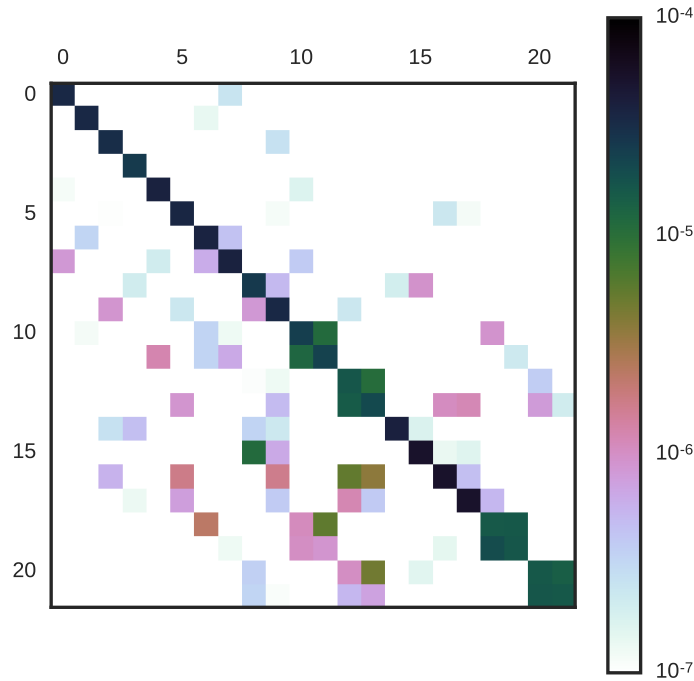| State	v	n_v	$\Delta E(cm^{-1})$
0	0	0	0.000
1	0	1	4.598
2	1	0	16.180
3	1	1	21.272
4	0	2	50.231
5	1	2	63.600
6	0	3	83.513
7	0	4	95.648
8	1	3	98.059
9	1	4	109.133
10	0	5	177.602
11	0	6	178.592
12	1	5	191.889
13	1	6	192.809
14	2	0	297.037
15	3	0	297.037
16	2	1	298.858
17	3	1	298.859
18	0	7	304.033
19	0	8	304.245
20	1	7	318.412
21	1	8	318.616

FIGURE 8.3: Matrix representation of the transition rates of pure adsorbate eigenstates, in reverse atomic units of time, for $T = 100\ K$. Rows correspond to initial states i and columns to final states f. See Tables 8.1 and 8.2 for the characterization of such states in terms of v and n_v.

8.4.2 Decay rates and lifetimes

In order to quantitatively assess the amount of coupling between the phonon bath and the hydrogen molecule we compute the decay rates and lifetimes for a hydrogen molecule in an initial energy state $\psi_{v,n_v,k_{mol}}$, corresponding to a 6D eigenstate in the frozen nanotube model, with no molecular momentum ($k_{mol} = 0$). Due to the coupling to the thermalized phonon bath, the hydrogen molecule might exchange momentum or be excited (or decay) to different vibrorotational confined eigenstates (cePES). The more efficient the coupling, the higher the decay rate and the shorter the lifetime of the initial state.

The resulting state-resolved decaying rates for the first 22 adsorbate eigenstates of the system are shown in Figure 8.3 in a matrix representation form for $T = 100\ K$. Each element of the matrix corresponds to the transition rate of a given initial eigenstate $\psi_i = \psi_{v,n_v,k_{mol}=0}$ to a final state $\psi_f = \psi_{v',n'_v,k'_{mol}}$ with any value of k'_{mol}. It is readily seen from this representation that the most efficient transitions generally correspond to those in the diagonal of the matrix. These elements involve only momentum exchange, because the initial and final state have the same quantum numbers n_v and v. This is consistent with the analysis of the coupling operator matrices. As the energy of the initial state increases, however, interstate transitions become more probable due to the increase of the density of the phonon and adsorbate's eigenstates spectrum.

TABLE 8.2: Lifetimes for the first 22 6D system eigenstates.

State	v	n_v	Lifetime (ns)
0	0	0	$0.6843 \cdot 10^{-3}$
1	0	1	$0.6955 \cdot 10^{-3}$
2	1	0	$0.7213 \cdot 10^{-3}$
3	1	1	$0.8946 \cdot 10^{-3}$
4	0	2	$0.5992 \cdot 10^{-3}$
5	1	2	$0.6100 \cdot 10^{-3}$
6	0	3	$0.5838 \cdot 10^{-3}$
7	0	4	$0.6066 \cdot 10^{-3}$
8	1	3	$0.5994 \cdot 10^{-3}$
9	1	4	$0.6116 \cdot 10^{-3}$
10	0	5	$0.6150 \cdot 10^{-3}$
11	0	6	$0.5838 \cdot 10^{-3}$
12	1	5	$0.5916 \cdot 10^{-3}$
13	1	6	$0.5822 \cdot 10^{-3}$
14	2	0	$0.6077 \cdot 10^{-3}$
15	3	0	$0.4463 \cdot 10^{-3}$
16	2	1	$0.4447 \cdot 10^{-3}$
17	3	1	$0.4382 \cdot 10^{-3}$
18	0	7	$0.6520 \cdot 10^{-3}$
19	0	8	$0.7226 \cdot 10^{-3}$
20	1	7	$0.7049 \cdot 10^{-3}$
21	1	8	$0.7850 \cdot 10^{-3}$

By summing the decay rates for all final states as of Eq. (8.19) (*i. e.* over columns in Figure 8.3) and inverting the resulting quantity, we obtain the lifetime of the different adsorbate eigenstates. These are shown in Table 8.2. Consistently with the state-resolved decay rates and the analysis of the coupling matrix, which showed that the most efficient coupling appeared between states belonging to the same cePES, all system eigenstates have a lifetime of the same order of magnitude, within tenths of picosecond. These values are comparable to the lifetimes obtained for the vibrorotational states of a hydrogen atom adsorbed in an (100) surface of Si by Andrianov and Saalfrank[155], who used a similar model.

It is instructing to compare this timescale with that of the diffusion process calculated in **Publication 3** within a frozen nanotube approximation. The required time to converge the cumulative reaction probability in that work, and therefore to obtain diffusion rates, was around 20 ps. The fact that the lifetimes of the system's eigenstates are 2 orders of magnitude smaller than this value seems to imply that the momentum exchange between the nanotube and the H_2 molecule can produce a significant friction which might alter the diffusion mechanism. A substantial step forward in the study of this system would then be the calculation of diffusion rates on the H_2@SWCNT system including the coupling with the phonon bath. This could be made directly by introducing all new DOFs in a ML–MCTDH scheme. It is known that the a recursive multilayer representation of the wave function allows to carry out propagations efficiently with even thousands of DOFs. Another possibility for further studies is to find a way to relate the transition rates and life–times for momentum exchange to a some sort of phenomenological friction coefficient which can

be externally included as a new term into the 6D calculations presented in the previous Chapters.

8.5 Summary and Conclusions

In this final Chapter we present the first attempt to go beyond the frozen nanostructure approximation which has been used in all the Thesis, as well as in most other works regarding quantum confinement of gaseous molecules. We have done so by using a system–bath coupling Hamiltonian, and defining the H_2 molecule as the system embedded in a bath of harmonic oscillators representing the phonons, being these two fragments coupled by a linear function. We have shortly reviewed the methodology needed to perform the analysis of the phonon modes in a periodic system, and the dependence of this modes with the *crystal momentum* of the material. The frequencies of the phonons have been included in the bath Hamiltonian using a second quantization formalism, and the eigenvectors which transform the Cartesian coordinates of the atoms to the phonon modes have been used to define the coupling functions. Finally, in order to test the model we have computed the transition rates and lifetimes of the eigenstates of the separable system (*i.e.*, the eigenstates of the system–bath Hamiltonian without the coupling term). The equations yielding these quantities have been obtained from Time–dependent Perturbation Theory. The final results confirm that there is indeed a coupling between the adsorbate and the substrate, with the initial functions exchanging a significant amount of momentum with the phonon bath. However, in order to be able to see more relevant transitions between rovibrational levels induced by phonon coupling, further calculations should be done increasing the temperature, so that we populate higher energy levels.

The final conclusions to be extracted from this Chapter are found below:

- A system–bath coupling Hamiltonian is a relatively simple, though effective method for introducing dispersion in a quantum system.

- Time–dependent Perturbation Theory provides us with the means to extract a limited amount of information about the dynamics of the system, such as transition probabilities between different states, without actually running any propagation.

- There is a significant amount of coupling between the nanotube and the H_2 molecule.

- The characteristic times for momentum exchange are two orders of magnitude lower than the total time needed to converge the diffusion calculations. This result suggests the possibility that momentum exchange has a relevant effect on the diffusion process. This observation is in good agreement with the general experience on the importance of phonons in surface diffusion processes.

Chapter 9

Conclusions

The Results of this Thesis are contained in Chapters 5 to 7, each of them containing a Summary and Conclusions section drawing the main ideas to be extracted from it. The aim of this Chapter is therefore to present all the conclusions of the Thesis in an ordered and summarized manner, in order to provide with a general view of the work.

General Conclusions

- Adsorption on cavities with some dimensions of the order of the nanometer induces relevant changes on the internal structure and dynamics of the trapped molecule.

- Confinement effects in the case of the hydrogen and deuterium molecules have to be treated in a full quantum framework in order to obtain physically accurate results.

On the confinement effects in the eigenstates of the adsorbate

- The confining potential of the nanotube introduces new quantizations on the molecular degrees of freedom, as well as a rovibrational–translational coupling which does not exist for the free molecule.

- Due to the couplings between the different degrees of freedom, the confined system cannot be described with the rotational and translational quantum numbers of a separable system.

- The study through overlaps and partial overlaps with a reference separable system provides with the means to identify and understand the system, despite being described through a 5D wave function.

On the diffusion dynamics of H_2 and D_2 along an (8,0) SWCNT

- The motion along the diffusion coordinate is only weakly coupled with the remaining degrees of freedom.

- This quasi–separability can be exploited to obtain an accurate and very efficient adiabatic representation of the Hamiltonian.

- Purely quantum effects dominate the diffusion process of the confined molecules: on one hand, the different ZPE of the isotopologues favor the diffusion of D_2 in

front of H_2 at low temperatures; on the other hand, resonance enhanced tunneling overcompensate ZPE effects and critically increases the diffusion of H_2 at $T < 100$ K.

- The flux correlation function formalism, together with the single–hopping approximation, yields diffusion rates in the low pressure limit in a quantum mechanics framework, which is essential to correctly describe the effects mentioned above, particularly tunneling.

- Time–extended propagations are needed to converge the results of the calculation, mainly due to the low energy barriers and the presence of low–energy resonances.

On the coupling between adsorbate molecule and the nanostructure

- A system–bath coupling model provides with a good framework to study the interaction between the nanotube and the trapped H_2 molecule.

- The lineal momentum exchange between the phonons of the nanostructure and the adsorbate is the most relevant process at low temperatures.

- The characteristic time scale of the linear momentum exchange process, obtained from Time–dependent Perturbation Theory, suggests that this exchange could be relevant for the diffusion process.

Bibliography

(1)   R. P. Feynman, *Journal of Microelectromechanical Systems*, Mar. 1992, **1**, 60–66.

(2)   G Binnig and H Rohrer, *Helvetica Physica Acta*, Dec. 1982, **55**, 726–735.

(3)   G Binnig and H. Rohrer, *Surface Science*, Mar. 1983, **126**, 236–244.

(4)   R. S. Becker, J. A. Golovchenko and B. S. Swartzentruber, *Nature*, Jan. 1987, **325**, 419–421.

(5)   J. S. Foster, J. E. Frommer and P. C. Arnett, *Nature*, Jan. 1988, **331**, 324–6.

(6)   D. M. Eigler and E. K. Schweizer, *Nature*, Apr. 1990, **344**, 524–526.

(7)   G. Binnig and H. Rohrer, *Angewandte Chemie International Edition in English*, July 1987, **26**, 606–614.

(8)   G. Binnig, C. F. Quate and C. Gerber, *Physical Review Letters*, Mar. 1986, **56**, 930–933.

(9)   G. Binnig, *Atomic force microscope and method for imaging surfaces with atomic resolution*, 1988.

(10)   H. W. Kroto, J. R. Heath, S. C. O'Brien, R. F. Curl and R. E. Smalley, *Nature*, Nov. 1985, **318**, 162–163.

(11)   S. Iijima, *Nature*, Nov. 1991, **354**, 56–58.

(12)   S. J. Gregg and K. S. W. Sing, *Adsorption, Surface Area and Porosity*, Academic Press Inc., London, 2nd, 1982, p. 303.

(13)   J. M. Drake and J Klafter, *Physics Today*, May 1990, **43**, 46–55.

(14)   A. C. Dillon, K. M. Jones, T. a. Bekkedahl, C. H. Kiang, D. S. Bethune and M. J. Heben, *Nature*, Mar. 1997, **386**, 377–379.

(15)   I. Holleman, G. von Helden, E. H. T. Olthof, P. J. M. van Bentum, R. Engeln, G. H. Nachtegaal, A. P. M. Kentgens, B. H. Meier, A. van der Avoird and G. Meijer, *Physical Review Letters*, Aug. 1997, **79**, 1138–1141.

(16)   S. A. FitzGerald, T. Yildirim, L. J. Santodonato, D. A. Neumann, J. R. D. Copley, J. J. Rush and F. Trouw, *Physical Review B*, Sept. 1999, **60**, 6439–6451.

(17)   Q. Wang, S. Challa, D. Sholl and J. Johnson, *Physical Review Letters*, Feb. 1999, **82**, 956–959.

(18)   C. Liu, Y. Fan, M. Liu, H. T. Cong and H. M. Cheng, *Science (New York, N.Y.)*, Nov. 1999, **286**, 1127–1129.

(19)   L Schlapbach and A Züttel, *Nature*, Nov. 2001, **414**, 353–358.

(20)   S Dunn, *International Journal of Hydrogen Energy*, Mar. 2002, **27**, 235–264.

(21)   J. J. M. Beenakker, V. D. Borman and S. Y. Krylov, *Physical Review Letters*, Jan. 1994, **72**, 514–517.

(22)   J. Beenakker, V. Borman and S. Krylov, *Chemical Physics Letters*, Jan. 1995, **232**, 379–382.

(23) C. M. Cunningham, D. S. Chapin and H. L. Johnston, *Journal of the American Chemical Society*, May 1958, **80**, 2382–2384.

(24) C. M. Brown, T. Yildirim, D. a. Neumann, M. J. Heben, T. Gennett, a. C. Dillon, J. L. Alleman and J. E. Fischer, *Chemical Physics Letters*, Oct. 2000, **329**, 311–316.

(25) A. Kuznetsova, J. T. Yates, J. Liu and R. E. Smalley, *The Journal of Chemical Physics*, June 2000, **112**, 9590.

(26) P. Dubot and P. Cenedese, *Physical Review B*, June 2001, **63**, 241402.

(27) B. Hathorn, B. Sumpter and D. Noid, *Physical Review A*, July 2001, **64**, 22903.

(28) T. Yildirim and a. B. Harris, *Physical Review B*, Dec. 2002, **66**, 214301.

(29) T. Yildirim and A. Harris, *Physical Review B*, June 2003, **67**, 245413.

(30) W.-L. Yim, O. Byl, J. T. Yates and J. K. Johnson, *The Journal of Chemical Physics*, Mar. 2004, **120**, 5377–5386.

(31) J. L. Atwood, L. J. Barbour and A. Jerga, *Science (New York, N.Y.)*, June 2002, **296**, 2367–2369.

(32) M. R. Johnson, S. Rols, P. Wass, M. Muris, M. Bienfait, P. Zeppenfeld and N. Dupont-Pavlovsky, *Chemical Physics*, Sept. 2003, **293**, 217–230.

(33) A. R. Millward and O. M. Yaghi, *Journal of the American Chemical Society*, Dec. 2005, **127**, 17998–17999.

(34) T. Lu, E. M. Goldfield and S. K. Gray, *The Journal of Physical Chemistry B*, Feb. 2006, **110**, 1742–1751.

(35) G. Garberoglio, M. M. DeKlavon and J. K. Johnson, en, *The Journal of Physical Chemistry B*, Feb. 2006, **110**, 1733–1741.

(36) J. Suarez and F. Huarte-Larrañaga, en, *The Journal of Chemical Physics*, Aug. 2012, **137**, 064320.

(37) A. V. A. Kumar and S. K. Bhatia, *Physical Review Letters*, 2005, **95**, 1–4.

(38) A. V. A. Kumar, H. Jobic and S. K. Bhatia, en, *The Journal of Physical Chemistry. B*, Aug. 2006, **110**, 16666–71.

(39) P. Kumar, F. W. Starr, S. V. Buldyrev and H. E. Stanley, *Physical Review E*, Jan. 2007, **75**, 11202.

(40) M. Hankel, H. Zhang, T. X. Nguyen, S. K. Bhatia, S. K. Gray and S. C. Smith, en, *Physical Chemistry Chemical Physics : PCCP*, May 2011, **13**, 7834–44.

(41) T. X. Nguyen, H Jobic and S. K. Bhatia, *Physical Review Letters*, Aug. 2010, **105**, 085901.

(42) C. I. Contescu, H. Zhang, R. J. Olsen, E. Mamontov, J. R. Morris and N. C. Gallego, *Physical Review Letters*, June 2013, 236102–5.

(43) M. Mondelo-Martell and F. Huarte-Larrañaga, *The Journal of Physical Chemistry A*, Aug. 2016, **120**, 6501–6512.

(44) M. Mondelo-Martell, F. Huarte-Larrañaga and U. Manthe, *The Journal of Chemical Physics*, Aug. 2017, **147**, 084103.

(45) A. Gijón, J. Campos-Martínez and M. I. Hernández, *The Journal of Physical Chemistry C*, Sept. 2017, **121**, 19751–19757.

(46) F. Huarte-Larrañaga and M. Albertí, *Chemical Physics Letters*, Sept. 2007, **445**, 227–232.

(47)   D. Henwood and J. D. Carey, *Physical Review B*, June 2007, **75**, 245413.

(48)   K. E. Gubbins, Y.-C. Liu, J. D. Moore and J. C. Palmer, en, *Physical Chemistry Chemical Physics : PCCP*, Jan. 2011, **13**, 58–85.

(49)   S. J. Kolmann, J. H. D'Arcy and M. J. T. Jordan, *The Journal of Chemical Physics*, Dec. 2013, **139**, 234305.

(50)   P. Kowalczyk, R. Hołyst, M. Terrones and H. Terrones, en, *Physical Chemistry Chemical Physics : PCCP*, Apr. 2007, **9**, 1786–92.

(51)   S. Fatemi, M. Vesali-Naseh, M. Cyrus and J. Hashemi, *Chemical Engineering Research and Design*, Sept. 2011, **89**, 1669–1675.

(52)   S. L. Candelaria, Y. Shao, W. Zhou, X. Li, J. Xiao, J. G. Zhang, Y. Wang, J. Liu, J. Li and G. Cao, *Nano Energy*, Mar. 2012, **1**, 195–220.

(53)   D. Giasafaki, G. Charalambopoulou, C. Tampaxis, K. Dimos, D. Gournis, A. Stubos and T. Steriotis, *Carbon*, Mar. 2016, **98**, 1–14.

(54)   S. A. FitzGerald, K. Allen, P. Landerman, J. Hopkins, J. Matters, R. Myers and J. L. Rowsell, *Physical Review B*, June 2008, **77**, 224301.

(55)   J. L. Belof, A. C. Stern and B. Space, *The Journal of Physical Chemistry C*, May 2009, **113**, 9316–9320.

(56)   G. Garberoglio, *Chemical Physics Letters*, Jan. 2009, **467**, 270–275.

(57)   J.-R. Li, R. J. Kuppler and H.-C. Zhou, en, *Chemical Society Reviews*, May 2009, **38**, 1477.

(58)   I. Matanović, J. L. Belof, B. Space, K. Sillar, J. Sauer, J. Eckert and Z. Bačić, *The Journal of Chemical Physics*, July 2012, **137**, 014701.

(59)   H. Amouri, C. Desmarets and J. Moussa, *Chemical Reviews*, Apr. 2012, **112**, 2015–2041.

(60)   S. A. FitzGerald, C. J. Pierce, J. L. C. Rowsell, E. D. Bloch and J. A. Mason, *Journal of the American Chemical Society*, June 2013, **135**, 9458–9464.

(61)   T. Pham, K. A. Forrest, E. H. L. Falcão, J. Eckert and B. Space, en, *Physical Chemistry Chemical Physics : PCCP*, Jan. 2016, **18**, 1786–1796.

(62)   H. Oh and M. Hirscher, *European Journal of Inorganic Chemistry*, Sept. 2016, **2016**, 4278–4289.

(63)   M. Kishima, H. Mizuhata and T. Okubo, *The Journal of Physical Chemistry. B*, July 2006, **110**, 13889–96.

(64)   C. Xue, Z. Zhou, B. Liu, Q. Yang and C. Zhong, *Molecular Simulation*, Apr. 2009, **35**, 373–380.

(65)   S.-S. Park, S.-B. Lee and N.-J. Kim, *Journal of Industrial and Engineering Chemistry*, July 2010, **16**, 551–555.

(66)   R. B. Getman, Y.-S. Bae, C. E. Wilmer and R. Q. Snurr, EN, *Chemical Reviews*, Feb. 2012, **112**, 703–723.

(67)   J.-R. Li, Y. Ma, M. C. McCarthy, J. Sculley, J. Yu, H.-K. Jeong, P. B. Balbuena and H.-C. Zhou, *Coordination Chemistry Reviews*, Aug. 2011, **255**, 1791–1823.

(68)   T. X. Nguyen and S. K. Bhatia, *Langmuir*, Jan. 2008, **24**, 146–154.

(69)   A. Valdés, D. J. Arismendi-Arrieta and R. Prosmiti, *Journal of Physical Chemistry C*, Feb. 2015, **119**, 3945–3956.

(70) O. Byl, J.-C. Liu, Y. Wang, W.-L. Yim, J. K. Johnson and J. T. Yates, *Journal of the American Chemical Society*, Sept. 2006, **128**, 12090–12097.

(71) C. Beduz, M. Carravetta, J. Y.-C. Chen, M. Concistrè, M. Denning, M. Frunzi, A. J. Horsewill, O. G. Johannessen, R. Lawler, X. Lei, M. H. Levitt, Y. Li, S. Mamone, Y. Murata, U. Nagel, T. Nishida, J. Ollivier, S. Rols, T. Rõõm, R. Sarkar, N. J. Turro and Y. Yang, *Proceedings of the National Academy of Sciences of the United States of America*, Aug. 2012, **109**, 12894–12898.

(72) M. K. Tripathy, K. R. S. Chandrakumar and S. K. Ghosh, en, AIP Conference Proceedings, American Institute of Physics, Feb. 2013, vol. 1512, pp. 168–169.

(73) G. Pérez-Hernández and B. Schmidt, *Physical Chemistry Chemical Physics : PCCP*, Apr. 2013, **15**, 4995–5006.

(74) S. M. Fatemi and M. Foroutan, *International Journal of Environmental Science and Technology*, Dec. 2016, **13**, 457–470.

(75) S. Mamone, J. Y.-C. C. Chen, R. Bhattacharyya, M. H. Levitt, R. G. Lawler, A. J. Horsewill, T. Rõõm, Z. Bačić and N. J. Turro, *Coordination Chemistry Reviews*, July 2011, **255**, 938–948.

(76) P. M. Felker and Z. Bačić, *The Journal of Chemical Physics*, Aug. 2016, **145**, 084310.

(77) M. Xu, S. Ye, R. Lawler, N. J. Turro and Z. Bačić, *Philosophical transactions. Series A, Mathematical, physical, and engineering sciences*, Sept. 2013, **371**, 20110630–15.

(78) P. M. Felker and Z. Bačić, *The Journal of Chemical Physics*, May 2016, **144**, 201101.

(79) S. Ye, M. Xu, S. Fitzgerald, K. Tchernyshyov and Z. Bačić, *The Journal of Chemical Physics*, June 2013, **138**, 244707.

(80) S. Ye, M. Xu, Z. Bacić, R. Lawler and N. J. Turro, *The Journal of Physical Chemistry A*, Sept. 2010, **114**, 9936–47.

(81) P Paniagua J.C.; Alemany, *Química Quàntica*, Llibres de l'Índex, Universitat de Barcelona, 1995.

(82) D. J. Tannor, *Introduction to Quantum Mechanics: A Time-Dependent Perspective*, University Science Books, Sausalito, 1st, 2007, p. 662.

(83) J. S. Briggs and J. M. Rost, *Foundations of Physics*, Sept. 2001, **31**, 693–712.

(84) R Schinke, *Photodissociation Dynamics: Spectroscopy and Fragmentation of Small Polyatomic Molecules*, Cambridge University Press, 1995.

(85) M. Born and R. Oppenheimer, *Annalen der Physik*, Aug. 1927, **389**, 457–484.

(86) G. A. Worth and L. S. Cederbaum, en, *Annual review of physical chemistry*, Jan. 2004, **55**, 127–158.

(87) D. Marx and J. Hutter, NIC Series Vol. 3: Modern Methods and Algorithms of Quantum Chemistry, ed. J. Grotendors, John von Neumann Institute for Computing, Jülich, Germany, 2nd, 2000, ch. Ab-initio, pp. 301–449.

(88) D Kosloff and R Kosloff, *Journal of Computational Physics*, Oct. 1983, **52**, 35–53.

(89) J. C. Light, I. P. Hamilton and J. V. Lill, en, *The Journal of Chemical Physics*, Feb. 1985, **82**, 1400–1409.

(90) E. A. McCullough and R. E. Wyatt, *The Journal of Chemical Physics*, Aug. 1969, **51**, 1253–1254.

(91)   R. Kosloff, *Dynamics of molecules and chemical reactions*, 1996, ed. R. R. E. Wyatt and J. Z. H. Zhang, 185–230.

(92)   M Beck, A. Jäckle, G. A. Worth and H.-D. Meyer, *Physics Reports*, Jan. 2000, **324**, 1–105.

(93)   D. O. Harris, G. G. Engerholm and W. D. Gwinn, *The Journal of Chemical Physics*, Sept. 1965, **43**, 1515–1517.

(94)   J. C. Light and T. Carrington, in *Advances in Chemical Physics*, ed. I. Prigogine and S. A. Rice, John Wiley & Sons, Inc., Mar. 2007, pp. 263–310.

(95)   R. Kosloff, *The Journal of Physical Chemistry*, Apr. 1988, **92**, 2087–2100.

(96)   J. M. Perxachs, Ph.D. Thesis, Universitat de Barcelona, Departament de Química Física, Barcelona, Oct. 2007.

(97)   H. Tal-Ezer and R. Kosloff, *The Journal of Chemical Physics*, Nov. 1984, **81**, 3967–3971.

(98)   T. J. Park and J. C. Light, *The Journal of Chemical Physics*, Nov. 1986, **85**, 5870–5876.

(99)   A. Askar and A. S. Cakmak, *The Journal of Chemical Physics*, Mar. 1978, **68**, 2794.

(100) M. Feit, J. Fleck and A. Steiger, *Journal of Computational Physics*, Sept. 1982, **47**, 412–433.

(101) R. Heather and H. Metiu, *The Journal of Chemical Physics*, May 1987, **86**, 5009–5017.

(102) C. Lubich, *From Quantum to Classical Molecular Dynamics: Reduced Models and Numerical Analysis*, European Mathematical Society, 2000.

(103) H.-D. Meyer, U. Manthe and L. Cederbaum, *Chemical Physics Letters*, Jan. 1990, **165**, 73–78.

(104) A. D. McLachlan and M. A. Ba, *Reviews of Modern Physics*, July 1964, **36**, 844–855.

(105) H. D. Meyer, F. Gatti and G. A. Worth, *Multidimensional Quantum Dynamics: MCTDH Theory and Applications*, ed. H.-D. Meyer, F. Gatti and G. A. Worth, Wiley-VCH Verlag GmbH & Co. KGaA, Weinheim, Germany, Apr. 2009, pp. 1–419.

(106) U. Manthe, H.-D. Meyer and L. S. Cederbaum, *The Journal of Chemical Physics*, Sept. 1992, **97**, 3199–3213.

(107) G. A. Worth, H.-D. Meyer and L. S. Cederbaum, *The Journal of Chemical Physics*, Sept. 1996, **105**, 4412.

(108) H.-D. Meyer, en, *Wiley Interdisciplinary Reviews: Computational Molecular Science*, Mar. 2012, **2**, 351–374.

(109) M. Nest and H.-D. Meyer, *The Journal of Chemical Physics*, July 2003, **119**, 24–33.

(110) H. Wang, M. Thoss and W. H. Miller, *The Journal of Chemical Physics*, Aug. 2001, **115**, 2979–2990.

(111) H. Wang, *The Journal of Chemical Physics*, Dec. 2000, **113**, 9948–9956.

(112) F. Huarte-Larrañaga and U. Manthe, en, *The Journal of Chemical Physics*, Oct. 2000, **113**, 5115.

(113) R. Welsch, F. Huarte-Larrañaga and U. Manthe, *The Journal of Chemical Physics*, Feb. 2012, **136**, 064117.

(114) R. Welsch and U. Manthe, *The Journal of Chemical Physics*, Nov. 2014, **141**, 174313.

(115) R. Welsch and U. Manthe, *The Journal of Chemical Physics*, Aug. 2014, **141**, 051102.

(116) B. Zhao, D.-H. Zhang, S.-Y. Lee and Z. Sun, *The Journal of Chemical Physics*, Apr. 2014, **140**, 164108.

(117) R. Welsch and U. Manthe, *The Journal of Chemical Physics*, Feb. 2015, **142**, 064309.

(118) O. Vendrell, F. Gatti, D. Lauvergnat and H.-D. Meyer, *The Journal of Chemical Physics*, Nov. 2007, **127**, 184302.

(119) O. Vendrell, F. Gatti and H.-D. Meyer, *The Journal of Chemical Physics*, Nov. 2007, **127**, 184303.

(120) M. D. Coutinho-Neto, A. Viel and U. Manthe, *The Journal of Chemical Physics*, Nov. 2004, **121**, 9207–9210.

(121) T. Hammer, M. D. Coutinho-Neto, A. Viel and U. Manthe, *The Journal of Chemical Physics*, Dec. 2009, **131**, 224109.

(122) H. Wang and M. Thoss, en, *The Journal of Chemical Physics*, July 2003, **119**, 1289.

(123) H. Wang, *Journal of Physical Chemistry A*, July 2015, **119**, 7951–7965.

(124) U. Manthe, *The Journal of Chemical Physics*, Feb. 2008, **128**, 64108–12.

(125) T. Hammer and U. Manthe, *The Journal of Chemical Physics*, Feb. 2012, **136**, 54105–17.

(126) M. Beck and H.-D. Meyer, *Zeitschrift für Physik D Atoms, Molecules and Clusters*, Nov. 1997, **42**, 113–129.

(127) U. Manthe, *Chemical Physics*, Oct. 2006, **329**, 168–178.

(128) U. Manthe, *Journal of Physics: Condensed Matter*, June 2017, **29**, 253001.

(129) U. Manthe, *The Journal of Chemical Physics*, June 2015, **142**, 244109.

(130) F. Gatti and C. Iung, *Physics Reports*, Nov. 2009, **484**, 1–69.

(131) A. Jäckle and H.-D. Meyer, *The Journal of Chemical Physics*, May 1996, **104**, 7974–7984.

(132) D. Peláez and H.-D. Meyer, *The Journal of Chemical Physics*, Jan. 2013, **138**, 014108.

(133) U. Manthe and F. Matzkies, *Chemical Physics Letters*, Apr. 1996, **252**, 71–76.

(134) W. H. Miller, S. D. Schwartz and J. W. Tromp, *The Journal of Chemical Physics*, 1983, **79**, 4889–4898.

(135) M. S. Dresselhaus and P. C. Eklund, *Advances in Physics*, Sept. 2000, **49**, 705–814.

(136) *Carbon Nanotubes*, ed. A. Jorio, G. Dresselhaus and M. S. Dresselhaus, Springer Berlin Heidelberg, Berlin, Heidelberg, 2008, vol. 111, p. 720.

(137) N. W. Ashcroft and N. D. Mermin, *Solid state physics*, Harcourt College Publishers, Orlando, 1st, 1976.

(138) H. Ibach and H. Lüth, *Solid-State Physics*, Springer Berlin Heidelberg, Berlin, Heidelberg, 2009, pp. 1–533.

(139) R. Hoffmann, *Angewandte Chemie International Edition in English*, Sept. 1987, **26**, 846–878.

(140) R. Dovesi, B. Civalleri, C. Roetti, V. R. Saunders and R. Orlando, in *Reviews in Computational Chemistry*, Jan. 2005, vol. 21, pp. 1–125.

(141) R. Dovesi, R. Orlando, B. Civalleri, C. Roetti, V. R. Saunders, C. M. Zicovich-Wilson, F. Pascale, K. Doll, N. M. Harrison, I. J. Bush, P. D'Arco and M. Llunell, *Crystal 09 User's Manual*, Torino, 2009.

(142) R. Dovesi, R. Orlando, B. Civalleri, C. Roetti, V. R. Saunders and C. M. Zicovich-Wilson, *Zeitschrift für Kristallographie*, May 2005, **220**, 571–573.

(143) P. Morse, *Physical Review*, July 1929, **34**, 57–64.

(144) S. J. V. Frankland and D. W. Brenner, *Chemical Physics Letters*, Feb. 2001, **334**, 18–23.

(145) D. Neuhauser, *The Journal of Chemical Physics*, Aug. 1990, **93**, 2611–2616.

(146) V. A. Mandelshtam and H. S. Taylor, *The Journal of Chemical Physics*, Mar. 1997, **106**, 5085.

(147) J. Bigeleisen, *The Journal of Chemical Physics*, Aug. 1949, **17**, 675–678.

(148) W. H. Miller, *The Journal of Chemical Physics*, Sept. 1974, **61**, 1823–1834.

(149) T. Yamamoto, *The Journal of Chemical Physics*, July 1960, **33**, 281.

(150) F. Huarte-Larrañaga and U. Manthe, *Zeitschrift für Physikalische Chemie*, Feb. 2007, **221**, 171–213.

(151) F. Matzkies and U. Manthe, *Journal of Chemical Physics*, Feb. 1997, **106**, 2646–2653.

(152) D. H. Zhang, J. C. Light and S.-Y. Y. Lee, *The Journal of Chemical Physics*, 1999, **111**, 5741–5753.

(153) J Barth, *Surface Science Reports*, Oct. 2000, **40**, 75–149.

(154) D. Skouteris and A. Laganà, *Chemical Physics Letters*, June 2013, **575**, 18–22.

(155) I. Andrianov and P. Saalfrank, en, *The Journal of Chemical Physics*, Jan. 2006, **124**, 034710.

(156) M. Bonfanti, B. Jackson, K. H. Hughes, I. Burghardt and R. Martinazzo, *The Journal of Chemical Physics*, Sept. 2015, **143**, 124703.

(157) M. Bonfanti, B. Jackson, K. H. Hughes, I. Burghardt and R. Martinazzo, *The Journal of Chemical Physics*, Sept. 2015, **143**, 124704.

(158) Q. Meng and H.-D. Meyer, *The Journal of Chemical Physics*, Oct. 2015, **143**, 164310.

(159) U. Weiss, *Quantum Dissipative Systems*, World Scientific, Singapore, 4th, Mar. 2012.

(160) G. Kresse and J. Hafner, *Physical Review B*, Jan. 1993, **47**, 558–561.

(161) G. Kresse and J. Furthmüller, *Computational Materials Science*, July 1996, **6**, 15–50.

(162) G. Kresse and J. Furthmüller, *Physical Review B*, Oct. 1996, **54**, 11169–11186.

(163) O. Dubay and G. Kresse, *Physical Review B*, Jan. 2003, **67**, 035401.

(164) D. Alfè, *Computer Physics Communications*, Dec. 2009, **180**, 2622–2633.

(165) G Kresse, J Furthmüller and J Hafner, *Europhysics Letters (EPL)*, Dec. 1995, **32**, 729–734.

(166) D. Alfè, G. D. Price and M. J. Gillan, *Physical Review B*, July 2001, **64**, 045123.